Novel technologies for transdermal delivery of active molecules

Mehrsa Rafie Jirdehi

THÈSE

Pour obtenir le grade de

DOCTEUR DE L'UNIVERSITÉ GRENOBLE ALPES

École doctorale : PHYS - Physique
Spécialité : Physique des matériaux
Unité de recherche : Laboratoire d'Innovation pour les Technologies des Energies Nouvelles (LITEN - CEA)

Nouvelles technologies pour la délivrance transcutanée de molécules actives

Novel technologies for transdermal delivery of active molecules

Présentée par :

Mehrsa RAFIE JIRDEHI

Direction de thèse :

Amélie REVAUX DIRECTRICE DE RECHERCHE, CEA CENTRE DE GRENOBLE	Directeur de thèse
Dorothée JARY CEA	Co-encadrante de thèse
Pascale PHAM DIRECTRICE DE RECHERCHE, CEA CENTRE DE GRENOBLE	Co-encadrante de thèse

Rapporteurs :

YOGESHVAR KALIA
FULL PROFESSOR, UNIVERSITE DE GENEVE
DAVIDE BRAMBILLA
ASSOCIATE PROFESSOR, UNIVERSITE DE MONTREAL

Thèse soutenue publiquement le **17 novembre 2023**, devant le jury composé de :

YOGESHVAR KALIA FULL PROFESSOR, UNIVERSITE DE GENEVE **DAVIDE**	Rapporteur
BRAMBILLA ASSOCIATE PROFESSOR, UNIVERSITE DE MONTREAL	Rapporteur
CONOR O'MAHONY SENIOR SCIENTIST, UNIVERSITY COLLEGE CORK	Examinateur
SOPHIE BLAISE PROFESSEURE DES UNIVERSITES, PRATICIENNE HOSPITALIERE, UNIVERSITE GRENOBLE ALPES	Présidente

Invités :

GILLES RICHARD
DIRECTEUR DE RECHERCHE, SEPTODONT
GAËLLE OFFRANC-PIRET
CHARGEE DE RECHERCHE HDR, ININSERM DELEGATION AUVERGNE RHONE-ALPES

A Dorothée,

Contents

Abstract

Transdermal delivery of active molecules being a developing research area, this thesis aims to study different technologies allowing a fast and painless drug release through a patch system. Particular attention is given to biomolecules such as proteins as they are even more challenging to deliver transdermally because of their important size. Two technologies are considered in this project to enhance protein delivery.

- Microneedles are micron to millimeter size tips used to painlessly perforate the outermost layer of the skin, the *stratum corneum*, which acts as an environmental barrier. The use of a biobased, biocompatible and bioresorbable material (PLA, PGA, PLGA) is preferred to provide safe, sustainable and customizable hollow microneedle arrays depending on the desired therapeutic application. Industrializable manufacturing processes (thermoforming, injection molding, 3D-printing) are also explored to study the viability of this technology on a larger scale.
- Iontophoresis is an electrically-assisted drug delivery technique causing the migration of ions under the effect of an electric field. Screen-printed flexible Ag/AgCl electrodes are used as sacrificial electrodes to avoid undesired electrochemical reactions in skin interstitial fluids (water electrolysis). Electrochemical characterizations (chronopotentiometry, electrochemical impedance spectroscopy) and numerical simulations are used to monitor electrode wear, understand diffusion mechanisms and avoid the risk of burns.

Finally, protein delivery is studied in a skin phantom, comparing their passive diffusion to the use of microneedles, iontophoresis and their combination. In the latter case, promising results are obtained, paving the way to continuous transdermal delivery of macromolecules such as insulin for patients with diabetes.

Keywords: *transdermal drug delivery, microneedles, iontophoresis, biomaterials, wearable device, stretchable electrodes*

Résumé

La délivrance de molécules actives par voie transdermique étant un sujet de recherche en développement, cette thèse vise à étudier différentes technologies permettant une libération rapide et indolore de médicaments par le biais d'un système de patch. Une attention particulière est accordée aux biomolécules telles que les protéines, qui sont plus difficiles à administrer par voie transdermique en raison de leur taille importante. Deux technologies sont considérées dans ce projet pour améliorer l'administration de protéines.

1. Les microaiguilles sont des pointes de taille micrométrique à millimétrique utilisées pour perforer de façon indolore la couche externe de la peau, le *stratum corneum*, qui agit comme une barrière environnementale. L'utilisation d'un matériau biosourcé, biocompatible et biorésorbable (PLA, PGA, PLGA) est préférable pour fournir des microaiguilles creuses sûres, durables et personnalisables selon l'application thérapeutique souhaitée. Des procédés de fabrication industrialisables (thermoformage, injection plastique, impression 3D) sont explorés pour étudier la viabilité de cette technologie à plus grande échelle.
2. L'ionophorèse est une technique d'administration de médicaments assistée électriquement provoquant la migration d'ions sous l'effet d'un champ électrique. Des électrodes Ag/AgCl sérigraphiées et flexibles sont utilisées comme électrodes sacrificielles afin d'éviter des réactions électrochimiques parasites dans les fluides interstitiels de la peau (électrolyse de l'eau). Des caractérisations électrochimiques (chronopotentiométrie, spectroscopie d'impédance électrochimique) et des simulations numériques sont utilisées pour suivre l'usure des électrodes, comprendre les mécanismes de diffusion et éviter les risques de brûlures.

Enfin, la délivrance de protéines est étudiée dans un fantôme de peau en comparant leur diffusion passive à l'utilisation de microaiguilles, d'ionophorèse et de leur combinaison. Dans ce dernier cas, des résultats prometteurs sont obtenus, ouvrant la voie à la délivrance transdermique continue de macromolécules telles que l'insuline pour les patients diabétiques.

Mots-clés : *Délivrance transdermique, microaiguilles, ionophorèse, biomatériaux, dispositif porté, électrodes étirables*

Acknowledgments

French version below

It is often customary to wait until PhD graduation before adding the Acknowledgments section. I personally believe that we are grateful to the road we travelled rather than the final destination. No matter the outcome, the past three years have been extremely enriching, both from a scientific and a human point of view.

First, I would like to warmly thank my **supervisors**, Dorothée Jary, Amélie Revaux and Pascale Pham for everything they taught me.

Dorothée, thank you for initiating my PhD subject and for your presence during the first year. You also taught me how precious health is and how it must always remain a priority. I wish we had spent more time together, but I hope you have found peace where you are. It was an honor to be your last PhD student and I will always cherish your memory.

Amélie, I am grateful to you for relentlessly taking me under your wing during these past three years, for protecting me like a second mother and for always having the right words not to offend my sensibilities. I am very lucky to have you as both supervisor and thesis director, you made this experience as simple as possible (relatively speaking…).

Pascale, you are truly the most rock'n'roll physicist I know and I am glad I was able to cross your path halfway through this journey. Your high standards allowed me to step out of my comfort zone and venture into very scary fields that are electrokinetics and numerical modeling. I also admire you for your connection to nature, mountains, animals, not to mention the most incomprehensible of all categories in my opinion, children.

I also would like to thank **the lab and service managers** that allowed me to join their team: Christophe Serbutoviez, Audrey Martinent and Séverine Vignoud. Special thanks to Christophe for the interest you showed in my project and the trust you placed in me from the beginning of my PhD. Your ability to unblock all kinds of situations helped me a lot. You also spotted my willingness to interact with research teams from all over the world, and I thank you for the opportunities you gave me.

I could write dozens of pages to thank my colleagues one by one, but I will try to keep it short. Although I met you all with a surgical mask, your faces and your smiles will always be engraved in my memory.

Thanks to **PhD students from Liten**: those I barely met before they defended (Amélie S., Agathe, Marie F.), those I started my PhD with (Lucile, Fatine), those I saw finishing their PhD one by one (Florian, Thibault, Javier, Valentin), and those I had the pleasure to welcome (Auriane, Simon T., Loïc, Joseph, Jakob). The second half of my journey at CEA brought me to the **PhD students from**

Leti: Mathilde, Antoine, Natalie, Juliette, Maxime, Paul, Thibaut, Louis, Pierre, Bastien, Lénaïc, Amelia, Marta, Axelle, Marie-Hélène and Rémy.

I also saw many **interns** come and go every year and each encounter was unique. The summer of 2021 was particularly special with our "7 dwarfs" who will identify themselves and be remembered. I would like to wish Adéléyè a good start to his PhD, as I understand he was unable to leave us after his internship. I finally thank Emilie N. for working on my project, I wish I could have been more present for you during this period and I apologize for this.

I warmly thank the **technicians and engineers** who helped me in my project and to whom I owe the biggest part of my thesis. I think of my screen-printing fellows, Cyrille, Séverine D., David, Jamal, Moh, and obviously Adélaïde without whom I would not have enjoyed my time in the cleanroom the same. I would also like to thank Simon C. and Cédric, who helped me complete the crazy (but successful) project of thermoforming microneedles. Special thanks to the electrochemists who adopted me as a part-time member of their team: Pascal, Mélanie, Maxime G., Fred, Yohann, Ayman, Charles, Gauthier and Ilaria. Thanks to the biomaterials team as well for allowing this research topic to exist: Marie, Dom, Emilie R., Laurabelle, Sacha, Claire V., Murielle, Antoine H. and Isabelle. Finally, thanks to Fabrice, Romain, Julien, Stéphanie, Karine, Didier, the Y-Spot FabLab and the DTBS microfabrication team, whom I have annoyed punctually but repeatedly over the past three years.

I am equally grateful to those who opened their doors to me for a chat, shared a cup of coffee with me, or simply checked up on me as I passed in the hallways. Among people I did not mention so far, I think about Christelle, Helga, Elodie T., Venceslass, Lina, Jean-Marie, Antoine L., Elodie F., Mahfod, Nico, Caro, Marion, Véro, and all the members of the "DTBeerS" group. Special thanks to Xavier, my poster-taxi, with whom I shared hours of train rides more or less on time.

I obviously have to dedicate an exclusive paragraph to my officemate, Laurent. Thank you for making me feel (maybe too) comfortable despite the unbeatable level of the previous PhD students at this desk. Thank you for all our discussions with many words, the "pipotrons", the homemade cheese tastings in the morning, the puff pastries, the hot water ready when I arrive for my tea, the great tests and many more kind attentions behind your fake grumpy face… I am going to miss the control tower, I hope the succession will be well assured!

Just a word for my one-month colleagues from the Lab Science Interface at the Tyndall National Institute of Cork, Ireland: thanks to Ryan, Andrea, Carlota, Claudia, Ajay, Bharathesh, Dennis, Om, Eileen, Eamonn, Sofia and Walter for your warm welcome. I am extremely grateful to Conor O'Mahony for giving me this opportunity. Special thoughts for Ryan for all the work done with Rebecca and me, you have been the greatest lab mate.

I will finish this paragraph by thanking the Verplanck family for taking care of my four-legged son during my stay in Ireland, as well as for offering me their cosy home as a writing residency last summer. Thanks to you, I know exactly how I to set my future home office!

I am really grateful for all these enriching encounters and I am sorry not to mention everyone. It has been a pleasure interacting with all of you. I remain convinced that fluid, sincere and selfless communication is the key to many problems, both professionally and personally.

I would also like to mention my long and less long-time **friends** with varying degrees of understanding of my research area. I am far from being an exemplary friend, I am the worst at expressing my feelings, but I am happy to count you in my close circle and my door will always be open to you. Camille, Claire, Jennifer, thank you for being a listening ear whenever I need to complain – thankfully it is not that frequent.

Finally, I would like to dedicate a paragraph to my dear **family**. Daughter of a PhD and a MD, sister of a lawyer, I strive to live up to the education and the values you have taught me. Mom, I know you do not always agree with my choices and that you always worry about me regardless of my age or the distance between us. Thank you for your presence and I hope to make you proud anyways. Dad, thank you for your tips and reassuring words throughout this journey. I still remember your defense when I was 6 years old – if I had known at that time that I would do a PhD, I would have listened more carefully instead of focusing on the pastries on the table. Sis, I am not the most affectionate of little sisters, but I see all you do for me and I thank you for your unfailing support over the years.

I would also like to thank my fiancé for continuously pushing me to my limits, supporting me in my craziest decisions and being a peaceful ally when I am feeling stressed and unsure. We sure have many more obstacles to overcome, starting with Canadian bureaucracy, but I am glad to take these steps with you. I will end this section by thanking my biggest moral support of all time even though it may sound silly to some people: my adorable dog. Thank you for your unconditional love, for cheering me up when I come back from work (or even the toilets), and for forcing me to go for a walk even when I do not feel like it. Adopting you during my PhD was one of the aforementioned crazy decisions, but it would have been a complete different experience without you.

Remerciements

Il est souvent coutume d'attendre la remise du diplôme de Docteur avant d'ajouter la section Remerciements. Je pense personnellement que nous sommes reconnaissants du chemin parcouru plutôt que de la destination finale. Quelle qu'en soit l'issue, les trois dernières années ont été extrêmement enrichissantes, tant d'un point de vue scientifique qu'humain.

Tout d'abord, j'aimerais remercier chaleureusement mes **encadrantes**, Dorothée Jary, Amélie Revaux et Pascale Pham, pour tout ce qu'elles m'ont appris.

Dorothée, je te remercie d'avoir été à l'origine de mon sujet de doctorat et de ta présence lors de ma première année. Tu m'as également appris à quel point la santé est précieuse et doit toujours rester une priorité. J'aurais aimé que nous passions plus de temps ensemble, mais j'espère que tu as trouvé la paix là où tu es. C'était un honneur d'être ta dernière doctorante et je chérirai ta mémoire pour toujours.

Amélie, je te suis reconnaissante de m'avoir pris sous ton aile sans relâche durant ces trois dernières années, de m'avoir protégé comme une deuxième maman et de toujours avoir eu les mots justes pour ne pas heurter ma sensibilité. Je suis très chanceuse de t'avoir eu à la fois en encadrante et en directrice de thèse, tu as rendu cette expérience aussi simple que possible (relativement parlant…).

Pascale, tu es la physicienne la plus rock'n'roll que je connaisse et je suis heureuse d'avoir pu te croiser à mi-chemin de ce parcours. Ton exigence m'a permis de sortir de ma zone de confort et de m'aventurer dans les domaines très effrayants que sont l'électrocinétique et la modélisation numérique. Je t'admire également pour ta connexion à la nature, la montagne, les animaux, sans parler de la plus incompréhensible des catégories selon moi, les enfants.

J'aimerais aussi remercier les **chefs de laboratoire et de service** qui m'ont permis d'intégrer leur équipe : Christophe Serbutoviez, Audrey Martinent et Séverine Vignoud. Je remercie particulièrement Christophe pour l'intérêt que tu as porté à mon projet et pour la confiance que tu m'as témoignée dès le début de mon doctorat. Ta capacité à débloquer toutes sortes de situations m'a énormément aidé. Tu as également repéré en moi ma volonté d'interagir avec des équipes de recherche du monde entier et je te remercie pour les opportunités que tu m'as offertes.

Je pourrais écrire des dizaines de pages pour remercier mes **collègues** un à un, mais je vais tenter de rester concise. Bien que je vous aie tous rencontré pour la première fois avec un masque chirurgical, vos visages et vos sourires resteront gravés dans ma mémoire.

Je remercie les **thésards et thésardes** du Liten : celles que j'ai très peu connu (Amélie S., Agathe, Marie F.), ceux que j'ai vu partir un à un (Florian, Thibault, Javier, Valentin), celles avec qui je suis arrivées (Lucile, Fatine), et ceux que j'ai eu le plaisir d'accueillir (Auriane, Simon, Loïc, Joseph, Jakob). La seconde moitié de mon séjour au CEA m'a également mis sur le chemin des thésards du Leti :

Mathilde, Antoine, Natalie, Juliette, Maxime L., Paul, Thibaut, Louis, Pierre, Bastien, Lénaïc, Amelia, Marta, Axelle, Marie-Hélène et Rémy.

J'ai également vu de nombreux **stagiaires** arriver puis repartir et chaque rencontre fut unique. L'été 2021 était un cru tout particulier avec nos « 7 nains » qui se reconnaîtront et resteront mémorables. Je souhaite également un bon début de thèse à Adéléyè qui n'a, je comprends, pas réussi à nous quitter suite à son stage. Je remercie enfin Emilie N. qui a travaillé sur mon projet, j'aurais aimé être davantage présente pour toi durant cette période et je m'en excuse.

Je remercie chaleureusement les **techniciens et ingénieurs** qui m'ont aidé dans mon projet et à qui je dois la plus grosse partie de ma thèse. Je pense à mes camarades de sérigraphie, Cyrille, Séverine D., David, Jamal, Moh, et évidemment Adélaïde sans qui je n'aurais pas aussi bien vécu toutes ces heures en salle blanche. Je remercie également Simon C. et Cédric qui m'ont permis de mener à bien le projet assez fou (mais réussi) de thermoformer des microaiguilles. Une pensée pour les électrochimistes qui m'ont adopté à temps partiel dans leur équipe : Pascal, Mélanie, Maxime G., Fred, Yohann, Ayman, Charles, Gauthier et Ilaria. Merci à l'équipe biomatériaux de faire exister cette thématique : Marie, Dom, Emilie R., Laurabelle, Sacha, Claire V., Murielle, Antoine H. et Isabelle. Enfin, merci à Fabrice, Romain, Julien, Stéphanie, Karine, Didier, le FabLab du Y-Spot et l'équipe de microfabrication du DTBS que j'ai embêté de façon ponctuelle mais répétée au cours de ces trois ans.

Je remercie tout autant ceux qui m'ont ouvert leurs portes pour discuter, qui ont partagé un café avec moi, ou simplement pris de mes nouvelles en me croisant dans un couloir. Parmi ceux que je n'ai pas cité précédemment, je pense à Christelle, Helga, Elodie T., Venceslass, Lina, Jean-Marie, Antoine L., Elodie F., Mahfod, Nico, Caro, Marion, Véro, et tous les membres du groupe « DTBièreS ». Une pensée particulière pour Xavier, mon taxi-poster, avec qui j'ai partagé des heures de trains avec plus ou moins de retard.

Je dois bien évidemment dédier un paragraphe exclusif à mon co-bureau, Laurent. Merci de m'avoir mis très (peut-être trop) à l'aise dès mon arrivée malgré le niveau imbattable de mes prédécesseurs thésards à ce même poste. Je te remercie pour les discussions avec beaucoup de mots, les pipotrons, les dégustations de fromages maisons dès le matin, les chouquettes, l'eau bouillante déjà prête pour mon thé, les grands tests, et toutes les autres gentilles attentions derrière ce faux air grincheux… La tour de contrôle va me manquer, j'espère que la relève sera bien assurée !

Un mot également pour mes collègues d'un mois du « Lab Science Interface » au Tyndall National Institute à Cork, en Irlande : merci à Ryan, Andrea, Carlota, Claudia, Ajay, Bharathesh, Dennis, Om, Eileen, Eamonn, Sofia et Walter pour votre accueil dans l'équipe. Merci à Conor O'Mahony de m'avoir donné cette opportunité, j'en suis extrêmement reconnaissante. Une pensée particulière pour Ryan pour tout le travail accompli avec Rebecca et moi, tu as été le meilleur des partenaires de laboratoire.

Je finirai ce paragraphe en remerciant la famille Verplanck d'avoir pris soin de mon enfant à quatre pattes pendant mon voyage en Irlande, et de m'avoir offert leur cocon comme résidence d'écriture l'été dernier. Grâce à vous, je sais comment aménager mon futur bureau de télétravail !

Je suis réellement reconnaissante pour toutes ces rencontres et je suis désolée de ne pas avoir cité tout le monde. Ce fut un plaisir d'interagir avec chacun d'entre vous. Je reste convaincue qu'une communication fluide, sincère et désintéressée peut permettre de résoudre de nombreux problèmes, tant professionnellement que personnellement.

J'aimerais également mentionner mes **amis** de plus ou moins longue date et avec un degré de compréhension plus ou moins développé de mon domaine de recherche. Je suis loin d'être une amie exemplaire, je suis la pire pour exprimer mes sentiments mais je suis heureuse de vous compter parmi mes proches et ma porte sera toujours ouverte pour vous. Camille, Claire, Jennifer, merci d'être à l'écoute dès que j'ai besoin de me plaindre – heureusement, ce n'est pas si fréquent que ça.

J'aimerais dédier ce dernier paragraphe à ma chère **famille**. Fille de docteurs, sœur d'avocate, je m'efforce d'être à la hauteur de l'éducation et des valeurs que vous m'avez transmises. Maman, je sais que tu n'adhères pas toujours à toutes mes décisions et que tu t'inquiètes toujours autant pour moi quel que soit mon âge et la distance entre nous. Je te remercie pour ta présence et j'espère te rendre fière malgré tout. Papa, merci pour tes conseils et tes mots rassurants durant mon parcours. Je me souviens encore de ta soutenance lorsque j'avais 6 ans – si j'avais su à cette époque que je ferais une thèse, j'aurais peut-être écouté un peu plus attentivement au lieu de m'intéresser aux pâtisseries sur la table. Ma sœur, je ne suis pas la plus affectueuse des petites sœurs mais je vois tout ce que tu fais pour moi et je te remercie pour ton soutien infaillible depuis toutes ces années.
J'aimerais également remercier mon fiancé de me pousser continuellement dans mes retranchements, me soutenir dans mes décisions les plus folles et d'être un allié paisible lorsque je suis tendue et incertaine. Nous avons encore bien des obstacles à surmonter, à commencer par la bureaucratie Canadienne, mais je suis heureuse de passer ces étapes avec toi.
Je finirai cette partie en remerciant mon plus grand soutien moral, même si cela peut paraître stupide pour certain : mon adorable chien. Merci pour ton amour inconditionnel, pour ta réjouissance de me voir lorsque je rentre du travail (ou même des toilettes), et de me forcer à aller me promener même lorsque je n'en ai pas l'envie. T'adopter pendant ma thèse fait partie des décisions folles mentionnées plus haut, mais je n'aurais pas vécu cette expérience de la même manière sans toi.

Acronyms

AC/DC alternating current/direct current

ACM acetaminophen

ACN acetonitrile

BSA bovine serum albumin

CPE chemical penetration enhancer

CE counter electrode

CM Creative Materials

COVID-19 coronavirus disease 2019

CP chronopotentiometry

DG dry gel

DIA drug-in-adhesive

DP daniplestim

DSC differential scanning calorimetry

ECG electrocardiography

EDL electrical double layer

EIS electrochemical impedance spectroscopy

FDA food and drug administration

FEM finite element method

FITC fluorescein isothiocyanate

HA hyaluronic acid

HPLC high performance liquid chromatography

IDE interdigitated electrode

IM intramuscular

IP intraperitoneal

IPA isopropyl alcohol

ISF interstitial fluids

ITP iontophoresis

IV intravenous

MEMS microelectromechanical systems

MN microneedle

NW nanowire

OCP open circuit potential

PB phosphate buffer

PBS phosphate-buffered saline

PC polycarbonate

PCB printed circuit board

PDMS polydimethylsiloxane

PET polyethylene terephtalate

PGA polyglycolic acid

PLA polylactic acid

PLGA polylactic-co-glycolic

PSA pressure-sensitive adhesive

PVP polyvinylpyrrolidone

PVA polyvinyl alcohol

RE reference electrode

SC stratum corneum

SLA stereolithography

SS semi-stretchable

TDD transdermal drug delivery

TER transdermal electrical resistance

TFA trifluoroacetic acid

TGA thermogravimetric analysis

TPU thermoplastic polyurethane

UV ultraviolet

WE working electrode

ZIF zero insertion force

List of Tables

List of Figures

General introduction

"Novel technologies for transdermal delivery of active molecules" is a multidisciplinary subject falling within the areas of biotechnology, pharmacokinetics and medicine. The main goal of this project is to develop an **active transdermal drug delivery device** and understand its underlying mechanisms.

Why using the transdermal route?

Most commonly, enteral and parental routes are used to deliver active molecules. They both present excellent advantages, but also important disadvantages.

Enteral administration includes oral and rectal drugs (BARDAL ET AL., 2011). Oral drugs are by far the most common type of drugs used and available in a variety of pill forms (tablets, capsules and caplets) (KAPALKA, 2010). They offer **easy storage** (usually at room temperature) and are the **least invasive** drug delivery option, even though children and seniors have difficulties swallowing pills. The most important drawbacks of this route though are **slow-acting**, **gastric irritation** and **low bioavailability**. Indeed, enteral administration necessary implies the passage through the gastrointestinal tract. In addition to the time required to be digested, the drug can be metabolized in the intestinal wall or the liver, which reduces the dose that actually reaches systemic circulation to only a fraction of the initial dose (WARD AND KERN, 2017). This fraction can be calculated compared to **I**ntra**V**enous (**IV**) injection that does not present such issue as the drug enters systemic circulation before reaching the liver.

Along with **I**ntra**M**uscular (**IM**), **I**ntra**P**eritoneal (**IP**) and subcutaneous injections, IV belongs to the **parenteral administration** route which consists in **bypassing the gastrointestinal tract** and its related drawbacks. Injections are preferred in case of emergency (cardiac arrest, anaphylactic shock…) because of their **fast-acting** delivery (ZHANG ET AL., 2017) or to reach **high therapeutic concentrations reliably** (FARRINGTON, 2012). On the other hand, these injections are usually performed by **healthcare professionals** and require **sanitized environment and tools**, and sometimes **particular storage conditions**. Finally, the use of a needle makes this administration route **invasive** and can cause **anxiety**, if not trypanophobia (needle phobia).

By definition, **Transdermal Drug Delivery (TDD)** can also be classified in the parenteral route. However, this pathway is considered to be painless and non-invasive in comparison, which provides a better patient **compliance** and **independence** (MANIKKATH ET AL., 2016). Its ability to provide a long-term release makes this route suitable for chronic treatments (SHINDE ET AL., 2022). Some disadvantages are still pointed out in the literature such as **drug limitation** to small lipophilic molecules (SONIA AND SHARMA, 2014) or **lack of reliability** of the dose delivered (FRANK H. AND MICHAEL A., 2005). The latter point is often explained by differences in skin composition between and within

individuals (SINGH AND MORRIS, 2011). Finally, some drugs may cause **irritations** when in contact with the skin (REDDY ET AL., 2012).

> In this project, we are willing to develop a prototype of TDD device that could combine the benefits of this route while avoiding its main disadvantages. Such device could eventually **deliver biomolecules** such as proteins in a **reliable and controlled** manner, without causing skin irritation.

How to develop a generic device?

Different TDD technologies exist in order to enhance drug diffusion across the skin. In this study, two of them are combined to obtain a device that can be generalized to a wide range of molecules.

1. Due to the barrier function of human skin that will be presented in the first chapter, we propose to use **MicroNeedles (MNs)** as a first technology to bypass the outermost layer of the skin, the ***S**tratum **C**orneum (**SC**)*. Bioresorbable hollow MNs are used **to keep the device as generic as possible**, as other kinds of polymeric MNs can involve drug loading directly in the polymeric network. In the latter case, the formulation of MN materials as well as their mechanical properties depend on the molecule to deliver, and only a small amount of drug can be loaded which limits the variety of applications.
2. To allow a broader range of molecules to be delivered and enhance the diffusion of heavy compounds such as biomolecules, an electrically-assisted technology, **IonToPhoresis (ITP)**, is implemented to the device. A close attention is given to this part, as misusing this technology can lead to disastrous consequences (skin burns) on patients' skin.

Figure 1 depicts the combination of both technologies, with the example of a cationic drug filled in the MN array placed at the anode (or positive pole).

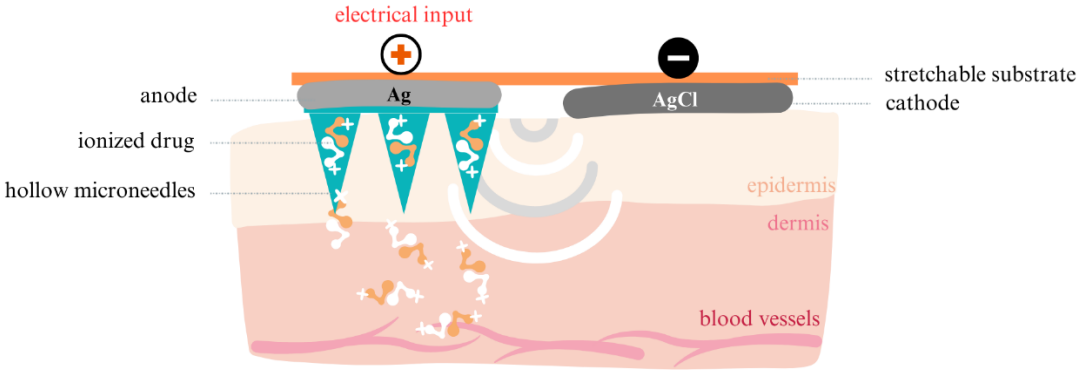

Figure 1. Schematic representation of the generic TDD device combining MNs and ITP in the case of a cationic drug

Throughout this thesis, the different steps towards the prototype will be described.

Thesis contents

The **first chapter** provides a better understanding of human skin structure and existing transdermal technologies to date. Knowledge of the state of the art allows to focus the rest of the study on the two challenging drug delivery techniques that are MNs and ITP.

The **second chapter** is dedicated to MNs, and more specifically to mechanical characterizations of polymer MNs thanks to a collaboration between CEA and Tyndall National Institute, Cork, Ireland, where I had the opportunity to work for a month during my final year thesis. New processes will then be explored for MN fabrication to evaluate the industrial viability of this technology and fulfill eventual large-scale needs. This chapter will lead to the choice of the most suitable MN arrays for drug delivery comparisons in the last chapter.

The **third chapter** focuses on ITP as an electrically-assisted drug delivery technique. The electrochemical behavior of silver/silver chloride (Ag/AgCl) electrodes is studied to understand the origin of the withdrawal of commercial ITP devices due to skin burns. As the lifetime of this type of electrode is not infinite, different options are experienced to optimize the system and provide a safe long-term use.

The **fourth chapter** adds another level of understanding using numerical modeling to visualize current distribution on ITP electrodes. This part provides information on an electrical point of view only and does not take into account electrochemistry. Numerical simulations help identifying different key parameters (input signal, electrode geometries, etc…) in order to reduce hot spots and bypass additional risks of skin burns.

The **final chapter** gets closer to the applicative setup with more concrete use cases. The mechanical viability of stretchable electrodes will first be studied with new geometries adapted to a wearable device. Then, the delivery of a protein will be quantified in different configurations using passive diffusion, MN, ITP and their combination. A proof of concept of a combined glucose biosensor and insulin delivery device is also presented.

The thesis will end on a conclusion section including a critical analysis of the project regarding the combination of MNs and ITP for drug delivery. Evolution perspectives are suggested requiring the collaboration of different areas of expertise other than materials science that is treated in this research project. Besides, the environmental impact of the project is also evaluated in **Appendix 1** to raise awareness and promote more sustainable research and development.

CHAPTER 1

Chapter 1: Literature review

To understand the key concepts behind this multidisciplinary project, the first Chapter summarizes the state of the art regarding transdermal drug delivery in general before focusing on iontophoresis, microneedles and their combination.

1.1. Human skin properties and challenges related to transdermal drug delivery

As hinted by the growth in the number of research papers published related to the topic (**Figure 2**), transdermal drug delivery (TDD) gains interest over the years. It is indeed a challenging yet promising drug delivery route that requires a good understanding of skin structure and properties.

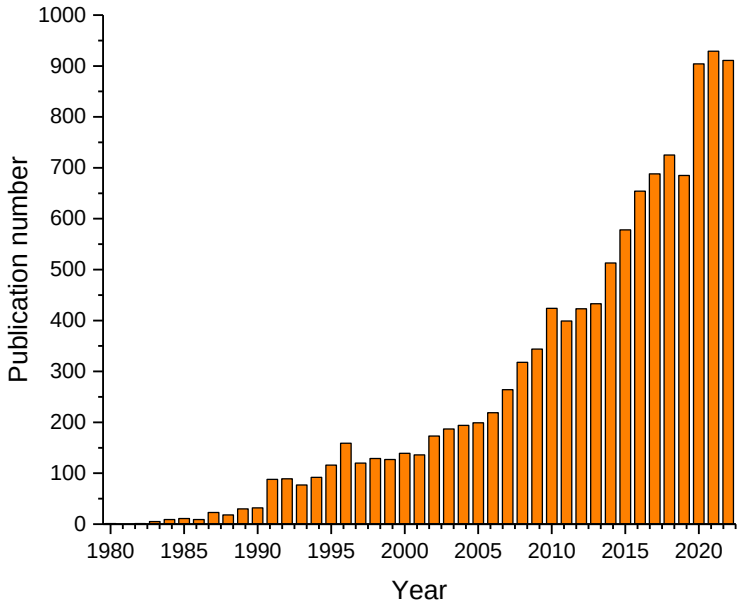

Figure 2. Number of publications from 1980 to 2022 for "transdermal drug delivery" on Web of Science

1.1.1. Skin as an environmental barrier

1.1.1.1. Structure of the skin

Skin not only is an organ but also the largest human organ, representing about 15% of an adult body weight (KOLARSICK ET AL., 2011). Its structure seems complex (**Figure 3A**) and is composed of three major layers: the epidermis, the dermis and the hypodermis. The epidermis itself is mostly made up of five layers, from deep to superficial: *stratum basale*, *stratum spinosum*, *stratum granulosum*, *stratum lucidum* and *stratum corneum* (SC) (**Figure 3B**) (BETTS ET AL., 2013; BRANNON, 2022).

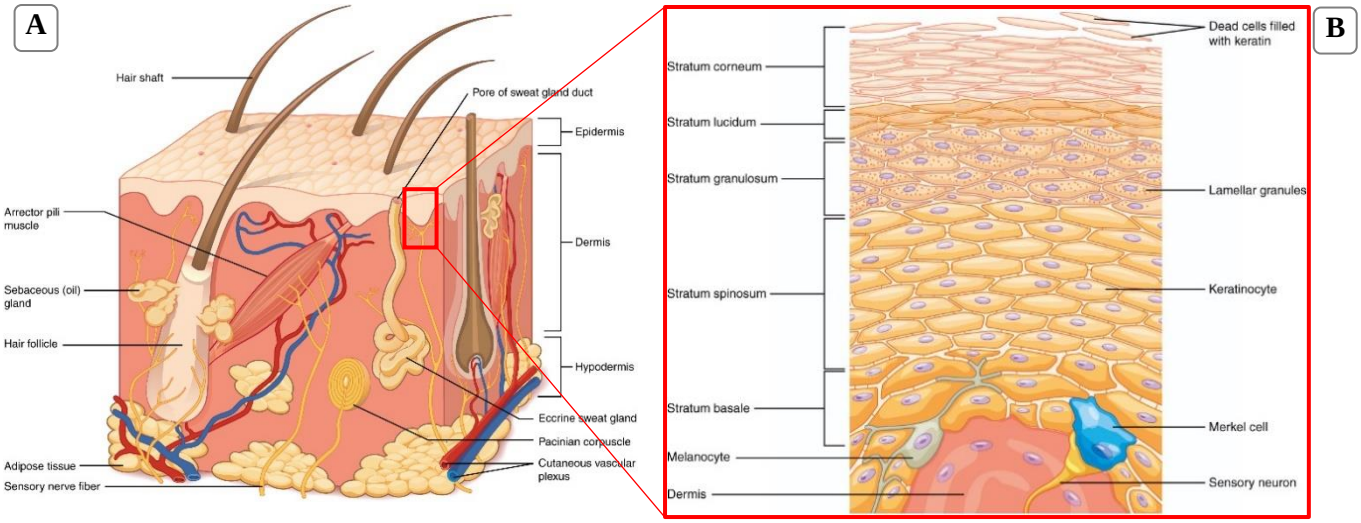

Figure 3. (A) Overall skin and (B) Epidermis structures (Betts et al., 2013)

Epidermis thickness varies between 0.1 to 1.5 mm (MARIEB, 2014) depending on body parts and other individual factors such as age, sex or ethnicity (OLTULU ET AL., 2018). The upper range is qualified as "thick skin" and is located on the palms of the hands and the soles of the feet, in opposition to "thin skin" which is missing the *stratum lucidum* layer, and is found on the eyelids, nipples and genitalia (BETTS ET AL., 2013).

The epidermis, and more specifically the SC, plays a major role in the body as it protects it from exogenous pathogenic microorganisms and maintains homeostasis (BOER ET AL., 2016), regulating biological parameters (BUCKLEY, 2016) such as temperature or water content (DRAELOS, 2009; KOLARSICK ET AL., 2011). 80% of the cells composing the epidermis are keratinocytes, manufacturing and storing keratin protein (KOLLROS, 2018). From basal layers upwards, keratinocytes undergo a three-week cornification process forming a keratin-rich SC made of 10 to 15 corneocyte layers (ÉVORA ET AL., 2021; KOLARSICK ET AL., 2011; KOLLROS, 2018), leading to a 10 to 30 µm thick SC on average (SANDBY-MØLLER ET AL., 2003).

1.1.1.2. Mechanical properties

Apart from their composition, it is necessary to evaluate the mechanical properties of skin layers to understand their roles and behaviors. More specifically for microneedles, these properties are essential to design a device that is able to painlessly perforate the skin.

Many types of mechanical tests are used in order to characterize human skin, using different constraints: stretching (tensile tests), normal loading (indentation or compression tests), rotating (torsion tests) or elevating (suction tests). Young Modulus or elastic modulus is often used as an indicator of materials stiffness. It corresponds to the slope of the first linear region of a stress versus strain curve (**Figure 4**), known as the elastic range where deformation is completely or mostly recoverable (KEATON, 2018).

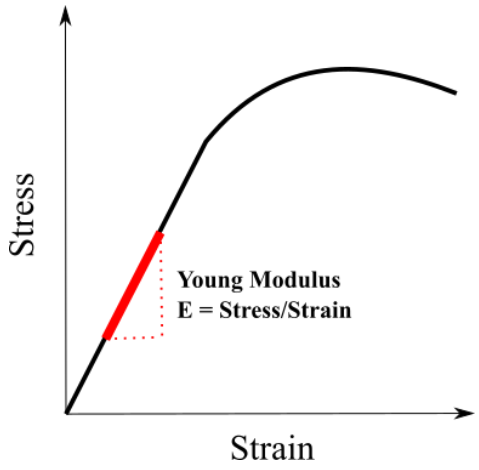

Figure 4. Schematic representation of a stress versus strain curve and associated Young Modulus calculation

Literature reviews show a significant variation in skin Young Modulus from 4 kPa to 160 MPa depending on test type, measurement speed and skin location (KAO, 2016). Additional differences may appear if the test has been performed *in vivo* or *ex vivo* (KALRA AND LOWE, 2016). A closer look at skin properties is therefore necessary to understand these variations.

Human skin is described as viscoelastic as it combines elastic (ability to change its length, volume or shape in response to a force) and viscous (internal resistance to flow) properties (EVERETT AND SOMMERS, 2013). In opposition to purely elastic materials (**Figure 5A**), viscoelastic materials do not immediately return to their original configuration when the constraint is removed (**Figure 5B**) (MANSCHOT, 1985). This feature however depends on one's hydration level, which is a reason why physicians use skin turgor as a quick and non-invasive test to assess the hydration status of patients (FAYOMI ET AL., 2007).

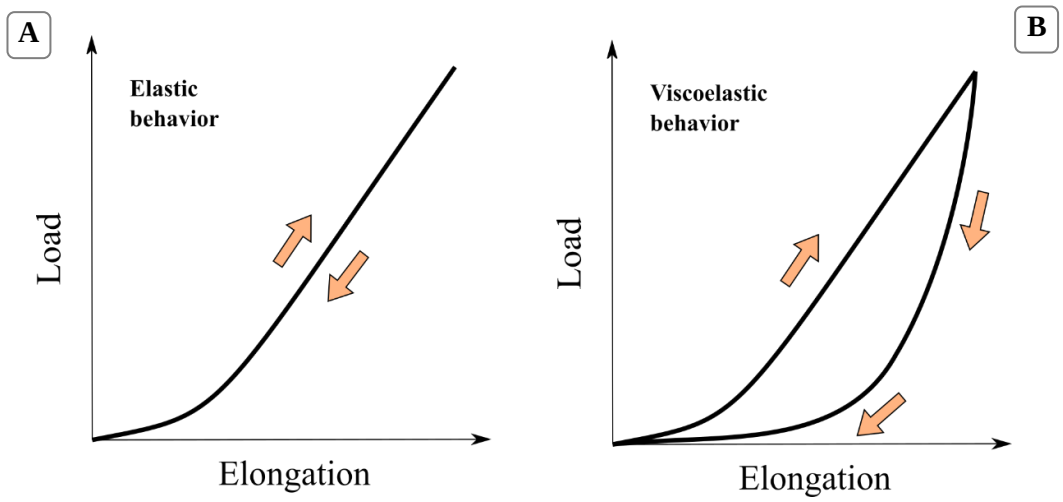

Figure 5. Schematic representation of (A) elastic and (B) viscoelastic behavior (modified from Thorpe et al., 2015)

It is first necessary to identify which layers are involved in mechanical tests. The epidermis and more specifically the cornified layer (SC) is mostly made of keratin and shows an ability to fold easily but resists to elongation forces (LÉVÊQUE ET AL., 1988). The dermis is composed of collagen and elastin which have completely opposite mechanical properties (DELALLEAU, 2018) but elastin dictates the mechanical response at small constraints, while collagen fibers straighten up to 30% tensile strain (JOODAKI AND PANZER, 2018).

Secondly, the appropriate mechanical test needs to be selected as each test provides a different kind of information. For instance, tensile tests inform on skin anisotropy while suction tests do not take into account this feature (DELALLEAU, 2018). Compression and indentation tests allow a more complex analysis of skin viscoelasticity (DALY, 1982; DELALLEAU ET AL., 2006).

1.1.1.3. Skin phantoms for in vitro experimentation

In vivo human testing is not always possible for ethical, practical or economic reasons and *ex vivo* samples obtained from cadavers or plastic surgery patients are rare (ABD ET AL., 2016). Animal skin is easier to obtain but its structure may be different than human's depending on the species (skin layers composition and thickness, hair density, etc…), which leads to different mechanical properties as well (DENG ET AL., 2012). Porcine ear skin is described as the closest animal skin model with a SC thickness of 21-26 µm and a hair-follicle density of 20 cm^{-2} compared to 14-32 cm^{-2} on human forehead (ABD ET AL., 2016). However, as many parameters can affect the properties of biological tissues, a real need to develop artificial skin models emerged to allow a better sample reproducibility, especially in early research phases. These skin phantoms have the ability to roughly mimic the mechanical, biological and sometimes optical, electrical or acoustical behavior of human skin (LOW ET AL., 2020; NEUPANE ET AL., 2020).

Simple polymer phantoms made of hydrogel (gelatin, agar) and silicone are often used in the literature to reproduce mechanical and optical skin properties (LAMOUCHE ET AL., 2012). Gelatin is a protein derived from collagen which is a major constituent of the dermis as previously mentioned (CHOI ET AL., 1999). It is used in dermis and epidermis models at different proportions (10 to 24 weight percentage (wt%)) to provide mechanical integrity, but is usually combined with glycerol as a plasticizer to increase flexibility (CHEN ET AL., 2016; DENG ET AL., 2012). Other studies use between 2 and 3 wt% agar to describe skin density but mechanical properties are then not reliable (CONDLIFFE ET AL., 2010; PAN ET AL., 1995). The main disadvantage of hydrogel phantoms is their short durability of about a week with refrigeration, but some additives may be included in the matrix such as formaldehyde to preserve gelatin and agar phantoms at room temperature (POGUE AND PATTERSON, 2006).

With the development of water-sensitive technologies, non-aqueous options are also necessary. Modeling clay or silicone phantoms can be used in this regard. Commercial clays composed of kaolin, sulfur and glycerin are available with different shore hardness (CHAMPEAU ET AL., 2020). Silicone is also an interesting base material for optical phantoms as it is transparent, compatible with a wide range of scatterers and stable in time. Mechanical properties can be controlled by varying the catalyst to cross-linker ratio, offering an elastic modulus range of ~100 kPa to ~5 MPa. Silicone phantoms allow the creation of complex shapes because of their low viscoelasticity but this feature is also a significant difference compared to biological tissues (LAMOUCHE ET AL., 2012). These phantoms are not the best candidates for drug delivery as they contain no water and are insoluble, two qualities that are necessary for permeation studies and drug quantification post-delivery respectively (DENG ET AL., 2012).

Commercial phantoms offer a more complete multilayered artificial skin model taking into account the specificities of each skin layer (NEUPANE ET AL., 2020). Strat-M™ (Merck Millipore, Massachussets, USA) for instance is made of polyethersulphone and polyolefin layers with different diffusivities, and has been used and validated for drug diffusion screening (UCHIDA ET AL., 2015). SynTissue® (SynDaver, Florida, USA) is a silicone-based artificial model matching not only human skin mechanical properties (tensile modulus, abrasion resistance, penetration force, coefficient of friction), but also other features like acoustical properties, thermal conductivity and dielectric constant (HART ET AL., 2016). The latter phantom will be used in this study as a mechanical model for microneedle perforation tests.

1.1.2. Towards transdermal drug delivery technologies

Despite its barrier functions, skin is a porous membrane allowing the percutaneous absorption of certain molecules (CLOWES ET AL., 1994). This feature is actually a real advantage for the development of transdermal therapies.

1.1.2.1. Drug diffusion mechanisms and kinetics of passive diffusion

There are three ways to penetrate the SC as depicted on **Figure 6**. The first two routes are both transepidermal routes, consisting in migrating across the SC through (intracellular) or in between (intercellular) cells (SHAHZAD ET AL., 2015). The first route is referred as the "aqueous pathway" as it allows polar and hydrophilic molecules to diffuse through corneocytes, but this contribution is considered unimportant for transdermal drug transport (CEVC AND VIERL, 2010). The second route is a tortuous pathway between corneocyte membranes (lipid bilayers), and the extracellular lipid matrix which is a favorable environment for lipidic and non-polar solutes (PRAUSNITZ ET AL., 2004; SHAHZAD ET AL., 2015). Finally, the transappendageal route involves transport through hair follicles and glandular ducts (ERDŐ ET AL., 2016). Earlier studies suggested that this route is negligible because of its limited surface area (0.1% of the total skin surface area (JUAN ET AL., 2012)), but it has been later demonstrated as an efficient pathway (JAVADZADEH AND AZHARSHEKOUFEH BAHARI, 2017), especially for ionic

and large polar compounds (BARRY, 1987). Overall, the SC is described to be permeable to low dose (~10 mg·day^{-1}), low molecular weight (<500 Da) and highly lipophilic drugs only (O'MAHONY, 2014).

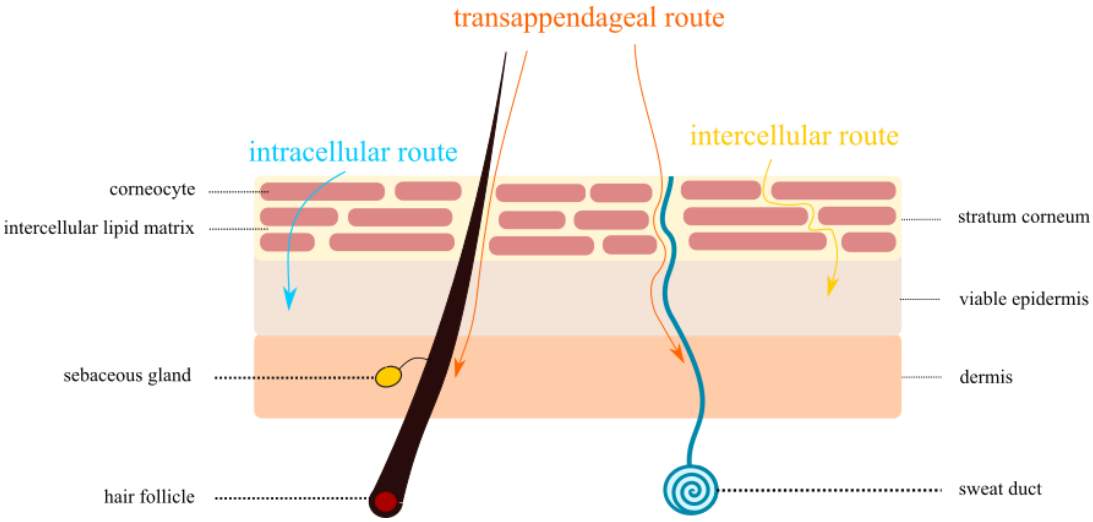

Figure 6. Diffusion pathways through the skin (modifed from Holmgaard and Nielsen, 2009)

Table 1 gives an estimation of sites, width and relative abundance (counts for a given skin area) for each path.

Table 1. Transdermal penetration pathways (Cevc and Vierl, 2010)

Path type	**Site/Species**	**Path width [nm]**	**Relative abundance [number·cm^{-2}]**
Sweat duct	Human	> $5 \cdot 10^4$	$2\text{-}2.5 \cdot 10^2$
Sebaceaous gland	Forehead	$5\text{-}15 \cdot 10^4$	$4\text{-}9 \cdot 10^2$
	Back		$2\text{-}6 \cdot 10^2$
	Forearm		$1\text{-}1.5 \cdot 10^2$
Hair follicle	Face	$5\text{-}70 \cdot 10^4$	$3\text{-}5 \cdot 10^2$
	Back		$0.3\text{-}2 \cdot 10^2$
	Forearm		$0.2\text{-}1 \cdot 10^2$ (≥ 50)
	Upper arm		20-30 (≥ 10)
Clusters-junction (major furrows or wrinkles)	Superficial SC	$3\text{-}8 \cdot 10^4$	~10^4
	Deep SC	~10^2	~10^4
Inter-cells-cluster (furrows or fine wrinkles)	Superficial SC	<< $5 \cdot 10^4$	~10^8 ($5 \cdot 10^6$-10^9)
	Deep SC	<10^2	~10^8 ($5 \cdot 10^6$-10^9)
Inter-corneocyte	Normal	0.5-7	~10^9 ($5 \cdot 10^7$-10^{10})
	Widened	20-30 (15-40)	~10^9 ($5 \cdot 10^7$-10^{10})

Kinetics of drug diffusion is usually described by Fick's law (**Equation 1**), which considers that a drug i flux $\vec{J_i}$ (µg·cm^{-2}·s^{-1}) will be maintained as long as a concentration c_i (µg·mL^{-1}) gradient is present between the reservoir and the target membrane (ALKILANI ET AL., 2015).

$$\vec{J_i} = -D_i \vec{\nabla} c_i \quad (1)$$

With D_i the diffusion coefficient of the drug (cm²·s^{-1}).

This expression also gives a hint on the effect of drug size (hence mass) on the passive drug flux: Stokes-Einstein equation describes the diffusion coefficient of a compound as inversely proportional to its approximate radius (MIYAMOTO AND SHIMONO, 2020). In terms of order of magnitude, a small drug like caffeine, ketoprofen or paracetamol is at least 10 times more mobile than a protein like **B**ovine **S**erum **A**lbumin (**BSA**) (DI CAGNO ET AL., 2018; YOUNG ET AL., 1980). However, this law only takes into consideration passive diffusion of molecules regardless of their ionization state, tissue affinity or the effect of regional liquid flow such as blood or **I**nter**S**titial **F**luids (**ISF**) (CHEMTOB, 2004).

1.1.2.2. Transdermal drug delivery applications

Transdermal therapies existed since the origin of mankind, as historians report different cultural practices using clay, oils, animal fats or perfumes to make cosmetic and dermatological products (PASTORE ET AL., 2015). Medicinal herbs are also used in traditional Chinese medicine to make topical patches despite the lack of quantitative evidence of efficacy (LEUNG ET AL., 2016).

Some famous names begin to appear after Christ. The Greek physician Galen was referred to as the "Father of Pharmacy" and invented around year 150 the first cold cream, leaving a cooling effect on the skin after water evaporation (WIVELL, 1996). The Persian physician Avicenna also presents his theories on topical drugs crossing the skin to the deepest tissue layers in his *Canon of Medicine* in year 1020 (AVICENNA AND GRUNER, 1973; MAHDIZADEH ET AL., 2015).

It was only in the 20th century that skin permeation was effectively proven through *in vivo* studies (PASTORE ET AL., 2015). The first clinically-approved transdermal system finally appeared in the United States in 1979 with a three-day scopolamine patch to treat motion sickness, followed by nitroglycerin in 1981 and two dozens of other drugs until 2007 (PRAUSNITZ AND LANGER, 2008). **Appendix 2** summarizes major transdermal drugs used for systemic delivery in the USA and EU.

Transdermal patches are commonly classified into three groups as described in **Figure 7**: matrix, reservoir and drug-in-adhesive (BIRD AND RAVINDRA, 2020). Matrix patches contain the drug in a polymer matrix, while drug reservoirs are usually liquid and can be subject to leakage despite the membrane-controlling system (PRODDUTURI ET AL., 2009). **D**rug-**I**n-**A**dhesive (**DIA**) patches directly

contain the drug in a **P**ressure-**S**ensitive **A**dhesive (**PSA**), capable of bonding to surfaces with a light pressure and being removed without noticeable residues (CILURZO ET AL., 2012).

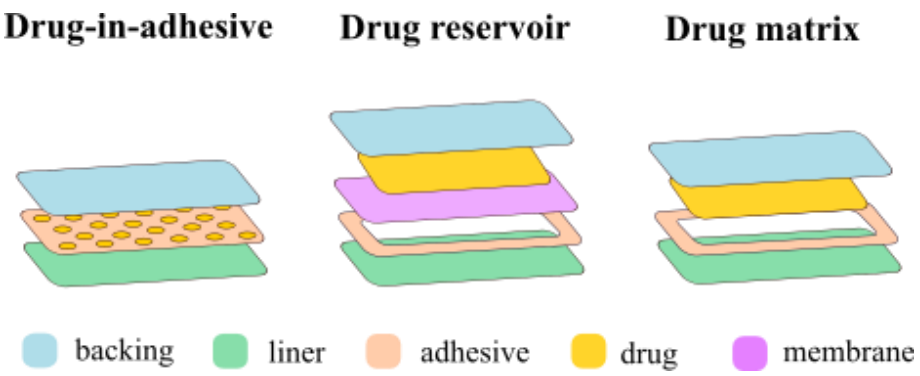

Figure 7. Representation of different types of patches (modified from Sozio et al., 2012)

Following generations of transdermal delivery systems recognize a need to enhance skin permeability in order to expand the scope of drug candidates (PRAUSNITZ AND LANGER, 2008). **C**hemical **P**enetration **E**nhancers (**CPE**) such as sulphoxides, alcohols, surfactants, phospholipids or terpenes can be included in formulations to improve drug flux, but their potencies appear to be drug-specific (WILLIAMS AND BARRY, 2012). The enhancement mechanism consists in the perturbation of the SC by protein denaturation leading to skin irritation and, as a results, safety concerns (KARANDE ET AL., 2005). A safer but also drug-specific approach is to use prodrugs by chemically modifying the structure of the drug of interest in order to favor its solubility in the skin (SLOAN ET AL., 2006). In this latter case, drug structure is altered instead of skin structure.

Finally, physical techniques are used to help drug penetration such as electrical (iontophoresis, electroporation), acoustical (sonophoresis), thermal (thermal poration) and mechanical (microneedles) assistances (TANNER AND MARKS, 2008). Even though the efficiency of electrically-assisted drug delivery has been proven by various research teams, devices remain too bulky and expensive for wearable use. Thankfully, the development of microelectronics helps evolving towards miniaturized, conformable and disposable devices (PRAUSNITZ ET AL., 2004).

This thesis is more specifically focusing on portable electrical and mechanical enhancement techniques and their combination to provide a generic and potent drug delivery system.

1.2. Electrically assisted therapies for drug diffusion enhancement

An electrical assistance can be used to enhance percutaneous absorption of a drug using an electromotive force. This type of drug delivery is referred to as **active delivery**, in opposition to passive delivery following Fick's law of diffusion described in the previous part (**1.1.2.1**). Different modes exist to apply an electrical field, such as iontophoresis or electroporation (RIVIERE AND HEIT, 1997). This part will first focus on iontophoresis and its role in accompanying drug delivery across the skin. Then, Ag/AgCl electrodes are presented as a safer alternative for iontophoretic applications. The last subsection will address the future of wearable electrodes with novel stretchable devices.

1.2.1. Iontophoresis

Iontophoresis (ITP) consists in setting ions in motion by applying an electric field between a working and a counter electrode. The concept was first described by Pivati in 1747 but started to become popular from the beginning of the 20th century with the introduction of iontotherapy by Leduc in 1900 (SLOAN, 1986). **Figure 8** describes a sudden growth in the number of publications in 1991. Since then, the interest on this topic remained stable with an average of 142 papers published per year.

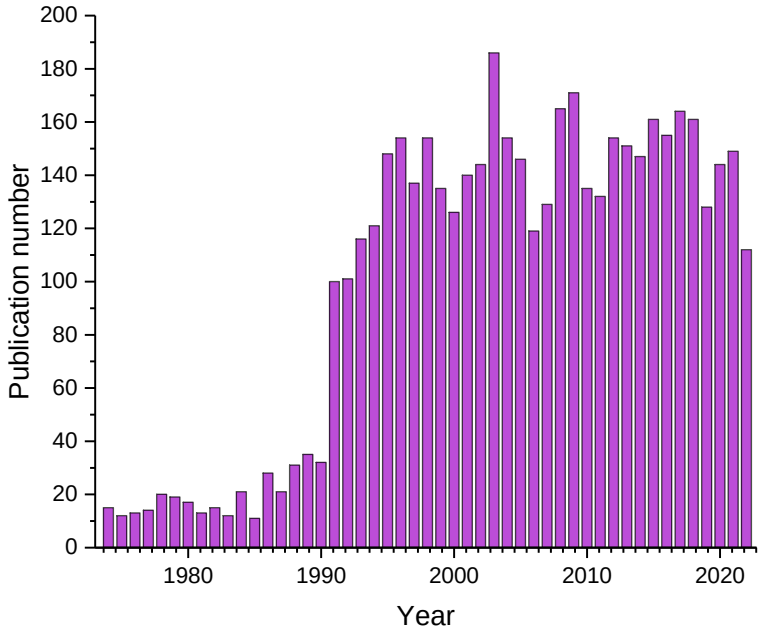

Figure 8. Number of publications from 1973 to 2022 for "iontophoresis" on Web of Science

1.2.1.1. Basic principles

ITP is presented as a non-invasive TDD technology using a low-intensity current density, usually below 0.5 mA·cm^{-2} (BAKSHI ET AL., 2020). Iontophoretic devices can be used either for drug delivery or

sensing as it is able to deliver (ITP) or to extract (reverse ITP) a molecule (KASHA AND BANGA, 2008). It follows two main mechanisms: electromigration and electroosmosis.

- **Electromigration** describes the movement of a charged molecule under the effect of an electric field $\vec{E}$ ($N \cdot C^{-1}$) due to the Coulomb force (**Equation 2**):

$$\overrightarrow{F_c} = q\vec{E} \quad (2)$$

Where $\overrightarrow{F_c}$ (N) is the electric Coulomb force and q (C) the overall electric charge of the molecule.

  This contribution is hence in favor of ionic drugs. The drug reservoir should be placed under the electrode of the same polarity, namely cations under the positive electrode and anions under the negative electrode (ROUSTIT ET AL., 2013). In this case, drug concentration in the reservoir varies with time and ionic displacement is not associated with a liquid flow.

- **Electroosmosis**, on the other hand, corresponds to the movement of molecules carried by a liquid flow starting from the positive towards the negative electrode. This phenomenon occurs as human skin is slightly negatively charged and acts like a cation-selective membrane (PIKAL, 2001). Although this motion is caused by charged species accumulating at the electrodes surface (PHAM ET AL., 2007), this flux not only transports cations but also neutral solutes present in the liquid. For this reason, electroosmosis is described as the major driving force for neutral solutes (KIM ET AL., 1993).

Overall, the delivery of cationic drugs is the most favorable scenario to use ITP as it is enhanced by both electromigration and electroosmosis mechanisms (KALIA ET AL., 2004).

1.2.1.2. Limitations

ITP can unfortunately cause different adverse effects that need to be considered to provide a safe drug delivery device. The most common risk is skin irritation (VRANIĆ, 2003) resulting in erythema or edema under both electrodes, usually not leading to permanent skin damage (ROUSTIT ET AL., 2013). Some studies however mention a potential irreversible drop in the electrical resistance of the skin at currents above the microamperic range, especially under the cathodal compartment (VAN DER GEEST ET AL., 1996). Current-induced vasodilatation has also been reported under the cathode (CRACOWSKI AND ROUSTIT, 2020). In the most severe cases, skin burns are observed leading to market withdrawal of commercial devices (**Figure 9**) like migraine sumatriptan patch Zecuity® (LODER ET AL., 2018). Three lidocaine and epinephrine-based patches, Iontocaine, LidoSite™, and Lidopel, were respectively withdrawn from the market in 2005, 2008 and 2011 (BAKSHI ET AL., 2020).

Figure 9. Examples of commercial iontophoretic devices withdrawn from the market. (A) Zecuity® (B) Lidosite™ (C) IONSYS®

Similar examples of product withdrawal are mentioned in the literature, reflecting a **need for a deeper understanding of the electrochemistry** behind iontophoretic devices. Several simple recommendations are discussed in the literature to avoid such risks of injury (ROUSTIT ET AL., 2013), among which:

- maintaining a current density below 0.5 $mA \cdot cm^{-2}$,
- ensuring homogeneous cleaning, wetting and sealing of the electrode/skin interface,
- adjusting electrodes materials to avoid parasitic reactions.

1.2.1.3. Electrode materials

Over the years, different types of electrodes has been experienced in order to find suitable materials for this technology. ITP was initially performed with "inert" electrodes using materials such as carbon or platinum. However, this electrical input is sufficient to induce the electrolytic reaction of water present in the skin tissues (**Equations 3 and 4**) (KASHA AND BANGA, 2008):

$$2H_2O \rightarrow 4H^+ + O_2 + 4e^- \quad (3)$$

$$2H_2O + 2e^- \rightarrow 2HO^- + H_2 \quad (4)$$

These redox reactions show the production of gas bubbles (O_2 and H_2), but also a pH drift where the anode becomes acidic (H^+) and the cathode basic (HO^-) (DIXIT ET AL., 2007). Numerous research groups describe this phenomenon as responsible for skin burns, referred to as electrochemical burns (BANGA, 1998; KALIA ET AL., 2004; ROUSTIT ET AL., 2013).

A solution to avoid these undesirable reactions is to use "sacrificial" electrodes that will participate in the electrochemistry of the system at lower voltages than those required for water electrolysis (CRACOWSKI AND ROUSTIT, 2020).

Silver/Silver chloride (Ag/AgCl) electrodes are the most appropriate redox couple for different reasons:

- First, they provide more thermodynamically favorable reactions (**Equations 5 and 6**) in comparison with the redox couples of water:

$$Ag + Cl^- \rightarrow AgCl + e^- \quad (5)$$

$$AgCl + e^- \rightarrow Ag + Cl^- \quad (6)$$

As the drug is delivered, both electrodes are consumed (**Figure 10**). Water electrolysis only starts either when AgCl is no longer available at the cathode, or when the anode is fully passivated with AgCl.

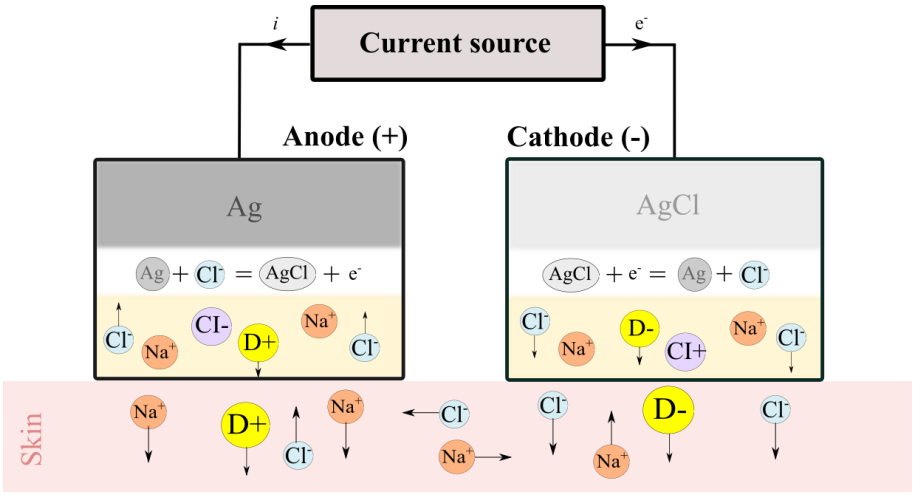

Figure 10. Ag/AgCl iontophoretic system (modified from Kalia et al., 2004). Cationic (D+) or anionic (D-) and their counter-ions (CI±) are placed under the electrode of the same polarity. Cations migrate from anode to cathode and anions migrate the opposite way

- Electrochemical reactions involved lead to insoluble products at their surface (BAKSHI ET AL., 2020), which allows their use without any risk of metal diffusion in the skin. However, other papers argue the risk of colloidal AgCl ejection depending on electrodes preparation method (BANGA, 1998).
- Finally, Ag/AgCl electrodes are known for their fast kinetics allowing a direct relationship between electronic and ionic current (CULLANDER ET AL., 1993). It is though necessary to keep in mind that chloride ions need to be abundantly present in the environment not to limit the desired reaction at the anode (**Equation 5**). Otherwise, another reaction would take place, leading to a possible silver migration in the skin due to silver oxidation without chlorination (**Equation 7**) (BANGA, 1998):

$$Ag \rightarrow Ag^+ + e^- \quad (7)$$

A saline environment is thus required for the proper function of this type of electrodes, implying however a possible competition between the drug to deliver and ions of the same charge.

1.2.1.4. Pulsating current

Another way to avoid electrochemical burns is to use a pulsating current instead of a continuous **D**irect **C**urrent (**DC**). Pulsed DC is, by definition, an **A**lternating **C**urrent (**AC**) with the exception of keeping the same electrodes polarity in time (**Figure 11**). This feature allows the ionized drug to keep moving towards the desired direction of delivery.

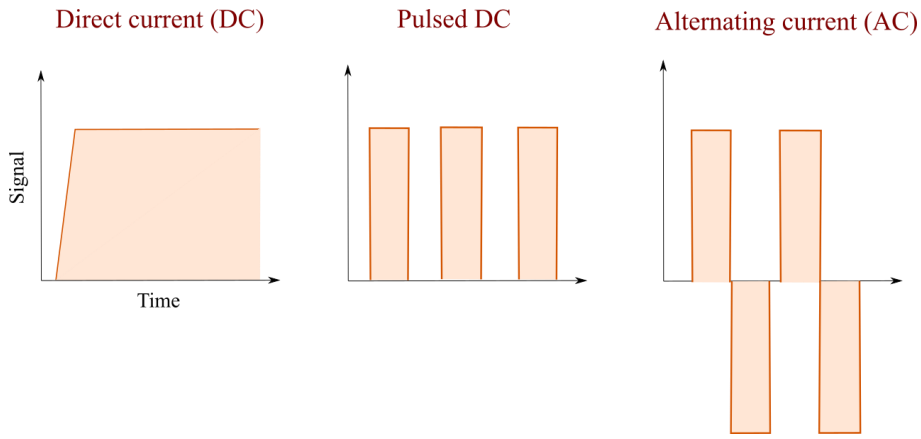

Figure 11. Schematic representations of direct current (DC), pulsed DC and alternating current (AC)

Pulsating current would help avoiding extended skin polarization and voltage increase leading to water electrolysis (RAWAT ET AL., 2008). Although this technique may reduce the amount of drug delivered and lengthen application time, the avoidance of prolonged exposure to an electrical signal is a safer alternative to continuous DC (SAEPANG ET AL., 2021). Some studies argue that the drug flux is actually similar with both DC and pulsed DC because of the progressive increase in skin permeability with current exposure (BAGNIEFSKI AND BURNETTE, 1990). However, it is frequently suggested to choose a "low" frequency to keep a sufficient flux enhancement (LVOVICH ET AL., 2010).

OKABE ET AL., 1986 first developed a pulsed iontophoretic device with promising results for metoprolol delivery with no sign of skin irritation or redness. Other research groups published similar results with different drugs, such as HOWARD ET AL., 1995 with a painless 4-hour delivery of hydroxocobalamin.

High frequency pulses (up to 50 kHz) have also been used as a mean to reduce both capacitance and nonlinear resistance of the SC (ZAKZEWSKI AND LI, 1991). At these frequencies, the contribution of electroosmosis is described as negligible but an additional mechanism, electroporation, takes over as its effect increases with increasing voltage (YAN ET AL., 2005). Electroporation temporarily alters skin permeability by creating nanopores within skin cells (MARTIN AND O'CONNOR, 2017), thus enhancing macromolecule migration (RIVIERE AND HEIT, 1997). Electroporation can still be used prior to ITP in DC configuration though, with high voltage pulses. Finally, another advantage of increasing frequency

is to push back the pain threshold as described by YAO ET AL., 2022 on the WeTac stimulation device used on the palm of the hand (**Figure 12**).

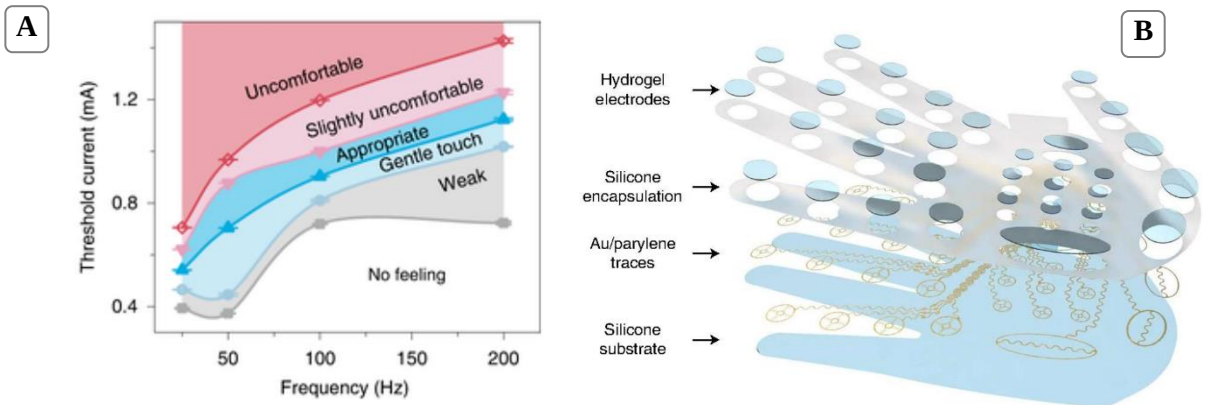

Figure 12. (A) Relationship between stimulation frequency, threshold current and sensation level on the (B) WeTac stimulation device with 32 electrodes (~6-7 cm²) (Yao et al., 2022)

1.2.2. Silver/silver chloride electrode fabrication

Ag/AgCl electrodes are widely used in the field of electrochemistry, mostly as reference electrodes, for their easy fabrication and stable potential (TJON AND YUAN, 2020) in saline environment. More recently, their application is extended to biosensing, electrostimulation or drug delivery as described above.

1.2.2.1. Silver chlorination process

Ag/AgCl electrodes can be obtained using pure silver in the form of plate or wire, or deposited on a substrate by thin film deposition, electroplating or screen-printing (SHINWARI ET AL., 2010). Silver chloride can then be deposited using current-assisted or spontaneous techniques (DUNARE ET AL., 2019):

- **Active electrochemical consumption**. Anodic AgCl growth occurs when applying a direct current between a silver **W**orking **E**lectrode (**WE**) and **C**ounter **E**lectrode (**CE)** (made of silver or any inert material) in a solution containing chloride ions, such as sodium or potassium chloride (NaCl and KCl respectively) (KATAN ET AL., 1974).
- **Spontaneous chemical reaction**. This second technique simply consists in dipping pure silver into hydrochloric acid (HCl) (KUBOTA ET AL., 1982) or ferric chloride ($FeCl_3$) (O'NEIL ET AL., 2013; RAHMAN AND ICHIKI, 2017). AgCl is then spontaneously formed by chloride ion exchange.

In both cases, a micrometer-scale AgCl layer is deposited at the surface with the remaining Ag material underneath (CHO ET AL., 2022). Some studies argue the fragility and lack of reliability of such deposition as it highly depends on the initial Ag microstructure (PARGAR ET AL., 2018). Although Ag/AgCl wires are suitable as reference electrodes in an electrochemical cell, other options need to be explored for TDD applications to provide a reliable and comfortable wearable device.

1.2.2.2. Evolution to stretchable devices

Wearable technologies experienced a booming growth since 2014 Consumer Electronics Show, accelerated by the mass popularization of smartphones (CHANDER ET AL., 2020). They are widely used for biosensors to provide real-time feedback on a person's physiology and activity (VIJAYAN ET AL., 2021). The same constraints can then be transposed to TDD applications with a need to provide stretchable systems for patients comfort. The fabrication process of Ag/AgCl electrodes have to be adapted to fulfill these requirements.

Such systems can be achieved using specific substrates, mostly elastomers, combined with printing (screen-printing, gravure-printing, inkjet printing,…) or solution coating (spin coating, drop casting, dip coating,…) techniques (WU, 2019). Printing techniques offer reproducible, large-scale and low-cost devices.

Screen-printing involves a direct contact transfer of ink from a stenciled mesh to a target substrate (**Figure 13**), offering a resolution of around 200 µm (ZAVANELLI AND YEO, 2021). Different parameters such as mesh size, squeegee pressure or printing speed are controlled to improve the resolution and define the volume of ink deposited on the substrate.

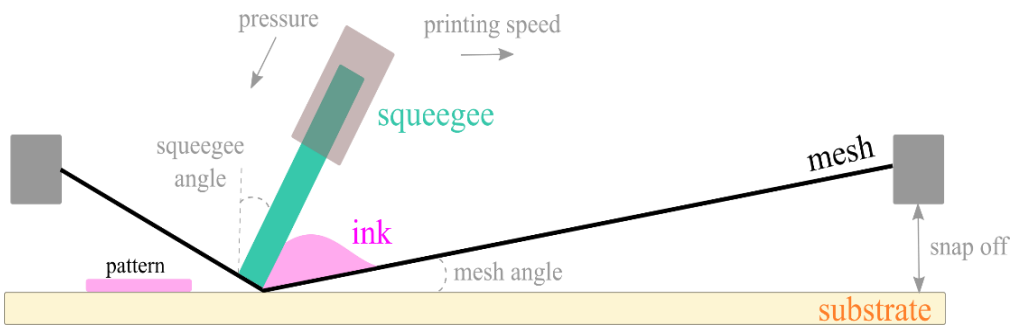

Figure 13. Schematic overview of screen-printing technique and associated parameters (in gray) (modified from Zavanelli and Yeo, 2021)

Ink formulation and **electrode designs** can also play a role in the resolution and stretchability of printed electrodes.

Conductive inks are generally made of conductive nano or microparticles, organic binders or rheological agents and solvents. Novel anisotropic particles structures like silver **N**ano**W**ires (**NW**) or carbon nanotubes provide high conductivity and resistance to strain (ZAVANELLI AND YEO, 2021). Other studies show the influence of ink rheological properties on the precision of printed designs (XU AND WILLENBACHER, 2018).

Finally, lattice geometries like honeycomb structures have a tunable Poisson's ratio, giving them the ability to bend, rotate and align to the constraint direction (DONG ET AL., 2021), which makes them suitable candidates for stretchable electrodes (**Figure 14**). Such lattice could also contain "rigid islands" where non-stretchable components could be placed while maintaining the stretchability of the entire device (MATSUHISA ET AL., 2019). This information is useful to develop a stretchable ITP+MN device combined, as MN arrays are likely to remain rigid to ensure skin perforation.

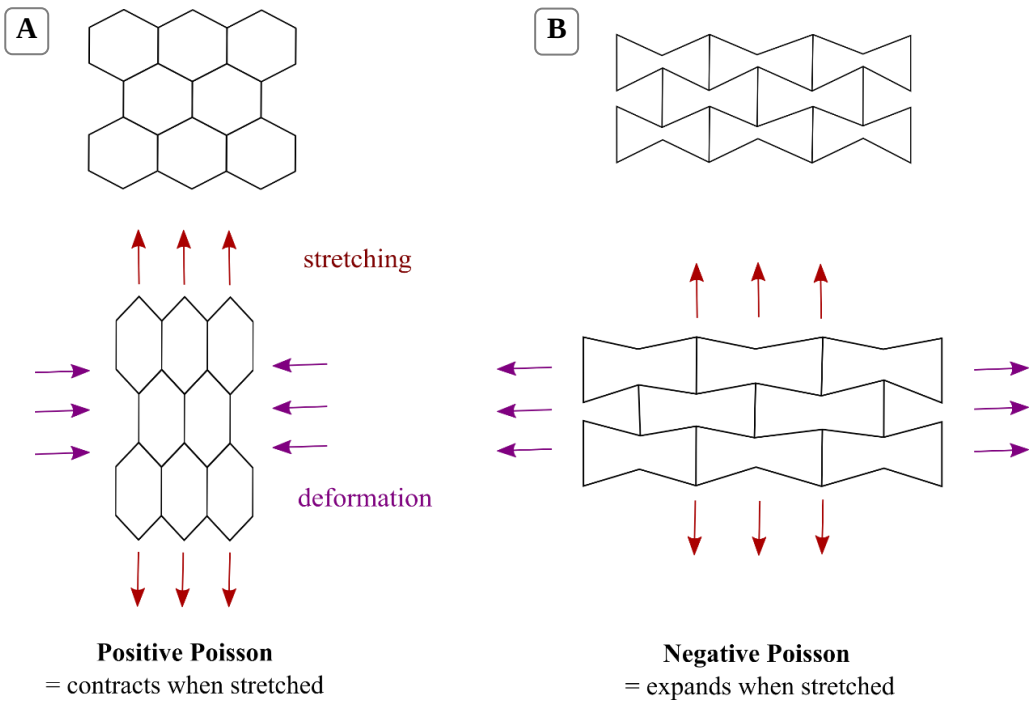

Figure 14. Example of honeycomb structures with (A) positive and (B) negative Poisson's ratio (modified from Sparavigna, 2014)

1.3. Microneedles therapies

A mechanical way to aid drug penetration is to use micro to millimeter scale needles in order to puncture the SC without inflicting any pain as nerve fibers are mostly located in deeper skin layers (TANNER AND MARKS, 2008). The concept of microneedles (MNs) was introduced with a patent filed in 1971 mentioning needle-like designs called "projections" with an aperture extending from a drug reservoir (GERSTEL AND PLACE, 1976). MNs were only demonstrated experimentally in the 1990s and were first manufactured from silicon wafers through ion etching and photolithography in 1998 (ALDAWOOD ET AL., 2021).

This technology is building a growing interest over the years especially from the beginning of the 21st century (**Figure 15**). Since 2005, the cosmetic field started to develop a wide range of products for local applications such as wrinkle removal, scar treatment, whitening or fat reduction (HUANG ET AL., 2022). Only recently have MNs been identified as a promising tool for sensing and systemic drug or vaccine delivery. To date, clinicaltrials.gov website reports 90 completed clinical trials involving MNs (accessed on January 4th 2023), the first one concerning delivery of flu vaccine completed by the end of 2007.

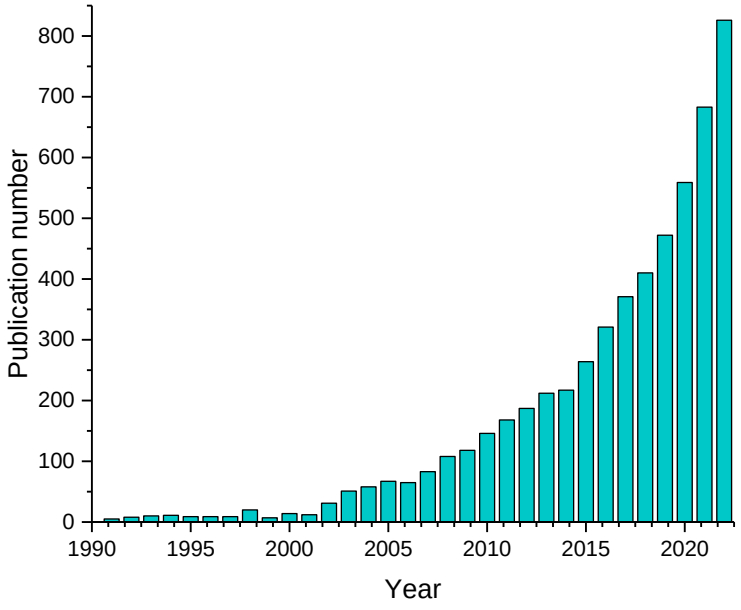

Figure 15. Number of publications from 1990 to 2022 for "microneedle*" on Web of Science

1.3.1. Types of microneedles

Five types of MNs are described in the literature (SARTAWI ET AL., 2022; TURNER ET AL., 2021) as drawn on **Figure 16**:

- Solid
- Coated
- Dissolving
- Swellable or hydrogel-forming
- Hollow

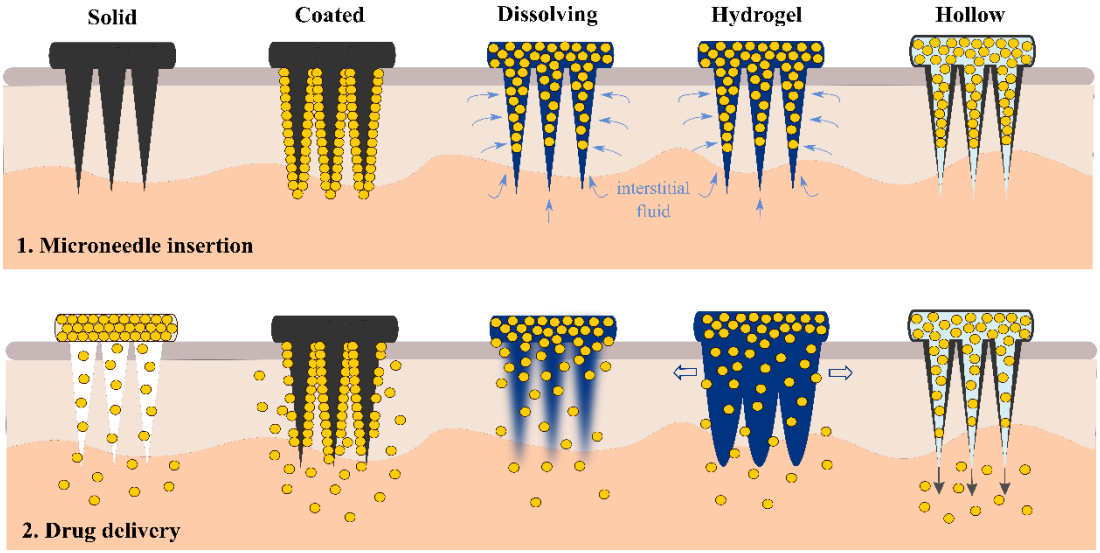

Figure 16. Microneedles types for drug delivery (modified from Kim et al., 2012)

1.3.1.1. Solid and coated microneedles

Solid MNs are used as a pretreatment to increase skin permeability to a wider range of molecules (NAGARKAR ET AL., 2020), following a "poke and patch" principle (VAN DER MAADEN ET AL., 2012). MNs are first inserted to create painless micron-scale pathways into the skin (PRAUSNITZ AND LANGER, 2008), then removed to apply the drug using a patch or a semi-solid topical formulation such as an ointment, cream, gel or lotion (Y.-C. KIM ET AL., 2012).

Coated MNs use the same MN base with a drug coating at their surface. The MN array can then stay in place while the drug diffuses through the dermis. Similarly, coated microneedles follow a "coat and poke" principle (VAN DER MAADEN ET AL., 2012). The main advantage of coated MNs is to preserve micro-channels during drug delivery, while these would reseal within 2 hours after MN removal with solid MNs (GUPTA ET AL., 2011). The coating process is overall challenging and several methods have been studied over time (NAGARKAR ET AL., 2020), such as dip-coating in a liquid solution (GILL AND PRAUSNITZ, 2007) or spray coating with a gas-jet to evenly disperse the drug on the MNs (CHEN ET

AL., 2009). Even though coated MNs can rapidly deliver a controlled amount of drug, this amount is limited by the small available surface area which restricts applications to low-dose or potent drugs only (TUAN-MAHMOOD ET AL., 2013).

1.3.1.2. Dissolving and swellable microneedles

Dissolving MNs appeared in 2005 (ALDAWOOD ET AL., 2021) while swellable (also referred to as hydrogel-forming) MNs are the most recent type of MNs, first reported in 2012 (DONNELLY ET AL., 2012; TURNER ET AL., 2021).

- Dissolving MNs allow a kinetic control of drug delivery depending on the dissolution rate of the chosen water-soluble matrix (CHAMPEAU ET AL., 2020). However, polymer metabolization and elimination may require an extensive investigation for regulatory reasons (DONNELLY ET AL., 2012). Also, this system may be limited to small (<500 Da) water-soluble molecules to allow drug diffusion from the baseplate as well (MIGALSKA ET AL., 2011).
- Swellable MNs are based on a cross-linked polymeric network capable of swelling several times its original volume without dissolving in aqueous solution (M. KIM ET AL., 2012). The drug can either be trapped in the matrix (DEMIR ET AL., 2022), or loaded into an accompanying reservoir (COURTENAY ET AL., 2020). Hydrogel-based MNs can be removed intact with no polymeric residues left (MIGDADI ET AL., 2018) and reused as they can undergo multiple swelling/drying cycles (DEMIR ET AL., 2022).

Most commonly, these two types of MNs contain the drug within the polymer matrix so that the amount of drug is limited to the space available in the pores. Additionally, drug delivery rate highly depends on the polymer dissolution or swelling rate, as the collection of interstitial fluid (ISF) from the skin is necessary to initiate drug diffusion.

1.3.1.3. Hollow microneedles

Hollow MNs can be seen as a miniature version of commonly used hypodermal needles (NAGARKAR ET AL., 2020). They can deliver a pressure-driven flow of liquid or simply pave a path for the drug to diffuse from a reservoir (Y.-C. KIM ET AL., 2012). Such device can be used with a wider range of drugs including high molecular weight compounds, as they are directly guided into the viable epidermis or the dermis (ITA, 2014).

However, hollow MNs are often referred as the most difficult to process and weakest form of MNs because of their thin wall (ALDAWOOD ET AL., 2021). An alternative is to create linear channels within solid MNs to provide more mechanically robust hollow MNs (O'MAHONY ET AL., 2023). Other studies

reported possible tissue clog during insertion, leading to more evolved MN designs with side openings such as the one depicted on **Figure 17** (LHERNOULD, 2012; ZHANG ET AL., 2009).

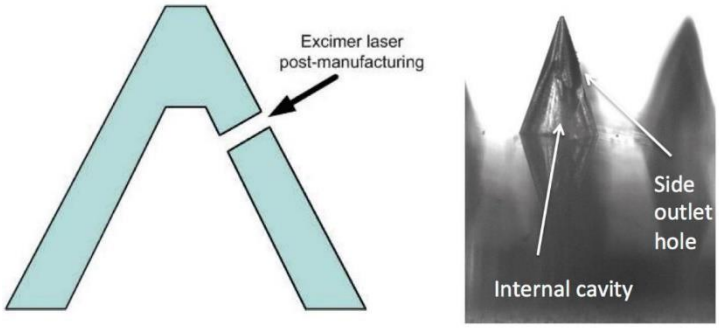

Figure 17. Side-opened microneedles developped from Novinject, Belgium (Lhernould et al., 2015)

1.3.2. Materials and processes

An important variety of materials and processes can be selected to fabricate MNs (**Figure 18**). Their choice mainly depends on the desired MN type, design and production scale.

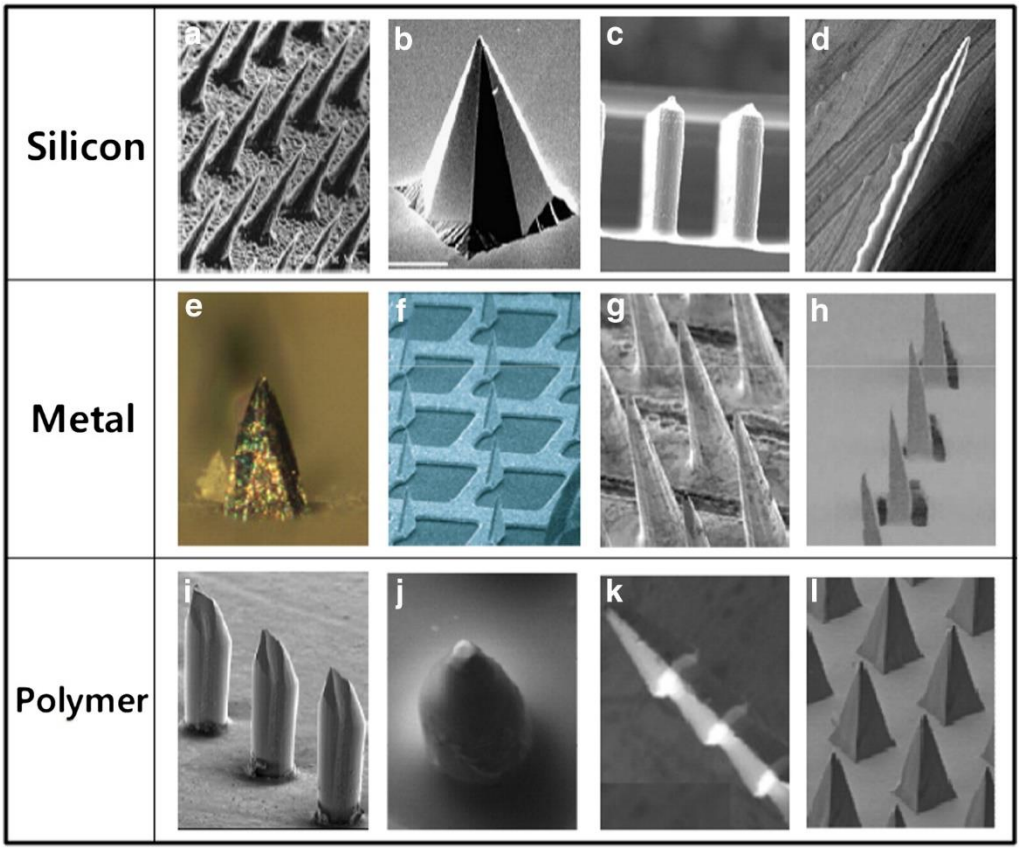

Figure 18. Examples of microneedles made of silicon (a-d), metal (e-h) and polymer (i-l) (Y.-C. Kim et al., 2012)

1.3.2.1. Inorganic materials : silicon, metal and ceramic

The first material used for MNs is silicon and it is to date still reported as the most commonly used material for solid, coated and hollow MNs. Multistep processes and expensive tools were developed by the microelectronics industry, and subtractive technologies such as wet or dry etching are most frequently used for MN fabrication (FARAJI RAD ET AL., 2021). This material however allows batch-production of various shapes and sizes of MN, but biocompatibility concerns emerged due to its brittle nature and possible fractures in the skin causing scarring or fibrosis (FARAJI RAD ET AL., 2021; LARRAÑETA ET AL., 2016). Porous silicon is a biocompatible and bioresorbable alternative, allowing potential broken fragments to degrade in tissue (ANGLIN ET AL., 2008; HERNANDEZ-MONTELONGO ET AL., 2015). Other studies proved however silicon reliability using ultrasharp MNs, showing no single point of failure under compressive thumb pressure (O'MAHONY, 2014).

Similarly to hypodermal needles, metal MNs bypass previous concerns by providing high mechanical strength and biocompatibility. They are mostly made of stainless steel and titanium, but other metals such as palladium, nickel or platinum are also mentioned. Metal MNs are solid, coated or hollow and can be prepared by stereolithography, injection molding, hot embossing, laser sintering, laser ablation and cutting, wet or dry etching and metal electroplating methods (Y.-C. KIM ET AL., 2012; SARGIOTI ET AL., 2023). These techniques however give access to a limited number of MN shapes and sizes that can be necessary to customize depending on the target application.

Ceramic MNs benefit from the same advantages but they also offer adjustable porosity where the drug can be loaded (ITA, 2018). Alumina (Al_2O_3) and zirconia (ZrO_2) are most commonly used and MNs are prepared by micromolding followed by sintering (BYSTROVA AND LUTTGE, 2011; ZHU ET AL., 2010). However, the latter step is usually performed under high temperature which does not allow heat sensitive drugs to be loaded in the matrix (ITA, 2018).

1.3.2.2. Polymer microneedles : from lab-scale to large-scale processes

Unlike inorganic materials, polymers are used for all types of MNs. They allowed the discovery of dissolving and swellable MNs. Dissolving MNs need a water-soluble material such as **H**yaluronic **A**cid (**HA**) or **P**oly**V**inyl**P**yrrolidone (**PVP**), while hydrogel materials are chosen for their swelling properties like **P**oly**V**inyl **A**lcohol (**PVA**) (WANG ET AL., 2022). Similarly to absorbable sutures, bioresorbable polymers are also interesting materials to provide a safe and biocompatible drug delivery with a relatively long-term degradation in case of MN fracture in the skin. These materials are sometimes referred to as "biodegradable" and are usually **P**oly**L**actic **A**cid (**PLA**), **P**oly**G**lycolic **A**cid (**PGA**) and their co-polymers **P**oly**L**actic-co-**G**lycolic **A**cid (**PLGA**) (**Figure 19**) (PARK ET AL., 2004).

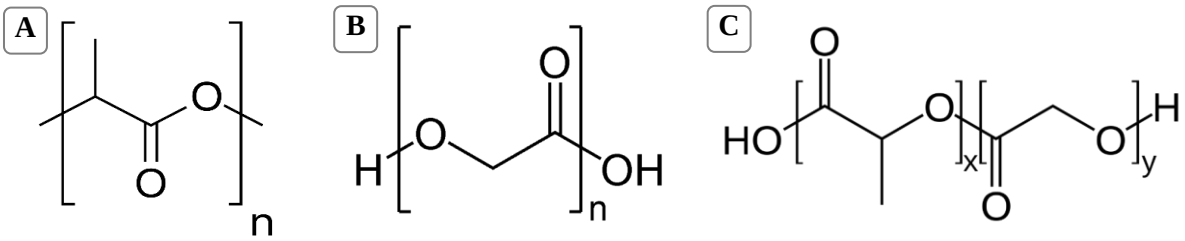

Figure 19. Chemical formula of (A) PLA (B) PGA and (C) PLGA

While glycolic chains slowly dissolve in aqueous solution, lactic chains can be degraded in biological fluids by hydrolytic de-esterification and remaining monomers are removed by natural pathways. Degradation time takes between a week to several months, depending on the ratio of each polymer in the case of PLGA, but also the stereochemistry of lactic monomers (GENTILE ET AL., 2014).

Even though these materials seem less costly than silicon and ceramics, micromolding is the most common process used for MN fabrication (GERA AND BURRA, 2022) which is suitable for lab-scale production only. A hard, usually metallic, master mold is first produced with positive MN designs. A liquid polymer solution such as **P**oly**D**i**M**ethyl**S**iloxane (**PDMS**) is then poured on top and peeled off after crosslinking (**Figure 20A**). MN material can then be deposited in the soft mold and arrays are formed under vacuum (**Figure 20B**) or embossing (FARAJI RAD ET AL., 2021).

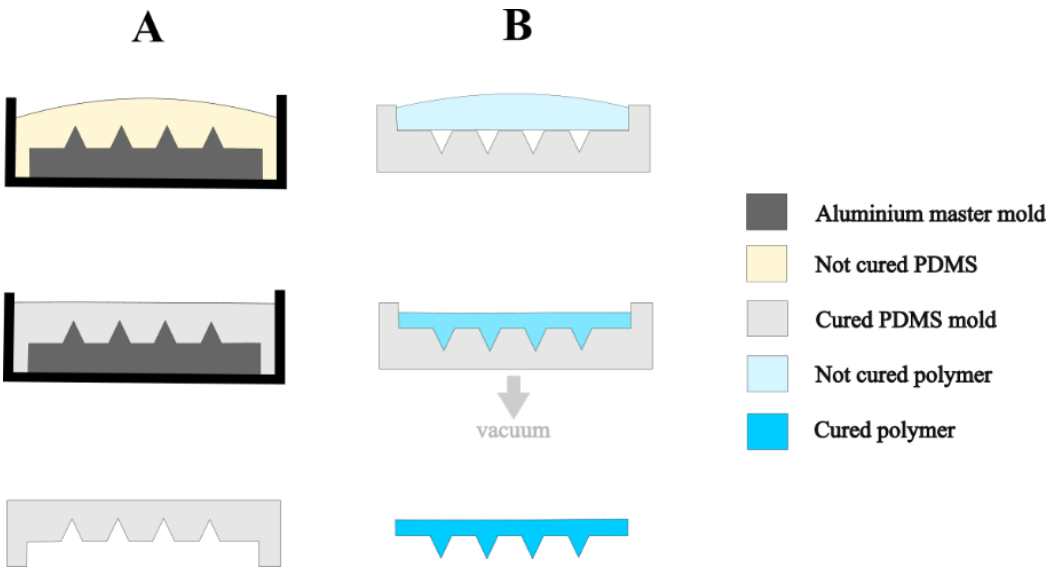

Figure 20. Microneedle molding steps. (A) PDMS mold fabrication (B) Polymer vacuum micromolding (modified from Bocchino et al., 2022)

More recently, additive manufacturing techniques and more specifically vat polymerization appeared to be an easy alternative to increase the production of MN arrays while reducing manpower. **S**tereo**L**ithography **A**pparatus (**SLA**) and **D**igital **L**ight **P**rocessing (**DLP**) are known as the most precise

3D-printing technologies to date (ZHANG ET AL., 2019). SLA is the first commercialized 3D-printing technique and consists in building high-resolution parts by curing a photoactive liquid resin layer by layer (AMIN ET AL., 2016). DLP uses a similar setup except for the light source: UV light is projected to cure a complete layer at a time, resulting in faster printing than SLA. **Figure 21** illustrates both configurations.

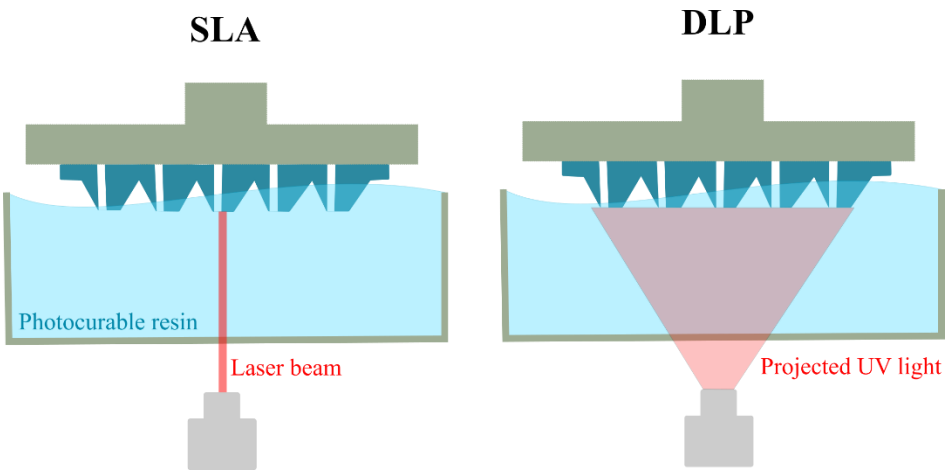

Figure 21. Schematic principles of SLA and DLP

KRIEGER ET AL., 2019 studied the performance and the limitations of SLA with parametric experiments from 200 to 3000 µm tall MN. Remarkable results are obtained for the tallest parts (**Figure 22**) but authors precise their height should be limited to submillimeter range to limit pain when inserted.

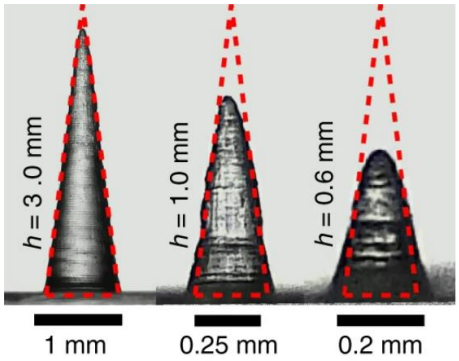

Figure 22. Example of mf 3D-printed MN with 4:1 aspect ratio (Krieger et al., 2019)

For an industrial production of microparts like MNs, microinjection molding and hot embossing are described as the most industrially viable processes (GIBOZ ET AL., 2007). Injection molding requires a hard mold and counter mold sealed together to inject the desired melted polymer at high pressure (**Figure 23**). Apart from the high cost of mold machining, a large waste of material also needs to be anticipated especially when using expensive polymers such as PLGA.

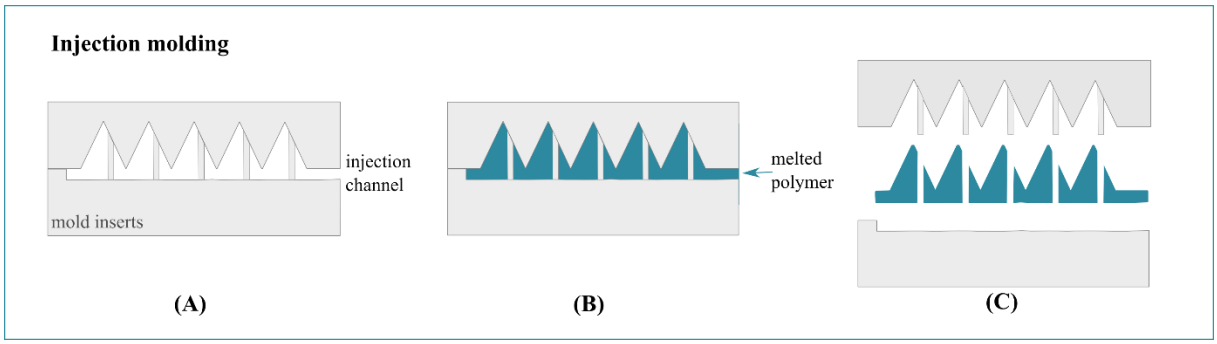

Figure 23. Principles of micro-injection moulding (modified from Heckele and Schomburg, 2003). (A) The mould is closed, emptied and heated above the polymer glass transition temperature. (B) The melted polymer is extruded through the injection channel. (C) The molding tools are cooled down and separated to unmould the injected piece

Hot embossing and thermoforming bypass this problem as extruded thermoplastic sheets are used and heated up between glass transition and melting temperatures, allowing to model the polymer to the desired shape between two molds. Thermoforming is a similar process but it uses vacuum or pressurized gas to press the polymer on a single mold (**Figure 24**) (HECKELE AND SCHOMBURG, 2003). A positive pattern can therefore be design to form hollow MNs, which is easier to manufacture.

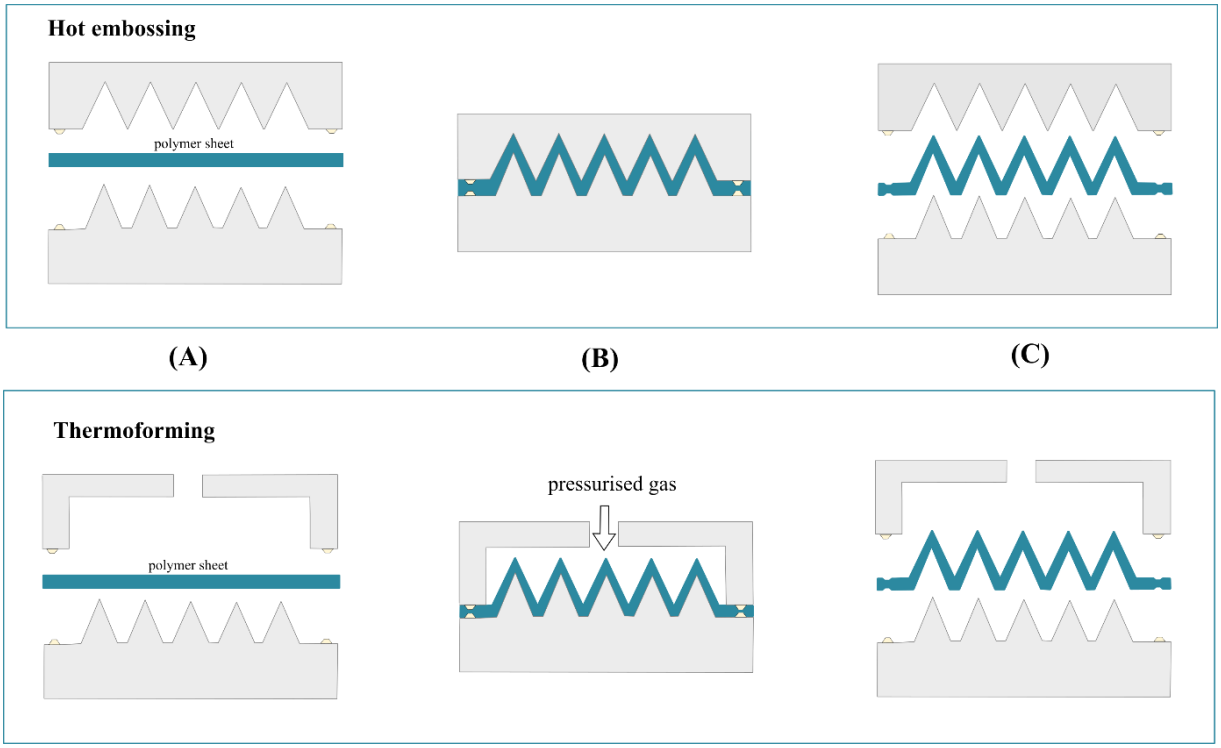

Figure 24. Principles of hot embossing (up) and thermoforming (down) (modified from Heckele and Schomburg, 2003). (A) The polymer sheet is placed between two inserts, (B) sealed and heated up above glass temperature. (C) In hot embossing, the desired shaped is obtained by mechanical compression of the mold and the counter mold, while in thermoforming uses a pressurized gas or vaccum

In both cases, it is necessary to extrude the material into sheets of homogeneous and desired thickness beforehand, which can be challenging to manufacture or even supply.

1.3.2.3. Array shape and design

Apart from materials properties, MN geometry is a crucial factor for a safe and efficient skin penetration, especially for hollow MNs that are considered as the weakest type of MNs. As a viscoelastic tissue, the insertion force required to perforate the skin may exceed the tensile strength of the MNs which may cause them to break (NAGARKAR ET AL., 2020). The probability of fracture also increases with MN length (CHAMPEAU, 2020) but a maximum of 900 µm is anyway suggested as their application becomes relatively painful above that threshold (GARLAND ET AL., 2012), which is consistent with epidermis thickness estimations.

Regardless of the MN type, different designs have been reported over the year (**Figure 25**) : conical (a), tapered-cone or pencil-tip (b), pyramidal (c), pyramidal-tip (d) (CORDEIRO ET AL., 2020), tetrahedral (e) (LOIZIDOU ET AL., 2016), cylindrical (f), beveled-tip cylinder (g), beveled-tip cone (h) (MCALLISTER ET AL., 2003). Conical and square pyramidal MNs are most commonly used but more complex geometries such as harpoon-shaped (i) (AOYAGI ET AL., 2020), arrowhead (j) (GILL AND PRAUSNITZ, 2007) or turret (k) (JOHNSON ET AL., 2016) MNs were more recently designed to improve needle penetration. Other studies use numerical simulations to sweep different MN designs and correlate geometrical parameters to penetration depths (DAVIDSON ET AL., 2008; OLATUNJI ET AL., 2009).

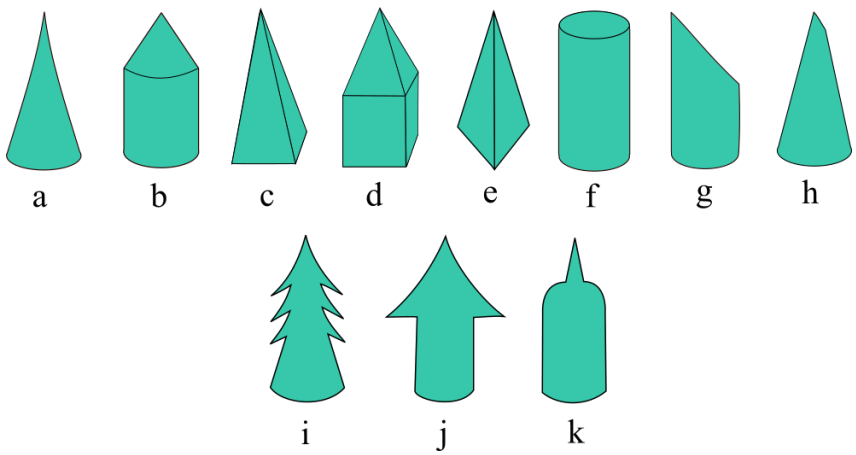

Figure 25. Existing MN designs. (a) conical, (b) tapered-cone, (c) pyramidal, (d) pyramidal-tip, (e) tetrahedral, (f) cylindrical, (g) beveled-tip, (h) beveled-tip cone, (i) harpoon-shaped, (j) arrowhead and (k) turret

Regarding the array density, it is intuitively believed that increasing the number of MNs also increases the number of pathways for drug diffusion. However, the elastic response of the skin creates a “bed of nails” effect reducing MN penetration (KOCHHAR ET AL., 2013; LHERNOULD ET AL., 2015). It is thus important to keep a **sufficient interspace** to make sure all the MN involved in the array contribute to the same extent to drug delivery.

1.4. Combination of iontophoresis and microneedles

The combination of ITP and MNs remains rare in the literature but the number of associated research papers starts to increase since 2011 (**Figure 26**).

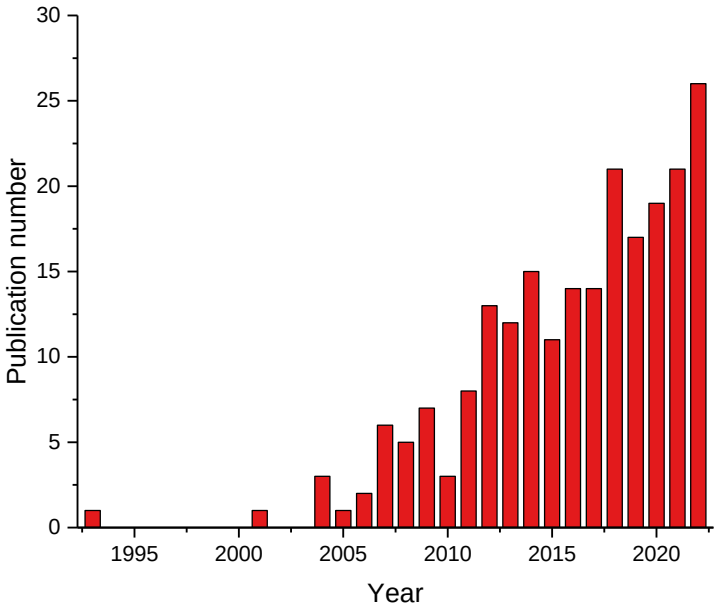

Figure 26. Number of publications from 1993 to 2022 for "microneedle* AND iontophoresis" on Web of Science

1.4.1. Consecutive use: resistance drop with stratum corneum perforation

Early studies combining ITP and MNs make a consecutive use of each technique using solid MNs prior to electrical drug enhancement (pretreatment). Electrical measurements using **T**ranscutaneous **E**lectrical **R**esistance (**TER**) testing (LANKE ET AL., 2009), impedance spectroscopy (GUPTA ET AL., 2011), or a simple multimeter (WING ET AL., 2013) can indeed highlight a significant drop in electrical resistance after MN application, which is directly correlated with skin permeability (KARANDE ET AL., 2006). This effect is beneficial to electrical enhancement technologies such as ITP that require a conductive and saline environment to function properly.

WU ET AL., 2007 show that the effect of MN pretreatment is more significant on high molecular compounds such as fluorescein isothiocyanate-dextran (FD4, 3.8 kDa) compared to deuterium oxide (D_2O) (**Figure 27**).

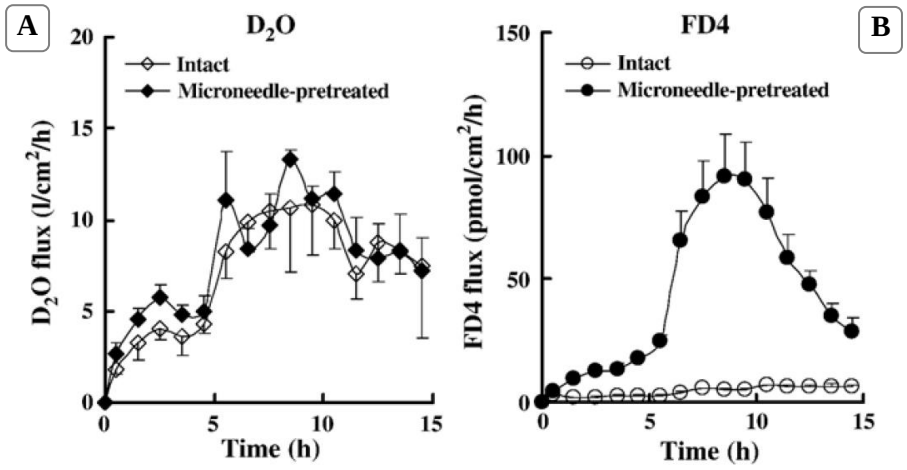

Figure 27. Flux of (A) D_2O and (B) FD4 through intact and MN-pretreated hairless rat skin before (0-5 h) during (5-10 h) and after (10-15 h) ITP at 0.3 mA·cm^{-2} (Wu et al., 2007)

Additionally, KATIKANENI ET AL., 2009 studied the influence of drug reservoir positioning on the protein flux actually delivered: **Figure 28a** shows that, despite negatively charged **D**ani**P**lestim (**DP**) at pH 7.5, results are similar if not better when the reservoir is placed under the anode (incorrect polarity). The **AC**eta**M**inophen (**ACM**) marker (neutral molecule) helps identifying that this phenomenon in due to the electroosmosis contribution that occurs at the anode (**Figure 28b**), enhancing drug delivery despite the drug charge.

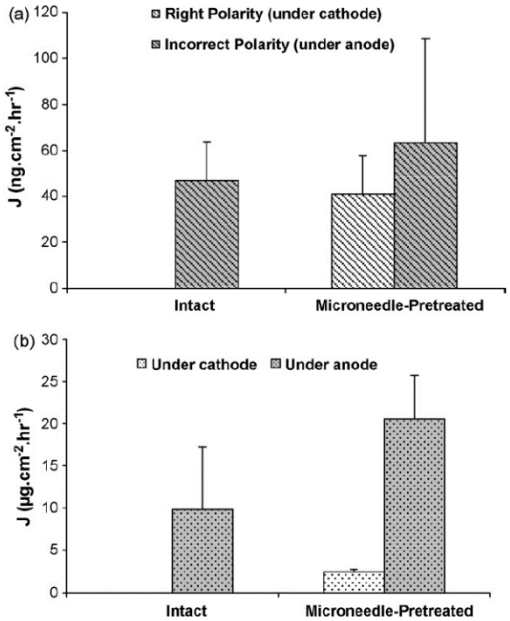

Figure 28. (a) DP and (b) ACM steady-state flux across intact and MN-pretreated hairless rat skin at pH 7.5 during 6 hours of ITP at 0.5 mA/cm², N=3 (Katikaneni et al., 2009)

1.4.2. Simultaneous use: delivery enhancement of heavy molecules

More recent studies simultaneously use both techniques to deliver macromolecules. GARLAND ET AL., 2012 indeed compare the permeation of compounds of different molecular weight using passive, ITP (0.5 $mA \cdot cm^{-2}$), MN, and ITP+MN delivery (**Figure 29**). For the smallest molecules (theophylline (A), methylene blue (B) and fluorescein sodium (C)), MN and ITP+MN give satisfying yet similar results which means that the additional ITP assistance does not further enhance drug diffusion. For larger molecules such as insulin (D) and FITC-BSA (E), a significant difference is observed and the combination of ITP and MN leads to the most satisfying results within the first hours of delivery.

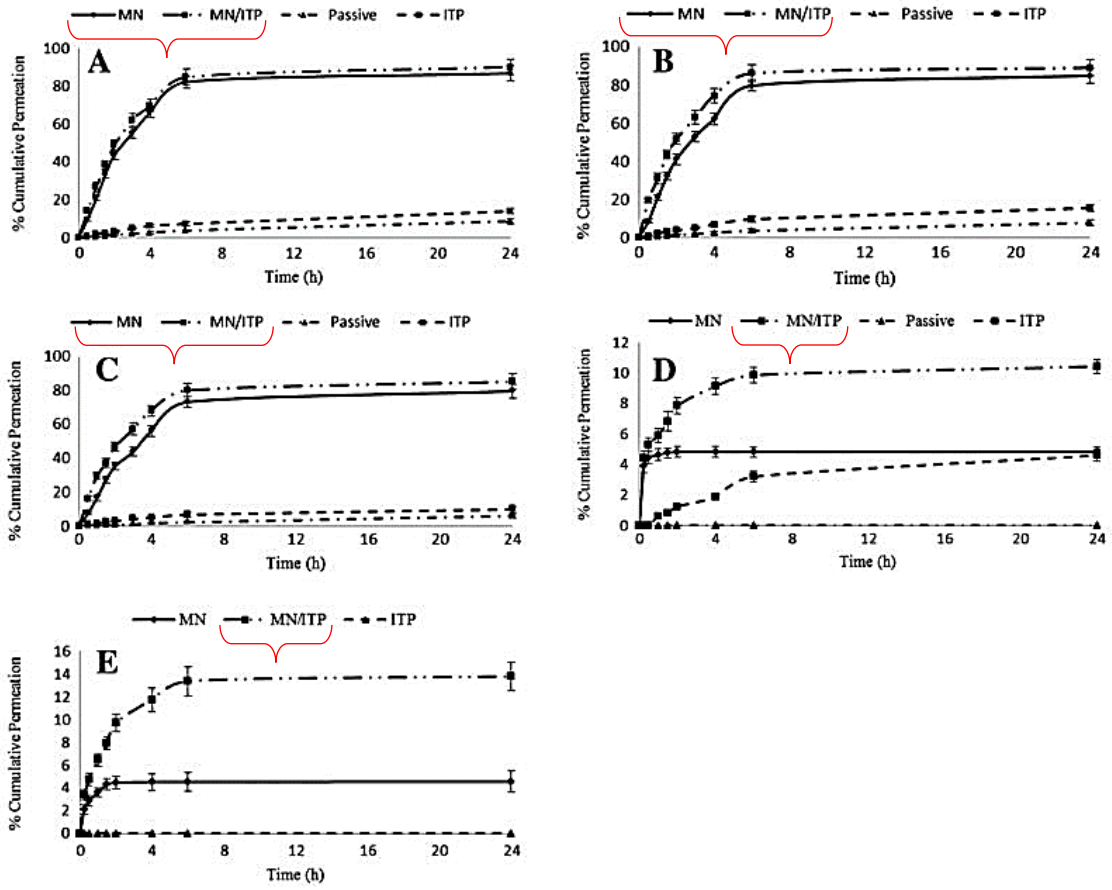

Figure 29. *In vitro* permeation profile across neonatal porcine skin of (A) theophylline, (B) methylene blue, (C) fluorescein sodium, (D) insulin, and (E) FITC-BSA (Garland et al., 2012)

X. Xie's team performed *on vivo* delivery of insulin nanovesicles on diabetic rats using ITP+MN. Blood glucose showed a successful level maintenance below normoglycemic threshold (below 200 $mg \cdot dL^{-1}$) for 6.8 hours compared to 0 and 5.7 hours for ITP (1 mA) and MN alone respectively (YANG ET AL., 2020). One year later, a closed-loop device is developed by the same team integrating three modules: (1) a glucose biosensor, (2) an ITP+MN-assisted insulin delivery component and (3) a flexible **P**rinted **C**ircuit **B**oard (**PCB**) as a recording and control section (LI ET AL., 2021).

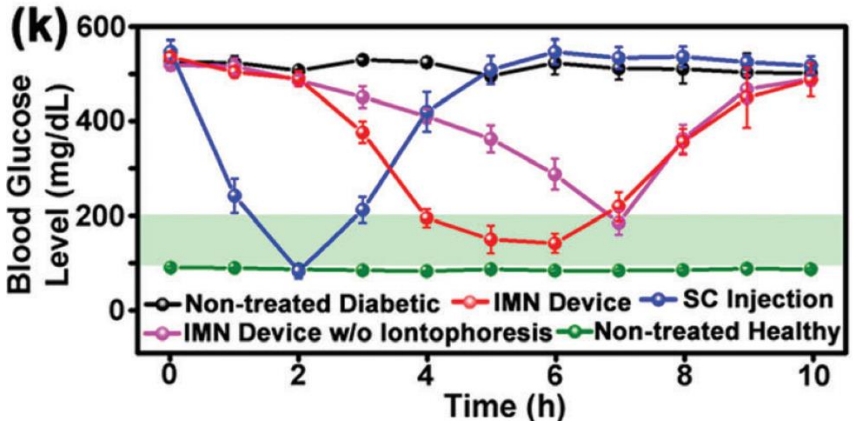

Figure 30. Blood glucose monitoring of rats (N=3). IMN = ITP + MN (red), IMN w/o Iontophoresis = MN alone (purple), SC = subcutaneous (blue). The green region corresponds to normoglycemia (Li et al., 2021)

Results obtained with this device (**Figure 30**) once more highlight the benefits of a transdermal device for a long-term delivery in opposition to subcutaneous injections that are preferred for their fast action. Differences between MNs alone and the combination of ITP and MNs start to appear after three hours, with a faster drop in the blood glucose level in the ITP+MNs configuration.

Finally, the **CO**rona**VIr**us **D**isease 20**19** (**COVID-19**) pandemic had an important impact on the development of transdermal vaccines. ZHENG ET AL., 2023 therefore studied the permeation of a model antigen, ovalbumin, in similar conditions. **Figure 31** supports previous observations as the combination of ITP and MN helps reaching a cumulative amount of ovalbumin after 30 minutes that is twice as important as MN alone and six times ITP alone (1 mA·cm^{-2}). Similar results are obtained with a current density lowered to 0.5 mA·cm^{-2} before pursuing *on vivo* vaccine delivery on mice.

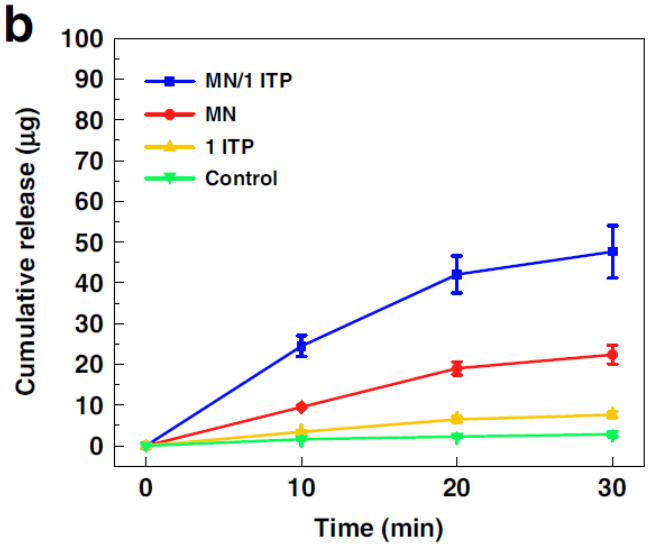

Figure 31. *In vitro* cumulative permeation profile of ovalbumin across rat skin (N=3) in control, cathodic ITP at 1 mA·cm^{-2} (yellow), MN (red) and ITP+MN (blue) groups (Zheng et al., 2023)

In conclusion, the combination of ITP and MNs appears as a promising strategy to deliver macromolecules transdermally. Even though the latter section presented the therapeutic interest of such device, this thesis focuses on the materials sciences behind it. The following chapters therefore study both fabrication and characterizations of MN arrays and ITP electrodes until developing a homemade prototype.

CHAPTER 2

Chapter 2: Microneedles for drug delivery

Introduction

The first part of this chapter presents an exploratory work on polymer microneedles (MNs) in general, in collaboration with Tyndall National Institute, Cork, Ireland. By combining different biomaterial formulations known in CEA lab with the MN geometry developed by Pr. Conor O'Mahony's team, polymer MNs have been prepared and a set of characterizations were carried out in Ireland for one month. The first part of the Chapter summarizes this project in the form of a scientific paper soon to be submitted.

In the second part, the PhD project focuses on bioresorbable hollow MNs. More specifically, different fabrication processes are explored in order to identify possible scale-up routes for the future of MN therapy.

Finally, different testing configurations are discussed in order to easily evaluate MNs ability to perforate the *stratum corneum* while using artificial skin models instead of biological tissues.

2.1. Polymer microneedles : a journey at Tyndall National Institute

Skin insertion and mechanical characterisations of multiple formulations of polymer microneedles for drug delivery

Mehrsa Rafie Jirdehi[a,b], Ryan Sebastian[c], Amélie Revaux[b], Conor O'Mahony[c]

[a] *Univ. Grenoble Alpes, CEA-Liten, DTNM, F-38000*

[b] *Univ. Grenoble Alpes, CEA-Leti, DTBS, F-38000*

[c] *Tyndall National Institute, University College Cork, Cork, Ireland*

Abstract

In this study, a catalogue of six biocompatible polymer formulations is presented on a single conical octagonal microneedle (MN) design. As the mechanical strength of this design has been thoroughly studied on silicon, this work aims to compare the mechanical properties of different polymer materials commonly used in MN therapy. Swellable MNs (poly(ethylene glycol) diacrylate or PEGDA), soluble MNs (carboxymethylcellulose or CMC, CMC+ polyvinylpyrrolidone or CMC/PVP, hyaluronic acid or HA) and MNs containing an active principle (lidocaine, 5-aminolevulinic acid or 5'ALA) are compared. Skin perforation tests on human abdomen explant showed satisfying results (> 73% probability of success) for all formulations except one: pure CMC. Compression tests help identifying a singular fragility on HA-based MNs that are later confirmed by shear tests: despite the controlled micromoulding process, the polymer remains at the perimeter of the mould leading to hollow MN arrays. CMC/PVP-based material appear on the contrary as very ductile as they are capable of being crushed and sheared without breaking. While PEGDA MNs are capable of holding up to 3 N normal force, they break below 1 N lateral force at 30% of the tip. Finally, the presence of 10 wt% lidocaine in a CMC/PVP matrix is shown to both increase MN ductility and degradation rate.

1. Introduction

Microneedles (MNs) are a painless and minimally invasive alternative to regular hypodermal needles not only for drug delivery but also for biosensing. This technology appeared in 1976 but only experienced an exponential growth since the 1990s with the development of microfabrication tools and microelectromechanical systems (MEMS) (Faraji Rad et al., 2021; Gerstel and Place, 1976).

MNs are used in the form of arrays in transdermal patches in order to perforate the outermost layers of the skin only, and more specifically the *stratum corneum* (SC). This cornified layer acts as an environmental barrier to protect the body from biological threats (Boer et al., 2016).

Silicon is the first material used for MN fabrication, combined with etching methods to reach various shapes and sizes. Three types of MNs are described: solid, drug-coated and hollow MNs. Despite its considerable mechanical strength though, materials cost is

high and the fabrication process is long and complex (LARRAÑETA ET AL., 2016).

These limitations can be overcome using polymeric MNs. In addition, polymers allowed the creation of new types of MNs: dissolving and hydrogel-forming (or swellable) MNs (DONNELLY ET AL., 2012). However, polymer MNs are often described as a weaker alternative and their mechanical properties must be verified on an individual basis.

In this study, the same design as previously studied silicon MNs (O'MAHONY, 2014) is used to prepare biocompatible polymers (later called "biopolymers") MNs. A catalogue of six biopolymer-based matrices is studied to compare their ability to perforate abdomen skin explant, and their mechanical properties (compression, shear, bending).

2. Materials and methods

2.1. MN fabrication

Silicon master moulds are prepared by KOH wet etching technique as described by O'MAHONY ET AL., 2023. An octogonal conical structure is obtained with a MN height of 500 µm and a pitch of 1750 µm.

2.1.1. Polymer micromoulding process

Negative moulds are prepared with medical grade polydimethylsiloxane (PDMS, MED-6015, NuSiL Technology, CA, USA) with a 10:1 ratio of elastomer to curing agent (O'MAHONY ET AL., 2016) (Tyndall National Institute, Ireland). An aluminium chuck is manufactured (CEA, France) and connected to a vacuum pump to reach an absolute pressure of 20 mbar. The vacuum program and post-processing are adapted for each material according to solutions viscosity and previously developed processes (CHAMPEAU ET AL., 2020, DEMIR ET AL., 2022).

Polymer solutions and MNs are prepared as follows. Those containing an active principle are presented with an asterisk.

- **PEGDA** : A solution of 99.5 wt% poly(ethylene glycol) diacrylate (PEGDA, average Mw 250 Da, Sigma-Aldrich, MA, USA) and 0,5 wt% of a biocompatible photoinitiator (Irgacure 2959, Sigma-Aldrich, MA, USA) is prepared and stored at 4°C protected from light. MNs are moulded at an absolute pressure of 100 mbar for 30 minutes, then 20 mbar for two and a half hours. MNs are crosslinked after moulding at 365 nm UV light for one minute and a half.
- **HA and HA*** : An aqueous solution of 7.3 wt% of hyaluronic acid (Low Mw ~55 kDa, Contipro, France) is prepared and mechanically stirred for 24 hours. HA* solution contains 10 $g \cdot L^{-1}$ or 0.9 wt% of 5-aminolevulinic acid (5-ALA, GMP Grade, Biosynth Chemistry & Biology, Switzerland) as described by CHAMPEAU ET AL., 2020. MNs are moulded according to the same protocol and the moulds are kept in a

40°C heat chamber for 24 hours post-processing.

- **CMC**: An aqueous solution of 4 wt% sodium carboxymethylcellulose (Na-CMC, Mw 95 kDa, Blanose™ 7LP EP, Ashland, DE, USA) is prepared and MNs are moulded according to the same protocol. The moulds are first kept in a 40°C heat chamber for 24 hours, then dried at 80°C for another 24 hours.
- **CMC/PVP and CMC/PVP*** : 5 wt% Na-CMC and 10 wt% polyvinylpyrrolidone (PVP, Kollidon® 90F, BASF, Germany) are dissolved in 25.5 g saline solution (0.9 wt%, prepared from solid NaCl, Sigma-Aldrich, MA, USA). For CMC/PVP* solution, 10 wt% lidocaine hydrochloride (Septodont, France) is added. Both solutions are mechanically stirred for 3 days. The moulding process takes 8 hours with 1 hour at 100 mbar and 7 hours at 20 mbar. As for HA and HA*, MNs are dried in their mould for 24 hours at 40°C.

During the moulding process, the polymer solution is poured in excess on the PDMS mould. Halfway through the vacuum process, the excess material is removed.

2.1.2. MN array sole

After post-processing, a photosensitive biocompatible resin (Surgical Guide, Formlabs, MA, USA) is poured on the mould. A

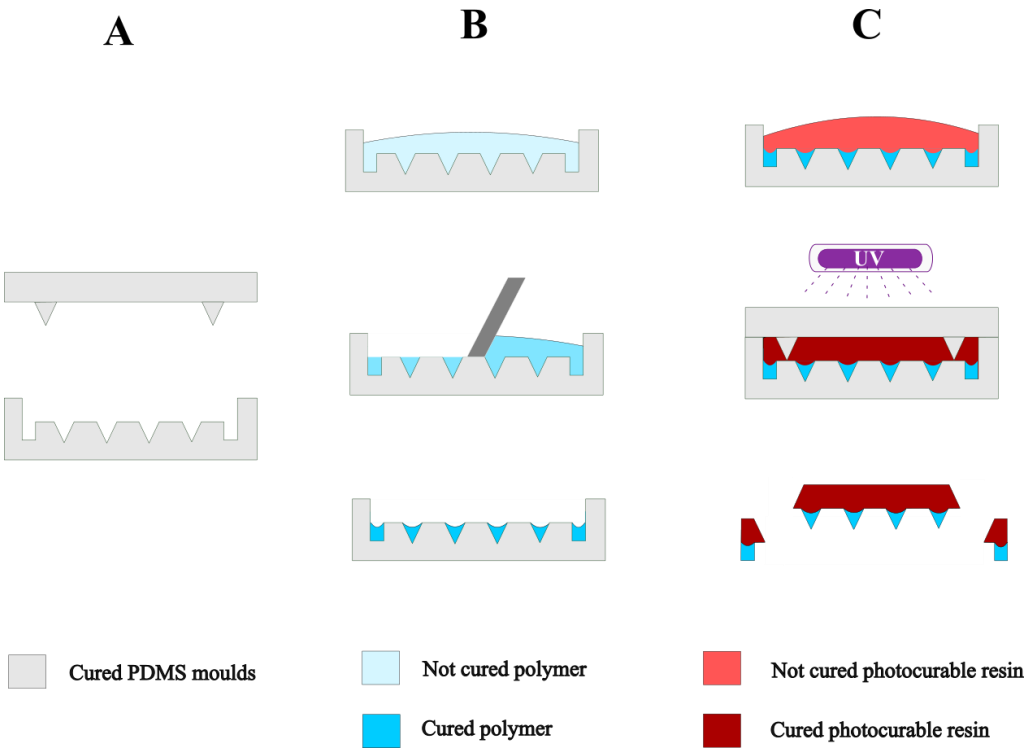

Figure 1. Multistep micromoulding process for microneedle fabrication. (A) Front and back PDMS moulds are prepared as described by Bocchino et al., 2022. (B) The desired polymer solution is moulded under vacuum, removing the excess material at the base halfway through the drying process. (C) A photocurable resin is poured at the back of the array and contained by the back mould while cured under UV light

backmould is placed on top and the resin is cured at 405 nm for 1 minute. **Figure 1** summarises the multistep MN fabrication process. Microneedle arrays are then unmoulded, inspected (see Imaging section) and stored in a dry heat chamber at 40°C for a couple of days. They are then kept in a desiccator under static vacuum until use.

2.2. Characterisations

2.2.1. Ex vivo skin perforation

Skin explant preparation

Ex vivo human abdomen skin was obtained from a female from a plastic surgical operation, following protocols approved by the Clinical Research Ethics Committee of the Cork Teaching Hospitals (CREC) and informed consent the patient. The skin was stored at -80°C after collection. Pieces of 35x35 mm were cut and underlying adipose tissue was removed using a scalpel. The samples were then placed in 0.1 M phosphate buffered saline solution (Sigma Aldrich, USA) for five minutes to rehydrate and reach room temperature. They are finally placed on a custom made jig to stretch the skin to its natural tension (**Figure 2**).

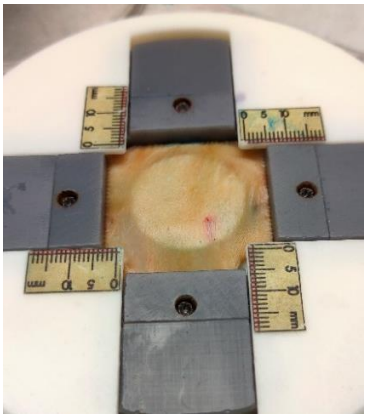

Figure 2. Skin explant stretched on a custom made jig

Perforation parameters

The MN arrays were applied to the *ex-vivo* skin using a custom made benchtop impact applicator based on a modified Abeco 2006 solder removal tool (Farnell, Dublin, Ireland) with an impact energy of 0.29 J (0.45 $J \cdot cm^{-2}$) and a residual force of 1.37 N which corresponds to 5 mm of spring compression.

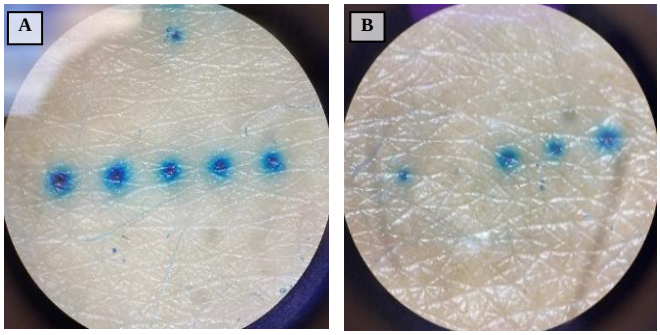

Figure 3. Example of methylene blue staining after application of a complete 5-MN row (A) Successful perforation (B) Failed perforation of the second MN (Magnification x25)

Methylene blue staining

In order to easily identify the success or failure of skin perforation, a methylene blue stain is applied on the skin following the array removal and left on for 2 hours. The methylene blue stain was removed after by thoroughly scrubbing the penetration site with an ethanol soaked tissue. If the SC was perforated, methylene blue diffuses to the deeper layers of the skin and the stain remains visible after stain removal (**Figure 3A**). On the contrary, if the SC is not perforated, the stain is removed during the cleaning process as depicted on **Figure 3B**.

Penetration depth cannot be precisely measured with this technique though as the cavities

created by the microneedles will retract for two reasons:

- A first retraction occurs when the array is removed. In practice, unlike solid microneedles, biomaterial based MNs remain in place after application.
- Once the skin is removed from the jig for sampling, no more tensile stress is exerted to keep it stretched which adds another level of retraction.

So even if the cavities are visible during imaging, their size will be underestimated. To precisely identify cavities dimensions, imaging must be performed with the array in place and stretched skin, which requires a challenging setup or the use of a transparent skin phantom that may not be mechanically reliable.

Penetration efficiency calculation

For each material, skin perforation tests using *ex vivo* abdomen skin were carried out in triplicates. For each perforation test, arrays containing a single row of MNs were selected. After the staining process, the number of stained holes were counted and a penetration efficiency was calculated as follows:

$$Penetration\ efficiency\ = \frac{\#\ perforations}{\#\ total\ number\ of\ needles} \times 100$$

2.2.2. Imaging

Imaging before and after mechanical experiments are performed on a 3D microscope (VHX-2000, Keyence, Japan). MN picture are taken at 85 degrees angle and with 200 fold magnification.

A x20 magnification lens (Skyvik, India) is used on top of a smartphone camera to reach 60x magnification for operando recordings of compression tests at 90° angle. Videos are processed to extract a picture every 10 seconds.

MN shapes are verified on a binocular microscope (Zeiss, Germany) after moulding as well as before and after perforations tests. Perforated skin samples are inspected similarly after methylene blue staining to count stained holes.

2.2.3. Mechanical testing

Shear tests (552, Royce Instruments, CA, USA) are performed using a load cell of 500 g with a test speed is set at 25 µm·sec^{-1}. MN tips are sheared at 30% of their initial height and each material was tested in replicates of 3 (N=3).

Compression and bending tests are performed on an Instron 5565 testing machine (Instron, MA, USA) using a 5 mm diameter aluminium rod as a probe:

- Compression tests parameters are set in a quasi-static manner with a speed of 1 µm·sec^{-1}. The displacement threshold is set at 30% of each MN initial height and each material was tested in triplicates (N=3).
- Bending test parameters are similar to shear tests with a test speed of 25 µm/sec and a force threshold of 4.9 N. Arrays are placed perpendicular to the

probe which is set at 30% of MNs initial height using feeler gauges as a spacer (**Figure 4**). Each material was tested duplicates (N=2).

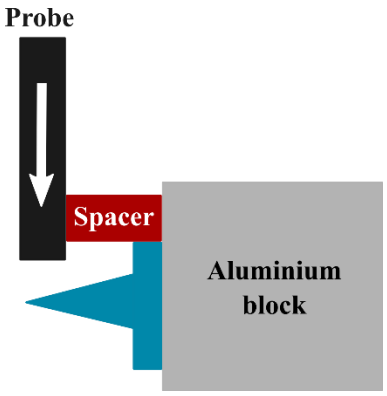

Figure 4. Schematic drawing of bending test setup

Compression and bending tests for each material yielded *N* sets of time, displacement and force data where *N* is the number of replicates for that particular mechanical test. The displacement was normalised by dividing with the initial height of the needles as each MN had a slightly different height due to manufacturing variations. The force values of these *N* datasets are averaged to give a representative force versus displacement curve for each material.

3. Results and discussions

3.1. Materials resistance to skin perforation

3.1.1. Perforation results

As described earlier, the main goal of microneedles is to create a pathway through the *stratum corneum* (SC) without inflicting pain to the patient. Perforation tests on human skin explant are performed to define if the microneedle material has an impact on a successful skin perforation.

Figure 5 shows that most materials considered in the study perforate the SC with at least 73% probability of success. Silicon MNs of the same geometry presented by O'MAHONY, 2014 are used as a reference material with 100% penetration efficiency.

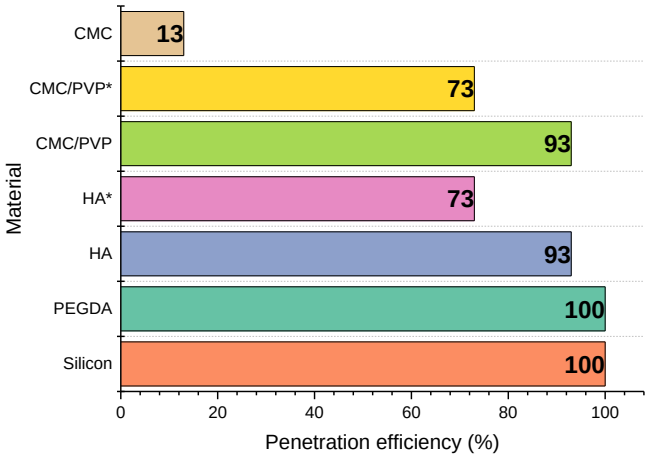

Figure 5. Perforation efficiency calculated on 15 microneedles for each material.

One material only, CMC, displays a low probability of success of 13%. The mechanical weakness of the material has indeed been mentioned by LEE ET AL., 2008. In addition, the low solubility of this polymer in water may cause the creation of a thin CMC wall during micromoulding, instead of a full CMC MN. These MNs indeed appear fragile during fabrication process, which justifies the use of a polymer mixture such as CMC/PVP for a better mechanical resistance to skin penetration. CMC alone is then left out of the rest of the study.

3.2. Materials resistance to axial and transverse stress

3.2.1. Compression tests

Compression tests are combined with operando imaging to correlate curve shapes with failure mechanism, as well as pictures of the MN after compression. Each polymer family is presented separately, and actually displays different mechanical behaviour under compression.

The PEGDA compression profile in **Figure 6A** appears as a curved line with no evidence of tip fracture, i.e. no sharp spike in the force recorded. By looking at the operando imagine on **Figure 6B**, the material seems to be crushed under the effect of the probe, without causing failure. Post compression imaging (**Figure 6C**) shows that the tip indeed remains intact, but the MN itself is bent to the side. PEGDA MNs therefore display a crushing behaviour with a plastic deformation in the studied configuration. A slight change in slope around 18% displacement (red arrow) suggests the beginning of MN bending as described by GITTARD ET AL., 2013. This hypothesis could be verified by repeating the tests at different displacements until starting to observe a plastic deformation.

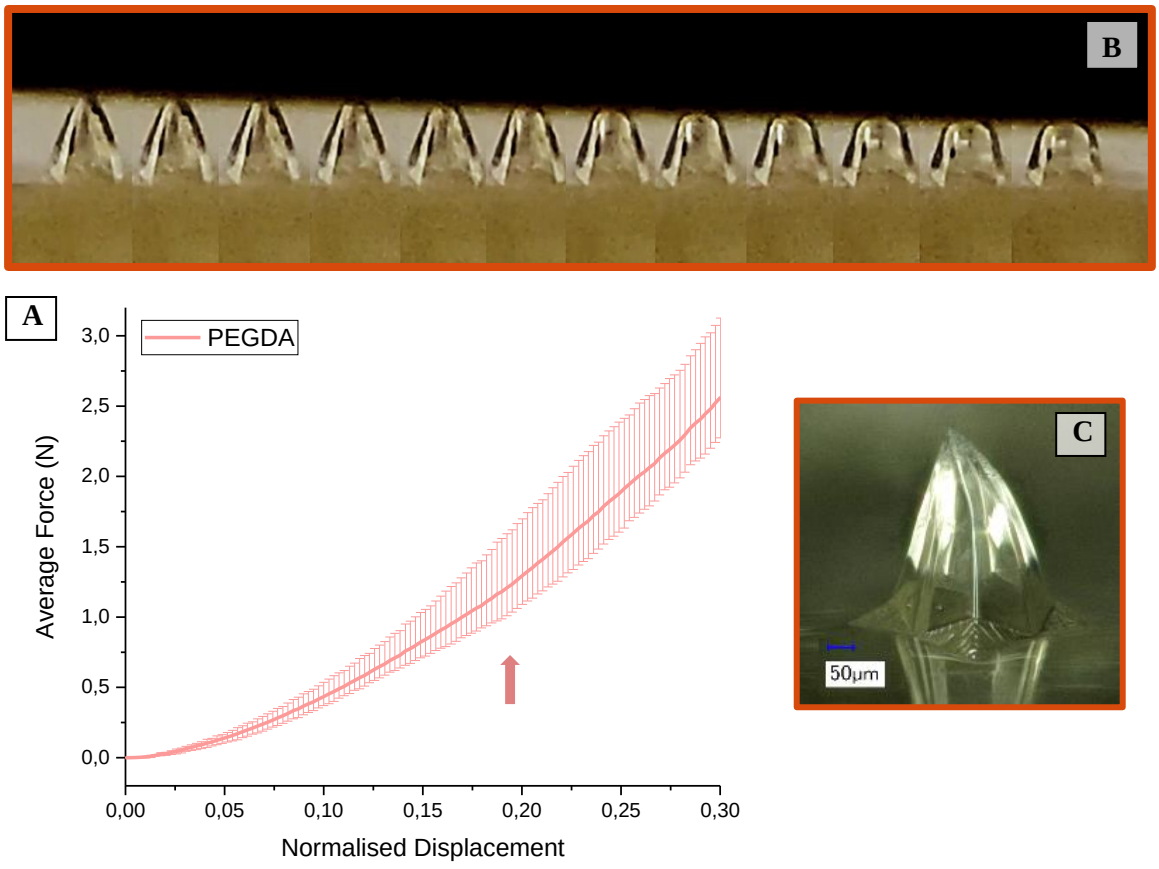

Figure 6. (A) Average compression curves with standard deviation, (B) Operando (x60, 90° angle) and (C) Post compression (x200, 85° angle) images for PEGDA microneedles until 30% compression (N=3). Red arrow indicates the possible beginning of MN bending (change of slope)

For CMC/PVP compression curves in **Figure 7A**, force values are 10 to 100 times lower than for PEGDA. These MNs therefore require a smaller amount of force to reach the same displacement. The presence of lidocaine also influences the mechanical properties of the MNs as two different curve profiles can be identified. The standard deviations of the light blue curve implies that the compression of CMC/PVP MNs is reproducible until tip failure that occurs between 16 and 22% displacement (yellow zone) which causes high dispersion of the standard deviation. At this point, a plateau starts to appear (MAKVANDI ET AL., 2021) as the cross section in contact with the probe increases. Additional dispersion after fracture could be due to the difference in the cross section in contact with the compression probe.

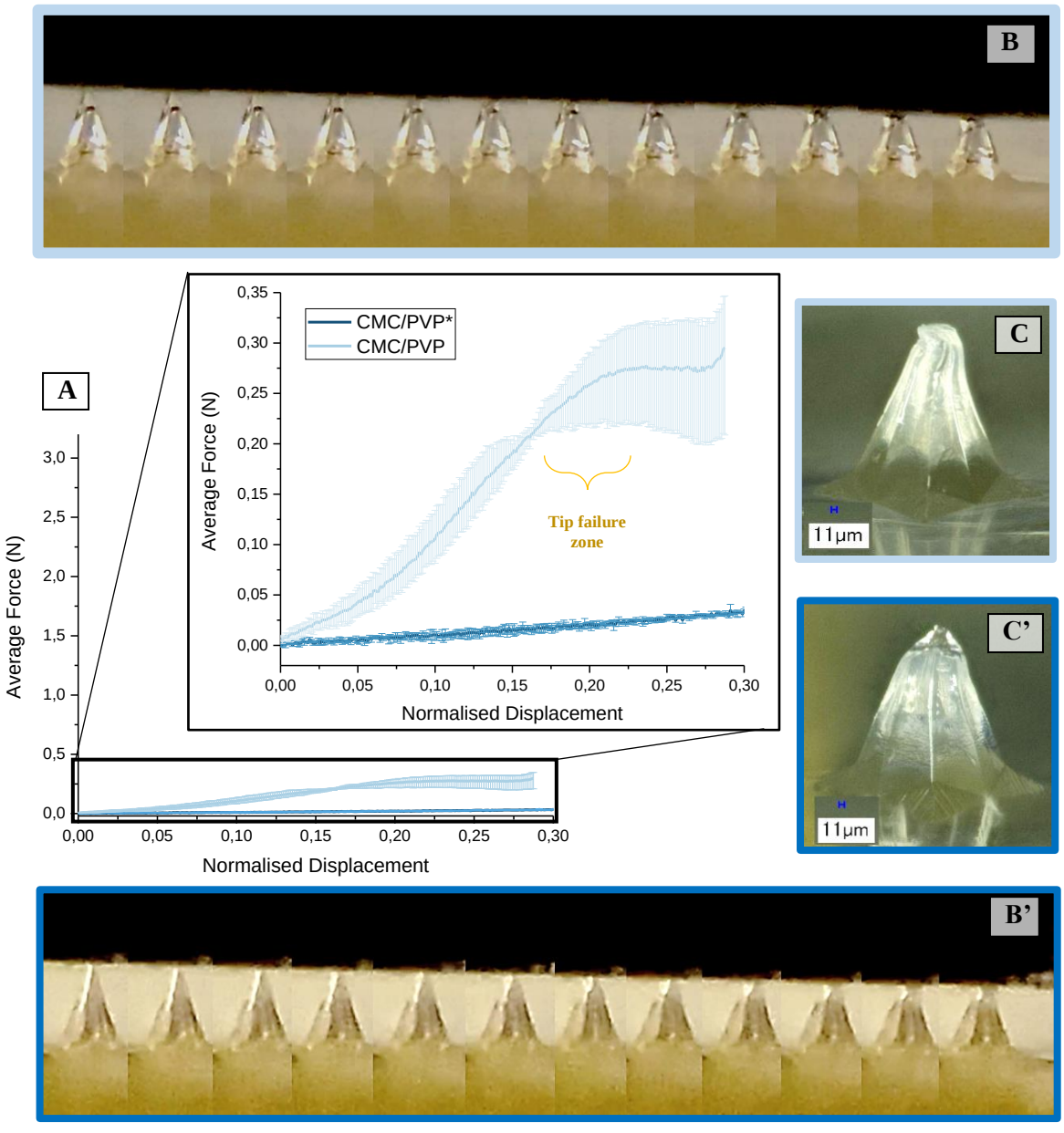

Figure 7. (A) Average compression curves with standard deviation, (B) Operando (x60, 90° angle) and (C) Post compression (x200, 85° angle) images for CMC/PVP-based microneedles until 30% compression (N=3)

As the force increases again above 27% compression, another fracture may be observed above the studied displacement range. Imaging data confirms the tip fracture without material removal.

On another hand, CMC/PVP* displays a linear relationship between force and displacement which suggests that the material is vertically compressed without causing bending or tip failure. By comparing MN heights before and after compression (**Figure 8**), we understand that the material is soft enough to be compressed without causing fracture. MN heights were reduced by 25% - in opposition to 15% for CMC/PVP (pictures not shown).

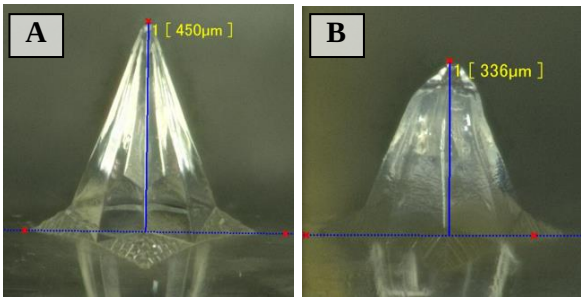

Figure 8. CMC/PVP* microneedle (A) Before and (B) After 30% compression. Magnification x200, 85°

Considering that these MNs are soluble, their mechanical behaviour also depends on relative humidity during storage and mechanical testing (WANG ET AL., 2018). Despite their low stiffness compared to the other materials studied in the same conditions, their insertion in the skin does not seem compromised, even though it does not guarantee a 100% success rate compared to stiffer materials such as silicon or PEGDA.

Both PEGDA and CMC/PVP based MNs demonstrate an important similarity, which is that they can withstand a quasi-static compression of 30% without breaking.

On the other hand, the compression profiles for HA and HA* show different signs of failure represented by arrows in **Figure 9A** with both force drop (HA*) and plateau (HA) as described by MAKVANDI ET AL., 2021. High dispersion is observed within the triplicates as tip fracture occurs at different displacements but force ranges and compression profiles remain similar for each test (minimum and maximum curve). This effect can also indicate the fragility of these MNs.

The average curve shows a tip fracture at similar displacements in both cases: around 14% and 17% compression for HA* and HA respectively (green arrows). While the force range is similar before fracture (0-0.4 N), differences in the curve profile then appear with a force increase for HA and a force drop to 0.2 N for HA*.

The post compression images show that both tips are highly damaged. Even though the application of a MN array in skin is made with an impact force and not under quasi-static conditions used here, this observation suggests that there is a risk of material fracture during insertion. This assumption is supported by the penetration efficiency presented in part 3.1.1, where HA* indeed offers poorer performances. Despite their fragility, tip failure is not a real danger for the patient though as these materials are soluble and yet perforate the *stratum corneum* as previously shown.

However, it could lead to unreliable kinetics of drug delivery.

Additionally, imaging data suggests that the material is only present on the MN walls, leaving the actual MN hollow. By the end of the test, HA* MNs indeed seem to crack open which could explain the force drop if the MN contains an inner cavity. A simple way to verify this hypothesis is to perform shear tests close to the tip of the MNs.

3.2.2. Shear tests

Shear test is initially performed to verify adequate adhesion of each material to the biocompatible sole. None of the MNs tested broke at the MN/sole interface, which confirms that the photocurable resin provides a satisfying adhesion to the materials used in this study.

In addition, these tests help identifying whether the MNs are full or hollow by imaging after

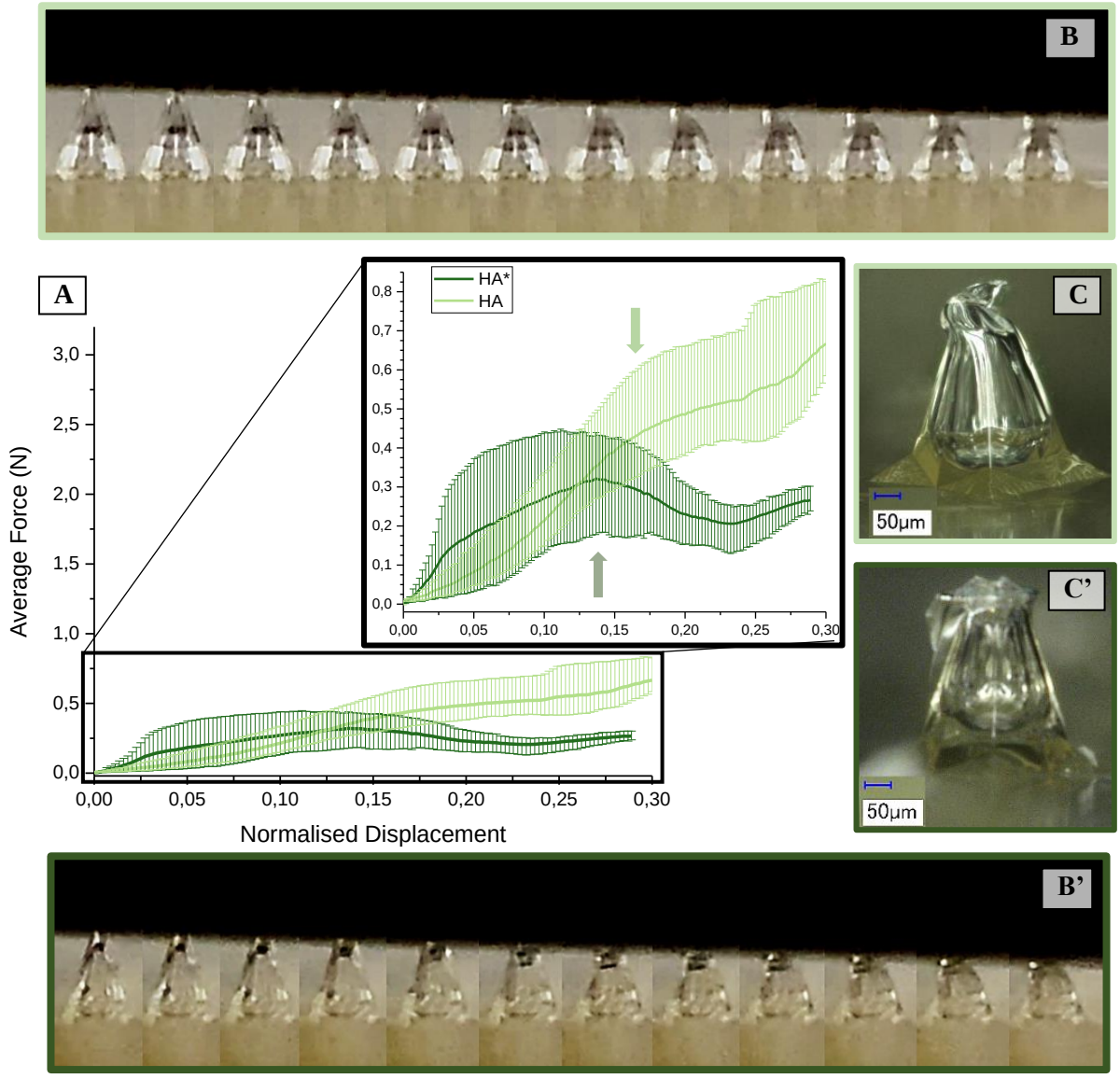

Figure 9. (A) Average compression curves with standard deviation (B) Operando (x60, 90° angle) and (C) Post compression (x200, 85° angle) images for HA-based microneedles until 30% compression (N=3)

shearing. In the case of HA-based MNs that both display the same behaviour, **Figure 10D** reveals their inner cavity, unlike PEGDA MNs (**Figure 10E)** that seem to break along one specific direction as previously observed on silicon MNs (O'MAHONY, 2014). Shear force values presented in **Figure 10A** are consistent with the hypothesis that HA-based MNs are hollow as they are 2 to 4 times easier to break with a lateral stress than PEGDA needles.

However, CMC/PVP-based MNs also display lower force values, but fracture does not occur. These results therefore represent a bending force as the MN simply complies with the lateral force. In the presence of the active principle, CMC/PVP-based MNs (CMC/PVP*) almost return to their initial position while those without the active principle (CMC/PVP) remain distorted as seen in **Figure 10C**.

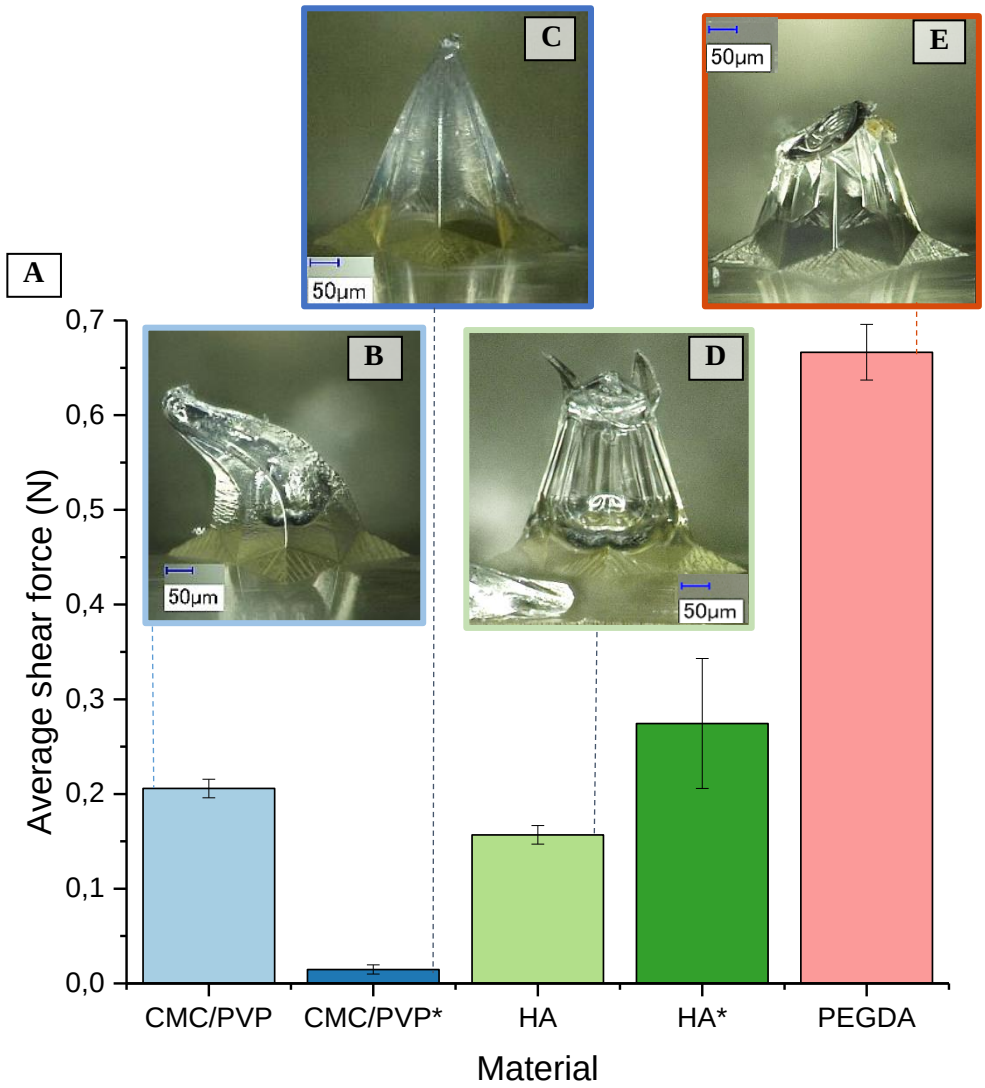

Figure 10. (A) Average shear force at 30% of the tip (N=3). Post shear images for (B) CMC/PVP (C) CMC/PVP* (D) HA-based (E) PEGDA microneedles (x200, 85° angle)

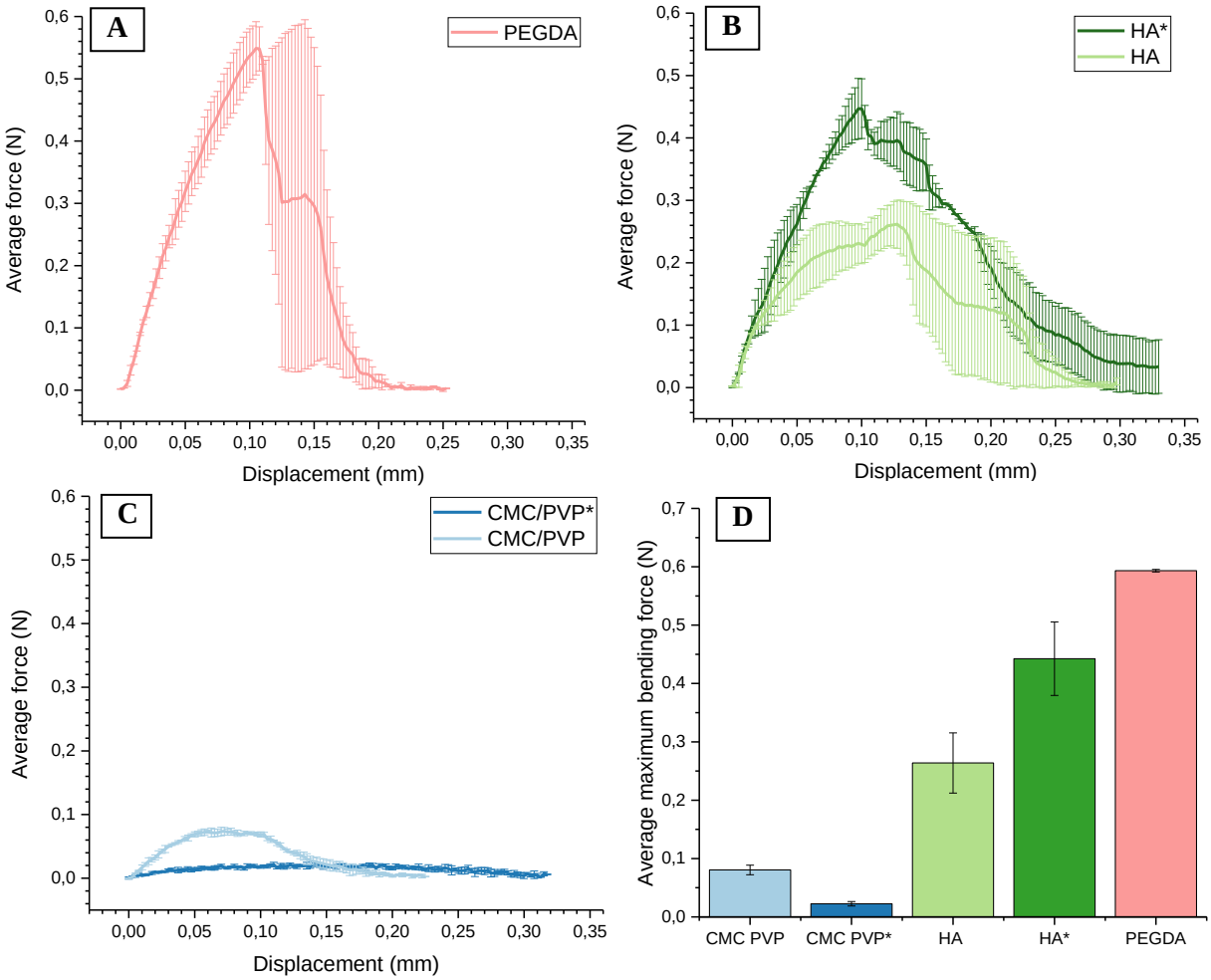

Figure 11. Bending curve profiles for (A) PEGDA (B) HA-based (C) CMC/PVP-based microneedles and (D) Associated average maximum force (N=2)

3.2.3. Bending tests

Considering the different behaviours observed during shear tests, an additional bending setup was designed. Unlike the aforementioned tests, these tests result in complete force versus displacement curves to better understand the mechanical resistance of each material to lateral stress. As hinted by previous imaging data (**Figure 11FigureB-D**), these curves help discriminating breaking and bending MNs.

MNs that break under lateral stress indeed display one (or more) sharp peaks as shown in **Figure 11A-B** for PEGDA and HA-based MNs. CMC/PVP-based MNs on the other hand present reproducible wide and low amplitude peaks (**Figure 11C**). CMC/PVP* in particular shows very little resistance to the applied force compared to the other polymer candidates, which is consistent with both compression and shear tests results previously presented.

Despite the slight differences in the force value, the maximum force obtained during bending tests (**Figure 11D**) show similar trends as the results obtained from the shear tests (**Figure 10A**), suggesting that the relative mechanical strength of the MNs in relation to each other holds true for both tests.

3.3. Influence of active principles in polymeric matrices

When used for drug delivery applications, soluble and swellable MNs contain one or more active principles inside the polymeric network. Depending on the chemical nature and the amount of drug loaded, the mechanical properties on the MNs can differ from those of the blank material.

Throughout this study, CMC/PVP and HA-based MNs have been considered with and without an active principle, respectively lidocaine and 5-ALA. These matrices are defined by previous studies performed in CEA for two different applications: local anaesthesia and dynamic phototherapy. In this part, we want to evaluate their influence on the MN properties. Despite similar mechanical profiles, some differences can be noticed.

In both cases, perforation success rates are reduced by 20% in the presence of the active principle. Compression loads suggest that CMC/PVP* is ten times softer than CMC/PVP alone in the same humidity conditions, while maintaining the MN tip integrity.

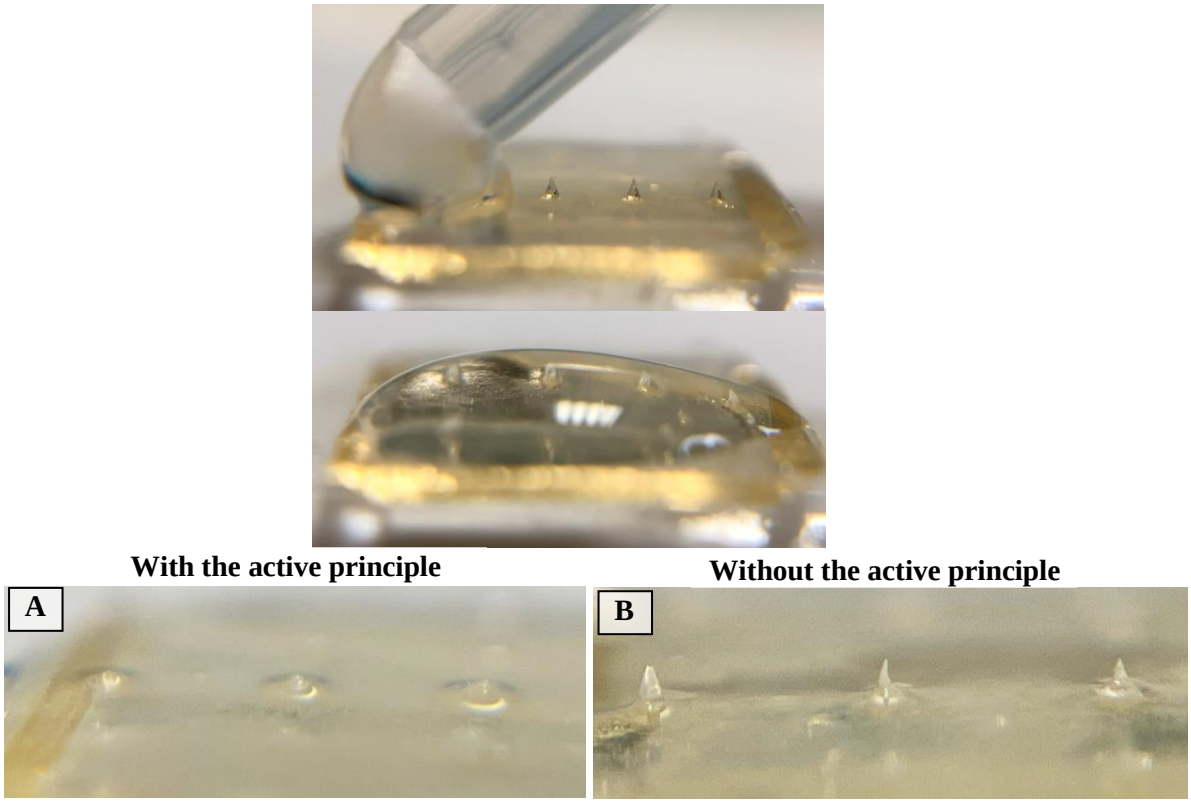

Figure 12. Degradation test procedure and result for A. CMC/PVP* and B. CMC/PVP

On the contrary, HA* appears more brittle and MN tips fail easier than for HA alone. However, the presence of 5-ALA in the HA matrix seems to increase the shear force (i.e. the resistance to lateral stress) but results are less reproducible as the standard deviation is the highest in this case.

Apart from mechanical differences, the active principle could also affect the degradation rate of the material. A quick observation of MN dissolution could be done with two drops of 0.1 M phosphate buffered saline solution for two minutes as depicted on **Figure 12**. The excess solution is gently removed with an absorbent paper without touching the needles. Results are only shown on CMC/PVP-based MNs as the dissolution rate of HA is lower (around an hour on *ex vivo* rat skin according to CHAMPEAU ET AL., 2020).

Figure 12A shows a complete dissolution of CMC/PVP* MNs after two minutes, while **Figure 12B** proves that CMC/PVP MNs are still in place although thinner. These tests highlight that the high percentage of lidocaine (10 wt%) in CMC/PVP* has a significant impact on the dissolution rate and actually helps the matrix to dissolve. If so, lidocaine could also help absorb ambient moisture and contribute to the matrix softening observed in mechanical tests compared to MNs without lidocaine (CMC/PVP).

4. Conclusion

Polymer MNs are considered as a low cost alternative to silicon MNs that are the pioneers of microneedle technology. Depending on the formulation used, they can also provide two additional MN categories, dissolving and swellable MNs. Both types are studied in this paper, where a catalogue of six biocompatible polymers are compared using a single octagonal conical structure developed at Tyndall National Institute, Cork, Ireland.

Perforations tests on *ex vivo* skin explant showed that most polymers give a satisfactory perforation efficiency using an impact force with a spring-based applicator. Only pure CMC MNs resulted in poor penetration efficiency as previously reported in the literature, and is therefore not a good candidate for MN fabrication. This polymer can however be either crosslinked (RAHMAN ET AL., 2021) or used as a copolymer as presented in this study with the addition of PVP.

Additional mechanical characterisations help identifying different failure mechanisms that can occur when a normal (compression) or a lateral (shear or bending) stress in applied to each MN:

- PEGDA MNs display an interesting ability to crush under compression up to relatively high forces without causing tip failure. At 30% compression, irreversible deformation occurs though as the resulting MN is bent. Other formulations should be studied to compare this behaviour with swellable MNs with higher porosity.

- HA-based MNs produce a significant dispersion in all the results due to their fragility: imaging after shear tests showed that these MNs are actually hollow and can easily fracture. Even though this material is soluble, such dispersion can cause irregular drug diffusion and therefore be an issue to control the kinetics of drug delivery.
- Finally, CMC/PVP-based MNs seem to be the most ductile material with a good resistance to both normal and lateral stress. During compression, tip failure occurs as it is crushed, but without separating from the MN. When subjected to a lateral force, these MNs have the ability to deform and either come back to their initial position (CMC/PVP*), or remain bent without breaking (CMC/PVP). These observations may differ depending on the moisture content of the MN related to the storage conditions prior to use.

Apart from MN material, the variation of other parameters could be considered such as MN design (shape, height, density) that is widely discussed in the literature, application parameters (quasi-static, dynamic or impact force) or even the fabrication process with multi-step micromoulding to avoid hollow MNs or other polymer forming processes (injection moulding, hot embossing,…).

5. Acknowledgments

The authors acknowledge the support of the Agence Nationale de la Recherche through the LabEx ARCANE program (ANR-11-LABX-0003-01) and the IDEX for funding M.R.J. mobility grant to conduct presented experiments at Tyndall National Institute, Cork, Ireland.

6. References

1. Boer, M., Duchnik, E., Maleszka, R., Marchlewicz, M., 2016. Structural and biophysical characteristics of human skin in maintaining proper epidermal barrier function. Adv. Dermatol. Allergol. Dermatol. Alergol. 33, 1–5. https://doi.org/10.5114/pdia.2015.48037
2. Champeau, M., Jary, D., Mortier, L., Mordon, S., Vignoud, S., 2020. A facile fabrication of dissolving microneedles containing 5-aminolevulinic acid. Int. J. Pharm. 586, 119554. https://doi.org/10.1016/j.ijpharm.2020.119554
3. Demir, B., Rosselle, L., Voronova, A., Pagneux, Q., Quenon, A., Gmyr, V., Jary, D., Hennuyer, N., Staels, B., Hubert, T., Abderrahmani, A., Plaisance, V., Pawlowski, V., Boukherroub, R., Vignoud, S., Szunerits, S., 2022. Innovative transdermal delivery of insulin using gelatin methacrylate-based microneedle patches in mice and mini-pigs. Nanoscale Horiz. 7, 174–184. https://doi.org/10.1039/D1NH00596K
4. Donnelly, R.F., Singh, T.R.R., Garland, M.J., Migalska, K., Majithiya, R., McCrudden, C.M., Kole, P.L., Mahmood, T.M.T., McCarthy, H.O., Woolfson, A.D., 2012. Hydrogel-Forming Microneedle Arrays for Enhanced Transdermal Drug Delivery. Adv. Funct. Mater. 22, 4879–4890. https://doi.org/10.1002/adfm.201200864
5. Faraji Rad, Z., Prewett, P.D., Davies, G.J., 2021. An overview of microneedle applications, materials, and fabrication

methods. Beilstein J. Nanotechnol. 12, 1034–1046. https://doi.org/10.3762/bjnano.12.77
6. Gerstel, M.S., Place, V.A., 1976. Drug delivery device. US3964482A.
7. Gittard, S., Chen, B., Xu, H., Ovsianikov, A., Chichkov, B., Monteiro-Riviere, N., Narayan, J., 2013. The Effects of Geometry on Skin Penetration and Failure of Polymer Microneedles. J. Adhes. Sci. Technol. 27, 227–243. https://doi.org/10.1080/01694243.2012.705101
8. Larrañeta, E., Lutton, R.E.M., Woolfson, A.D., Donnelly, R.F., 2016. Microneedle arrays as transdermal and intradermal drug delivery systems: Materials science, manufacture and commercial development. Mater. Sci. Eng. R Rep. 104, 1–32. https://doi.org/10.1016/j.mser.2016.03.001
9. Lee, J.W., Park, J.-H., Prausnitz, M.R., 2008. Dissolving Microneedles for Transdermal Drug Delivery. Biomaterials 29, 2113–2124. https://doi.org/10.1016/j.biomaterials.2007.12.048
10. Makvandi, P., Kirkby, M., Hutton, A.R.J., Shabani, M., Yiu, C.K.Y., Baghbantaraghdari, Z., Jamaledin, R., Carlotti, M., Mazzolai, B., Mattoli, V., Donnelly, R.F., 2021. Engineering Microneedle Patches for Improved Penetration: Analysis, Skin Models and Factors Affecting Needle Insertion. Nano-Micro Lett. 13, 93. https://doi.org/10.1007/s40820-021-00611-9
11. O'Mahony, C., 2014. Structural characterization and in-vivo reliability evaluation of silicon microneedles. Biomed. Microdevices 16, 333–343. https://doi.org/10.1007/s10544-014-9836-6
12. O'Mahony, C., Grygoryev, K., Ciarlone, A., Giannoni, G., Kenthao, A., Galvin, P., 2016. Design, fabrication and skin-electrode contact analysis of polymer microneedle-based ECG electrodes. J. Micromechanics Microengineering 26, 084005. https://doi.org/10.1088/0960-1317/26/8/084005
13. O'Mahony, C., Sebastian, R., Tjulkins, F., Whelan, D., Bocchino, A., Hu, Y., O'Brien, J., Scully, J., Hegarty, M., Blake, A., Slimi, I., Clover, A.J.P., Lyness, A., Kelleher, A.-M., 2023. Hollow silicon microneedles, fabricated using combined wet and dry etching techniques, for transdermal delivery and diagnostics. Int. J. Pharm. 637, 122888. https://doi.org/10.1016/j.ijpharm.2023.122888
14. Rahman, Md.S., Hasan, Md.S., Nitai, A.S., Nam, S., Karmakar, A.K., Ahsan, Md.S., Shiddiky, M.J.A., Ahmed, M.B., 2021. Recent Developments of Carboxymethyl Cellulose. Polymers 13, 1345. https://doi.org/10.3390/polym13081345
15. Wang, Q.L., Ren, J.W., Chen, B.Z., Jin, X., Zhang, C.Y., Guo, X.D., 2018. Effect of humidity on mechanical properties of dissolving microneedles for transdermal drug delivery. J. Ind. Eng. Chem. 59, 251–258. https://doi.org/10.1016/j.jiec.2017.10.030

2.2. Hollow microneedles and large scale processing

As presented in the previous part, vacuum micromolding is commonly used by various research teams for MN processing (GERA AND BURRA, 2022). This process is suitable for lab scale production, but cost issues may arise if larger-scale options are not considered prior to market launch.

In this part, we focus on hollow MN processing as their fabrication represent an additional challenge as mentioned in Chapter 1 (**1.3.1.3**). Unlike the HA case presented in section **2.1** where the material properties caused the formation of an internal cavity, this section is dedicated to the manufacturing method regardless of the MN material used.

2.2.1. Injection molding

Definition 🕮

Injection molding *is a processing technique widely use to shape complex objects from thermoplastics, i.e. polymers that can soften with heat and harden once cooled. It consists in heating polymer pellets until viscous, then forced into a mold with pressure* (EBNESAJJAD, 2003). *The material is then cooled until solid to obtain the finished part (Chapter 1,* ***Figure 23****).*

Micro-injection molding is first considered as a mean to shape polymers into the desired object with a micron-scale resolution. The device available in the department (MicroPower 15T, Wittmann Battenfeld, Austria) is indeed suitable to manufacture micro-parts for medical applications. A CAD file of the mold is therefore designed according to the plans of the machine and the desired hollow MN array to obtain (**Figure 32**). Two MN shapes (beveled-tip cone and pencil tip) are designed on the mold with a 100 µm base diameter pillar creating the conduct inside each MN to make them hollow. Such mold allows the use of a flat counter-mold instead of manufacturing both mold and counter mold as previously depicted.

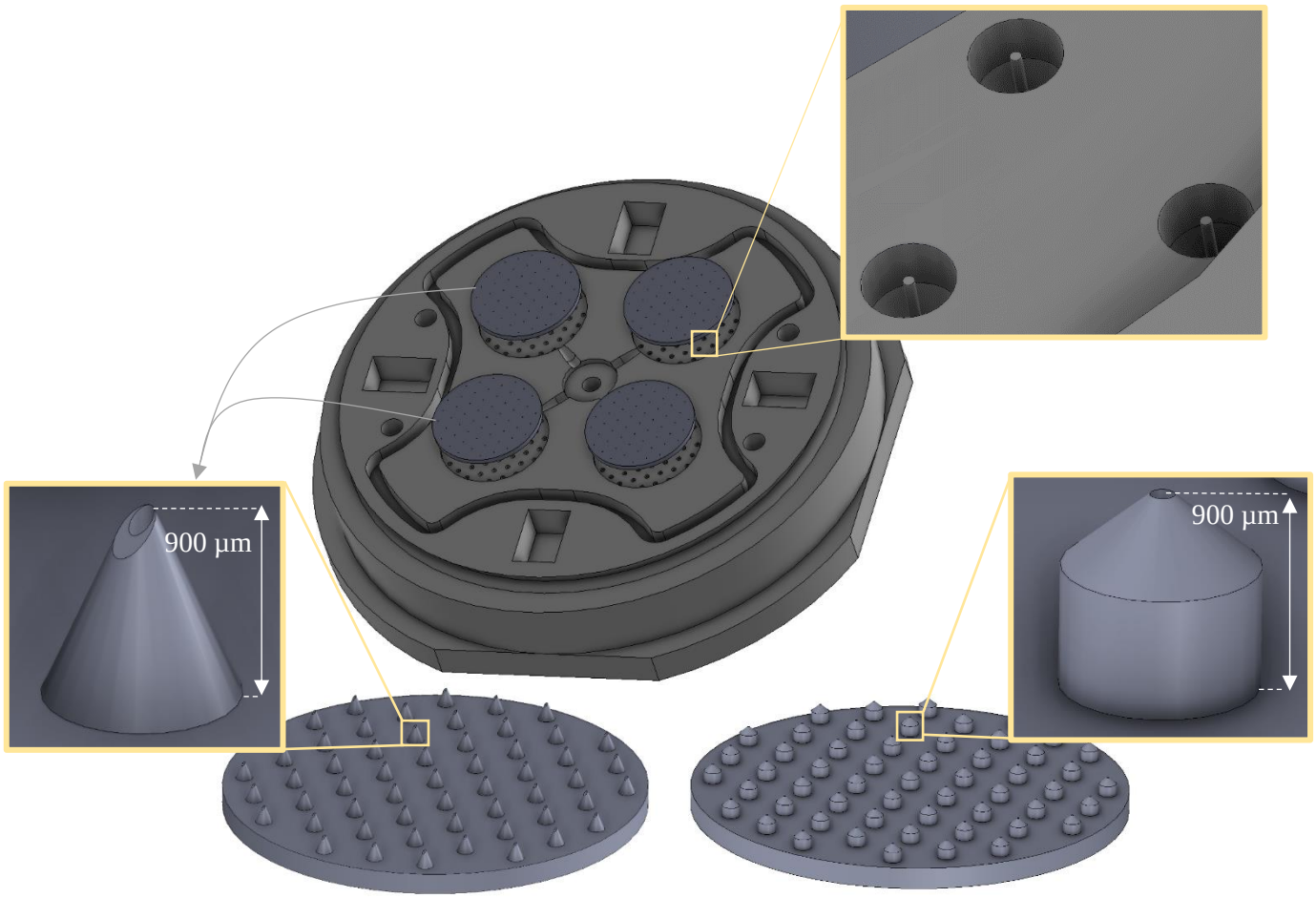

Figure 32. CAD file of the injection mold and associated hollow MN array to obtain

Learning from mistakes 🔍

Unfortunately, such negative mold is not easy to manufacture and we did not succeed in obtaining an aluminium mold by micromilling. Another option explored to fabricate the mold is to use 3D-printing with heat and pressure-resisting resins. Once more, a negative mold could not be obtained with satisfactory resolution and the homemade injection-molding project came to an end.

Additionally, numerical simulations would have been necessary to determine the injection parameters prior to use, considering the viscosity of the material to inject and its flow in the channels. This step would save a significant amount of time compared to an empirical optimization of these parameters.

Thankfully, commercially available injection-molded hollow MNs were provided by Yamada Seiko Co., Ltd., Japan. Both poly-L-lactic acid (PLLA, **Figure 33A**) and polyglycolic acid (PGA, **Figure 33B**) were ordered to compare the degradation rate of both materials. Weathering tests in saline conditions maintained at 35°C with a cryothermostat (Julabo™, Fisher Scientific, MA, USA) indeed showed a relatively fast degradation of PGA MNs (1-2 weeks) compared to PLLA MNs (4-6 months). A faster degradation is expected in biological fluids though, as the ester groups of PLLA could be degraded by enzymes (mentioned in Chapter 1, 1.3.2.2).

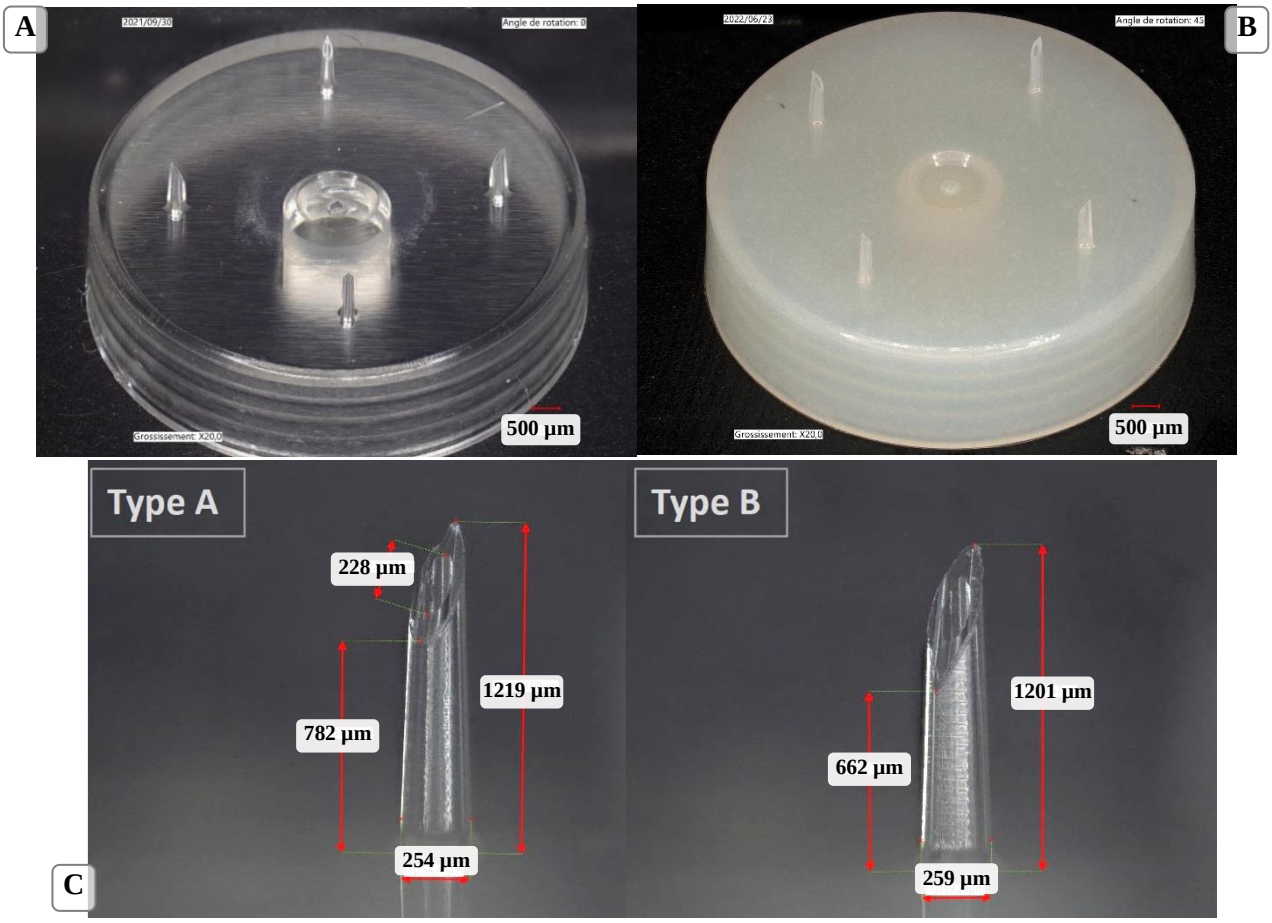

Figure 33. (A) PLLA and (B) PGA injection molded MNs provided by Yamada Seiko Co., Ltd., Japan. (C) Associated MN types on the array (two of each)

Two types of geometry were used as depicted on **Figure 33C**, with a standard beveled cylinder (Type A) and a more leaf-shaped structure (Type B). MNs of the same geometry are placed face to face. Only four MNs are available on the array with a 4.5 mm interspace, which minimizes the risk of "bed of nails" effect once applied. PLLA arrays will therefore be used in Chapter 5 treating usecases to compare MN-assisted delivery to passive and electrically assisted delivery.

2.2.2. 3D-printing

Stereolithography (SLA) was initially used in this project to print the injection mold as previously described, without success. We can however question whether this technique is suitable to directly print MNs, as it is considered as a semi-industrial process.

Different 3D-printing devices (Miicraft, Formlabs, Prodways) and photocurable resins were experienced to print the arrays presented on the **Figure 32**. The best results obtained are once more not satisfactory considering these specific designs, as the resolution is not sufficient to print either the inner duct or sharp tips (**Figure 34**).

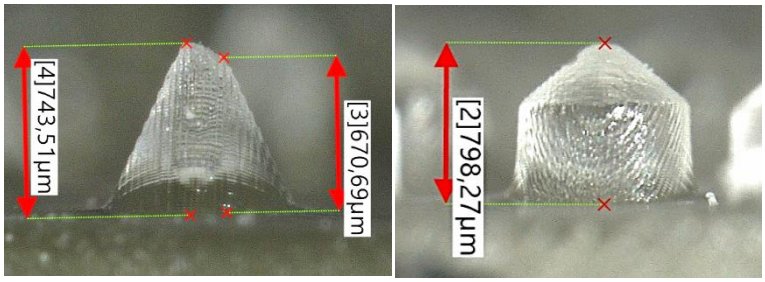

Figure 34. 3D-printed solid microneedles

Other MN designs were experimented with greater heights and duct diameters. **Figure 35** shows successful 3D-printed cylinder-shaped 1200 µm tall MNs with a 300 µm ducts. Painless perforation should however be verified as these dimensions belong to the highest range of MN size.

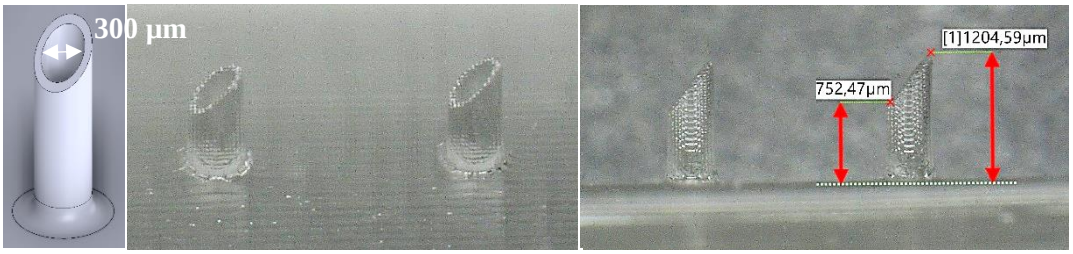

Figure 35. 3D-printed hollow microneedles and associated CAD file

The choice of the resin can strongly impact the resolution of the printed parts though. In this case, the resin giving the best results (Nano Clear, FunToDo, Netherlands) is not sold as a medical grade material. Unless cytotoxicity experiments are carried out on sterilized arrays to prove its biocompatibility, this material is not suitable for the desired application.

Even though 3D-printing is widely used in dentistry to print models, dentures or surgical guides (YE, 2021), ongoing research aim to develop biocompatible photocurable formulations to create high resolution bioresorbable implants by 3D-printing (SOULLARD ET AL., 2023). Such materials could also

be used to print hollow MN arrays. Cellulose-based materials developed by a fellow PhD student, Lénaïc Soullard, lead to promising 3D-printed hydrogel and associated cryogel MNs in our lab (**Figure 36**).

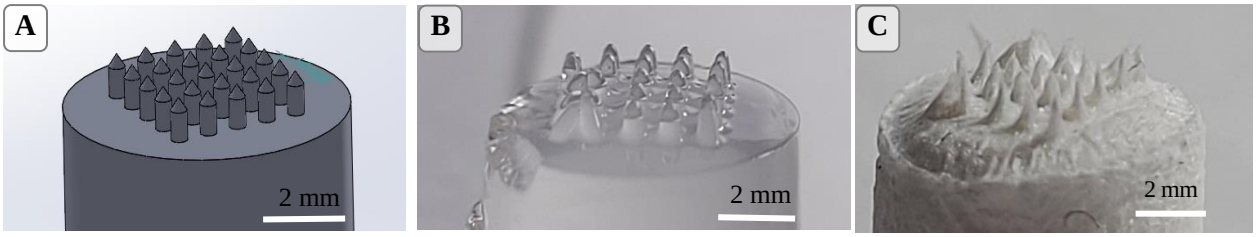

Figure 36. Pencil tip MN (A) CAD file (B) 3D-printed hydrogel and (C) associated cryogel by L. Soullard

To remember

3D-printing is initially used in this project to fabricate the MN injection mold, but the resolution of negative parts is not good enough for this purpose. SLA can also be used to directly print MN arrays in an automatized manner. Hollow MN arrays could be successfully obtained above a certain MN height and duct size. New materials are however necessary to create biocompatible and bioresorbable materials for transdermal application.

2.2.3. Thermoforming

Definition

Similarly as injection molding, ***thermoforming*** *is used to shape thermoplastic materials. The polymer takes the form of an extruded sheet of homogeneous thickness. The sheet is heated up above its glass transition temperature before being plated on top of a mold insert under the effect of either vacuum or pressurized gas* (HECKELE AND SCHOMBURG, 2003) ***(Chapitre 1, Figure 24)****.*

Thermoforming can be another industrial option to shape polymers without needing a negative mold. As presented on the drawing in Chapter 1 (**Figure 24**), a single positive mold can be used to manufacture hollow MNs. In this case though, as polymer sheets are used, the MN is made of a thin wall and larger cavity instead of a simple duct (**Figure 37**).

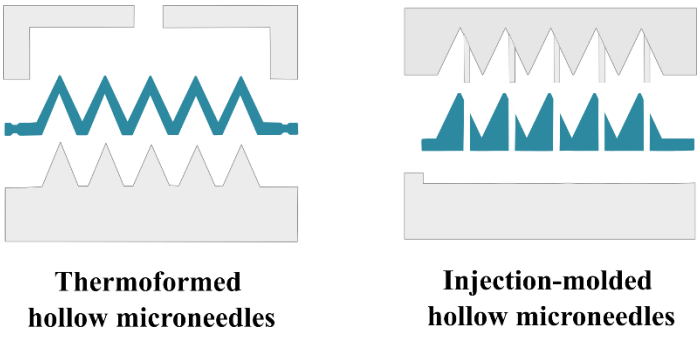

Figure 37. Mold insert and associated hollow MNs obtained with thermoforming versus injection molding

2.2.3.1. Molds

Two different molds were fabricated one after the other: while the first mold required more machining time and material, the second mold proposes more customizable options.

Fixed mold

A first aluminium mold (**Figure 38**) is manufactured in the lab by micromilling, based on the machine plans. 16 patterns are designed with 3 different MN shapes (cone, pencil-tip, beveled-tip cylinder), 3 interspaces (1, 1.5 and 1.8 mm) and 2 tip angles. Considering the thin sheets used, MN heights are reduced to 700 µm compared to previous designs. MN parameters are summarized in **Appendix 3**.

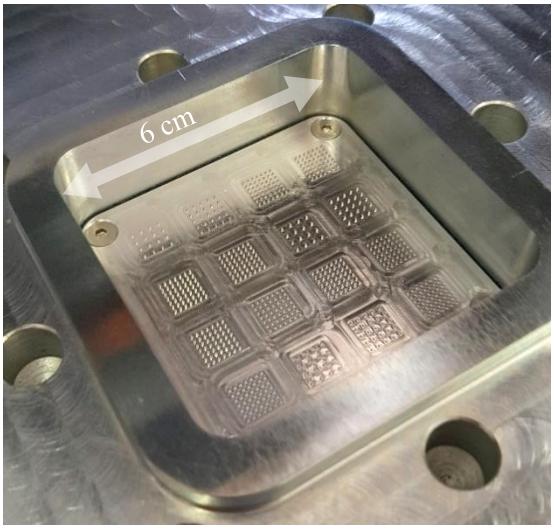

Figure 38. Picture of the first MN mold inside the mothertool

However, this mold implies the use of a 2 cm thick aluminium block each time a new mold is necessary which can cause aluminium resourcing issues. Additionally, unsuccessful MN patterns cannot be removed from the mold as all the patterns are fixed on the block.

Customizable mold

A second mold is therefore manufactured after the first results to adjust some MN parameters. At the same time, a different system is engineered to add more flexibility for parametric study and reduce aluminium consumption (**Figure 39**):

- Two fixed parts are designed to remain unchanged throughout thermoforming experiments: a thick aluminium block at the bottom of the mold to fit in the mothertool (1), and a thinner aluminium plate at the top with 16 numbered slots to place the inserts (2)
- 9 mm diameter MN inserts (3) can be independently micromilled and placed at the desired position between the block and the plate. When all the slots are not occupied, flat inserts can be used to fill the gap between the two fixed parts (not represented on the picture).

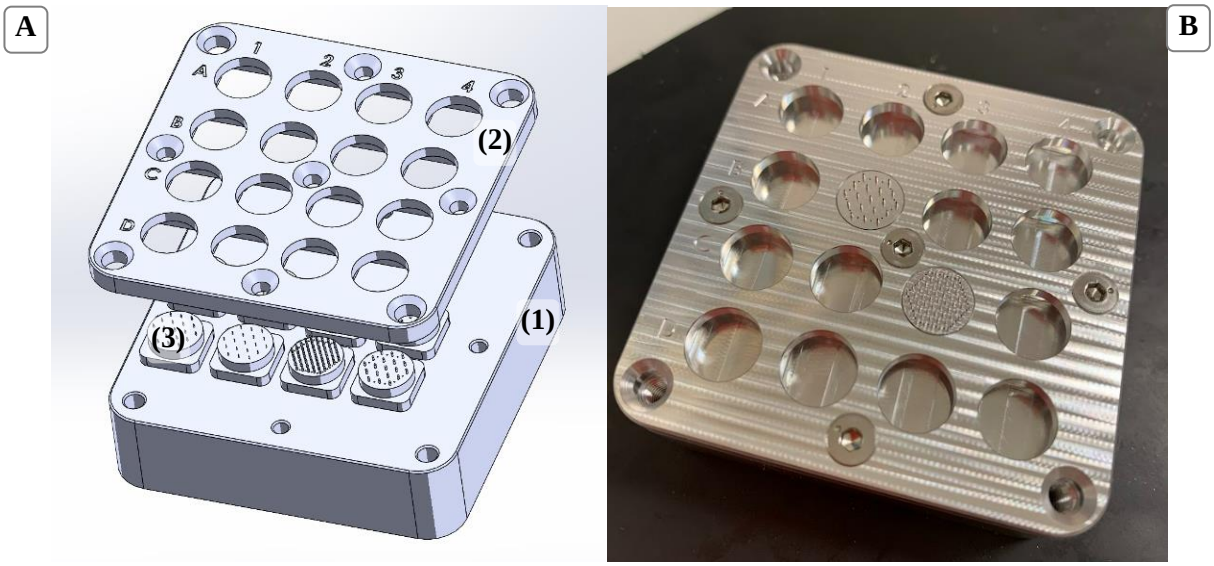

Figure 39. Customizable mold (A) CAD file and (B) picture with two MN inserts

New MN parameters are therefore experienced and also summarized in **Appendix 3**.

2.2.3.2. Materials and process parameters

50 µm thick PLLA sheets were provided by Goodfellow, UK, and laser cut to obtain 10x10 mm squares adapted to the machine's mothertool. This polymer format is not easy to supply and thin and homogeneous thicknesses are required to produce high resolution micro-objects. To verify sheets biocompatibility, cytotoxicity assays were performed in triplicates by a fellow PhD student, Bastien Darmau, leading to an average cell viability of 99% ±4%.

In opposition to amorphous PLA, PLLA is a semi-crystalline material. This feature may be an advantage in terms of mechanical properties for skin perforation, but it also reduces the molding window for this process (**Figure 40**).

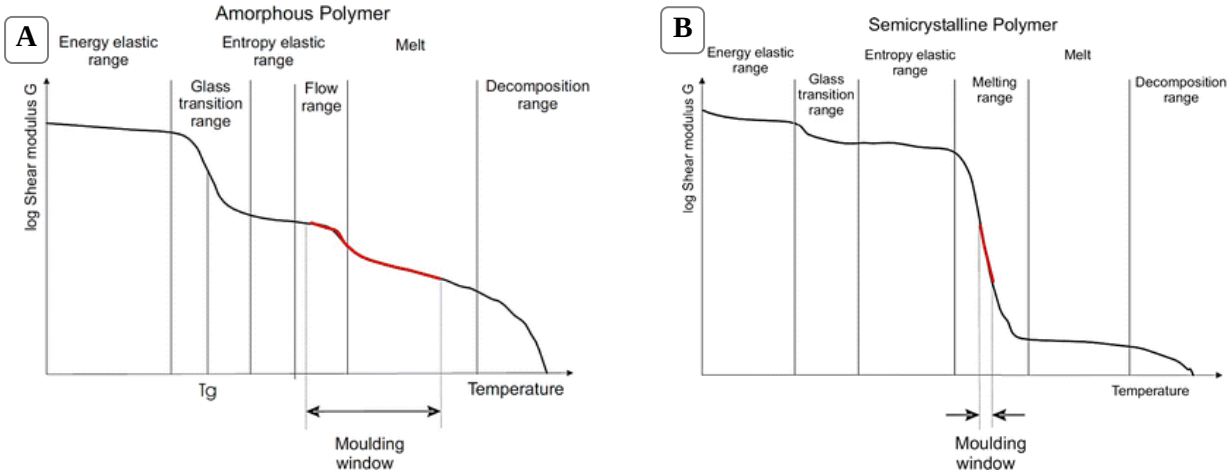

Figure 40. Mechanical behavior versus temperature of (A) Amorphous and (B) Semi-crystalline polymers, by Worgull et al., 2011

The study of microtip fabrication using polymers with low glass transition temperature lead to the patent FR2212767 filed with C. Ducros and S. Charlot.

Different process parameters are tuned to reach the desired MN shape and mechanical properties:

- Sheet heating parameters and associated temperature
- Compressed air pressure
- Compressed air temperature
- Blowing time (pressure gradient) and time at which the maximum pressure is maintained

In this part, only the first two parameters are compared along with MN design parameters.

MN shape and interspace

The first mold helps identifying the array parameters that are not suitable for this process. **Figure 41A** shows that conical MNs are not properly formed. Later verifications on a binocular microscope showed that the pattern on the master mold is actually damaged (data not shown). Similar phenomenon is observed on the outer beveled-tip cylinders (**Figure 41B**). Such design is therefore not adapted to hold high pressure as those applied in thermoforming.

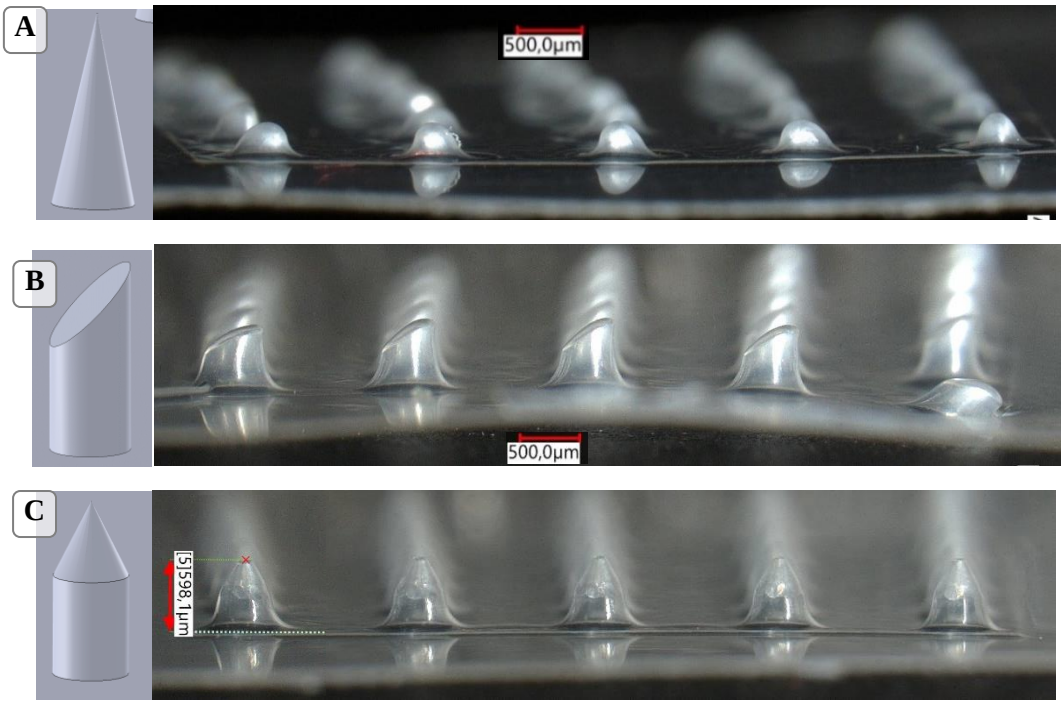

Figure 41. Thermoformed (A) conical, (B) beveled-tip cylinder and (C) pencil-tip PLLA microneedles

Best results are obtained with pencil-tip MNs (**Figure 41C**), even though the actual MN formed is smaller than on the mastermold (~600 µm instead of 700 µm). Taller MNs inserts are therefore prepared for the second mold.

Finally, the interspace also has an impact on the resulting MN shape. **Figure 42** shows that the largest interspace (1.8 mm) provides a flat sole between MNs in opposition to the densest scenario (1 mm) with the same applied air pressure. This effect would compromise skin insertion as it would both reduce the actual MN height available and its stability once inserted if the sole is not in contact with the skin.

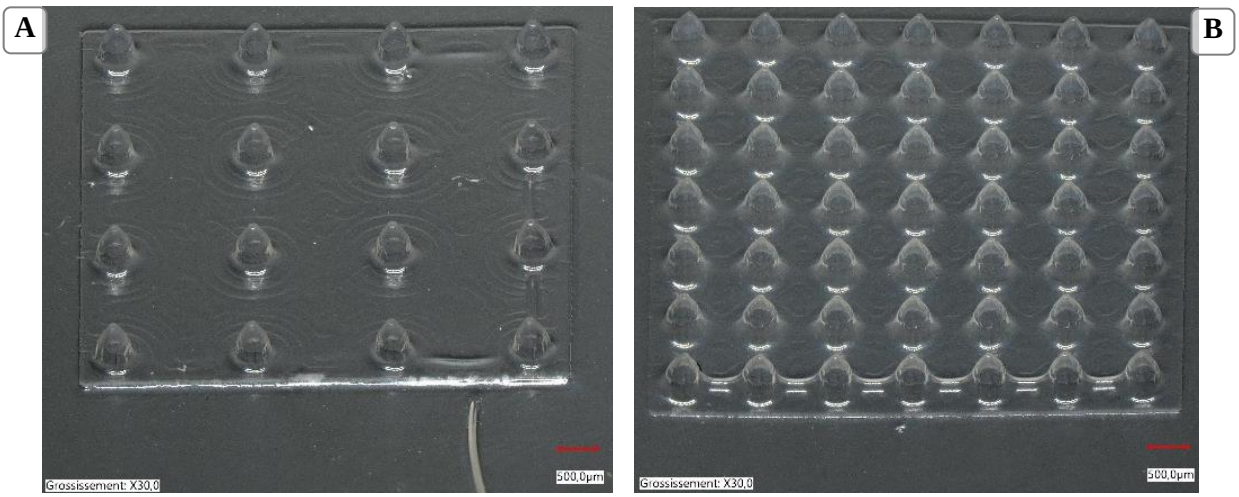

Figure 42. Thermoformed pencil-tip PLLA microneedles with (A) 1.8 mm and (B) 1 mm interspace

To remember ❗

Cones and beveled-tip cylinders studied in the first mold do not appear as suitable options for thermoforming as the aluminium master mold cannot hold the air pressure used in this process. Pencil-tip MNs give satisfactory results though, especially when the MN density is low enough to keep a flat array sole. This design was already described as more mechanically resistant in the literature (CHAMPEAU ET AL., 2020).

Sheet temperature

As mentioned earlier, mechanical properties of PLLA can be influenced by sheet temperature. Depending on the sheet temperature during the process, MNs can therefore remain transparent (**Figure 43A**) or display a translucent crystalline chain arrangement (**Figure 43B**). This information also implies, for other types of applications, that the optical properties of the material also differ.

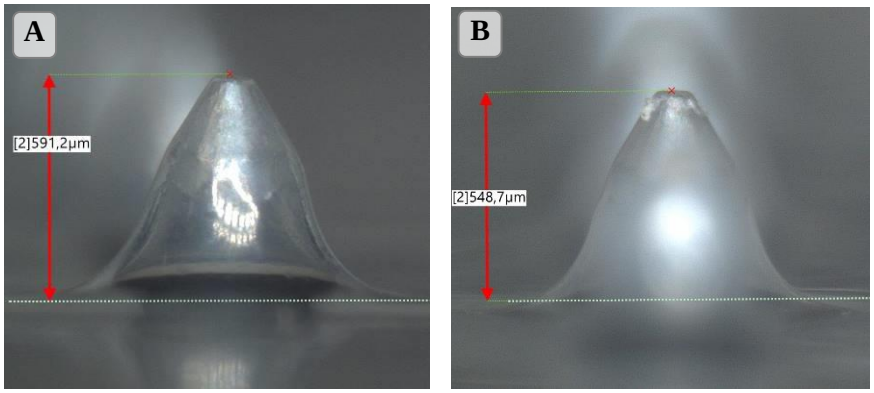

Figure 43. (A) Amorphous and (B) Semi-crystalline form of thermoformed PLLA microneedle

As we expect these MNs to have different mechanical properties, compression tests were carried out on the entire MN array (TA.XT Plus, Stable Microsystems, UK) by applying a 10 mm diameter metallic probe at 0.1 $mm \cdot sec^{-1}$ until reaching a maximum force of 49 N. Load versus distance curves are qualitatively compared to avoid any approximations on the surface actually compressed.

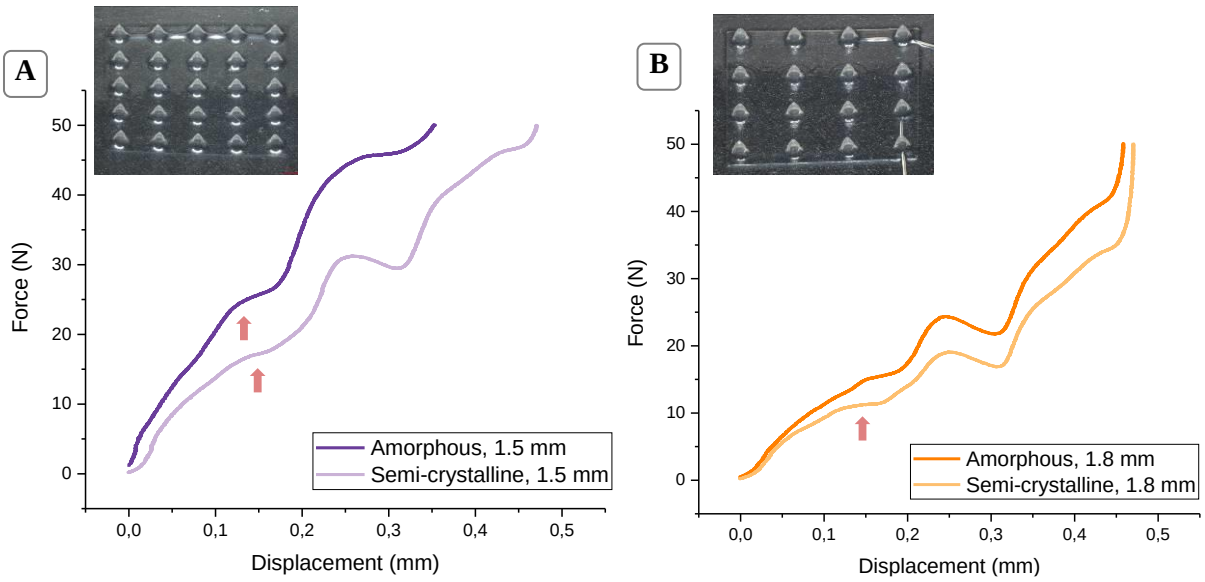

Figure 44. Load versus displacement curves for amorphous and semi-crystalline MNs on arrays with (A) 1.5 mm pitch and (B) 1.8 mm pitch. Red arrows indicate MN fracture

Figure 44 first shows that the amorphous curves are always above the semi-crystalline ones, which means that a higher force is necessary to compress the array to a given displacement. This result suggests that the material is more resistant to normal load when amorphous. Comparison of **Figure 44A** and **B** shows however that the effect of the polymer chain structure is more significant on a denser array. To make sure this difference is not due to the dispersion of the experiment, these tests are repeated on the same patterns of another amorphous batch (**Figure 45**), showing reproducible mechanical properties before MN fracture.

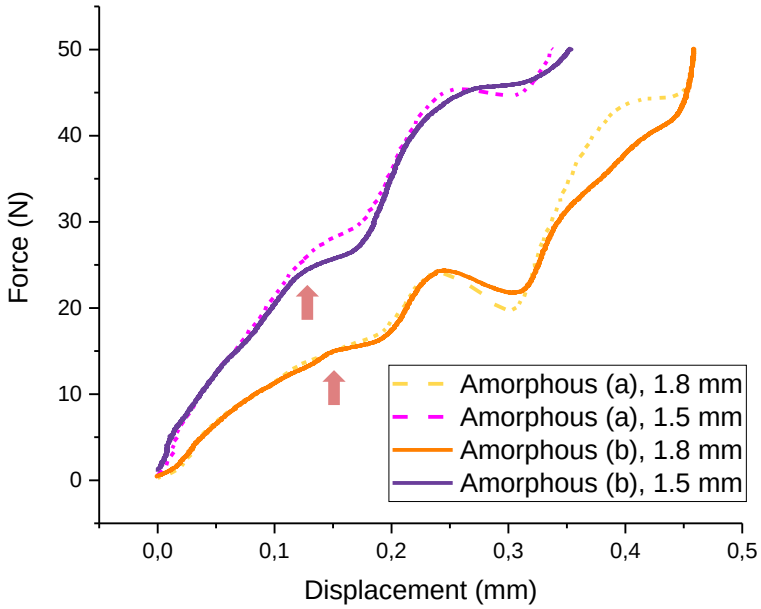

Figure 45. Load versus displacement curves for amorphous arrays of two different batches of amorphous PLLA MNs

Regardless of the polymer structure, denser arrays require more force to cause failure, which is coherent as a higher number of MNs are compressed.

To remember

Heating parameters chosen in the process can affect the crystallinity of the material, which is already visible on the aspect of the MN: transparent MNs are amorphous while translucent MNs have crystalline regions. Compression tests show that, especially on the densest arrays, semi-crystalline MNs are more fragile than in the amorphous form, as it requires less force to reach MN fracture.

Air pressure

In order to compare different pressure setpoints by imaging on a 3D microscope (VHX-7000, Keyence, Japan), 1.2 mm tall MNs were designed in the second mold.

Learning from mistakes

Taller MNs could not be thermoformed using a single 50 µm thick sheet since the deformation required is too important. As thicker PLLA was not commercially available, successful results are obtained by using two 50 µm sheets on top of the other.

Figure 46 shows that the air pressure applied affects how the sheet is clamped onto the mold and therefore conforms to the desired pattern. This effect is more visible at the bottom of the MN, where the diameter at the base becomes smaller as the pressure increases. Even though mechanical properties of smaller MNs previously shown are not affected by this parameter, MN tips also look sharper with pressure. This feature may be important to consider for MN insertion in the skin.

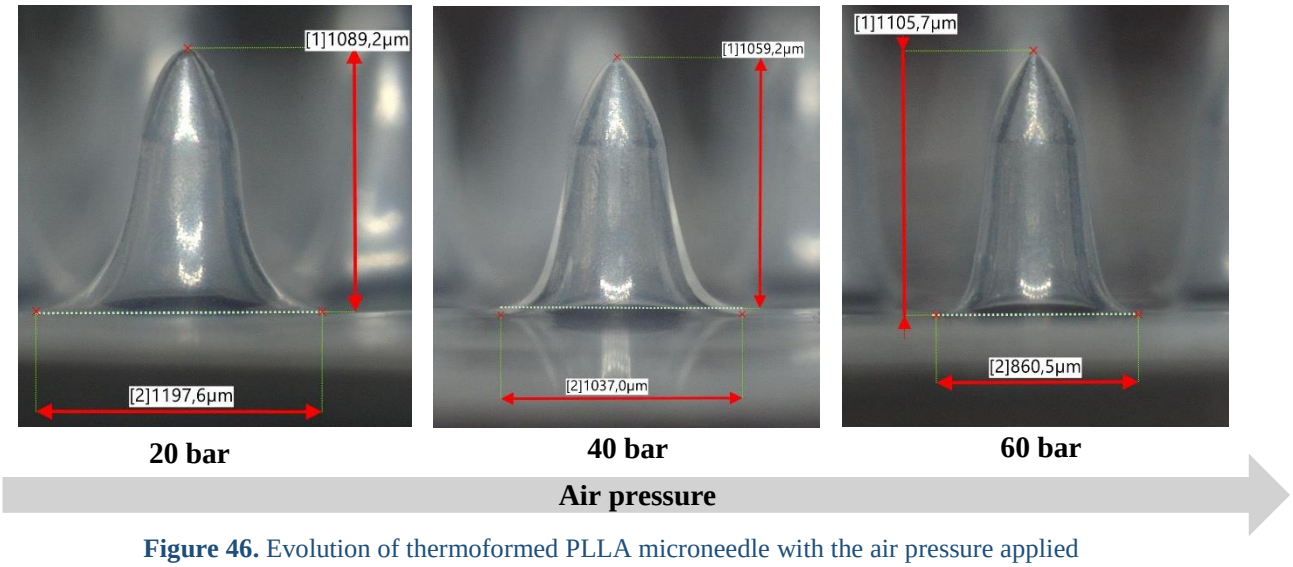

Figure 46. Evolution of thermoformed PLLA microneedle with the air pressure applied

Hollow PLLA MNs were successfully obtained by thermoforming. Different parameters, either related to the design or the process, were adjusted to optimize the resulting arrays. However, even though they are hollow, drug delivery is not possible at this stage without openings...

2.2.3.3. Laser openings

As presented in Chapter 1 (**Figure 17**), a side opening is suggested by LHERNOULD ET AL., 2015 to avoid skin clog during insertion. A precise laser cutting machine (S4, 20 ± 2 µm laser beam, 532 nm, 25-300 kHz, 12 W, LPKF Laser & Electronics, Germany) is used to create a similar side opening on both small (~600 µm) and tall (~900 µm) thermoformed MNs.

Such device requires a precise knowledge of the MN geometry as the laser beam is focused at a specific (x, y, z) position with 10 µm accuracy. **Figure 47** shows the target zone defined to create a side opening.

Successful openings are obtained for both small (A) and tall (B) thermoformed MNs. Additionally, multiple side openings could be targeted (C) and expanded to the whole array in an automatized manner.

To remember ❗

An additional step is necessary after thermoforming to create a side opening to use these hollow MNs for drug delivery. A precise laser-cutting machine is used in this regard, successfully creating a 50 µm large hole at the side of each MN without burning the material, which corresponds to the order of magnitude targeted for this application. This step needs to be adjusted to the MN geometry, but also the material used as each material may react differently to the laser beam.

Besides, laser parameters such as power and pulse frequency can be adjusted to increase the ablation depth. Such feature could be used to create a duct inside a solid MN, therefore creating another type of hollow MN.

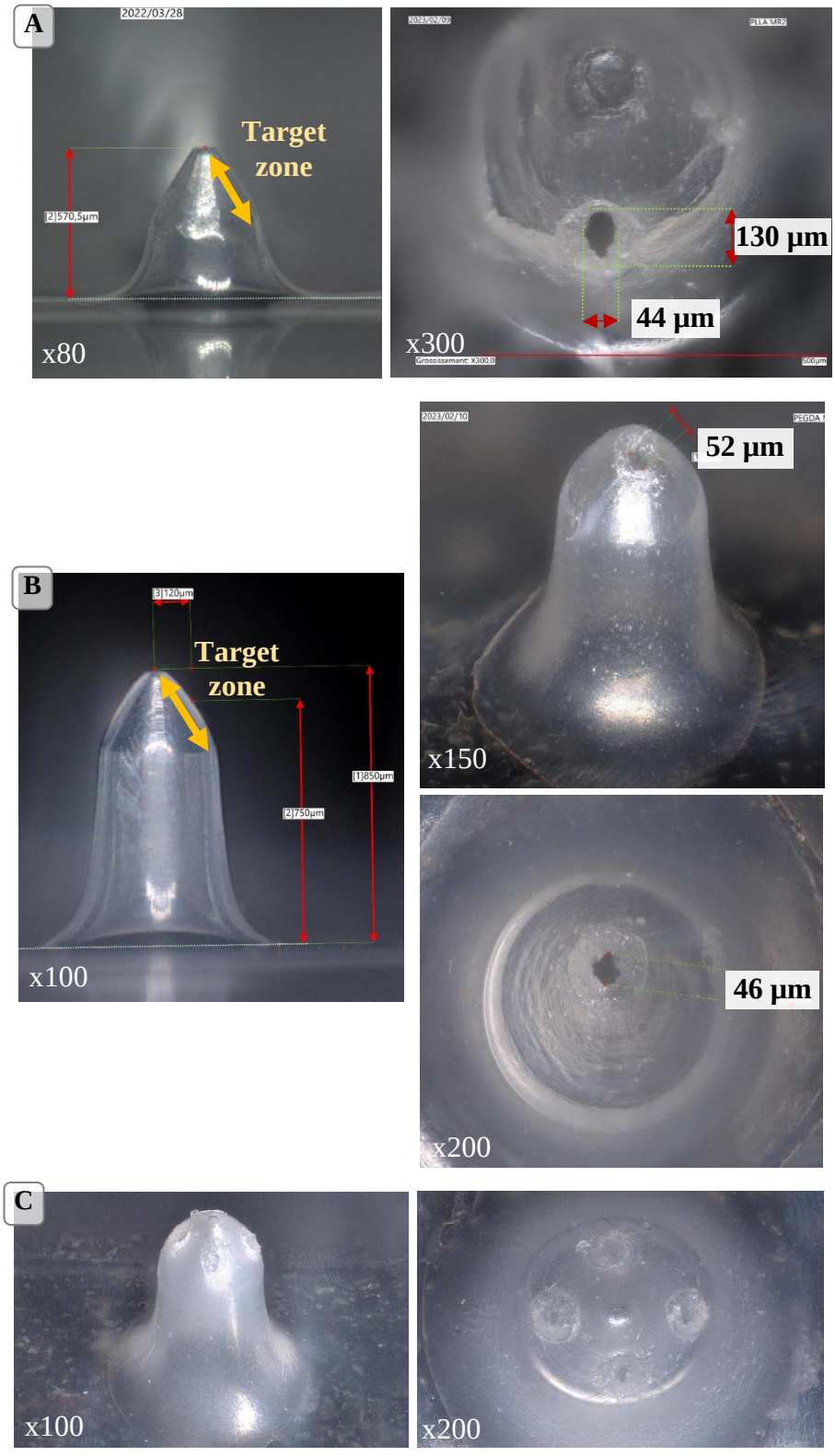

Figure 47. Single laser side opening obtained on (A) small and (B) tall thermoformed MNs. (C) Multiple side openings and top view

To conclude on MN fabrication, three different industrial processes were studied in this section. Even though each of them can provide a satisfying object resolution, they present different advantages and limitations (**Table 2)**.

Table 2. Comparative table of different hollow MN fabrication techniques investigated

MN fabrication technique	Number of molds	Polymer form	Suitable for biobased, biocompatible and bioresorbable materials?
Injection-molding	2 (mold and counter mold)	Pellets	Yes
3D-printing (SLA or DLP)	0	Photocurable liquid resin	No
Thermoforming	1 (positive mold)	Sheets	Yes

- Injection molding is first investigated for its high resolution and **easy material supply** in the form of pellets. However, we quickly realized that **mold production** will be the biggest limitation as a negative mold needed to be manufactured.
- 3D-printing technologies such as SLA and DLP were then studied to first print the negative molds (in vain), before **directly printing customizable hollow MNs**. However, the **materials available on the market do not meet our standards** yet as we aim to use biobased, biocompatible and bioresorbable materials.
- Finally, thermoforming appeared as the **most suitable candidate** for this project. However, we need to keep in mind that **polymer supply** can be challenging for this process, as thin sheets remain rare and expensive.

2.3. Perforation tests in artificial skin phantoms

In the first part of this chapter, perforation tests were performed on *ex vivo* skin explant using methylene blue staining. However, human skin can be difficult to supply and displays heterogeneous properties depending on the individuals and the location on the body. Artificial skin models can therefore be a suitable alternative to evaluate the ability of hollow MNs at the early stages of research.

2.4.1. Mechanical testing of gelatin/glycerol skin phantoms

Different polymer formulations are suggested in the literature in order to mimic the mechanical behavior of human skin. In reality, as its mechanical properties vary between and within individuals, a wide range of Young Modulus are mentioned from one study to another (from 4 kPa to 160 MPa, KAO, 2016).

In addition, methods can significantly affect the resulting modulus obtained as they not necessarily imply the same polymer chain rearrangements. Even though the elastic modulus is often obtained by tensile testing, it is not described as the most reliable method to evaluate MNs ability to perforate (DELALLEAU, 2018). Finally, testing parameters such as speed also plays a role in this regard, as dynamic and quasi-static conditions do not lead to the same force versus displacement profiles.

In this part and as suggested in Chapter 1, **1.1.1.3**, a simple gelatin/glycerol skin phantom is prepared at different ratio to compare the influence of both components on the mechanical properties of the gel: 40:60, 50:50 and 60:40.

Compression tests (Syntax, 3R, France) are carried out at two different test speeds (0.05 $mm \cdot s^{-1}$ and 0.025 $mm \cdot s^{-1}$) on 23.5 mm radius (r) and 9 mm thick (L_0) disks. Unlike for MN testing, the cross section remains constant throughout the test and stress (σ, MPa) versus strain (ε, %) curves are obtained (**Figure 48**) from the force (F, N) and displacement (ΔL, mm) raw data as follows:

$$\sigma = \frac{F}{S} = \frac{F}{\pi r^2} \tag{8}$$

$$\varepsilon = \frac{\Delta L}{L_0} \times 100 \tag{9}$$

Compression moduli are calculated in the linear range around 10% elongation with R^2 values above 0.99 (not shown on the Figure).

Both testing parameters result in similar moduli values, even though values obtained at the lowest speed (0.025 $mm \cdot s^{-1}$) are slightly higher for all the samples. Similarly as ALARCÓN-SEGOVIA ET AL., 2021, we can observe that the compression moduli decreases with glycerol proportion which is consistent with its role of plasticizer in the matrix. Its increase also changes the shape of the curve with a more linear stress/strain response which is characteristic of elastic materials as previously mentioned.

However, the moduli range studied in this case (2-4 kPa) belongs to the low end of the elastic modulus interval reported for skin. Additional compounds can therefore be included in the matrix: CHEN ET AL., 2016 add for instance 0.01 to 0.1% glutaraldehyde as a crosslinker to reach an epidermis elastic modulus of 1 MPa.

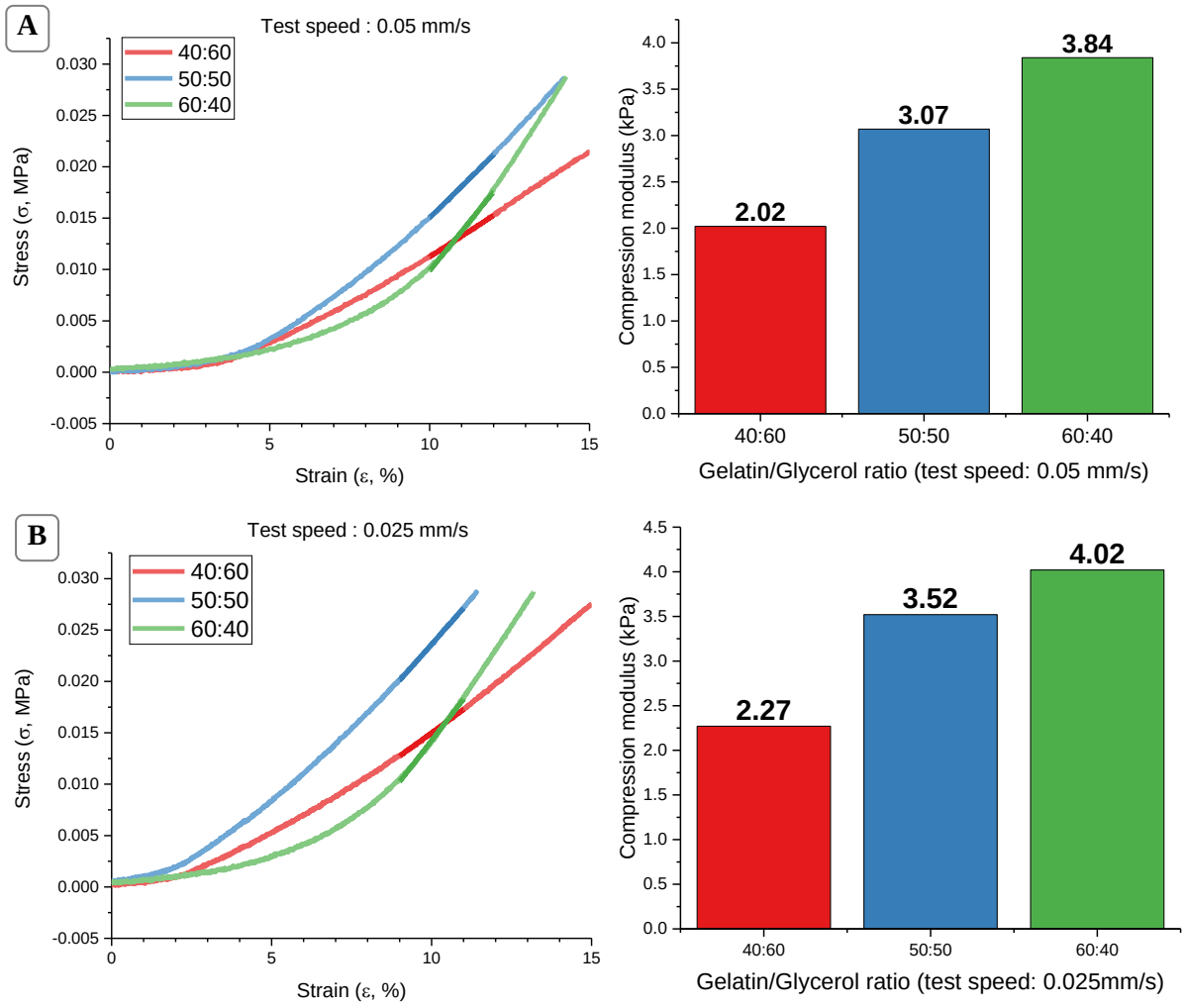

Figure 48. Stress vs strain curve of artificial skin phantom disks under compression depending on their gelatin/glycerol ratio (A) Tests performed at 0.05 mm·s^{-1} and (B) at 0.025 mm·s^{-1}

2.4.2. Microneedle application

2.4.2.1. Thumb force application and easy to cut skin models

First perforation tests are carried out on simple monolayer skin models in order to determine perforation depth by making a cross section with a razor blade. Injection molded PLLA arrays previously presented (**Figure 33A**) are used on both 60:40 gelatin/glycerol and modeling clay (hardness 50 Shore A 28/32, Plastiline®, Clairefontaine Rhodia, France). In these tests, arrays are applied in a quasi-static manner

either applying a thumb force or using a compression bench (TA.XT Plus, Stable Microsystems, UK) at 0.05 $mm \cdot s^{-1}$ loading up to 4 N.

Figure 49A and B show the cross section of a hole generated by a MN. We notice a significant increase in penetration depth in the clay than in the gel. After MN removal, the gel phantom retracts just as real skin. The modeling clay though keeps the accurate dimensions of the needle. Even though these results are not representative of the actual penetration depth when the array remains inserted, it gives an information on the reliability of the model used. The lack of elastic response from the modeling clay makes it a questionable option as a mechanical phantom.

Additionally, the use of a handmade cross section can also be disputed as the razor blade or scalpel may distort the actual hole. Thanks to the transparency of the gel phantom and 3D microscope functions, a cross section close to the hole is enough for in-depth imaging leading to similar observations (**Figure 49C**).

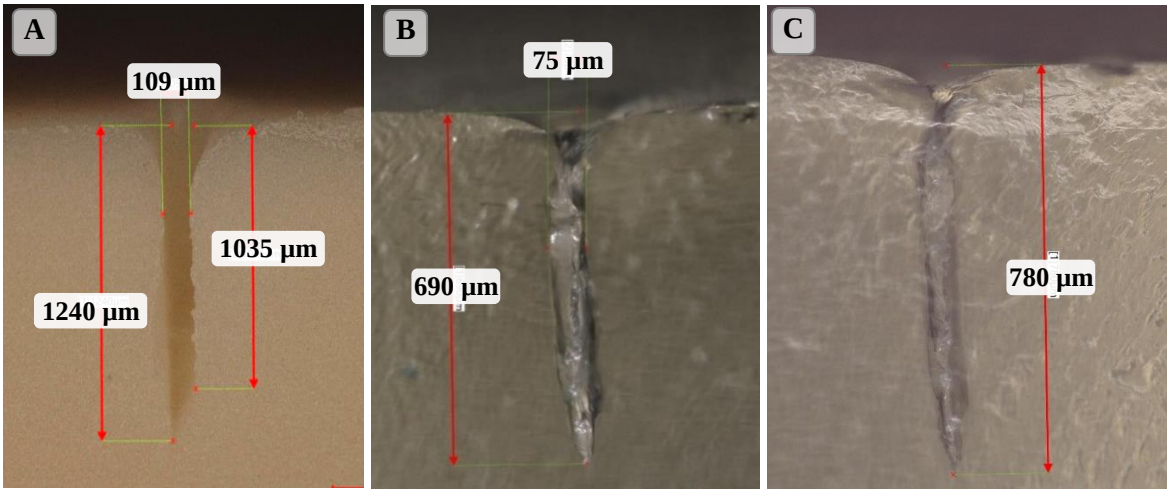

Figure 49. Cross section after injection-molded MN insertion (A) inside the hole in modeling clay, (B) inside the hole in gelatin/glycerol, (C) outside the hole in gelatin/glycerol (3D microscope).

Later on, more complex phantoms are selected for their reliability as well as an impact force application that provides a more efficient skin perforation compared to a pressing force (LEONE ET AL., 2018).

2.4.2.2. Impact force application and multilayered phantoms

In the first part of this Chapter, a spring-based applicator is used along with methylene blue staining to reveal the successful perforation of SC at Tyndall National Institute, Cork, Ireland.

Similar experiments are carried out at CEA using a commercial applicator (mylife Orbit Inserter, Ypsomed, Belgium) and a multilayered silicone-based skin phantom (SynTissue®, SynDaver, Florida, USA).

Learning from mistakes 🔍

*In this case, methylene blue staining led to undesired diffusion across the artificial pores. Thankfully, 3D imaging using both reflection and transmission light helps verifying successful MN perforation (**Figure 50**).*

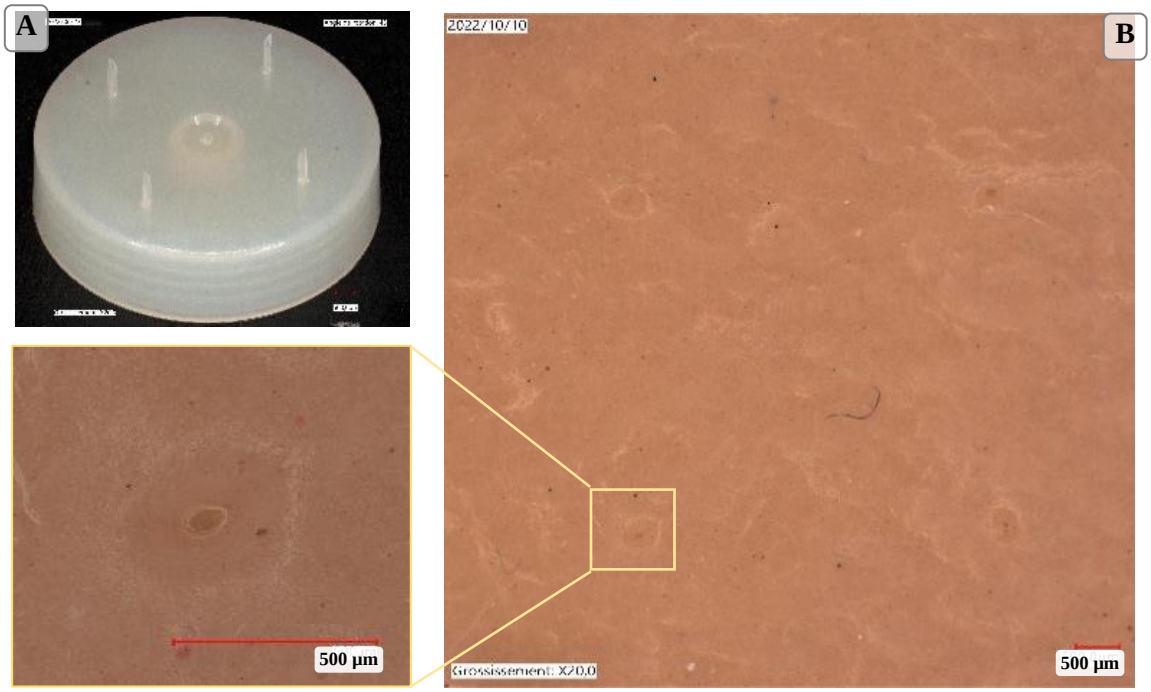

Figure 50. (A) Injection molded hollow PGA MNs and (B) Top view of Syndaver skin phantom after insertion. Pictures by E. Rustique and D. Lauro

In order to mimic natural skin tension, the skin phantom is later placed on a tensile deck developed in the lab during the internship of Adéléyè Chogolou (**Figure 51**).

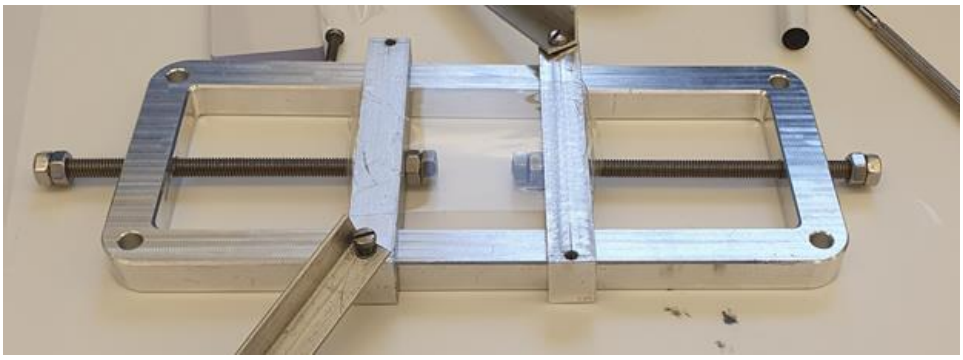

Figure 51. Tensile deck for skin phantoms stretching during MN insertion (picture by A. Chogolou)

In this configuration though, injection molded PGA MNs remain inside the phantom after array removal (**Figure 52**).

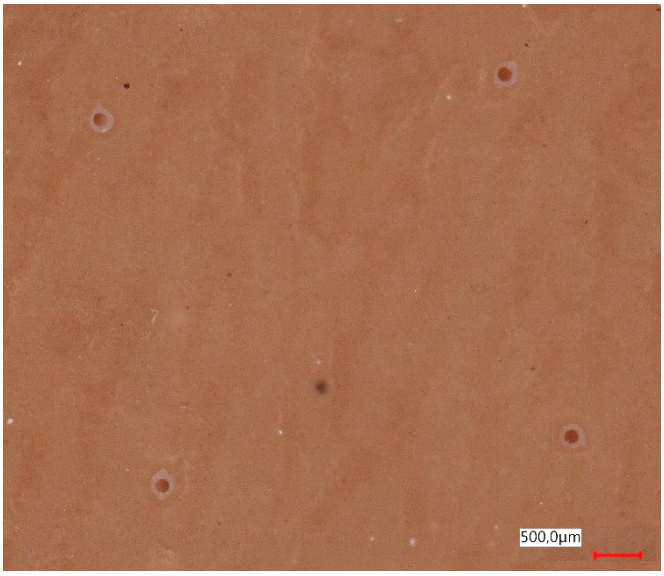

Figure 52. Top view of stretched Syndaver skin phantom after PGA array removal

In opposition to the previous test, the stretched skin model exerts a more important lateral force. As these MNs are thin, tall, and isolated from their neighbors, they are more likely to break under lateral stress. Thankfully, as PGA resorbs in a matter of days, this phenomenon presents no danger to the user. Actually, such feature can be used to create painless micrometer scale channels in place until natural resorption.

Finally, successful perforation of thermoformed PLLA MNs is also verified on the same setup (**Figure 53**).

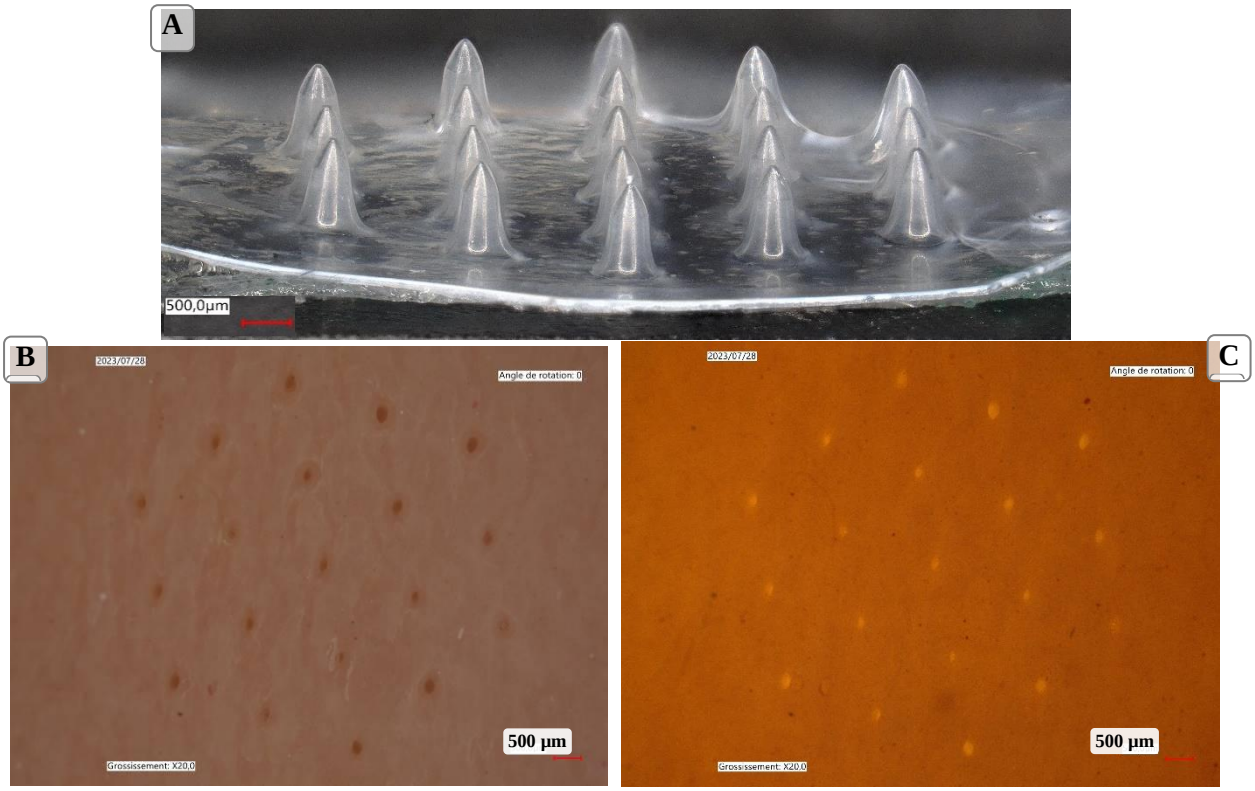

Figure 53. (A) Thermoformed PLLA MN array and perforated SynTissue® skin phantom with (B) reflexion and (C) transmission lights

To remember ❗

After experimenting different artificial skin phantom formulations and testing procedures, an optimized perforation setup is developed in the lab. The latter uses a multilayered silicone-based skin phantom (also suitable for dissolving and swellable MNs) stretched on a tensile deck to mimic skin natural tension – that inevitably declines with age. A spring-based applicator can then be placed on top of the deck and applies the MN array with an impact. Once the array is removed, imaging on a 3D microscope helps identifying the channels formed without removing the skin phantom from the deck.

Apart from the setup, this part also highlights the advantages and limits of the MN arrays presented in the Chapter.

- Even though injection-molded MNs perforate the skin phantom, their important height can cause lateral breakage, leaving the MNs in the skin when the array is removed. Using a resorbable material is therefore necessary to progressively degrade the polymer, which is the case of PGA.

- Thermoformed PLLA MNs leave a satisfactory perforation print with no obvious signs of bed of nails effect that can create missing holes in the middle of the array. Similar tests must be repeated with laser-cut MNs to make sure the side opening does not affect perforation efficiency.

Conclusion

Mechanical testing (compression, shear, bending) and human *ex vivo* skin insertion of different polymer formulations were carried out for one month at Tyndall National Institute, Cork, Ireland, leading to a common research paper. Results highlight different types of MN failure under compression, yet not necessarily compromising their ability to perforate the SC with an impact force.

Injection molding and thermoforming are identified as promising options to develop MN-assisted technologies on a larger scale. Further improvements are necessary to provide biocompatible and bioresorbable photocurable resins with suitable resolution to use 3D-printing (vat polymerization) for MN fabrication.

Thermoforming allowed to obtain hollow MNs from 500 to 1200 µm tall. However, an additional step such as laser cutting is necessary to produce side-openings allowing the drug to flow out of the reservoir.

Thanks to complex multilayered skin phantoms developed over time, MN testing can be performed in the lab without using animal or human skin kept in storage conditions that may alter their mechanical properties. 3D microscopy appears to be a powerful tool to identify success or failure in SC perforation.

Before looking at a combined MN+ITP device, the following chapter is dedicated to the iontophoretic system only. From their fabrication to their electrochemical consumption, Ag/AgCl electrodes are studied to improve their performances and patients' safety during electrically-assisted drug delivery.

CHAPTER 3

Chapter 3: Flexible iontophoresis electrodes

Introduction

The development of wearable devices require to take into account different constraints such as patient compliance, comfort, stability in time, reliability despite motion or individual variability. Unlike biosensors that evolve towards miniaturization, drug delivery devices are mostly in the centimeter range which can feel inconvenient to wear on a daily basis if rigid.

Screen-printing is an appropriate technique to manufacture flat and flexible electrodes on relatively large surface with a low amount of metal deposition (thickness in the micrometer range). Screen-printed silver/silver chloride (Ag/AgCl) electrodes are therefore used for iontophoresis (ITP), as the literature review present them as the safest option to avoid skin burns. Commercial Ag/AgCl inks are used, including references dedicated to iontophoretic applications. Some of them will be compared to understand these distinctions.

To improve comfort, a stretchable substrate can be used to completely fit the shape of the body. The first part of the chapter is dedicated to screen-printed electrodes on **T**hermoplastic **P**oly**U**rethane (**TPU**). These electrodes are used as the standard system of the thesis, and are characterized electrochemically (**O**pen **C**ircuit **V**oltage (**OCV**), **C**hrono**P**otentiometry (**CP**) and **E**lectrochemical **I**mpedance **S**pectroscopy (**EIS**)). Complementary surface analyses are used to suggest techniques to increase electrodes lifetimes.

The second part of the chapter focuses on means to improve the iontophoretic system from flexible to stretchable. To make sure that current distribution remains constant regardless of the patient movements, stretchable inks can be used in addition to the stretchable substrate. Another option explored is to modify the geometry of the electrodes to provide a more tensile-resistant device.

3.1. Standard electrodes

Iontophoresis (ITP) electrodes are screen-printed on a flat substrate following a four-layer stack according to McAdams et al., 2000. A set of two electrodes (anode and cathode) is required to complete the ITP system. Layers are printed on top of each other in the following order:

- **L1: Silver -** This conductive layer allows to distribute the current from the electrical contact to the surface of the electrode. The high electrical conductivity of silver minimizes current loss and provides a reliable signal.
- **L2: Carbon -** This layer acts like a spacer between the conductive and the electrochemically active layer. It protects the conductive layer from the reactions occurring at the surface, and helps providing a continuous electrical input all over the surface. Studies with and without the spacer show a significant increase in potential due to the electrochemical degradation of the conductive layer (**Appendix 4**).
- **L3: Silver/silver chloride** - This electrochemically active layer is consumed on both sides to form silver and silver chloride respectively. Electrochemical mechanisms involved will be further detailed in this chapter.
- **L4: Insulator or dielectric** – This final layer is applied on 500 µm at the perimeter of each disk to avoid electrode dysfunction in case of misalignment during the printing process. It can also help keeping the edges of the electrodes inert as they may present heterogeneous thickness between the edges and the center of the deposited layer. Finally, it also protects the electrical track from any contact with the aqueous environment.

Figure 54 summarizes each step and electrodes dimensions.

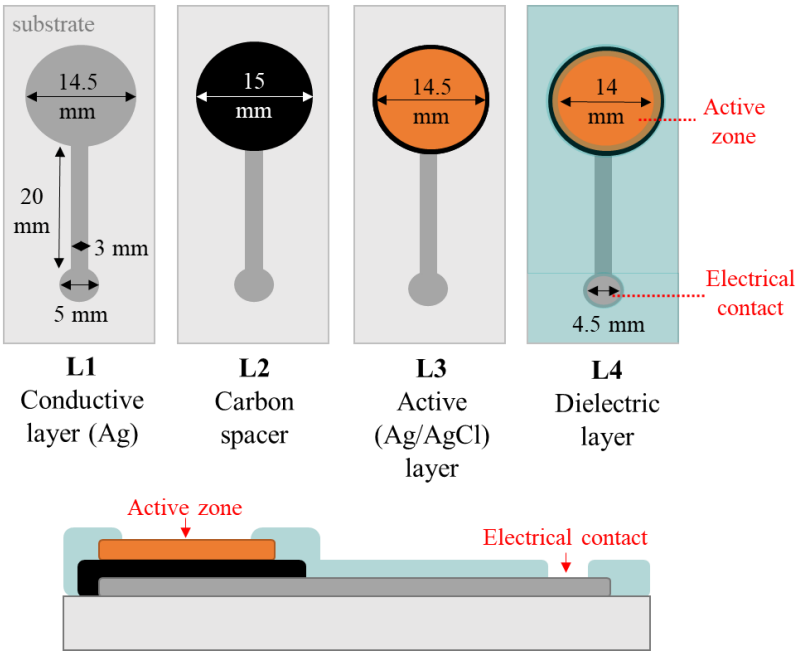

Figure 54. Top view and cross section of standard iontophoresis electrodes stack and dimensions

Once printed, the electrode exposes a 14 mm diameter disk corresponding to the active zone, in contact with the working saline environment. A smaller 4.5 mm disk, at the other end of the 20 mm conductive Ag track, is dedicated to the electrical contact with the potentiostat and is kept in dry conditions.

3.2. Process and characterizations

3.2.1. Screen-printing on flexible substrates

Definition 🕮

Screen-printing *is a printing technique using a mesh screen to transfer a stenciled design onto a substrate (**Figure 55**). In a planar system such as the one used in this study, the ink is pushed down by a squeegee (or rubber blade)* (Cruz et al., 2018). *Mesh apertures follow a specific user-defined layout. Different inks can be printed using several screens subsequently.*

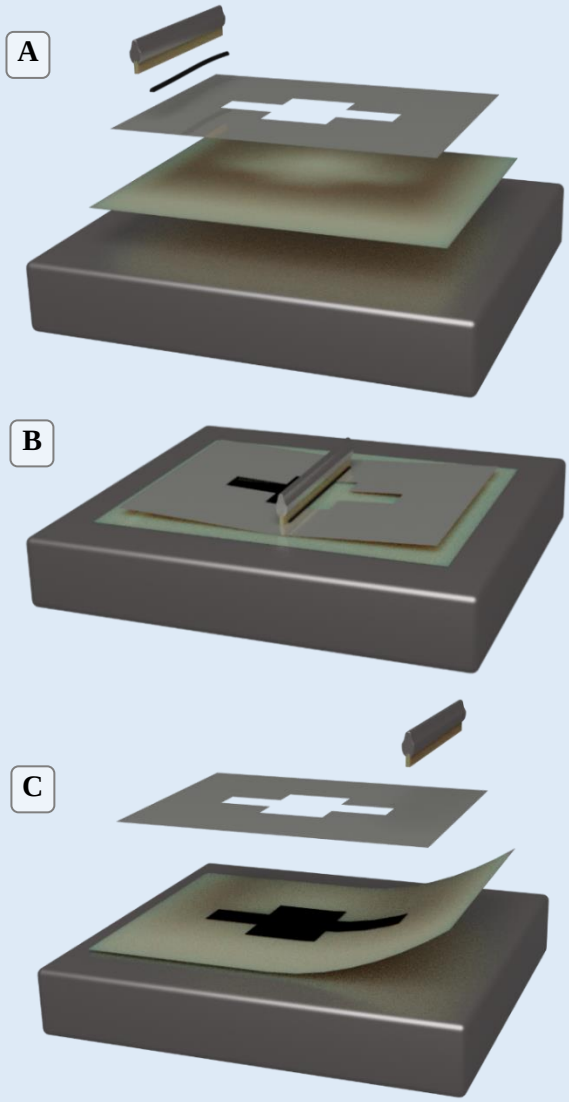

Figure 55. Simplified screen-printing principle (A) Placing the mesh screen on top of a substrate (B) Printing the desired ink with a squeegee (C) Removing the substrate for annealing. Designed by L. Tournon

3.2.1.1. Equipment, process and parameters

Screen-printing (EKRA X5 Professional, Asys Group, USA) is chosen as a low cost, easy, automatized and reproducible process to produce Ag/AgCl electrodes. They are composed of a four-layer stack printed on a flat substrate as previously described.

Each step requires the use of one screen (Christian Koenen GmbH, Germany). The mesh is chosen to deposit an ink volume of 40 to 43 $cm^3 \cdot m^{-2}$ according to the supplier's guidelines. A stainless steel mesh is used for layers Ag (L1), C (L2) and dielectric (L4), as commonly used in screen-printing. However, to avoid any possible interaction between chloride ions and the mesh, the screen used for layer Ag/AgCl (L3) is made of polyester. Similarly, no metallic utensil is used in contact with Ag/AgCl inks.
Apart from mesh size, different parameters can be controlled by the user to adapt the program to the viscosity of the inks:

- Squeegee hardness, angle, pressure and speed
- Distance between the substrate and the screen (snap-off)
- Separation speed between the substrate and the screen

After printing, each layer is annealed either in an IR oven for L1 (IRCO400, Exelsius, France), a nitrogen oven for L2 and L3 (UFE600, Memmert, Germany), or a UV-conveyor for L4 (UV-Star 2, Concept Plus, VA, USA).

All the parameters are optimized and summarized in **Appendix 5** for each reference used.

The superimposed screen layouts are depicted in **Figure 56**, corresponding to a batch of 27 electrodes. The surface of the electrode in contact with the skin (A) and the electrical contact to be connected to a potentiostat (B) are displayed on the Figure. On the right side of the layout, different test patterns are designed for tensile and electrical tests (C) as well as resistance and thickness measurements (D).

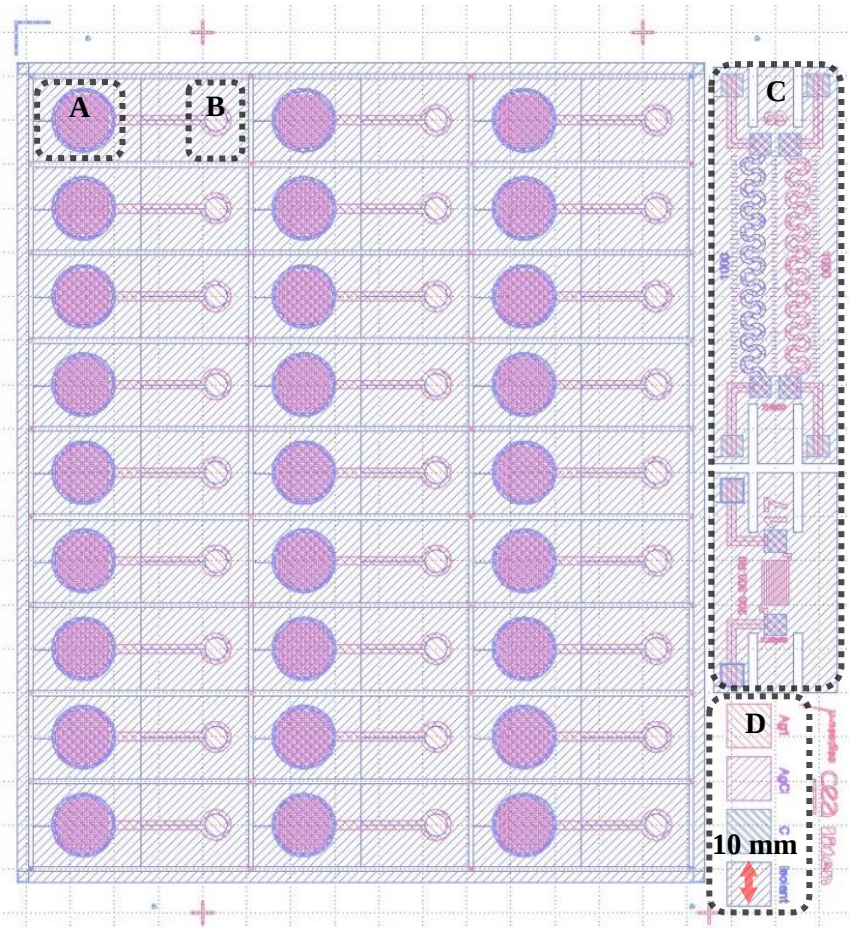

Figure 56. Complete four-layer layout of iontophoresis electrodes. (A) Surface of the electrode (B) Electrical contact (C) tensile and electric test patterns (D) Thickness test patterns of 10x10 mm

Finally, laser cutting (Isoptec45-CO2, Optec, Belgium) is used post-processing to separate the different elements of the layout.

3.2.1.2. Materials

Substrate

250 µm-thick **P**oly**E**thylene **T**erephtalate (**PET**) and **P**oly**C**arbonate (**PC**) are first used as flexible substrates for the first batches of electrodes. Despite their flexibility, these substrates are not stretchable and cannot provide any information on the system working under tensile stress. Moreover, as the electrodes are quite large, they do not have the ability to properly fit body curves (for example the forearm) and follow the motion of the patient. Electrodes printed on PC are however used later on as pseudo-reference electrodes for electrochemical measurements.

Thermoplastic polyurethane (TPU 100 µm, Dupont, USA) is then selected as a suitable candidate for a comfortable wearable device, with a typical Young Modulus in the MPa range (CHITRAKAR ET AL., 2022). It allows the study of electrochemical performances while stretched on a tensile deck as shown

on **Figure 57**. Also, unlike other stretchable substrates such as PDMS, its high surface energy provides a satisfying adhesion between the metallic ink and the substrate (SUIKKOLA ET AL., 2016). It can therefore be used without any surface treatment prior to printing, significantly reducing the processing time and number of steps.

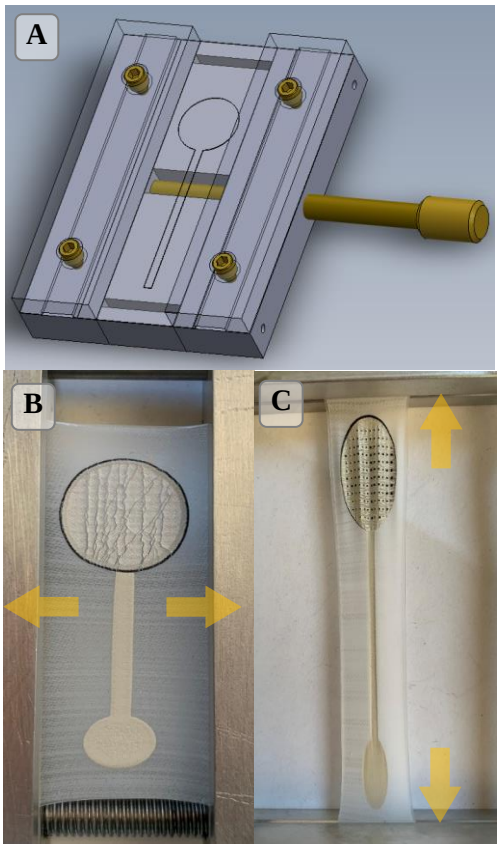

Figure 57. (A) Tensile deck (designed by F. Emieux) and examples of TPU electrodes stretched on the (B) lateral and (C) longitudinal axes. Yellow arrows indicate the direction of the constraint. N.B. Cracks are visible due to the use of non-stretchable inks

Inks

A set of silver, carbon, silver/silver chloride (30:70) and dielectric inks are used respectively as the conductive layer, spacer, active layer and insulator (5000, 7102, 5876 and 5018, Dupont, DE, USA – referred to as "standard" inks). Pseudo-reference electrodes are also screen-printed with a 65:35 silver/silver chloride ink (5874, Dupont, USA) on PC. Both Ag/AgCl inks used in this study are specifically commercialized for ITP, where metallic particles need to be available at the surface to allow the desired electrochemical reactions to occur.

3.2.2. Ink characterizations

The conductivity of metallic inks are calculated using the thicknesses measured with a profilometer and the resistance per square measured by four-point probe method on the square test pattern.

Thickness

Thickness patterns previously shown in **Figure 56D** are used to estimate the ink volume deposited on each independent pattern. A stylus profilometer (DEKTAK-XT, Bruker, Germany) is used with a porous vacuum deck to prevent the substrate from sliding when the tip is moving.

Learning from mistakes 🔍

Soft substrates such as TPU can be dragged by the tip of the stylus during measurements. Another alternative used, yet destructive, is to metallize the sample by sputtering few nanometers of metal such as titanium, keeping the surface rigid enough for profilometry measurements.

The average thickness (~10000 data points) at the surface of each layer is calculated (dotted red lines on **Figure 58**) and implemented to the following table (**Table 3**). The dielectric ink displays a bigger variation due to the large mesh used on the associated screen. This value will not be taken into account for the rest of the calculation though, as the main goal in this part is to calculate the conductivity of metallic inks only.

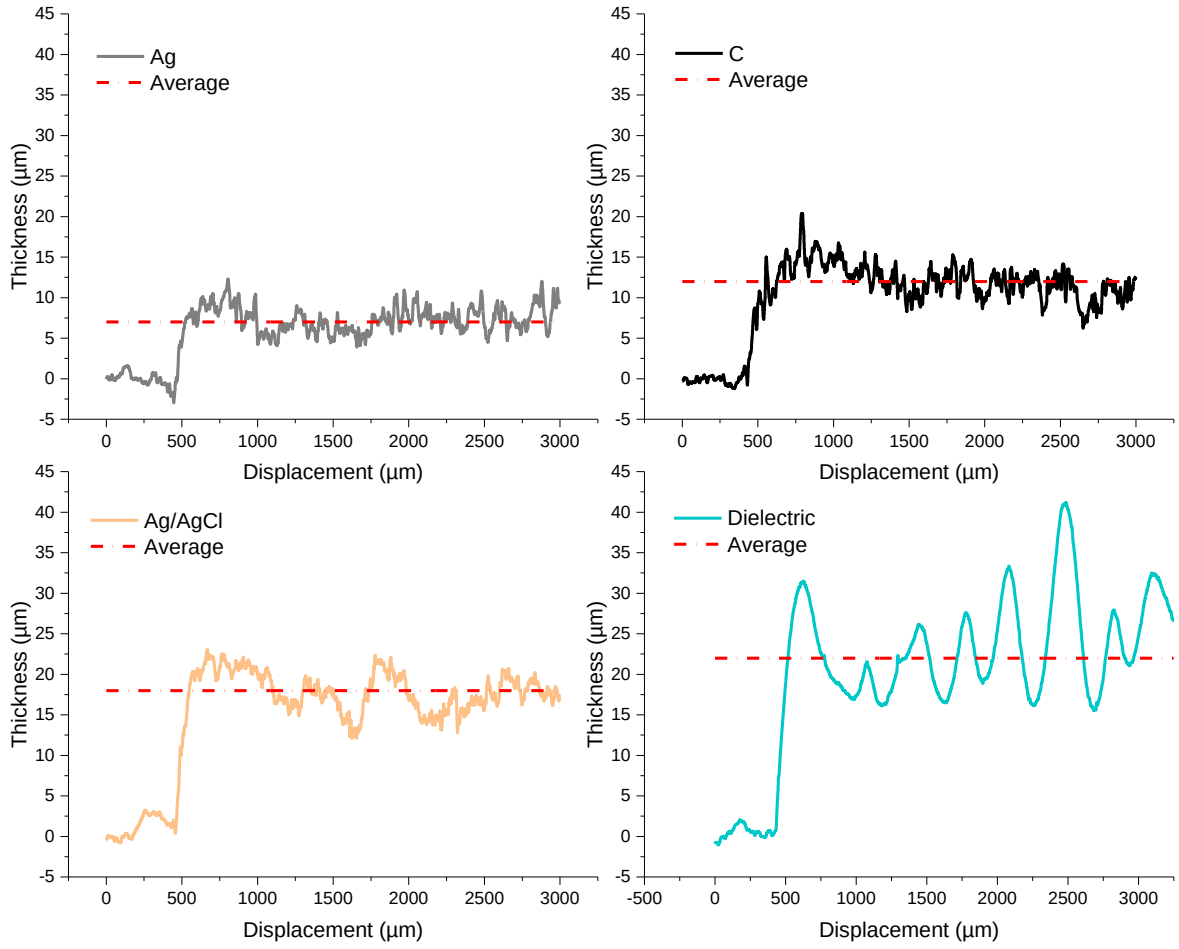

Figure 58. Thickness measured on the first 3 mm of test patterns. The first 500 µm displacement corresponds to substrate (zero value) and average thicknesses are calculated beyond this value (deposited ink)

Sheet electrical resistance

Ink electrical resistance is measured on the same 10x10 mm patterns using a four-pin probe instrument with an interpin distance of 1.5 mm (Loresta-EP MCP-T360, Mitsubishi, Japan). A correction factor must be used considering the distance between each probe (s) and the side of the square sample (D) as tabulated in **Appendix 6**. In our case D/s is equal to 6.7 which corresponds to a correction factor of ~3.8.

By implementing this correction factor to the instrument, each measurement is repeated three times and an average sheet resistance per square and associated standard deviation are obtained in **Table 3**.

Table 3. Average deposited ink thickness and sheet resistance (calculated on 3 measurements).
N.B: The number of digits is determined by the position of the unique significant figure used in the standard deviation (Purdue University, Department of Physics and Astronomy)

Ink (reference)	Average thickness *e* (µm)	Mean resistance R (Ω□)	Standard deviation (Ω□)
Ag (5000)	7	0.0073	0.0008
C (7102)	12	37	1
Ag/AgCl (5876)	18	0.38	0.02

Ink electrical conductivities

Table 3 finally allows the calculation of the resistivity and conductivity of the conductive inks used in the standard stack summarized in **Table 4**. Ag/AgCl is not easily comparable with the literature due to the specific ratio used, but silver and carbon (amorphous) perfectly correspond to the tabulated order of magnitudes (JEFFERSON LABS RESOURCES, 2016; PAULEAU AND BARNA, 1996).

Table 4. Conductivities calculated for silver, carbon and silver chloride standard inks

Ink (reference)	Resistivity ρ (Ω.m)	Conductivity σ (S·m^{-1})
Formula	$\rho = R \cdot e$	$\sigma = \frac{1}{\rho}$
Ag (5000)	$5.11E \cdot 10^{-8}$	$1.96 \cdot 10^{7}$
C (7102)	$4.44 \cdot 10^{-4}$	$2.25 \cdot 10^{3}$
Ag/AgCl (5876)	$6.84 \cdot 10^{-6}$	$1.46 \cdot 10^{5}$

Learning from mistakes 🔍

Thickness probes are independent and directly deposited on the substrate, unlike electrode layers that are stacked on top of each other. Values are therefore different from thicknesses measured at the electrodes surface and used in the numerical model in Chapter 4, as the underneath layers play a role on ink adhesion. ***Thickness probes are therefore only used for ink characterization****, i.e. to calculate the electrical conductivity with the measurement of both thickness and resistivity on the same pattern.*

3.3. Comprehension of the electrochemical system

Electrochemical characterizations are conducted on ITP electrodes to better understand the electrochemical reactions involved in the system. For these tests, a three-electrode assembly is described on **Figure 59A**. The distance between the working (WE) and the counter electrode (CE) is constant thanks to a homemade 3D-printed holder such as the one presented on **Figure 59B**. An additional screen-printed Ag/AgCl electrode on PC is used as a pseudo-reference electrode.

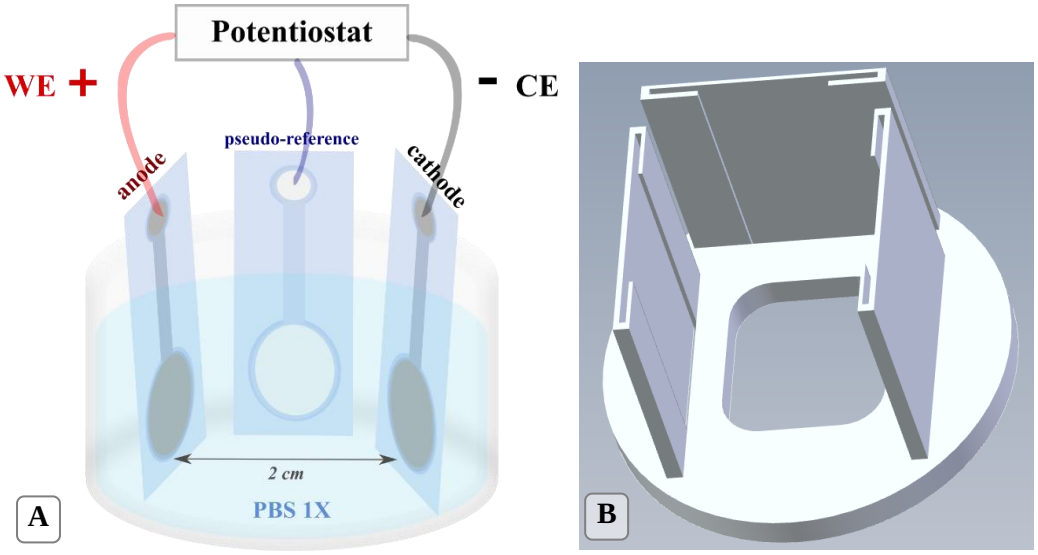

Figure 59. (A) Three-electrode assembly for electrochemical analyses and (B) Associated electrode holder

3.3.1. Reliability of the pseudo-reference electrode

Definition 🕮

A ***pseudo-*** *or* ***quasi-reference electrode*** *is a metallic material immersed in the working solution* (AJ TORRIERO, 2019)*. The pseudo-reference potential thus varies with the ions present in the electrolyte, unlike* ***R****eference* ***E****lectrodes (****RE****) that are continuously at thermodynamic equilibrium with their associated salt in a galvanic cell (e.g. silver with silver chloride in concentrated KCl as depicted on* ***Figure 60****).*

A preliminary study is conducted to validate the use of a pseudo-reference electrode instead of a commercial RE that is more expensive and bigger than screen-printed electrodes. The difference in size also makes the three-electrode assembly more difficult to set and to keep identical throughout the tests.

Ag/AgCl electrodes are the most commonly used RE due to materials availability. They also provide good environmental compatibility and resistance to higher temperatures compared to calomel and mercury-based reference electrodes (SOPHOCLEOUS AND ATKINSON, 2017).

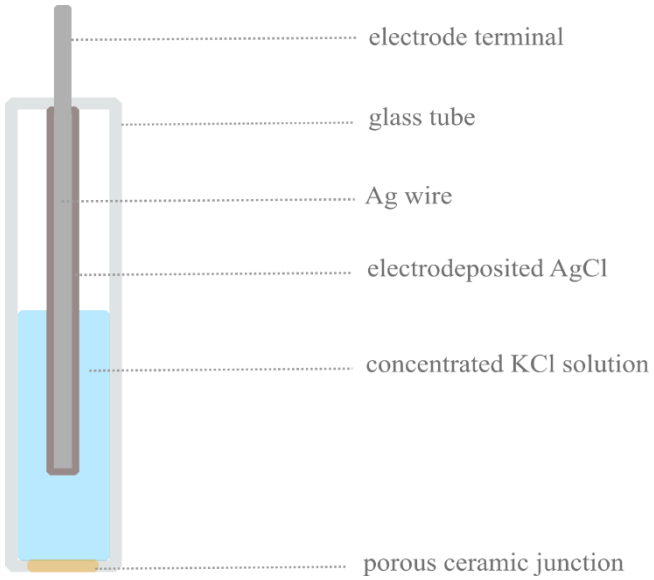

Figure 60. Schematic representation of the reference Ag/AgCl electrode (modified from Sophocleous and Atkinson, 2017)

Despite these advantages, the regular structure of Ag/AgCl RE (**Figure 61**) is not suitable for wearable applications and alternatives must be found to monitor the electrochemical behavior of a biosensor or a stimulating device such as the ITP device developed in this thesis. Screen-printed pseudo-reference electrodes can therefore be prepared using similar Ag/AgCl inks as ITP electrodes (65:35 ratio, 5874, Dupont, USA). The electrode design also remains unchanged, apart from the carbon spacer that is not required – no electrochemical reaction is involved in this case as no current flows through this electrode.

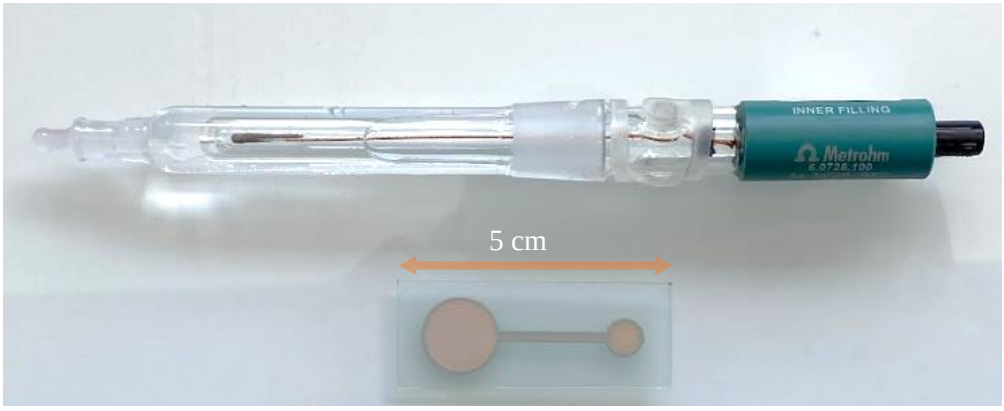

Figure 61. Metrohm reference electrode (up) and screen-printed pseudo reference electrode (down)

To make sure these electrodes are reliable for the rest of the experiments, the three-electrode assembly is installed using either the commercial double-junction RE (Metrohm, Switzerland) or the homemade PC pseudo-reference electrode (**Figure 61**).

The open-circuit potential is measured in different aqueous solutions:

- Potassium chloride (KCl, 0.1 and 1 M or mol·L^{-1}, from solid, Sigma Aldrich, MO, USA),
- **P**hosphate **B**uffer (**PB**, 0.1 M, from solid, Sigma Aldrich, MO, USA)
- **P**hosphate-**B**uffered **S**aline (**PBS** 1X, 137 mM NaCl, 2.7 mM KCl, 10 mM Na2HPO4 and 1.76 mM KH2PO4, diluted from PBS 10X, Sigma Aldrich, MO, USA).

Definition 🕮

*The **open circuit potential (OCP)** or **open circuit voltage (OCV)** is a passive technique consisting in measuring the voltage between the WE and the RE while the system is at rest i.e. no signal (current or voltage) is applied between WE and CE. The system is however not necessarily at equilibrium if spontaneous reactions can occur* (PEROFF, 2019).

As the Ag/AgCl reactions between the working and the counter electrodes are not spontaneous and require an energy input, this system is expected to be at equilibrium. **Figure 62** proves indeed that OCVs remain stable with time for both reference and pseudo-reference electrodes, and only the first 38 seconds of the measurements are plotted. This Figure shows however significant differences in the OCVs depending on the reference electrode and the electrolytes used.

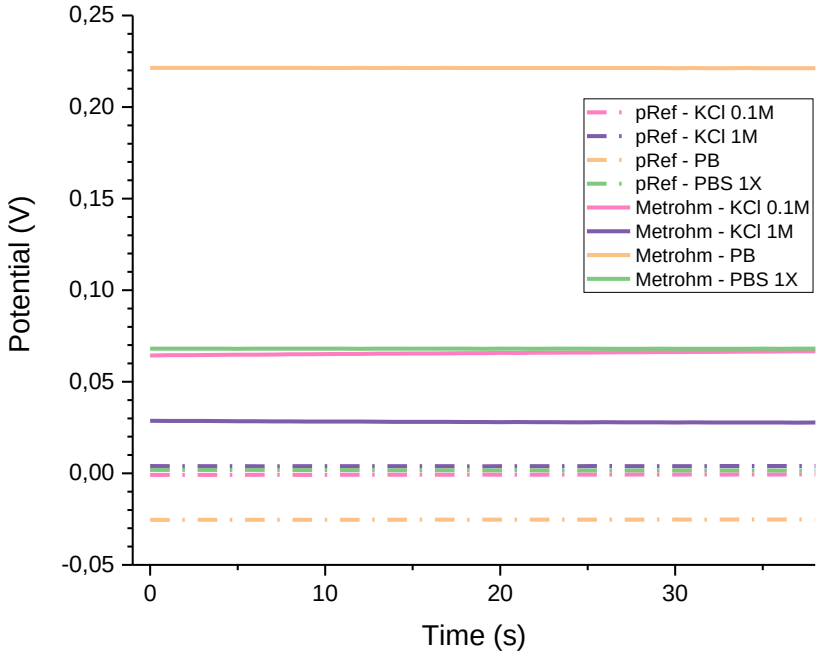

Figure 62. OCV of the system using Ag/AgCl commercial reference electrode (Metrohm) or homemade pseudo-reference electrode (pRef)

For all the electrodes present in the system, the same chemical compounds (Ag/AgCl) are involved and the potential of each electrode is given by Nernst equation:

$$E = E^0 - \frac{RT}{F} \ln a_{Cl-} \quad (10)$$

Where E^0 is the standard electrode potential of the redox couple, R ($J \cdot K^{-1}.mol^{-1}$) is the ideal gas constant, T (K) the temperature, F ($C \cdot mol^{-1}$) the Faraday constant and a_{Cl-} the activity of chloride ions.

This relationship shows a direct influence of the chloride concentration on an Ag/AgCl electrode potential. The different curves on **Figure 62** can thus be explained as follows:

- In the case of the commercial (Metrohm) RE, the Ag/AgCl wire is contained in its own galvanic cell with a constant concentration of chloride ions. The RE potential therefore remains constant regardless of the working solution. The potential of the WE however changes depending on the ions present in the medium. In the end, the difference in potential (voltage) between the WE and the RE electrodes changes with the electrolyte type.
- On the other hand, the pseudo-reference electrode potential varies just like the WE as they are both composed of the same metallic compounds. On **Figure 62** (dashed lines), the difference in potential is then always close to 0 V, except in the case of PB. Indeed, PB is the only electrolyte that does not contain chloride ions. As the Ag/AgCl ratio of the pseudo-electrode (65:35) and the WE (30:70) is different, so is the potential at rest as it only depends on the chlorides present in the ink.

However, to make sure the Ag/AgCl ratio does not impact the electrode potentials, it is still preferable to work in a saline environment. Thankfully, the desired redox reactions for iontophoretic delivery can only occur in these conditions as mentioned in Chapter 1 (**1.2.1.3**). The following electrochemical characterizations will be performed in PBS 1X as it is often used in biochemistry to mimic pH, osmolarity and ion concentrations of extracellular fluids (AAT BIOQUEST, INC., 2023).

To remember

A screen-printed Ag/AgCl pseudo-reference electrode is a suitable alternative to commercial reference electrode to follow the ITP electrodes wear during delivery (saline conditions), and can easily be miniaturized for wearable applications.

3.3.2. Lifetime measurements by chronopotentiometry (CP)

In this part, CP is used to follow the electrodes wear and estimate the time at which the desired redox reaction is over.

Definition 🕮

Chronopotentiometry (CP) *is a galvanostatic technique consisting in applying a fixed or variable electric current for a given time while monitoring the resulting potential of the working electrode* (PICARD ET AL., 2003).

As the current is applied, Ag and AgCl particles available at the electrode surface react according to **Equations 11 and 12** and as described in Chapter 1, **1.2.1.3.** A more resistive AgCl passivation layer starts to form by the arrival of chlorides at the anode and the potential increases until reaching a plateau.

$$Ag + Cl^- \rightarrow AgCl + e^- \quad (11)$$

$$AgCl + e^- \rightarrow Ag + Cl^- \quad (12)$$

Due to the AgCl passivation layer, reagents are no longer available to react and one or both electrodes can act like inert electrodes as described by KASHA AND BANGA, 2008. Water electrolysis takes over according to **Equations 13 and 14**, and gas bubbles appear on the electrode surfaces. As commonly described in the literature, an anodic overpotential explains the potential of 1.7 V at the plateau (compared to the standard potential $E^0_{O2/H2O}$=1.23 V), due to the additional energy necessary to overcome the ohmic resistance of the electrolyte (XIANG ET AL., 2016).

$$2H_2O \rightarrow 4H^+ + O_2 + 4e^- \quad (13)$$

$$2H_2O + 2e^- \rightarrow 2HO^- + H_2 \quad (14)$$

The latter reactions are undesired because besides gas, the production of H^+ and HO^- ions locally modifies the pH and can cause chemical burns at the surface of the skin. Ag/AgCl electrodes thus act like sacrificial electrodes to avoid such skin reactions during the electrical drug delivery.

For the rest of this study, a current of 1 mA is applied corresponding to a current density of 0.65 mA·cm^{-2}. The electrodes lifetime (represented by the dotted line on **Figure 63**) is defined as the time required to reach water electrolysis, i.e. the time at which the curve reaches a plateau. The value of lifetimes are given more precisely using the time derivative dV/dt (blue) of the V curve (black). The reproducibility of this technique is verified with a maximum variation of 68 seconds on 3 measurements.

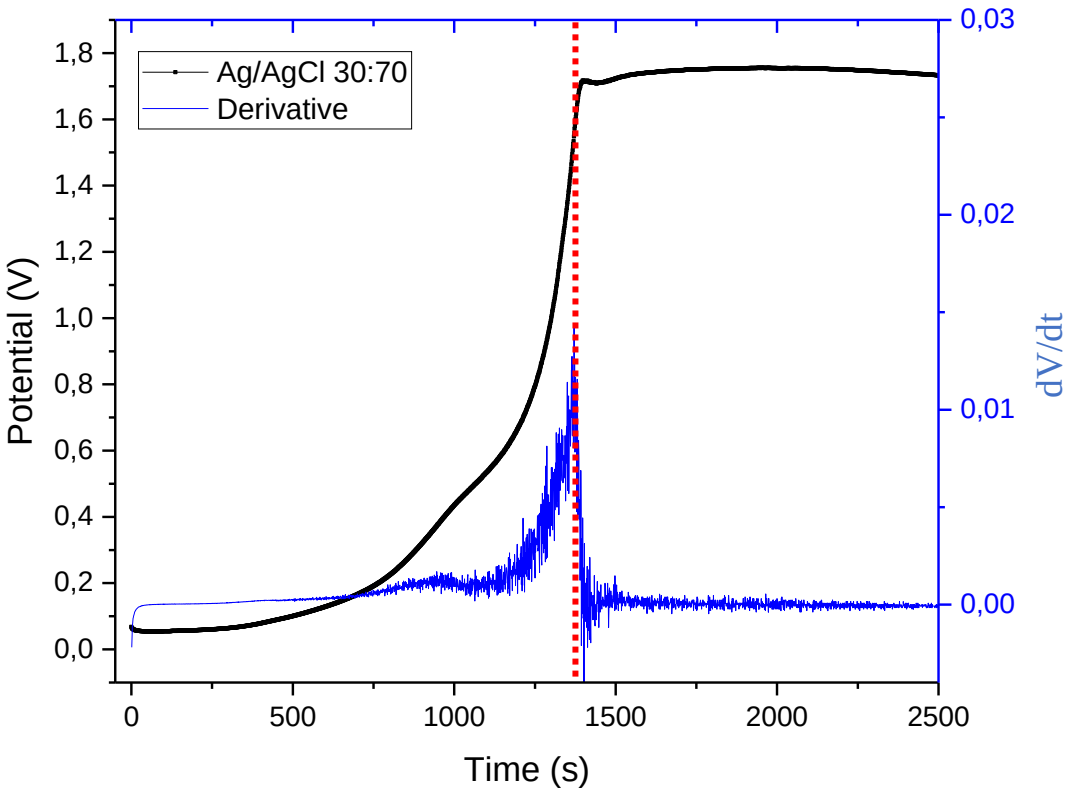

Figure 63. Example of chronopotentiometry (CP) profile of Ag/AgCl electrodes in PBS 1X when applying a direct current density of 0.65 mA·cm-² (black). The time derivative curve (blue) indicates electrode lifetime at its maximum value

To remember 🕯

Chronopotentiometry helps monitoring the time at which a parasitic electrolysis reaction takes over the desired redox reactions between Ag and AgCl. This technique is used throughout the chapter to compare electrodes performances in different configurations.

3.3.3. Identification of a passivation layer by Electrochemical Impedance Spectroscopy (EIS)

Definition 🕮

Electrochemical Impedance Spectroscopy (EIS) *is used to evaluate the electric impedance Z (Ω) spectra of a complete electrochemical system: electrodes, electrolyte and their interface. The electric impedance corresponds to the ability of materials to resist to an applied alternating electric signal (current or voltage). A small sinusoidal excitation is applied to the system around the potential or current of interest, while monitoring its response signal (GAMRY INSTRUMENTS).*

*Results are presented in the form of Nyquist (-ImZ = f(ReZ)) or Bode (NormZ ; PhaseZ = f(Freq)) diagrams (**Figure 64**).*

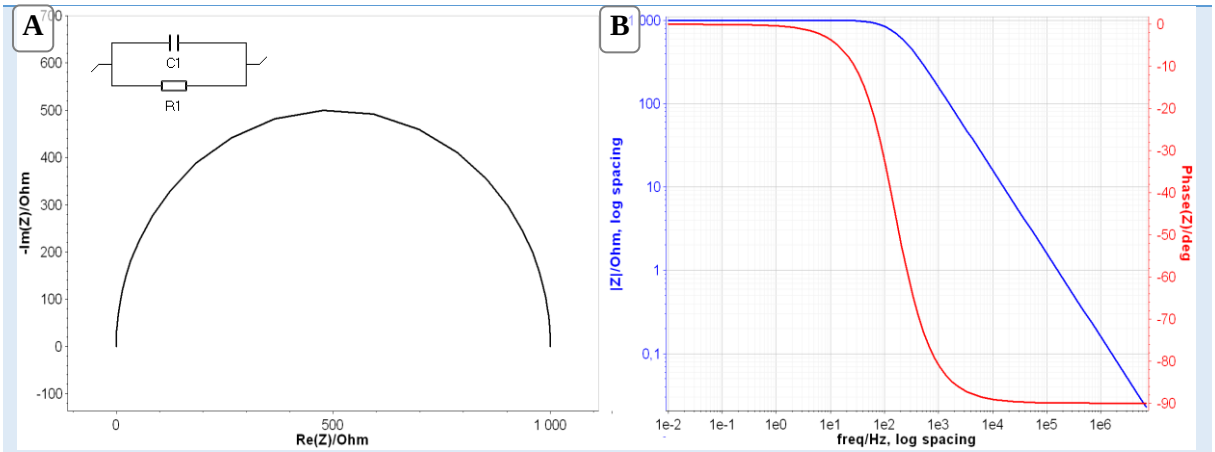

Figure 64. Example of impedance spectra representations for a R/C circuit. (A) Nyquist diagram (B) Bode diagram

In this part, EIS is used at 0 V versus OCP with a potential stimuli of 10 mV amplitude on a frequency range from 10 mHz to 7 MHz. Results are presented with Bode plots to visualize the frequency dependence on the x-axis. The same three-electrode assembly as CP is used to compare the impedance profiles of ITP electrodes before (new) and after (used) their consumption.

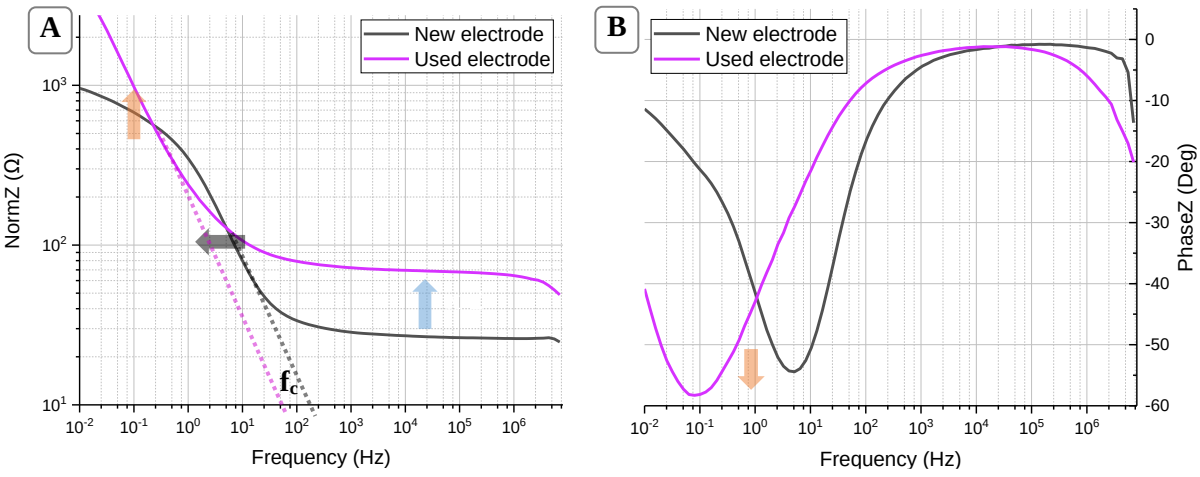

Figure 65. Bode representation of impedance spectra on new (black) and used (purple) electrodes. Plots are separated with (A) the norm of the impedance Z and (B) its phase

Figure 65 displays differences between the two cases, which is consistent with the change in surface structure expected before and after ITP. A simple Randles circuit can be used to model the processes occurring at the electrochemical interface (**Figure 66**) (RANDLES, 1947).

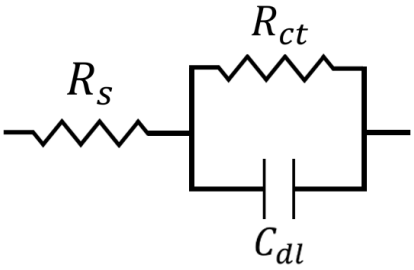

Figure 66. Randles circuit with R_s (Ω) the resistance in series, R_{ct} (Ω) the charge transfer resistance and C_{dl} the electrochemical double layer capacitance (F)

Definition 🕮

*The **Electrical Double Layer (EDL)** is a capacitive interfacial layer that forms when a polarized electrode attracts counterions present in the electrolytic solution (**Figure 67**).*

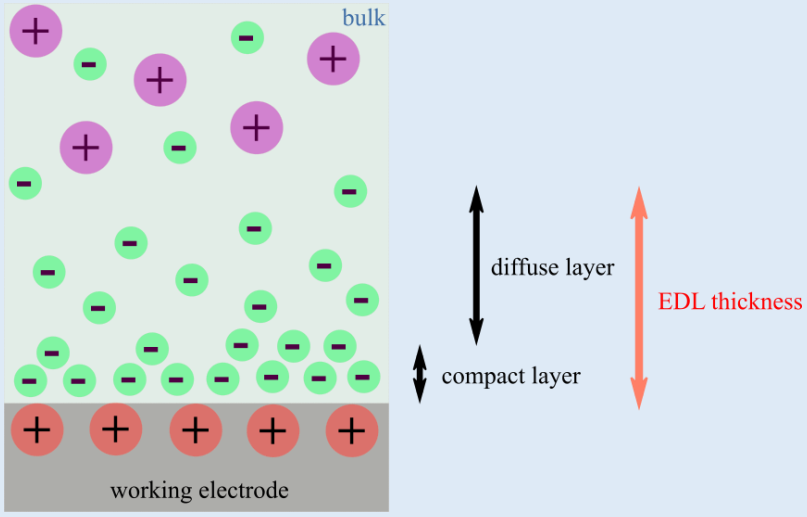

Figure 67. Stern representation of the EDL with a compact and a diffuse layer (modified from Pham et al, 2007)

To better understand differences in both resistive and capacitive behaviors, we can look at each region separately above and below the cutoff frequency.

Cutoff frequency f_c

Definition 🕮

*The **cutoff frequency** is the frequency at which the major impedance contribution switches from resistive to capacitive. It can be identified on the graph by extending the linear region (dotted lines) to intercept the x-axis. It is also described as a function of R_s (Ω) and C_{dl} (F)* (SAGHAFI ET AL., 2023):

$$f_c \propto \frac{1}{R_s C_{dl}} \quad (15)$$

We can first notice that f_c slightly shifts to lower frequencies when the electrodes are used (black arrow). If the working electrode is indeed passivated by AgCl, the active surface area is reduced. Charge transfer at the electrode/electrolyte interface is therefore slowed down and cannot keep up beyond a new cutoff frequency.

Above f_c : dominance of R_s

Above the cutoff frequency, we usually consider that electrochemical reactions are inhibited as the polarities change too fast for these reactions to keep up. The plateau observed therefore corresponds to a purely **resistive behavior due to materials electrical properties**. This hypothesis is confirmed by the phase plot progressively reaching a plateau around 0 deg, which is characteristic of a resistor. On used electrodes, the impedance value is doubled in this region (blue arrow) which is consistent with the deposition of a more resistive material at the surface of the working electrode. Above 10^5 Hz, the phase drop is due to the noise caused by electrical contacts and induction effects. Results in this region are therefore not taken into account.

Below f_c : dominance of R_{ct} and C_{dl}

Below the cutoff frequency, interfacial processes such as charge transfer, mass transport and electrical double layer formation are predominant. Again, the formation of a passivation layer at the surface limits charge transfer compared to new electrodes with a large active surface area, which translates into a shift towards higher impedance values (orange arrow on **Figure 65A**). The capacitive effect of the EDL is also intensified as charges accumulate on each side of the passivation layer acting as a dielectric. This effect is visible on the phase diagram that reaches a lower minimum (orange arrow on **Figure 65B**). We can also notice that the frequency associated with the phase minimum is also shifted to lower values. This frequency corresponds to the resonance frequency (fully charged capacitor) that follows a similar relation as **Equation 15**, but using R_{ct} instead of R_s. As both R_{ct} and C_{dl} increase, the resonance frequency decreases to lower frequencies than in the case of new electrodes.

Resistance and capacitance values given by the literature also corroborate these observations as silver chloride is certainly more resistive ($\sigma \cdot 10^{13}$) and more capacitive ($\varepsilon_r \cdot 10$) than pure silver which is defined as the best electrical conductor among metals (HA AND PAYER, 2011; JEFFERSON LABS RESOURCES, 2016; KORTH KRISTALLE, 2021).

To remember

EIS spectra confirm the presence of an insulating passivation layer after electrode use. Apart from the overall resistance in series that increases because of the low conductivity of AgCl, charge transfer resistance also increases as the active surface area is reduced. The capacitance is also higher on used electrodes since charges accumulate on either side of the passivation layer.

Pseudo-quantitative results could be obtained using an equivalent circuit to define the values of the resistors and capacitors involved. Considering the complexity of this system though (multiple stack, porosity, unknown polymeric formulations), the use of an equivalent circuit is not recommended as the number of unknown elements are too important and can lead to false assumptions. Instead, a chemical quantification by surface analysis is provided to identify the limiting reagent of the electrochemical system.

3.3.4. Identification of the limiting reagent by Energy Dispersive X-Ray Spectroscopy (EDX)

In this electrochemical system, one reaction occurs at each electrode: silver oxidation at the anode, and silver chloride reduction at the cathode. Theoretically, these reactions are independent and activated by the electrical input provided. However, as it has been proven that water electrolysis can cause skin damage, we will call "***limiting reagent"*** the reactant that first causes a water electrolysis reaction.

Scanning **E**lectron **M**icroscopy (**SEM**) (EHT 10 kV, LEO, Zeiss, Germany) and SEM coupled with **E**nergy **D**ispersive **X**-ray spectroscopy (**EDX**) (image size 47x35 µm, 10 kV, 2 detectors, MERLIN, Zeiss, Germany) are used to identify Ag and AgCl regions and quantify their ratio at the electrodes surface. EDX mapping is performed at different time of CP measurements: before applying the current, halfway through the reaction (at 1 V), and after complete consumption. Selected analyzed elements are silver, chlorine, carbon and oxygen to not only identify elements of interest but also potential polymer regions and oxidized compounds. Silver and silver chloride colors were equally enhanced to better discriminate each region.

New electrodes (**Figure 68**) distinctly show the shape and distribution of Ag (red) and AgCl (green) particles at the surface. The organic content of the screen-printing ink is partly present (blue) but does not encapsulate metallic particles. Quantifications of silver and chlorine elements allow to calculate the proportions of Ag and AgCl on the selected window.

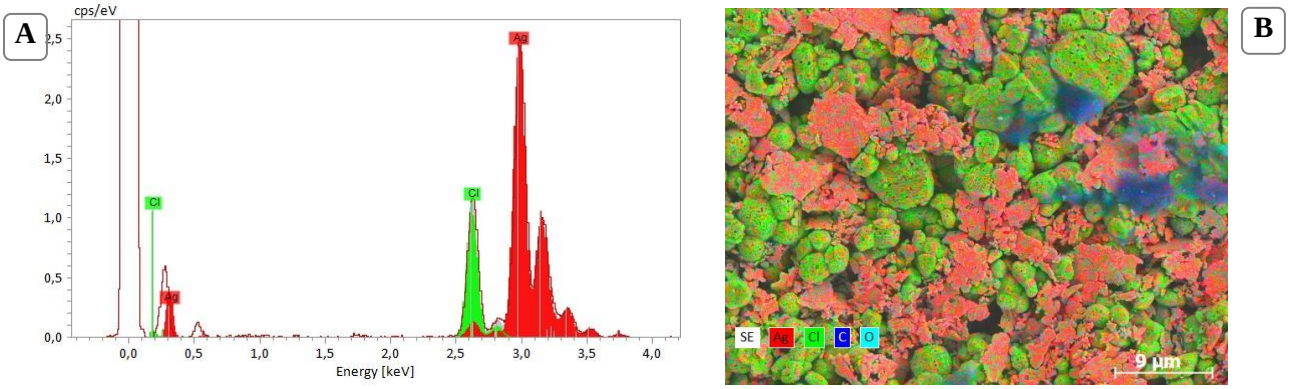

Figure 68. EDX (A) Spectrum and (B) Map (x2.5k magnification) of the electrode surface before consumption. Label: silver (red), silver chloride (green), organic content (dark blue)

EDX quantifications of Ag/AgCl on cathode and anode are summarized on **Figure 69**. Before the redox reactions start, both electrodes have an Ag/AgCl atomic ratio of 63:37 available on their surface. At the end of the reaction, as theoretically expected, the amount of silver increases at the cathode and decreases at the anode while the amount of silver chloride evolves reversely. However, it is not possible to identify the limiting compound based on this technique as around 20% of the reagents seem available on each side after reaction.

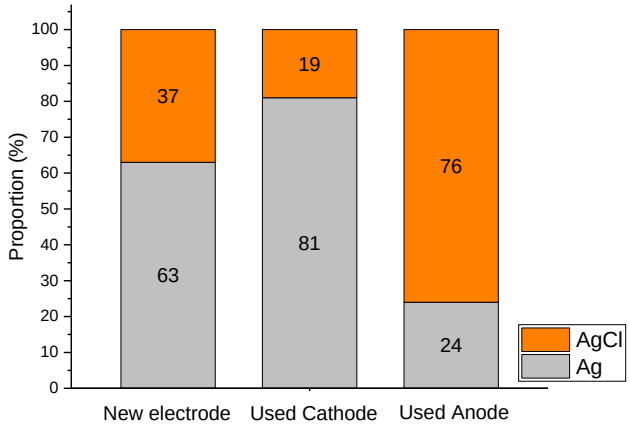

Figure 69. Evolution of silver (gray) and silver chloride (orange) proportions on used electrodes compared to a new electrode (starting composition of both electrodes) based on EDX quantifications

EDX maps are used to better understand why Ag/AgCl reactions stop while, a priori, reagents are still available on both sides. Used anodes (**Figure 70**) show indeed a progressive passivation of the electrode with AgCl (green). **Figure 70A** shows that in the middle of the reaction, Ag particles (red) are still present in between AgCl (green) aggregates. However, at the end of the reaction, only small Ag particles are available at the surface but they do not seem to be part of the electrical circuit. These particles are therefore counted in the quantitative results while they actually cannot participate to the reaction.

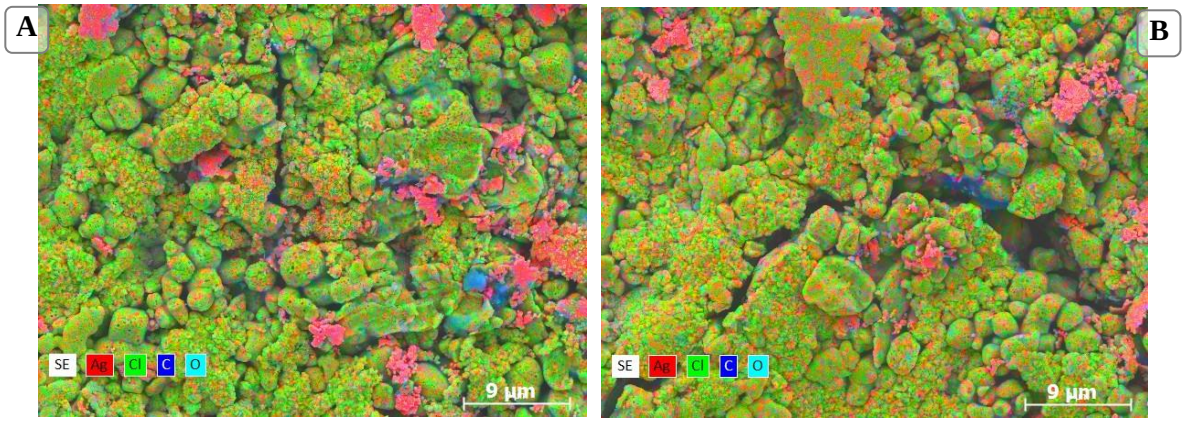

Figure 70. EDX map on (A) partly and (B) completely used anodes (x2.5k magnification)

Similarly, used cathode (**Figure 71**) show a progressive dechlorination. This time, AgCl is still available in between Ag particles while the reaction occurs (**Figure 71A**), but also at the end of the reaction

(**Figure 71B**) unlike the previous case. AgCl aggregates are still trapped in the structure yet accessible for the electrolyte to pursue the reaction.

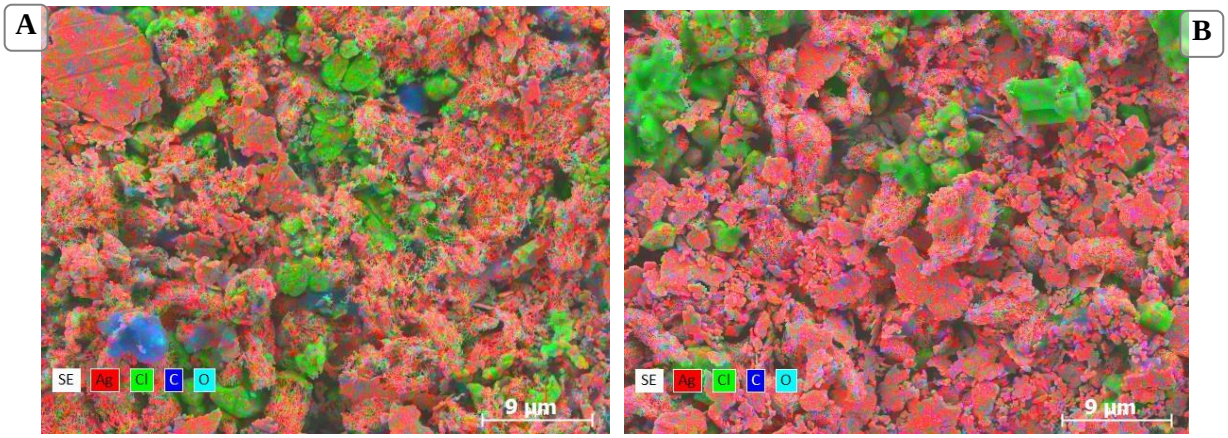

Figure 71. EDX map on (A) partly and (B) completely used cathodes (x2.5k magnification)

Learning from mistakes 🔍

EDX mapping shows the evidence that the presence of a compound at the surface of the electrode does not imply its ability to electrochemically react. In this case, the remaining Ag particles are not bound to the rest of the network while AgCl ones still look available to react.

This phenomenon could be explained by observing the silver structure produced at the cathode (**Figure 72**). Reduction of silver chloride implies the liberation of free chloride ions, thus leaving dendritic silver. This porous structure allows the electrolyte to penetrate deeper and to continue the reaction until using all of the AgCl particles available at the cathode. A bigger amount of reagent is therefore available at the cathode than at the anode that is only consumed at the surface.

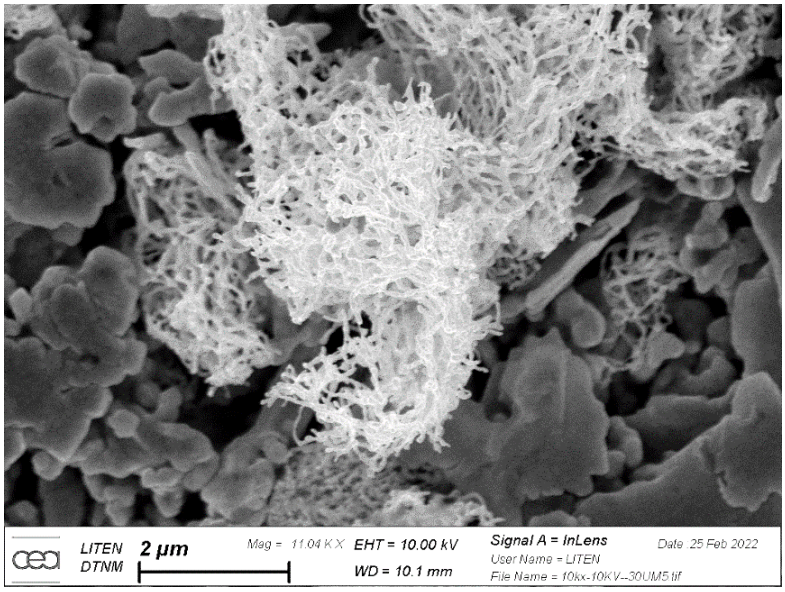

Figure 72. SEM image (x11k magnification) of a used cathode showing the formation of dendritic silver

To remember 🗣

The oxidation of Ag to AgCl at the anode implies a deposition of an additional layer on top of the electrode, blocking the access to the rest of the reagents. At the cathode on the other hand, the reduction of AgCl to Ag implies the release of chloride ions, leaving a porous Ag structure enabling the reaction to proceed further down the active layer. The anode is then most likely to limit the reaction and cause undesired water oxidation.

To validate the hypothesis that Ag is the limiting reagent in this system, the cathode is slightly modified to provide respectively more and less AgCl than the standard system.

- In the first case, a used Ag-rich cathode is chlorinated in a $FeCl_3$ solution forming AgCl aggregates all over the surface of the electrode as shown on **Figure 73**.

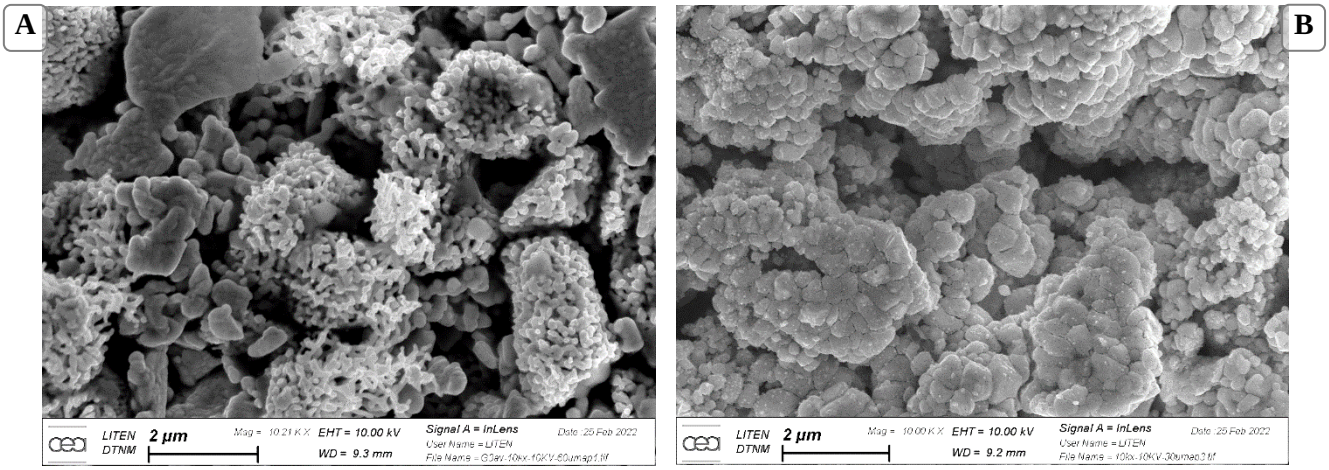

Figure 73. SEM image (x10k magnification) of a used cathode (A) before and (B) after chlorination with $FeCl_3$

- In the second case, the cathode surface is reduced to a diameter of 5 mm using a perforated adhesive sheet (MicroAmp Clear Adhesive Film, Thermo Fisher Scientific, MA, USA).

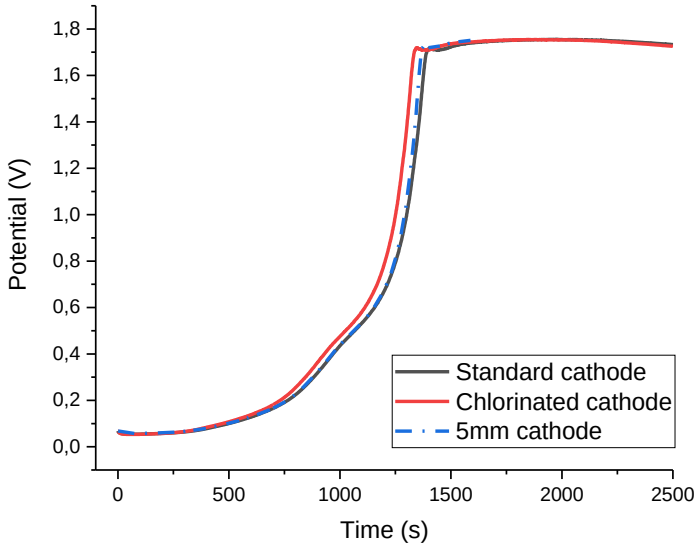

Figure 74. CP measurements using three different cathode configurations

Figure 74 shows that these modifications have a negligible impact on the CP curve profile and hence electrode lifetime.

To remember 💡

In this configuration, the cathode size and composition have a limited impact on the electrodes lifetime. We can therefore assume that Ag (anode side) limits the sacrificial reactions, considering this specific electrode geometry, layer thickness and Ag/AgCl ink ratio.

To improve electrodes performances, further modifications are proposed to increase silver availability.

3.3.5. How to improve electrodes lifetime?

In this part, different techniques are studied in order to increase electrode lifetime, i.e. to delay as much as possible water electrolysis, without impacting drug diffusion efficiency. Modifying the current density is therefore not considered as an option, even though it will obviously decelerate the electrochemical reactions involved.

3.3.5.1. Increasing the proportion of silver

As silver is identified as the limiting reagent, increasing the proportion of silver is the most intuitive option to lengthen electrodes lifetime. A 65:35 Ag/AgCl ink is used to verify this hypothesis compared to the previously used 30:70 ratio ink (according to data sheets). CP measurements indeed show that the electrodes lifetime is almost multiplied by 3 (**Figure 75**). Silver is however still limiting the reaction as an increase in AgCl at the cathode (65:35 at the anode, 30:70 at the cathode) does not affect the results.

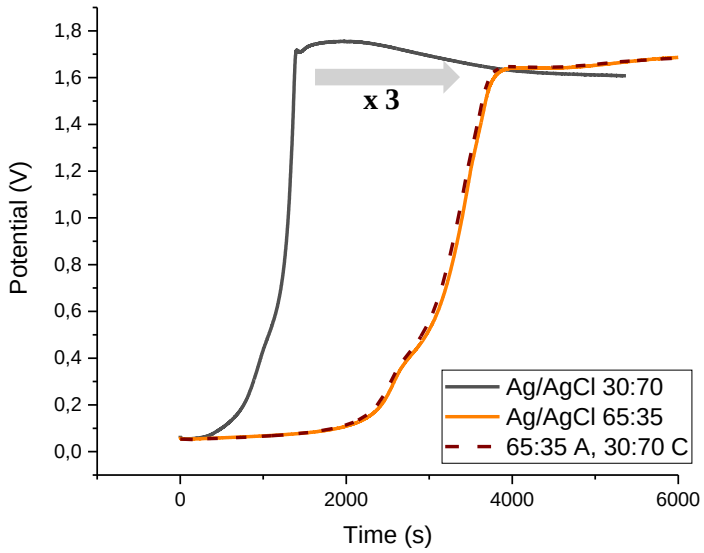

Figure 75. Lifetime comparison of two Ag/AgCl inks with a 30:70 ratio (black) and 65:35 ratio (orange) and their combination (Ag-rich anode, AgCl-rich cathode, dashed line)

Learning from mistakes 🔍

Ideally, a pure silver anode should be used to maximize the electrode lifetime. CP results however showed a lower performance due to the fact that none of the pure Ag ink available were described as "ITP-grade". These differences can be due to Ag particles availability at the surface that is reduced if encapsulated in the polymer resin.

To further increase silver concentration and surface roughness, a sample of the 65:35 ITP-grade ink has been doped with 6.5 wt% of a 20 wt% silver **N**ano**W**ires (**NW**) solution in **I**so**P**ropyl **A**lcohol (**IPA**). Counter-productive results are obtained on CP measurements, showing an actual decrease in lifetime (**Figure 76A)**.

SEM images of **Figure 76B and C** show that NW are hardly visible at the surface and bring a negligible amount of surface structure compared to the microstructure of the screen-printing ink. In fact, despite increasing silver concentration, NW may fit into the ink micropores and reduce the active surface area. The screen-printing process may also impact the direction of the wires as they are printed with a high squeegee pressure forcing the structure to lay in the plane of the substrate instead of being oriented in all directions.

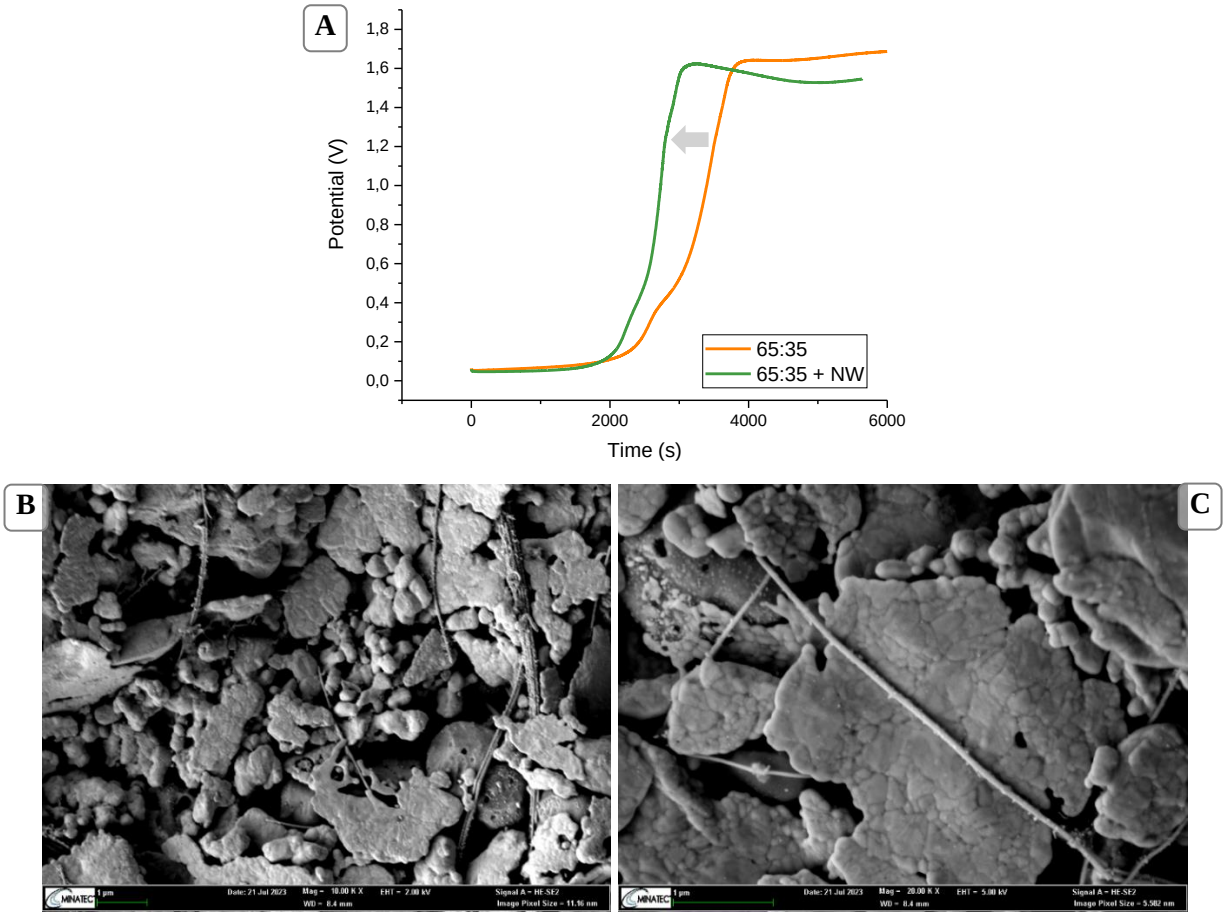

Figure 76. (A) CP profiles with and without the addition of silver NW, (B) 10k and (C) 20k magnification of SEM images of the surface of the electrodes doped with 2w% silver nanowires (NW) (Pictures by Y. Thomas)

To remember ❗

Silver nanowires have been added to the initial formulation to increase the proportion of Ag as well as particles surface area, but lower electrodes performances are recorded. Actually, the opposite effect happens: because of the scale difference between NW and ink microparticles, NW possibly fill the gaps in the matrix instead of increasing surface roughness.

Even though this aspect is not further explored in this thesis because of time constraints, the limited number of commercial Ag/AgCl inks available for ITP encourages homemade formulations. They could help optimizing electrochemical availability of particles and providing a stoichiometric amount of both reagents to avoid metallic waste.

3.3.5.2. Changing the electrode design

A second electrode design is suggested with grid-shaped conductive layer providing 500 µm wide cavities (**Figure 77**).

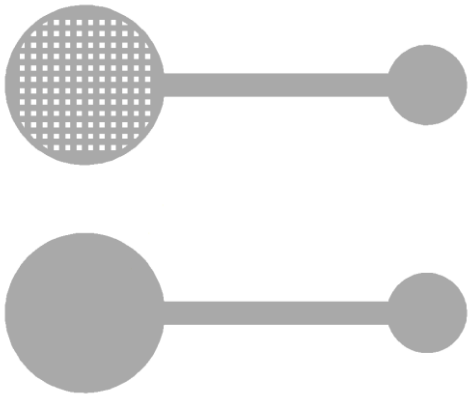

Figure 77. Grid-shaped conductive layer (up) compared to plain standard conductive layer (down)

Initially, this design is suggested to improve current distribution at the surface of the electrodes. This aspect will be discussed in the following chapter with the help of numerical simulations.

Another benefit that the grid-shape could provide is to create more surface roughness and therefore increase active surface area. As the numerical model discussed in Chaper 4 does not take into account this feature, this assumption is verified experimentally.

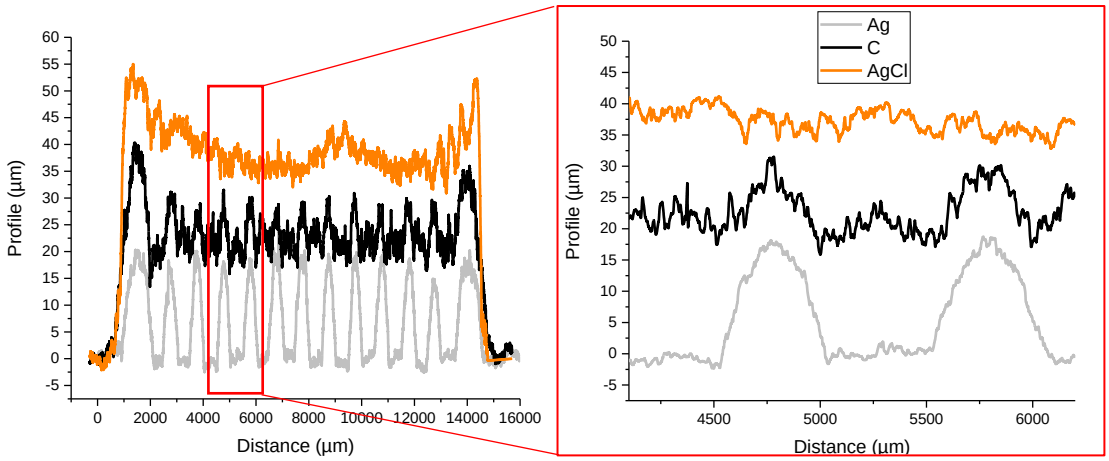

Figure 78. Profilometry measurements on each layer of the grid-shaped electrodes. Label: Ag in gray, Carbon in black, AgCl in orange

We can legitimately expect the grid-shaped geometry to have an influence on the following layers printed on top.

Figure 78 shows however that the grid silver layer indeed changes the shape of the carbon layer (black), but does not have a significant impact on the Ag/AgCl layer (orange). This phenomenon can be due to the fact that layers deposited by screen-printing are too thick for the grid-shape to affect the surface layer. A solution would be to change the mesh or the process to deposit only a thin layer of carbon spacer to increase the active AgCl surface, or to increase the grid size. These suggestions will be verified numerically in the following chapter.

The fact that the active surface area remains similar is consistent with CP measurements in **Figure 79B** showing no difference in electrodes lifetime with and without the grid. Used electrodes presented on **Figure 79A** show a homogeneous consumption of the surface at the macroscopic level.

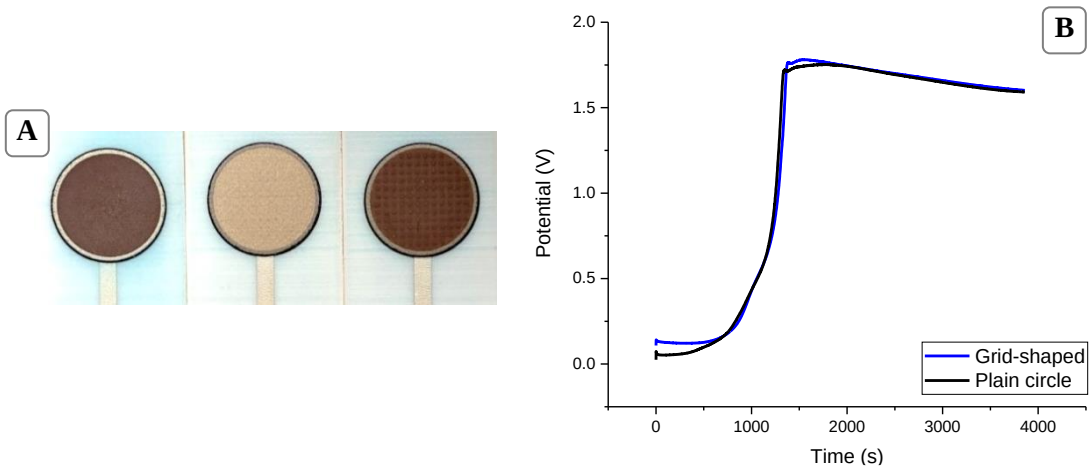

Figure 79. (A) Picture of a new (middle), used plain (left), used grid-shaped (right) electrodes. (B) Chronopotentiometry measurements on plain (black) and grid-shaped (blue) electrodes

We can however notice that a slight grid design appears at the surface once the electrode is consumed. This observation could suggest that the reaction occurs preferably around the cavities of the grid, or that local hot spots are created at the surface. Once again, the next chapter will help improving our understanding of the current distribution at the surface of the electrodes.

To remember 💡

Changing the geometry of the conductive layer could help creating more roughness at the surface, thus increasing the active surface area and the access to reagents. A grid-shaped conductive layer is used in this regard, but only having a negligible effect on the uppermost layer.

We can also point out that even though the potential at the beginning of the reaction is higher in the grid-shaped configuration, it does not affect electrodes performances despite the use of less material on the conductive layer because of grid cavities. Such optimization could help saving metallic materials whose demand is increasing every year (DiRienzo and Newman, 2023).

3.3.5.3. Using a pulsed current (pulsed DC)

Another option to improve electrodes lifetime is to avoid a continuous consumption of the reagents. Pulsed currents of 0.1 Hz are therefore compared to previously used DC, with a 1 mA magnitude applied every 10 seconds (**Figure 80A, blue**). CP results on **Figure 80B** confirm that the use of this "on and off" signal almost doubles the lifetime of the electrodes. Another experiment is performed at 1 Hz with comparable lifetime values (data not shown). Higher frequencies should be applied to verify if the performances could be further enhanced, but data could not be saved above 1 Hz because of the high number of points recorded in potentiometric monitoring. Such signals could be easily used for stimulation purposes like drug delivery though, as the potential does not need to be precisely monitored if the electrodes lifetimes are well defined prior to use. A potential threshold would be enough to ensure patients safety.

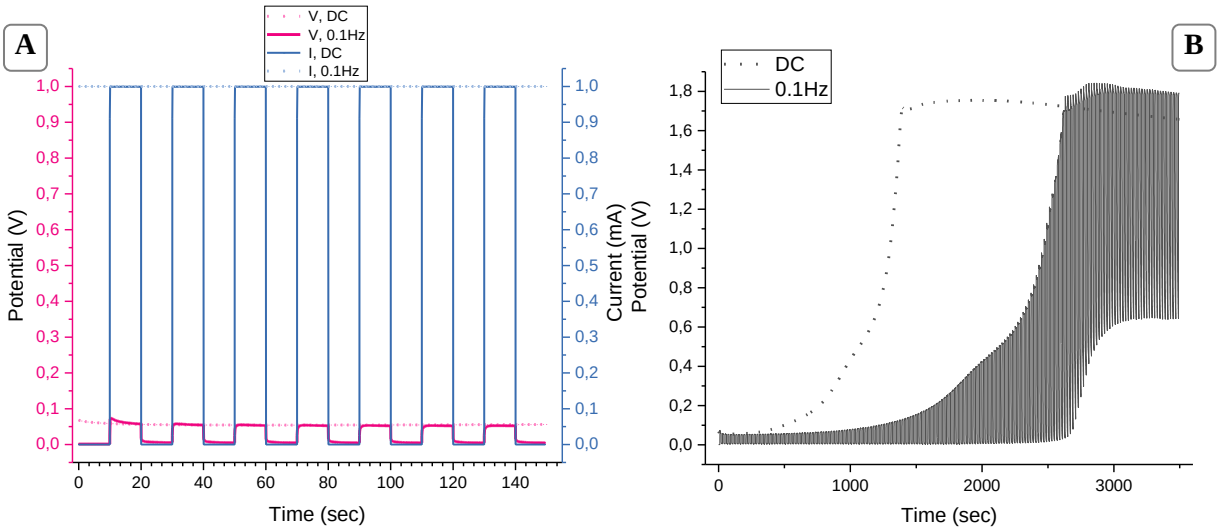

Figure 80. (A) First 150 seconds of a pulsed CP measurement and associated current applied at 0.1 Hz compared to DC (dotted lines). Label : Currents in blue, measured potentials in pink. (B) Full CP measurement

To remember

CP experiments show a noticeable improvement on electrodes lifetime at low frequencies (0.1 Hz). The input signal is therefore a key parameter to choose in order to avoid skin burns with iontophoretic devices.

We can argue that the alternating nature of the electric signal has a similar impact than reducing the current in DC as it reduces charge transfer for the electrochemical reaction of interest, and thus the diffusion speed of charged species. We need to keep in mind though that the target molecules to deliver are biomolecules, which have a significant mass. Their diffusion is therefore slow enough compared to the variation of the current that will affect the electrochemical consumption of the electrodes without interfering with the drug diffusion speed. This reasoning can possibly explain why some studies have noticed no significant difference between AC and DC iontophoresis at frequencies below 10 kHz (Bagniefski and Burnette, 1990; Harden and Viovy, 1996).

3.3.5.4. Recycling electrodes by changing their polarity

Surface analyses previously shown (3.3.4) prove the enrichment of AgCl at the anode and Ag at the cathode by the end of the reaction, which is characteristic of this reversible redox couple. Such compositions seem ideal for ITP electrodes, except that anode and cathode need to be reversed.

Positive and negative poles have therefore been switched after the first consumption, and CP measurements on **Figure 81** show a significant increase in lifetime in the second measurement (1rst

switch, in brown). The process is repeated multiple times, but the lifetime starts to decay after the second switch. The potential at the plateau also reduces from 1.7 to 1.2 V. This phenomenon may be due to the degradation of the electrodes surface causing water electrolysis to occur on the carbon layer if the reactions are thermodynamically more favorable than on silver or silver chloride. If this assumption is true, polarities cannot be changed forever as the electrode layers progressively degrade.

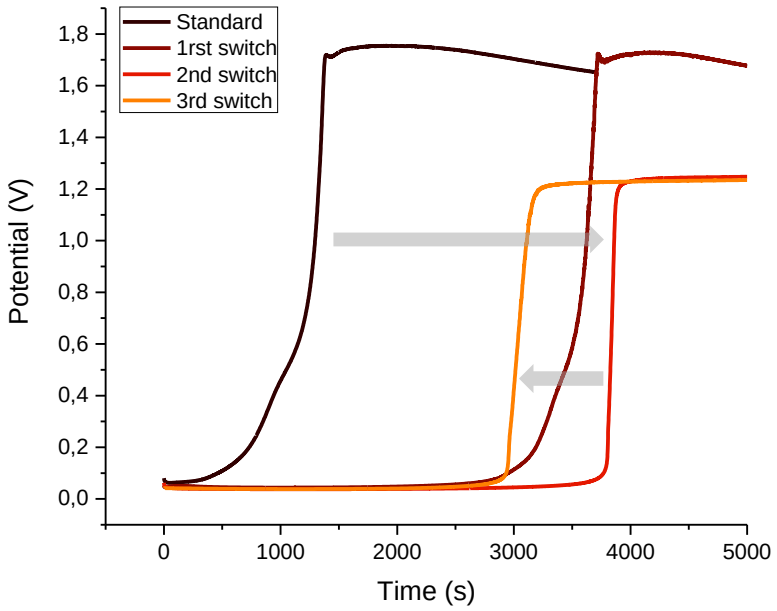

Figure 81. CP measurements of the standard configuration followed by 3 polarity inversion (or switch)

These results however show that the electrodeposition of Ag and AgCl as a consequence of the first current application (Standard) is beneficial to the system as long as a threshold potential is set. On an applicative point of view, this information can be used in two ways:

- As the electrode lifetime is almost tripled after the first switch, we can imagine an iontophoretic device that could be **activated prior to use** with the application of a current in the opposite direction of the drug to deliver. Once activated, polarities can be changed and the electrodes can be used once, but with enhanced performances (**Figure 82**).

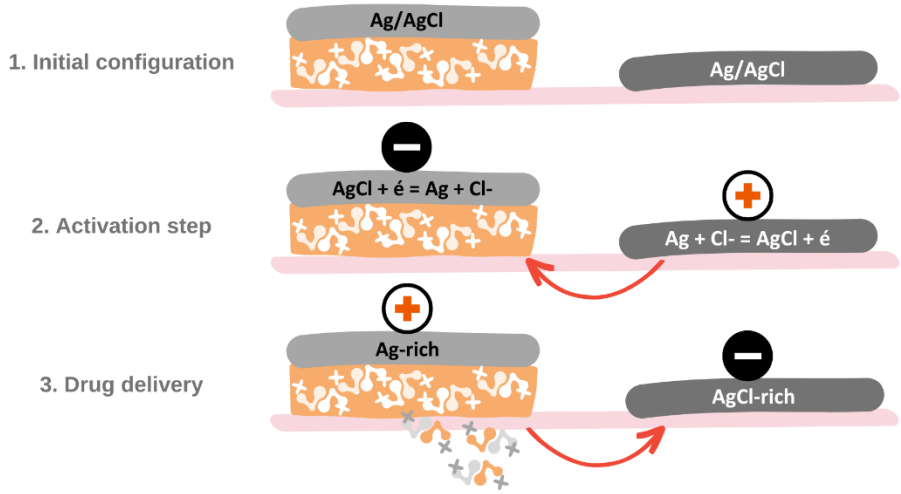

Figure 82. Pre-activated electrodes configuration

- Another option would be to take advantage of this reversible behavior by re-using the device multiple times. This recycling could not be infinite though, due to possible material degradation and performance loss as mentioned above. If properly controlled, such iontophoretic device could be installed with a reservoir under each electrode, and deliver the desired drug from one side or the other by switching their polarity once consumed (**Figure 83**). Not only it leads to a more performant device that can be worn for a longer period of time, but it also reduces materials waste as the delivery stops either when no more drug is to delivered in the reservoirs, or when the electrodes are no longer usable.

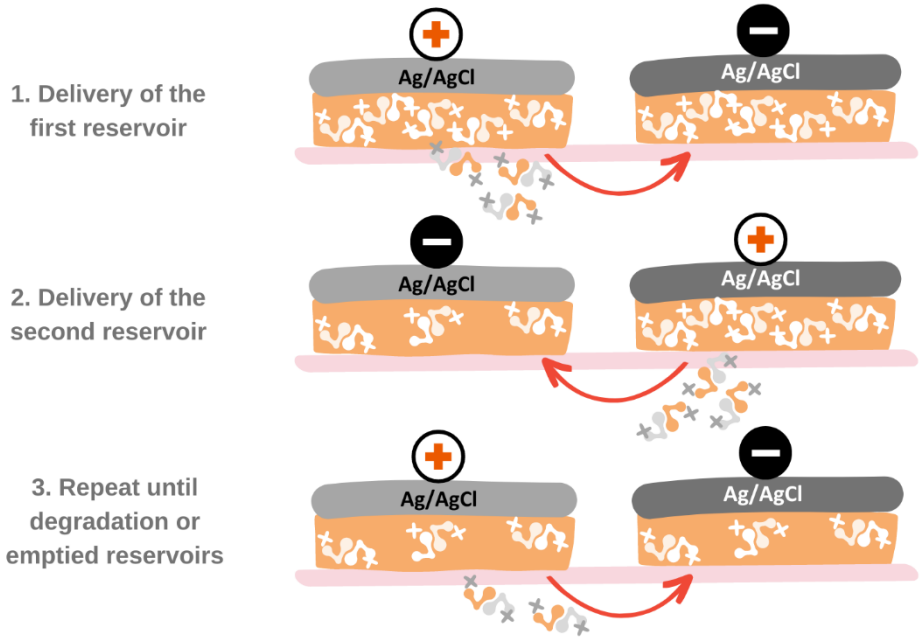

Figure 83. Two-reservoir configuration

To remember 🔔

Thanks to the reversible properties of the Ag/AgCl redox couple, electrodes can be re-used multiple times before starting to degrade. This feature allows to develop smarter systems that go beyond the single-use electrodes initially considered.

Conclusion

This chapter focuses on the fabrication and characterization of screen-printed Ag/AgCl ITP electrodes.

- Surface analyses (SEM/EDX) confirmed the redox equations involved and the formation of a passivation layer at the anode. Silver could be identified as the limiting reagent in these conditions as this layer blocks the access to the remaining Ag underneath. At the cathode though, AgCl remains accessible throughout its consumption thanks to the dendritic structure of the reduced Ag.
- The passivation layer could also be identified using EIS, as the impedance spectra differ before and after consumption with both an increase in resistance at high frequencies and capacitance at low frequencies.
- CP is presented as a useful tool to estimate electrodes lifetime and compare different configurations to identify parameters that may increase their performances. Different solutions are proposed such as using a silver-rich anode, increasing roughness, using a pulsed signal, pre-activating the electrodes or alternating between the two poles with two drug reservoirs.

To improve our understanding of these multilayered Ag/AgCl electrodes and have a closer look at local electrical phenomena, numerical simulations can be used to spatially visualize the current distribution within each layer of the stack and at the electrode/electrolyte interface.

CHAPTER 4

Chapter 4: Numerical simulations

Introduction

In this chapter, numerical modeling is used to better understand the iontophoretic device on an **electrical** aspect as it allows to:

- Visualize the current density spatial distribution inside and around the electrodes, and therefore the theoretical ion electromigration trajectories
- Identify hot spots (high current density areas) potentially causing skin burns
- Suggest means to improve the currently used system and evolve towards novel geometries.

Numerical simulations are performed using the Finite Element Method (FEM) software COMSOL Multiphysics®.

The underlying numerical models will first be introduced with their associated mathematical equations and approximations. Then, the standard electrode geometries available for experimentation are compared along with different input parameters. Finally, numerical simulations are used to suggest different ways of improving the electric current distribution at the electrode surface by reducing hot spots on its periphery.

4.1. Description of the numerical model

4.1.1. Geometry

4.1.1.1. Electrode design

Ag/AgCl ITP electrodes are composed of a four-layer stack as presented in Chapter 3, 3.1. To understand their behavior when subjected to an electrical stimulus, the electrodes are designed in the model according to their real geometry, with an additional 10 nm thick layer which accounts for the Electrical Double Layer phenomena at the electrode/electrolyte interface for the specific case of metallic surface in contact with PBS (PHAM ET AL., 2013).

Finally, a 20 µm radius of curvature is added to the edges of each layer to avoid sharp peaks and properly mimic screen-printing depositions. For illustration purposes only, a dilatation factor is used in the normal direction to visualize the stack in a cross section as on **Figure 84**.

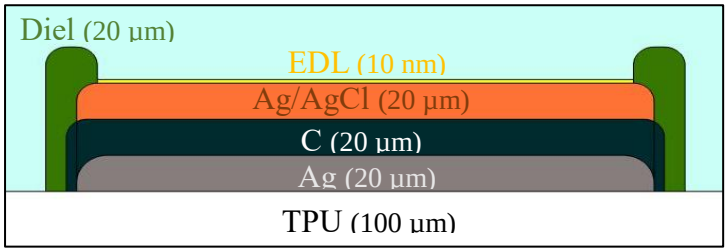

Figure 84. Schematic representation of the vertical cutplane of the electrode stack (dilatation x50) composed of Ag (gray), C (black), Ag/AgCl (orange), insulator (green) and the interfacial EDL (yellow, dilatation x10000) in PBS (light blue)

To correlate experimental results with numerical simulations, the same electrochemical system as depicted in Chapter 3 (3.3) will be considered in the model. Only the reference electrode is not represented as it is used as a reference potential throughout the electrochemical consumption of the anode that is not considered in the numerical model. Electrodes are therefore placed face-to-face at a working distance of 2 cm in a beaker filled with phosphate-buffered saline (PBS) 1X (**Figure 85**). In the final part of the chapter, electrodes geometry and relative positions will be questioned.

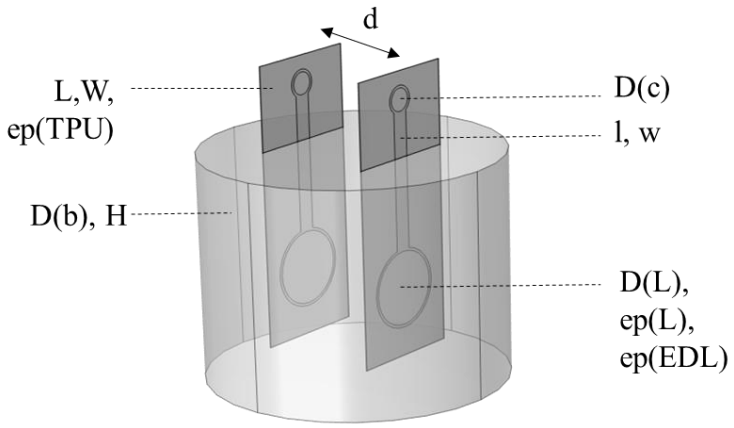

Figure 85. 3D geometry of the numerical model parameters annotations for Ag/AgCl ITP electrodes according to the experimental setup

All the geometrical parameters involved are summarized in **Table 5**.

Table 5. Geometrical parameters used in the model

Parameter	Details	Name	Value [Unit]
Diameter	Electrical contact	D(c)	5 [mm]
	Beaker	D(b)	5 [cm]
	Layer 1 and 3	D(L1,L3)	14.5 [mm]
	Layer 2	D(L2)	15 [mm]
Distance	Track length	l	20 [mm]
	Track width	w	3 [mm]
	Substrate length	L	5 [cm]
	Substrate width	W	2 [cm]
	Beaker height	H	4 [cm]
	Electrodes interspace	d	2 [cm]
Thickness	Layer 1	ep(L1)	20 [µm]
	Substrate (TPU)	ep(TPU)	100 [µm]
	Layer 2	ep(L2)	20 [µm]
	Layer 3	ep(L3)	20 [µm]
	Layer 4	ep(L4)	20 [µm]
	EDL (order of magnitude)	ep(EDL)	10 [nm]

In a second stage, grid-shaped electrodes are implemented to the model with 500 µm cavities to compare both structures (**Figure 86**).

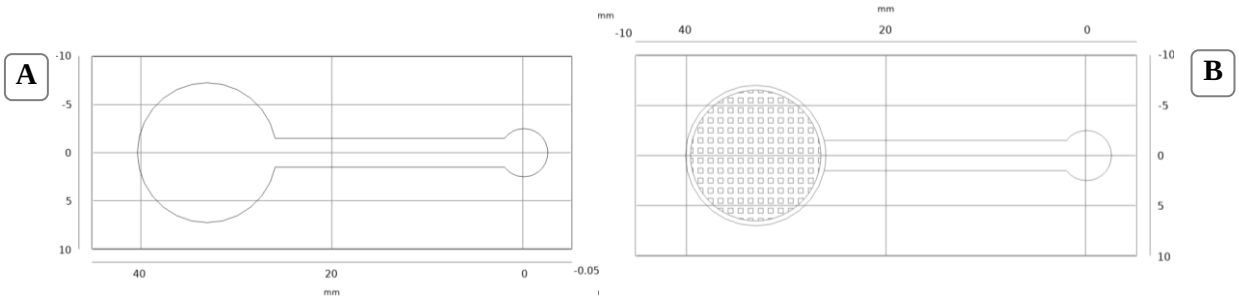

Figure 86. Design of the (A) standard and (B) 500 µm grid-shaped conductive layer

4.1.1.2. Optimization of computation time

Despite its appearance, the 3D geometry is very complex and hard to mesh as the domains involved have different order of magnitudes of sizes: nanometric (EDL thickness), micrometric (screen-printed layers thickness) and centimetric (electrode surface and beaker size) (**Figure 87**):

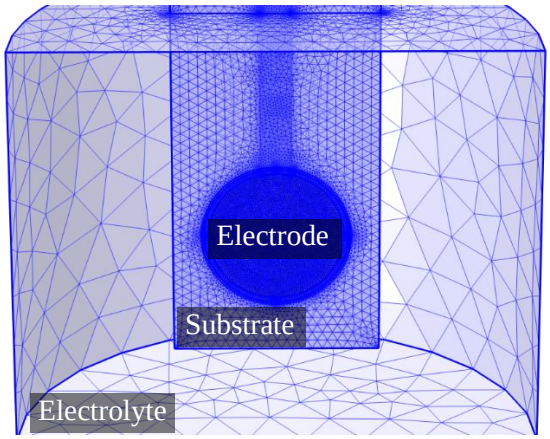

Figure 87. Mesh difference depending on the domain size

Two techniques are used to overcome this dimensional problem:

- The "thin layer" function available in the software is used for modeling the EDL and the screen-printed layers to avoid meshing their thickness.

Definition 🕮

*The **thin layer** physics interface defines a virtual thickness to a 2D-object* (COMSOL DOCUMENTATION). *While the thickness is taken into account in the computations, it does not appear on the geometry.*

- Computations are performed on the half-geometry (**Figure 88**), which accounts for the antisymmetry plane of the system.

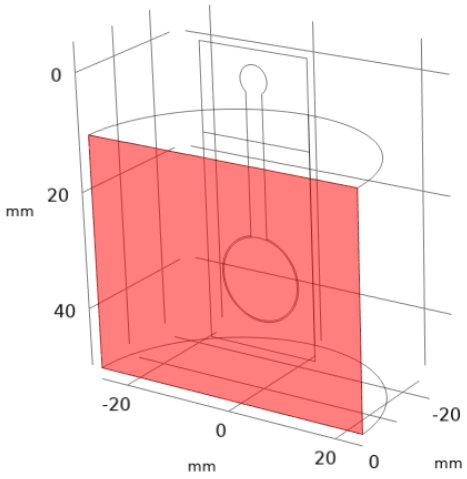

Figure 88. Half-geometry used for 3D-computations (antisymmetric plane in red)

Definition 🕮

*An **antisymmetry plane** is the plane along which the dependent variable (in this case, the electric potential V) is equal to zero. Results on the rest of the geometry are oppositely balanced on either side of this plane* (COMSOL LEARNING CENTER).

These adjustments allow the 3D numerical simulations to be computed in around three hours.

4.1.2. Mathematical model

4.1.2.1. Electrokinetic equation

The mathematical model focuses on the electrical behavior of the iontophoretic system. The starting point of the demonstration is current conservation in the computational domain (**Equation 16**).

$$\vec{\nabla} \cdot \vec{J} = 0 \tag{16}$$

The current density $\vec{J}$ (A·m^{-2}) can be described as the sum of conduction and displacement current densities, namely $\vec{J}_C$ and $\vec{J}_D$, that are both correlated with the electric field $\vec{E}$ (V·m^{-1}) (**Equation 17**):

$$\vec{J} = \vec{J}_C + \vec{J}_D = \sigma\vec{E} + \varepsilon\frac{\partial\vec{E}}{\partial t} \tag{17}$$

$\vec{J}_C$ is defined by Ohm's law and describes the displacement of free electric charges in conductive materials while $\vec{J}_D$ is associated with bonded charges in dielectrics depending on the time variations of the electric field. The latter contribution is considered in the model, as alternating currents of different frequencies (f, Hz) are taken into account in the following numerical simulations.

The previous expression can be simplified (**Equation 19**) using the complex electrical conductivity σ^* as a function of electrical conductivity σ (S·m^{-1}), dielectric permittivity $\varepsilon = \varepsilon_0\varepsilon_r$ (ε_0 the permittivity of free space and ε_r the relative permittivity) and angular frequency $\omega = 2\pi f$ (rad·s^{-1}) (**Equation 18**).

$$\sigma^* = \sigma + i\omega\varepsilon \tag{18}$$

$$\vec{J} = \sigma^*\vec{E} \tag{19}$$

Besides, the electric field $\vec{E}$ can be expressed as a function of **electric potential V** (V) (**Equation 20**), which is the **unknown parameter in the computational domain** allowing a spatial representation of the current density $\vec{J}$ (**Equation 21**) responsible for ionic electromigration as described in Chapter 1, **1.2.1.1** .

$$\vec{E} = -\vec{\nabla}V \tag{20}$$

$$\vec{J} = -\sigma^*\vec{\nabla}V \tag{21}$$

Finally, the current conservation can be written as the complex Electrokinetic equation implemented in the software (**Equation 22**):

$$\vec{\nabla} \cdot \vec{J} = \vec{\nabla} \cdot \left(-\sigma^*\vec{\nabla}V\right) = 0 \tag{22}$$

Considering the electrical parameters involved in these equations, the main information to advise to the model are therefore the electrical conductivity and dielectric permittivity values for each material. All the parameters are summarized in **Table 6**, such that:

- Conductivies of conductive inks (Ag, C, Ag/AgCl) are acquired by four-pin probe measurements as previously described in Chapter 3, 3.2.2,
- Permittivity of dielectrics (insulator, substrate) are given by supplier data sheets and literature reviews,
- Arbitrary values are given for the conductivities of dielectrics and dielectric constant of conductive inks as both are expected to be negligible in the computations,
- The order of magnitudes of EDL parameters are chosen according to the model developed by PHAM ET AL., 2013 based on EIS measurements on platinum electrodes in saline solution. Values are then adapted to EIS measurements on Ag/AgCl electrodes studied to fit numerical and experimental curves.

Table 6. Physical parameters used in the numerical model

Parameter	Details	Value [Unit]
Input signal	Voltage between WE and CE	10 [mV]
Capacitance (C)	EDL (order of magnitude)	3 [$F \cdot m^{-2}$]
Electrical conductivity	Ag ink	$1.96 \cdot 10^{7}$ [$S \cdot m^{-1}$]
	C ink	$2.25 \cdot 10^{3}$ [$S \cdot m^{-1}$]
	Ag/AgCl ink	$1.14 \cdot 10^{5}$ [$S \cdot m^{-1}$]
	Insulator ink (arbitrary)	$1 \cdot 10^{-6}$ [$S \cdot m^{-1}$]
	TPU substrate (arbitrary)	$1 \cdot 10^{-6}$ [$m \cdot S^{-1}$]
	Electrolyte	18.45 [$mS \cdot cm^{-1}$]
	EDL (order of magnitude)	$2.5 \cdot 10^{-7}$ [$S \cdot m^{-1}$]
Dielectric permittivity	Ag ink (arbitrary)	1
	C ink (arbitrary)	1
	Ag/AgCl (arbitrary)	1
	Electrolyte	78
	Insulator ink (datasheet)	4.4
	TPU substrate (literature)	6
	EDL (order of magnitude)	$(C(EDL) \cdot ep(EDL))/\varepsilon_0$

4.1.2.2. Boundary conditions

Two types of boundary conditions are considered in the model and are shown on **Figure 89**:

- Dirichlet boundary conditions are applied on:
  - the electrode, as it is connected to the potentiostat : V = $V_0/2$ = 5 mV,
  - the antisymmetry plane, which is equidistant from both electrodes: V = 0 V.
- Neumann boundary conditions are applied on the peripheries (boundaries) of the rest of the geometry to mimic their insulation character :

$$-\sigma^*\vec{\nabla}V \cdot \vec{n} = \vec{J} \cdot \vec{n} = 0 \quad (23)$$

Where $\vec{n}$ is the unit vector normal to the concerned boundary.

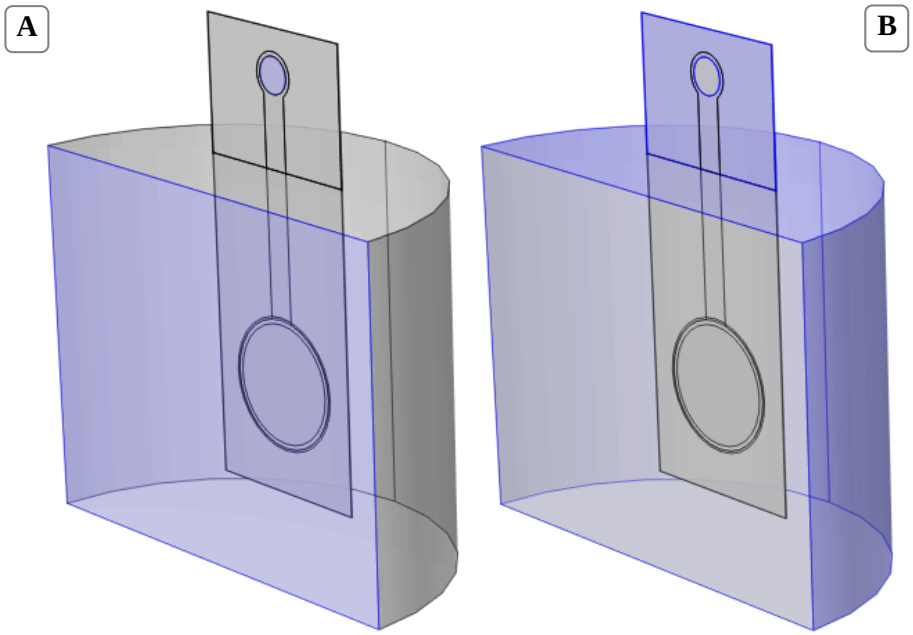

Figure 89. Blue highlights of (A) Dirichlet and (B) Neumann boundary conditions

4.1.3. Resulting numerical model

4.1.3.1. Current conservation

The first step towards the validation of the numerical model is to check the mesh discretization. To do so, we compare the total electrical current entering and leaving the computational domain.

The total current I (A) is computed as follows:

$$I = \oiint \vec{J} \cdot \vec{n}\, dS \quad (24)$$

Where S is the surface (m²) of the electrical contact where the input signal is applied (working or positive electrode), or the output signal leaves the circuit (antisymmetry plan).

.

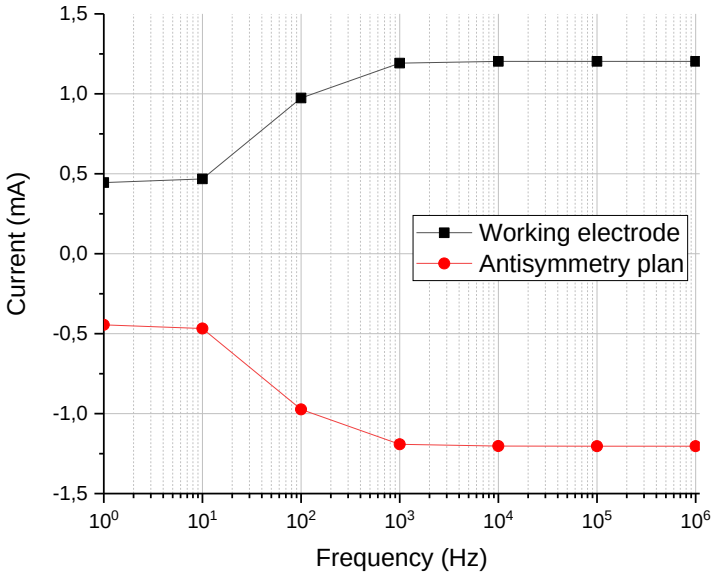

Figure 90. Current values entering (working electrode) and leaving (antisymmetry plan) the computational domain

Figure 90 confirms that the current that enters indeed leaves the system, so the selected mesh is fine enough to provide reliable computations.

4.1.3.2. Numerical and experimental impedance spectra

Despite the geometrical similarities with the real geometry, the numerical model should be first validated by comparing numerical and experimental results. Electrochemical impedance spectroscopy (EIS) is used in this regard. Like in the previous chapter, only Bode diagrams are considered as they clearly show the frequency dependence on the x-axis.

Experimental results are measured around the potential at rest of the system (0 V vs OCP), so no electrochemical reaction is expected to occur. A sine-wave voltage of 10 mV is applied around this potential, in a 7 MHz to 10 mHz frequency range.

Learning from mistakes 🔍

The frequency range could actually be reduced on both sides. At high frequencies, parasitic response may appear from the electronics of the potentiostat or the connectics. At low frequencies, electrochemical reactions may occur despite the small excitation amplitude. To validate the numerical model, we can only focus on the 6 MHz to 100 Hz range.

The numerical impedance spectrum can be obtained using Ohm's law applied to AC, where the impedance of the system Z is described as :

$$Z = \frac{\Delta V}{I} \tag{25}$$

Where ΔV is the applied voltage (V) and I the resulting current (A). The voltage is known from the input and output parameters (V_0) and the current is computed on both the mirror plane and the electrode electrical contact.

Numerical Bode plots are compared with experimental plots in **Figure 91.** The parameters of the EDL (thickness, electrical resistivity and capacitance) are adjusted within the orders of magnitude of the literature to fit the experimental curve profiles (PHAM ET AL., 2013). **Appendix 7** presents the influence of the variation of EDL parameters on the resulting Bode plots. This comparison step shows the significant influence of the EDL parameters on the overall impedance profile. This observation is consistent with the conclusions of SAGHAFI ET AL., 2023 on the domination of the EDL capacitance on the EIS response.

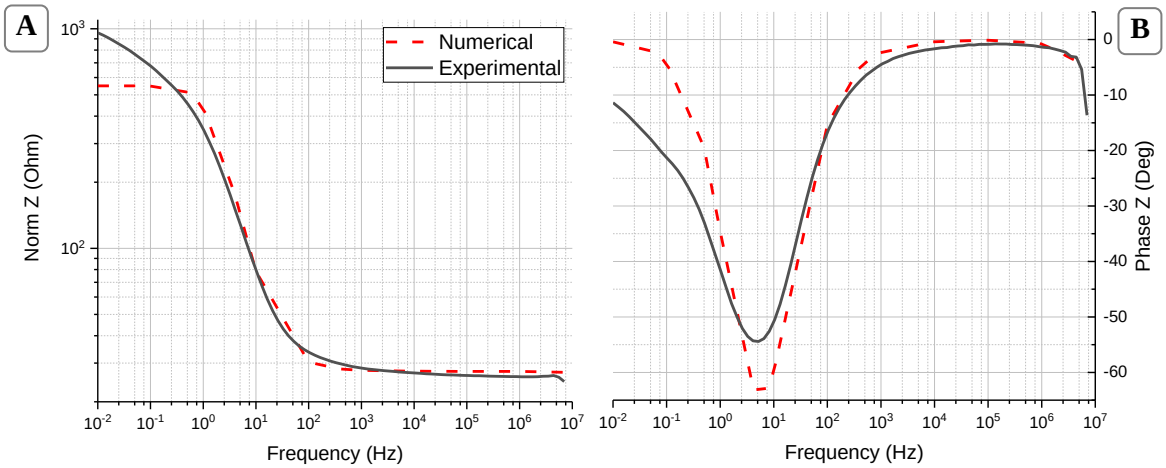

Figure 91. Bode plots of numerical (red) and measured impedance (black) of the standard Ag/AgCl electrodes in PBS

Additionally, the conductivity of the electrolyte is also adjusted by 1.5 times its initial value (12.3 mS·m^{-1}) so that the plateau above 100 Hz on **Figure 91A** matches the measurement. This difference could be due to uncertainties of measurements (during electrolyte preparation or conductivity measurement), or a change in temperature in the lab that modifies the ionic conductivity of the electrolytic solution.

To remember

A validation step is implemented by matching numerical to experimental EIS spectra. The EDL parameters have a significant impact on the EIS profile and need to be adjusted to get a good fit between simulations (red) and measurements (black).

4.2. 2D simulations

To expand the model to the grid-shape geometry previously presented (**Figure 77**), we are forced to switch to the 2D model as this complex structure cannot be represented using the thin layer interface. Such approximation is only possible because the electrodes are large enough compared to the thickness of the studied electrode stack. Both models are therefore built subsequently on the 2D plane presented on **Figure 92.**

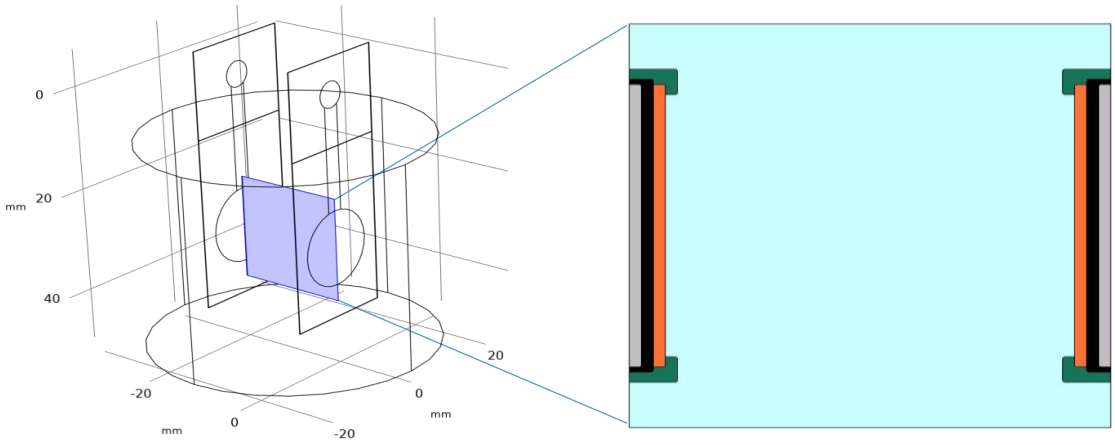

Figure 92. 2D-plane (blue) used in 2D numerical simulations. Electrode stack (right) is presented with a dilatation factor of 50.

Following results are presented in the plane (2D) or on a cut line (1D) 1 µm below the interfaces of interest (**Figure 93**).

Learning from mistakes 🔍

Computation of the current density vectors at the interface between two domains is not mathematically reliable as the material properties (σ,ε_r) are different at either side of the interface. To avoid this confusion, we look at the current density ***inside*** *the domain of interest, but close enough to the interface with the upper domain (dotted lines on* ***Figure 93****).*

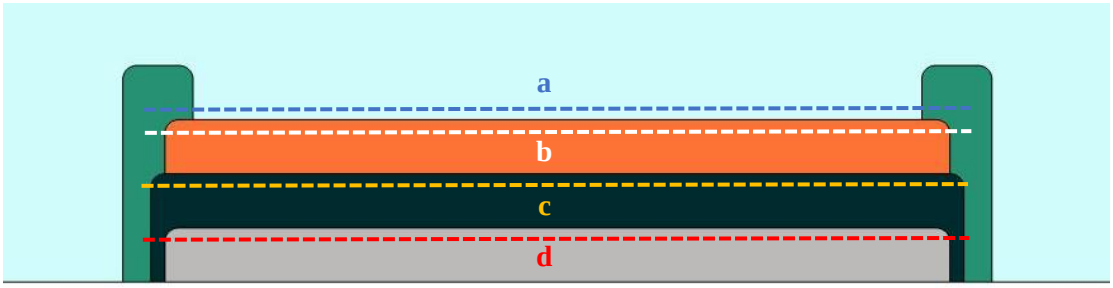

Figure 93. Schematical electrode stack (dilatation x50) with cut lines dashed in (a) PBS (b) Ag/AgCl (c) C and (d) Ag.

The following section presents and verifies different hypotheses to further simplify the model and allow numerical simulations in different configurations.

4.2.1. Working parameters

4.2.1.1. Layers

In the 2D numerical model, each screen-printed layer is represented in the geometry with their real thicknesses. The EDL is added in the model with the "Contact Impedance" function, acting as a thin layer only at the electrode/electrolyte interface.

4.2.1.2. Electrical contact

Figure 94, obtained with the 3D numerical model, shows that the input signal remains constant along the conductive Ag track and the potential is homogeneous and equal to $\frac{V_0}{2}$ at the surface of the electrode. In the 2D numerical model, the input signal is therefore applied at the bottom of the electrodes and the conductive track and contacts are no longer represented.

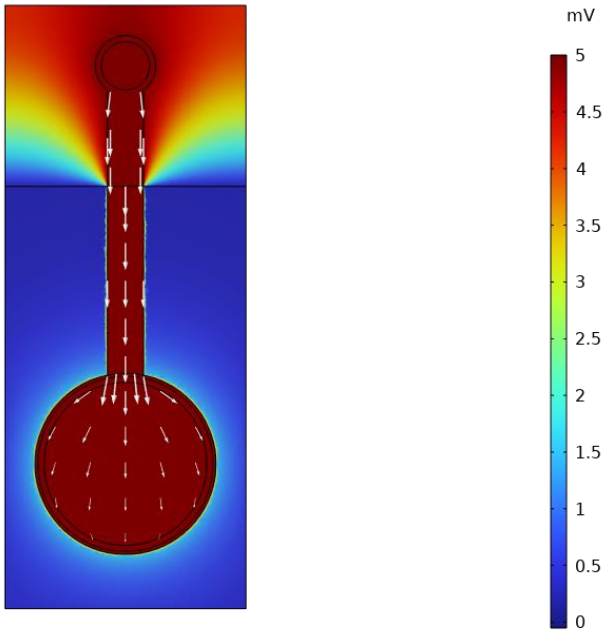

Figure 94. Potential distribution across the full electrode on the 3D model

4.2.1.3. Input signal

Nature of the applied signal

ITP is usually controlled in current to avoid electrical injuries (REILLY, 1998). However, iontophoretic delivery can occur as long as an electrical field is applied. A stimulus in potential is therefore selected in the model as it is more convenient to use and directly correlated to the current density (**Equation 21**).

Working frequencies

As ITP is most commonly used in DC, the working frequency is initially set at 0 Hz. We will later see that a DC signal does not necessarily correspond to this unique frequency.

Input value

The input voltage value is arbitrary chosen as V_0 does not affect the curve profile as shown by the results on the pink zone of the electrodes on **Figure 95**. The increase of V_0 proportionally increases the resulting current density norm. These results are obviously not realistic as **we do not take into account the electrochemical reactions** occurring in the system. A low input signal of 10 mV is therefore also maintained, allowing relative comparison of curve profiles before any chemical reaction occurs.

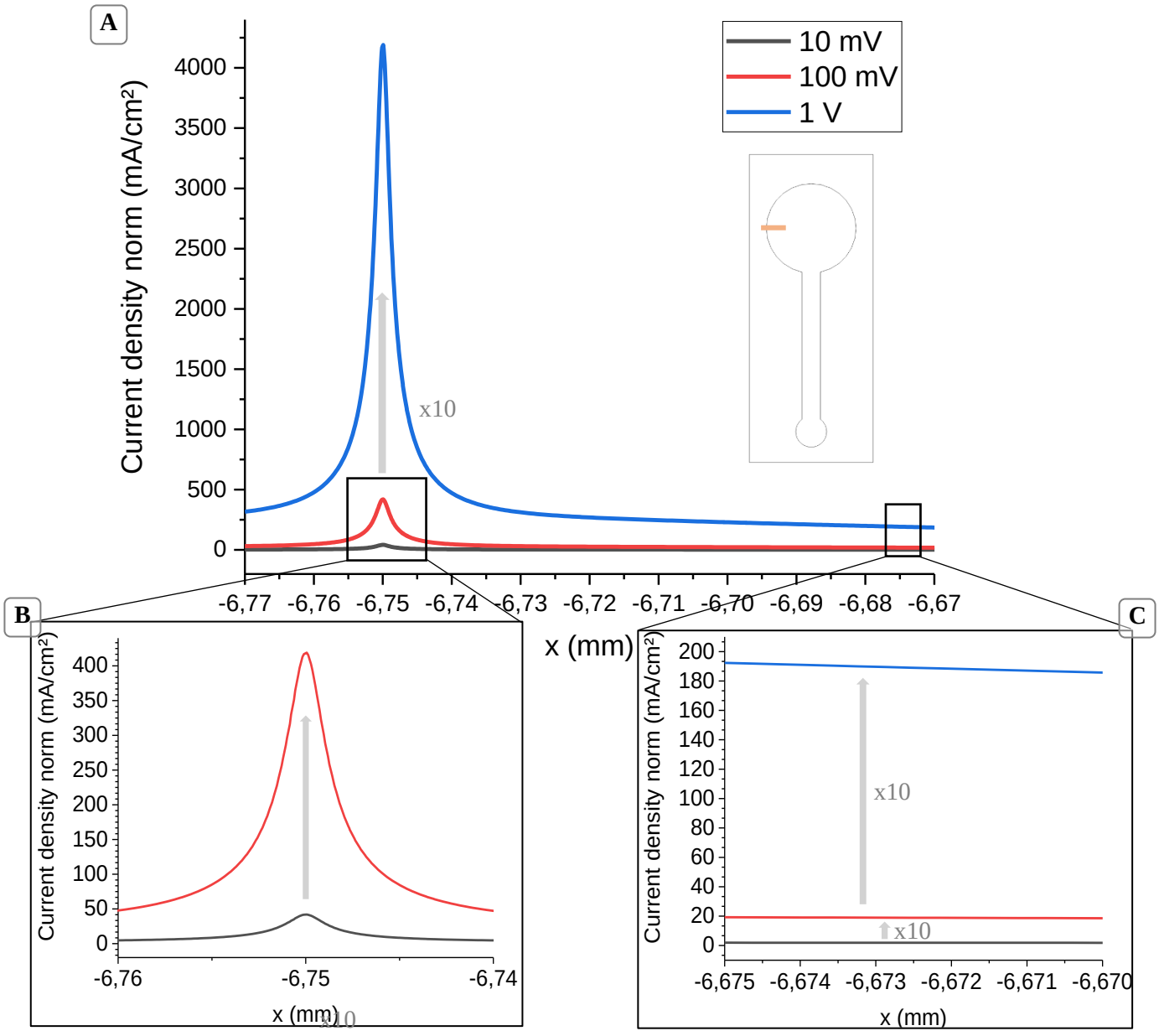

Figure 95. Numerical simulations of current density norm profile at the electrode/electrolyte interface (cut line b, see Figure 105) for different input values V_0. (A) Full profile and Zoom on (B) the edge and (C) the center of the electrodes

Zoomed plots on the edge and the center of the electrodes will be mainly used in the following figures to discriminate results.

To remember ❗

Additional approximations are made to define the standard configuration of the 2D geometry and the input settings. These parameters are only the starting points of the study and will be questioned and challenged in the following part to define an optimized ITP device.

4.2.2. Comparison of currently used systems

4.2.2.1. Geometry of the conductive layer

Among electrodes available for experimental comparison, two conductive layer designs (Ag) are suggested as mentioned earlier (**Figure 86)**: the standard plain disk and the grid-shaped disk.

The second design is initially implemented to reduce the edge effect at the perimeter of the electrode by creating local edge effects at the surface, thus locally increasing the current density. We expect to see current density maxima at the surface due to the 500 µm large cavities. Such effect would allow the electrodes to be consumed more homogeneously and therefore reduce the risk of electrochemical burns.

As we are interested in the current that enters the electrolyte, only the component of the current density normal to the electrode surface $\vec{J}_y$ will be represented in the following results.

Current distribution on the conductive layer (Ag)

When looking at the surface of the conductive layer only (**Figure 93**, cut line d), the current density seems on the contrary to increase at the perimeter with the grid-shaped geometry (**Figure 96A**). The presence of the cavities also generates local maxima at the surface in the normal direction (y-axis), multiplying $\vec{J}_y$ by almost 50 (**Figure 96B)**. The propagation of these effects through the following layers of the stack needs to be verified.

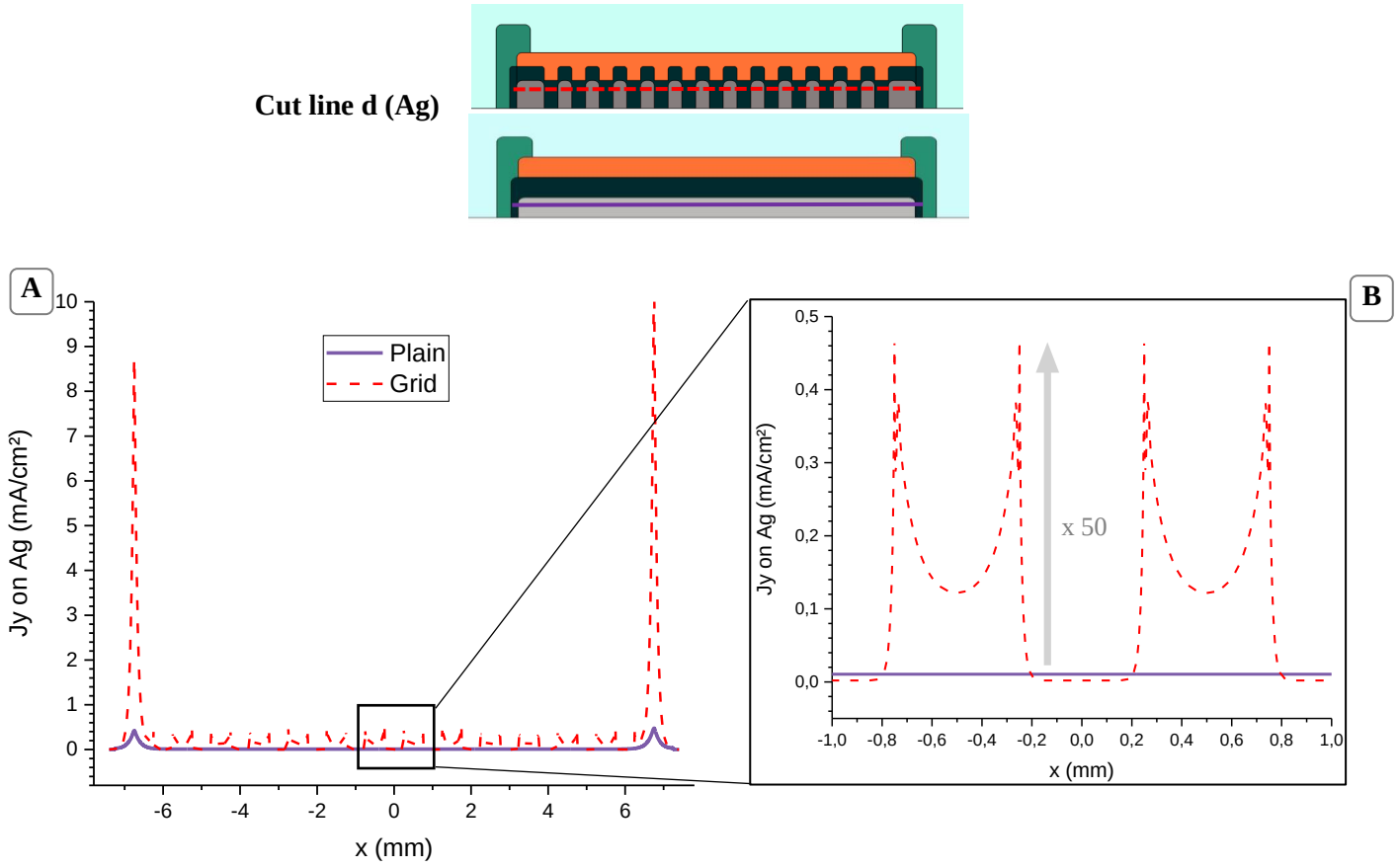

Figure 96. (A) Current density on y-axis in the conductive layer (cut line d) for grid (dashed red) and plain (purple) electrode (B) Zoom on the center of the electrodes

Current distribution on the active layer (Ag/AgCl)

Once the following layers are added, the current density profile changes. The zoomed plot at the surface (**Figure 97B**) highlights local maxima providing a current increase of around 15% in the grid-shaped configuration. These peaks seem negligible compared to the previously observed current enhancement on the Ag layer, which is unlikely to have an effect on the electrochemical consumption of the electrodes. At the edges though, no improvement is observed and both configurations display 4,000 times higher current values than on the surface (**Figure 97A**).

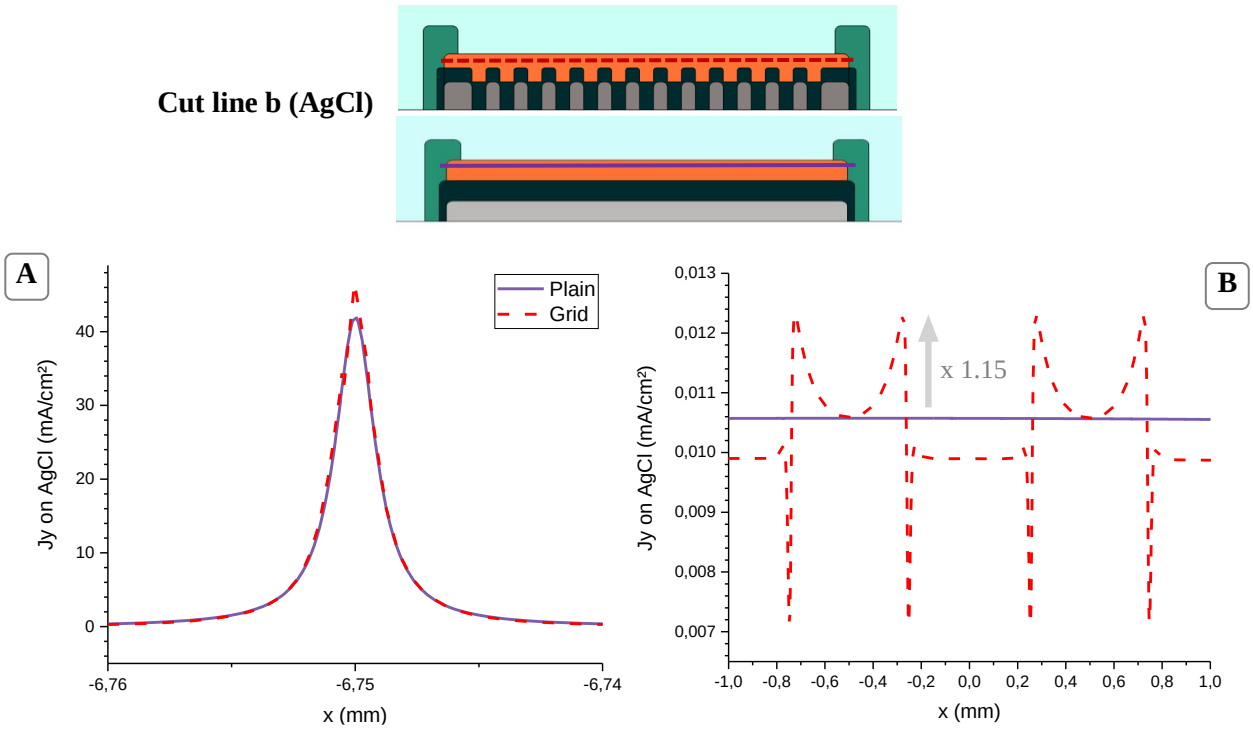

Figure 97. Current density on y-axis on the active layer (cut line b). Zoom on (A) the edge (B) the center of the electrodes

Focus on the surface

To better understand why the peak effect observed in the silver layer is not maintained throughout the stack, a plane view can be used. **Figure 98** presents the current density norm distribution in a color range, as well as the current streamline to visualize its preferred pathway in the different layers (arrows). It should be noted that the apparent difference in thickness of C and Ag/AgCl on the Figure is only due to the grid cavities that create a visual layer shift, but their volume remains similar in both cases.

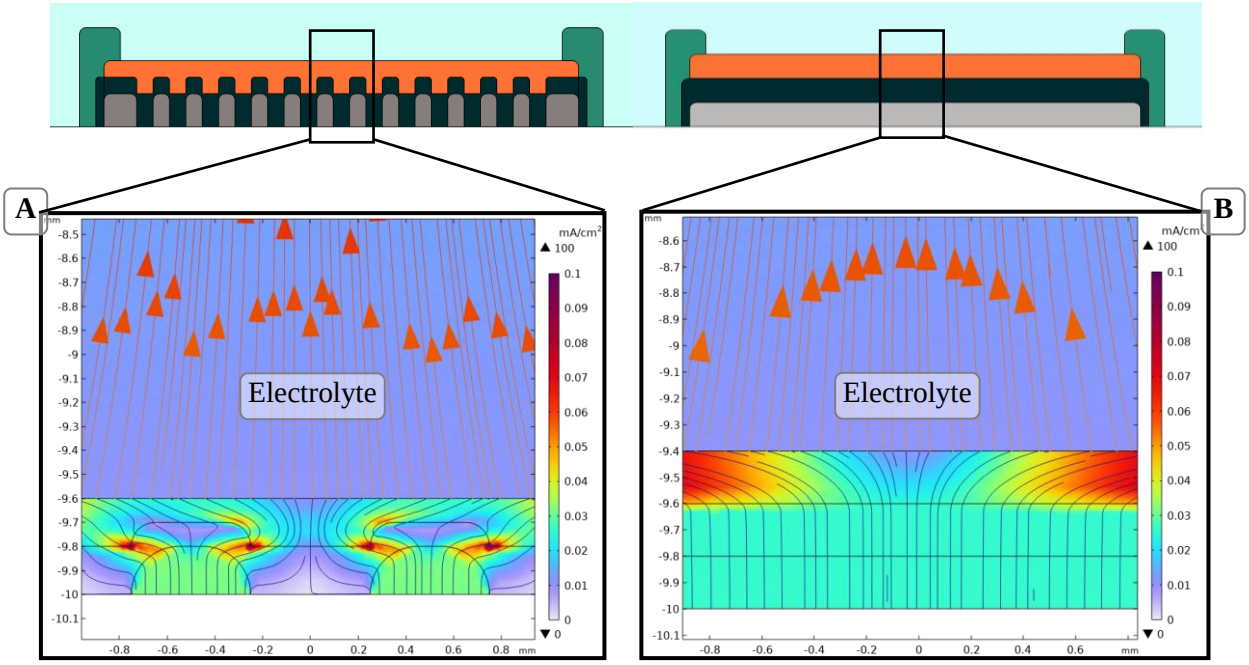

Figure 98. Surface current density norm distribution at the center of (A) the grid-shaped electrode and (B) the standard plain electrode (dilatation x10)

In the grid-shaped configuration, we can easily identify current maxima (red color) at the interface between the carbon spacer and the active layer (**Figure 98A)**, which is consistent with the peaks observed in **Figure 96**. However, this effect seems to dissipate inside the active layer, also as previously hinted by **Figure 97**. In both configurations, the current deviates towards the edges of the electrodes. This phenomenon is due to the high conductivity of the active Ag/AgCl layer compared to the carbon spacer below and the electrolyte above. Current therefore flows preferentially inside the active layer: this effect is highlighted in the standard geometry (**Figure 98B**) by the red zone in the active layer.

Focus on the electrode edges

If we look at the perimeter of the electrodes, a significant current peak can be noticed in both cases (**Figure 99**). This phenomenon can be referred to as **field enhancement** or **edge effect** and is commonly observed at the edges of conductive materials where the electric field lines tend to accumulate (WANG ET AL., 2014). This effect is even more intensified at sharp corners. Darker shades of red are noticeable in the grid-shaped configuration, which shows again no improvement of the edge effect due to this change of geometry.

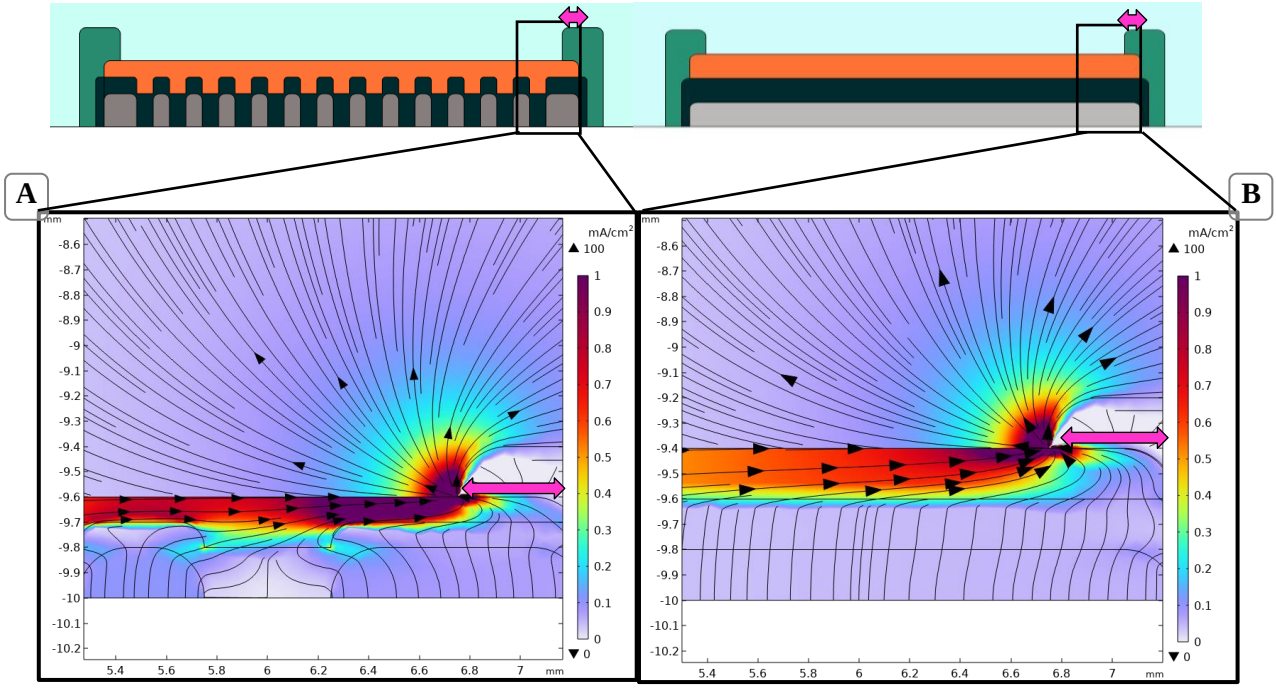

Figure 99. Surface current density norm distribution at the edge of the (A) grid-shaped and (B) plain electrode (dilatation x10). Pink arrows represent the dielectric overlap on the electrode

To remember 💡

A grid-shaped conductive layer does not reduce the hot spots at the perimeter of the electrodes. It seems to provide a small increase in $\vec{J}_y$ around the cavities at the center of the electrode, but not significantly enough to localize the electrochemical consumption, as hinted by CP results in Chapter 3 (3.3.5.2), where no differences in lifetime were recorded between the grid-shaped and the standard electrodes.

Furthermore, the dielectric overlap represented by pink arrows may cause an additional factor of current accumulation at the edge of the electrodes. This aspect will be questioned in section 4.3.1.

4.2.2.2. Direct versus Alternating current

Apart from the electrode design, the influence of the nature of the input signal on the current density distribution can also be investigated. ITP is most commonly used in DC or pulsed DC in order to continuously push the ion of interest towards its target location. So far, a DC signal is described as a working frequency of 0 Hz. In reality, multiple frequencies are covered once a DC signal is applied if we look at the Fourier transform of a DC pulse (**Figure 100**) (DUPONT, 2014).

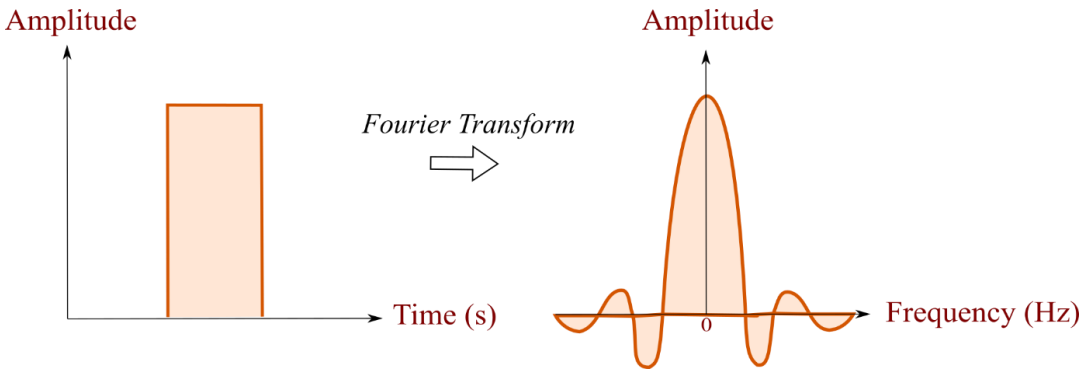

Figure 100. Fourier transform of a rectangular electrical pulse (modified from Jamali et al., 2019)

To consider this factor in numerical simulations, different input frequencies are compared on **Figure 101**. **Figure 101A** shows that increasing the frequency of the applied voltage actually reduces the current peak at the edges. At the center of the electrodes, the current density increases until 100 Hz, and then stabilizes at higher frequencies (**Figure 101B**).

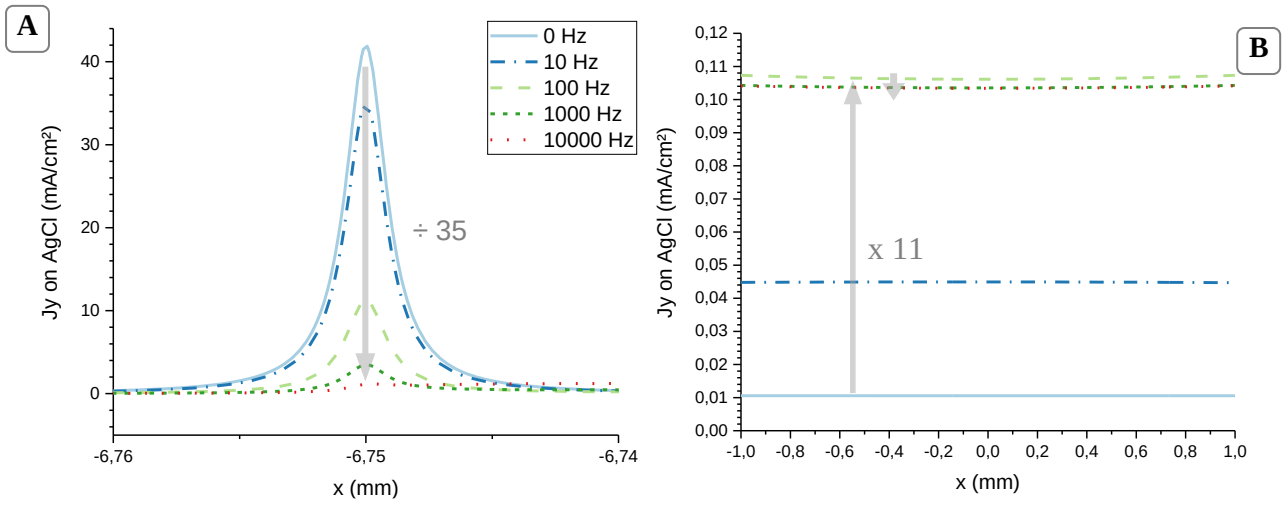

Figure 101. Current density on y-axis on the active layer (cut line b) with input frequencies of 0, 10, 100, 1000 and 10000 Hz. (A) Zoom on the edge (B) Zoom on the center of the electrode

These results suggest that high frequencies are actually beneficial to lower hot spots at the perimeter of the electrodes. At the center of the electrode though, the current density is no longer affected above a certain threshold.

To remember

In practice, a DC pulse corresponds to a multitude of frequencies. Numerical simulations show that higher frequencies can actually be beneficial to reduce the edge effect around the electrodes while increasing the current density at the surface until a certain threshold. To take advantage from this phenomenon, a pulsed DC signal could help reaching high frequencies repeatedly without inhibiting the desired electrochemical reactions. Their rate would however be lowered, which is consistent with the increase in lifetime recorded in Chapter 3 when using pulsed DC.

Learning from mistakes

Initial numerical simulations were computed without considering the EDL, leading to results in ***Figure 102*** *with strictly no influence of the frequency value on the normal current density and a significant reduction of the edge effect (B) compared to* ***Figure 101*** *where the EDL is implemented in the model. Its presence is therefore important to the reliability of the model as it affects the current distribution profile both at the edges and the center of the electrodes.*

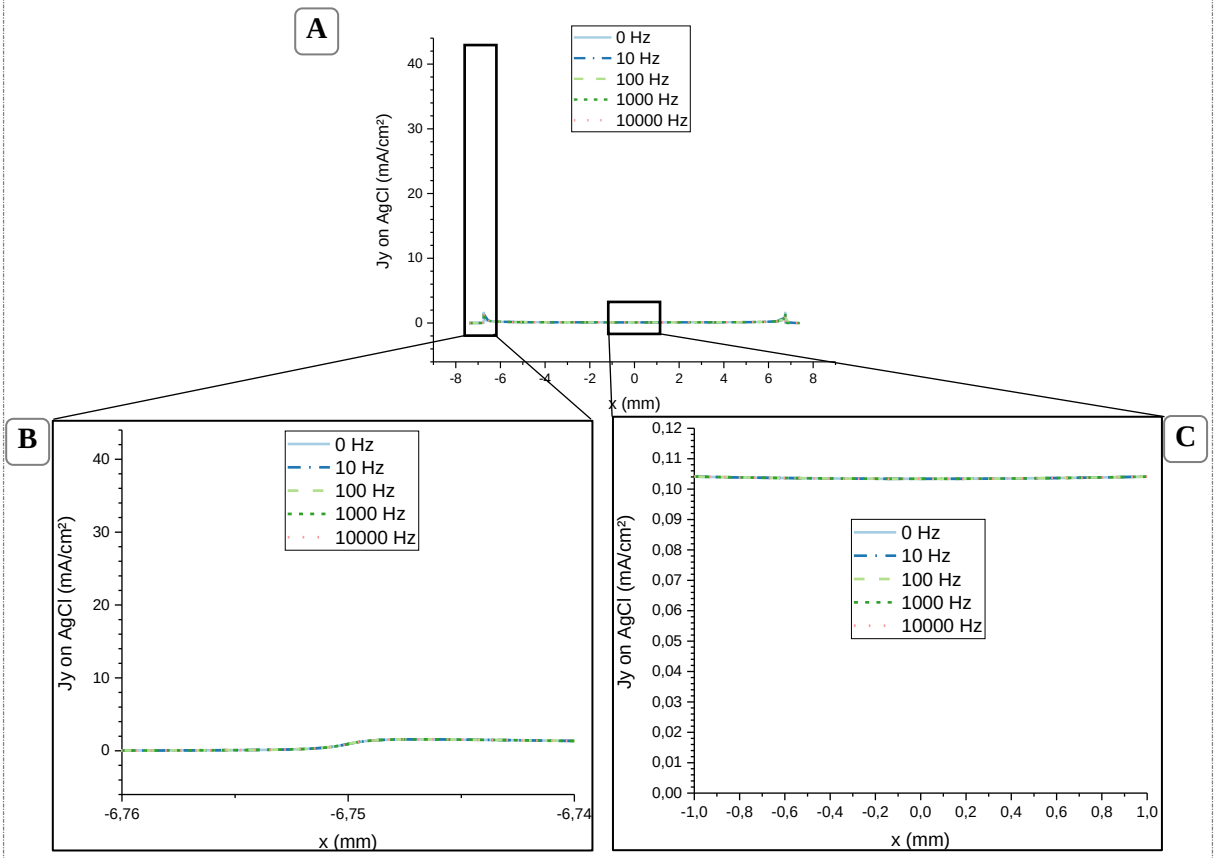

Figure 102. Current density distribution on y-axis at different frequencies without the EDL layer. (A) Full profile and Zoom on (B) the edge and (C) the center of the electrodes – To be compared with Figure 113 (with EDL)

In comparison to an AC signal, a pulsed DC should not induce an alternating change in polarity that may affect drug diffusion trajectory. Some studies however present the use of AC as a mean to reduce the risk of skin burns without altering drug delivery efficiency (BAGNIEFSKI AND BURNETTE, 1990). In this case, the working frequency may need to be adapted to the drug to deliver and further numerical simulations may be required with the consideration of ionic mobility to choose the optimal input signal parameters.

4.3. Improvement prospects

Numerical simulations give a hint on the behavior of our electrodes and help screening different parameters to identify the most favorable options. In this part, changes in the geometry are suggested in order to improve the ITP device to reduce the risk of skin burns, increase its performance and adapt it to a wearable application.

4.3.1. Optimization of the stack to reduce edge effects

The insulator overlap on the edges of the electrodes was questioned in part 4.2.2.1. Such design is indeed commonly used in printing techniques for two main reasons:

- To cover layer heterogeneities on the egdes. Depending on ink viscosity and its surface tension on the substrate, the borders of the deposited layers may be either too thin (**Figure 103A**) or too thick (**Figure 103B**) compared to the surface of the layer. The latter effect is visible on the profilometry measurements presented in Chapter 3 (**Figure 78**).

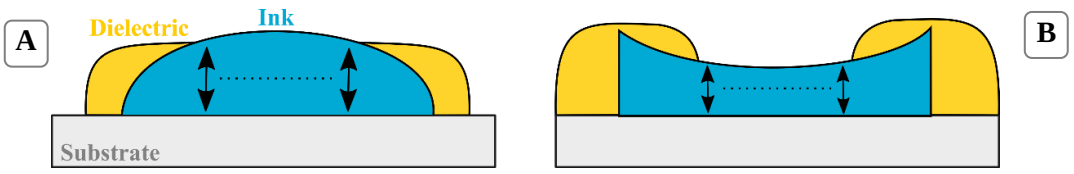

Figure 103. Schematic representation of possible edge heterogeneities caused by a deposited ink with (A) thin edges and (B) thick edges

- To avoid short-circuits due to misalignments. Concerning the process itself, many parameters (operator, sight recognition by the camera, heat exposure of the substrate, etc…) can cause a misalignment between the different layers of the stack. A dielectric overlap can therefore help avoiding short-circuits in this case.

Unfortunately, these precautionary measures may also cause the increase of the hot spots at the perimeter of the electrodes as previously shown. In the case of presented ITP electrodes, there are no risk of short-circuits as working and counter electrodes are printed separately. The dielectric (green) overlap can therefore be removed. However, the carbon spacer (black) should remain larger than the conductive Ag layer (gray) to avoid any contact with the active Ag/AgCl layer (orange) and the electrolyte if a misalignment occurs.

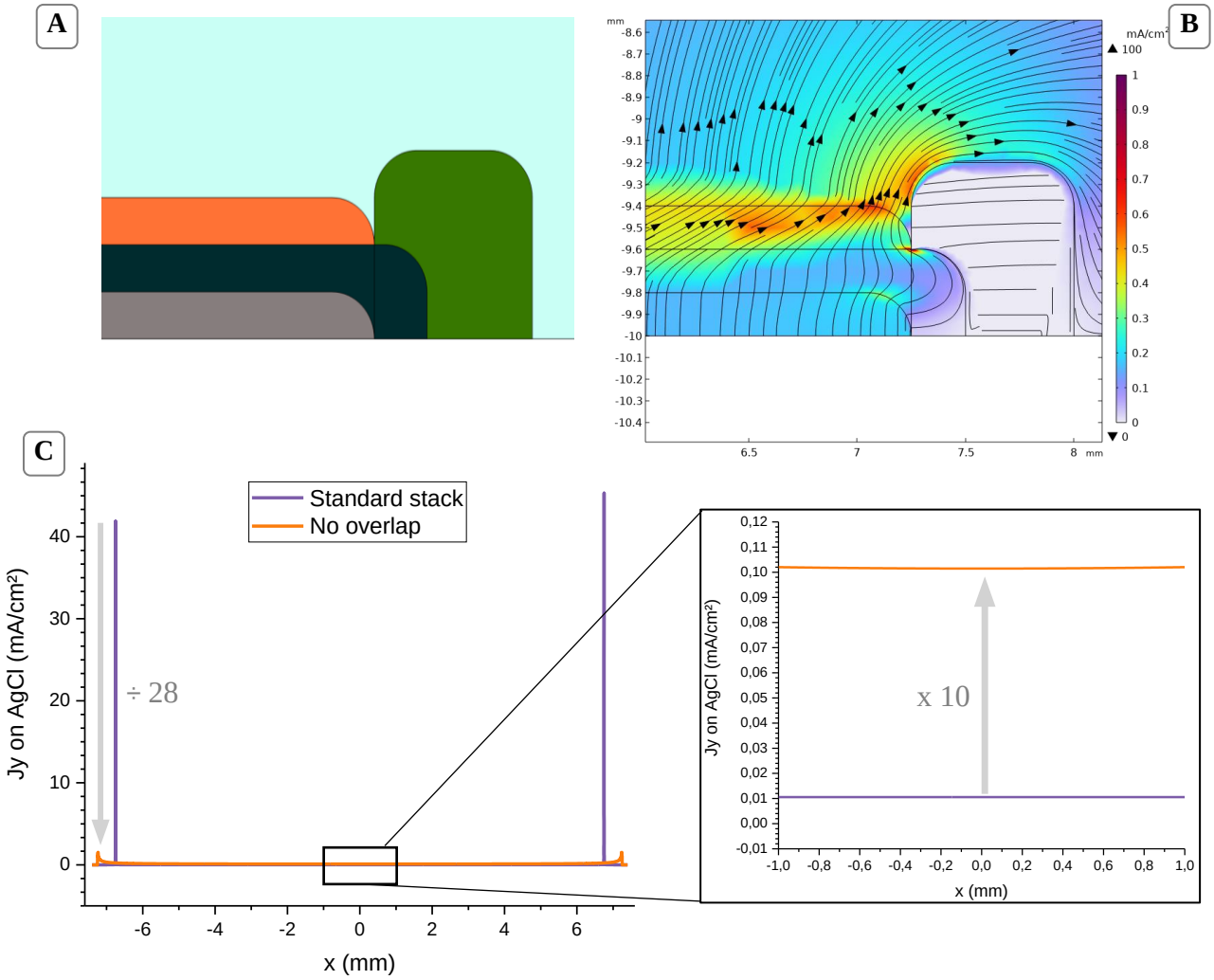

Figure 104. (A) Stack modification with no dielectric overlap (dilatation x10) and associated current density norm distribution (B) on the working plane and (C) at the surface of the active layer (cut line b) compared to the standard geometry

Numerical results on **Figure 104B and C** show that the current maxima is significantly reduced compared to **Figure 99B**. Additionally, the current density at the surface increases by an order of magnitude.

To remember 💡

A dielectric overlap is conventionally used in printing processes to prevent short-circuits in case of misalignment. Numerical simulations show that it can also be responsible for undesired current peaks at the perimeter of the electrodes. This precaution is unnecessary in the case of independent ITP electrodes and can actually be removed in future stacks to reduce the risk of skin burns and provide a more homogeneous delivery at the surface.

4.3.2. Optimization of the stack to homogenize the current distribution at the center of the electrode

4.3.2.1. Effect of the grid size of the conductive layer

The grid-shaped geometry presented in this Chapter (**Figure 86**) and available in the lab is composed of 500 µm large cavities. This parameter can also be questioned and similar geometries of Ag-layer are constructed: 250, 1000 and 1500 µm large cavities. Results are computed on the complete stack but are only shown at the level of the conductive layer for relative comparison to the standard 500 µm grid (**Figure 105**).

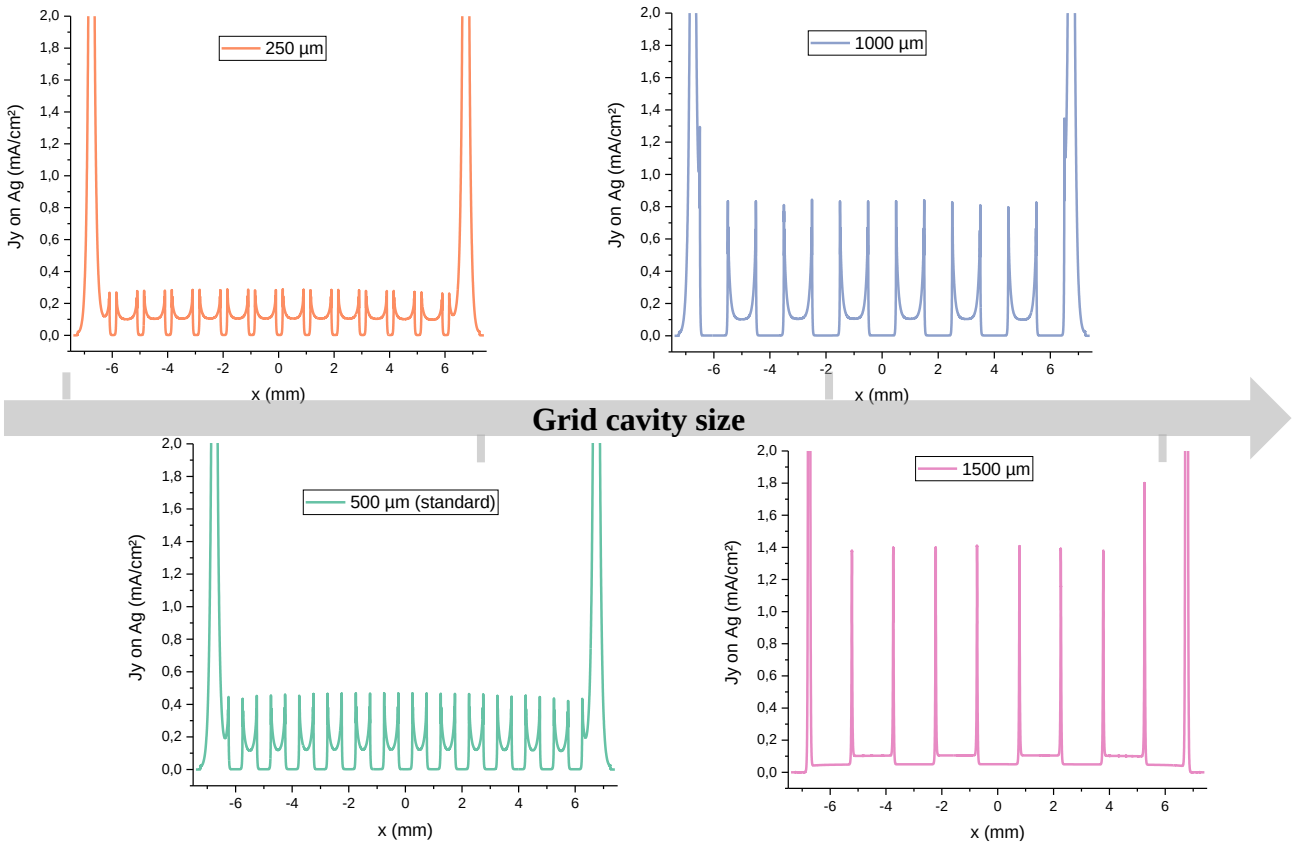

Figure 105. Evolution of the current density normal to the surface of the conductive layer depending on the grid cavity size

Not surprisingly, the number of peaks decreases as the cavity size increases, because a smaller number of cavity can fit a given electrode dimension. Even so, different advantages of increasing the cavity size can be highlighted:

- Local current maxima increase with cavity size,
- Less ink is used for a similar if not better electrical performance,
- Better resolutions can be obtained by screen-printing compared to smaller patterns,
- Increasing the cavity size may help creating a visible microstructure at the surface of the active layer (**Figure 106**).

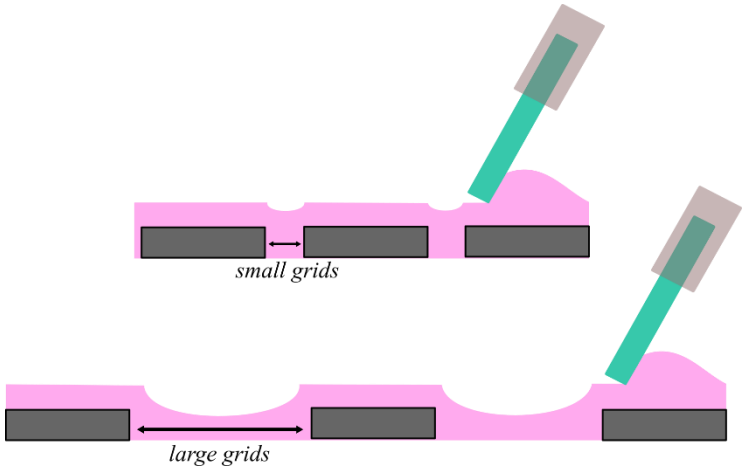

Figure 106. Schematic representation of microstructure generated by the conductive layer depending on the grid size

This effect can however be influenced by the presence of the carbon spacer between the conductive and the active layer, as it can cover up this microstructure if too thick.

4.3.2.2. Thin-layered spacer

In the configurations previously suggested, the carbon spacer is structured similarly to the grid shape of the silver layer below, but the following AgCl layer remains relatively flat. This effect is verified by profilometry prior to numerical model construction (Chapter 3, **Figure 78**).

This phenomenon could be due to the important thickness of the deposited layers by screen-printing. If the spacer was thinner, we could expect the shape of the conductive layer to affect the profile of the electrochemically active layer as well.

Numerical simulations are carried out with a 2 µm thick spacer inducing the active layer to fill the cavities as depicted on **Figure 107A**.

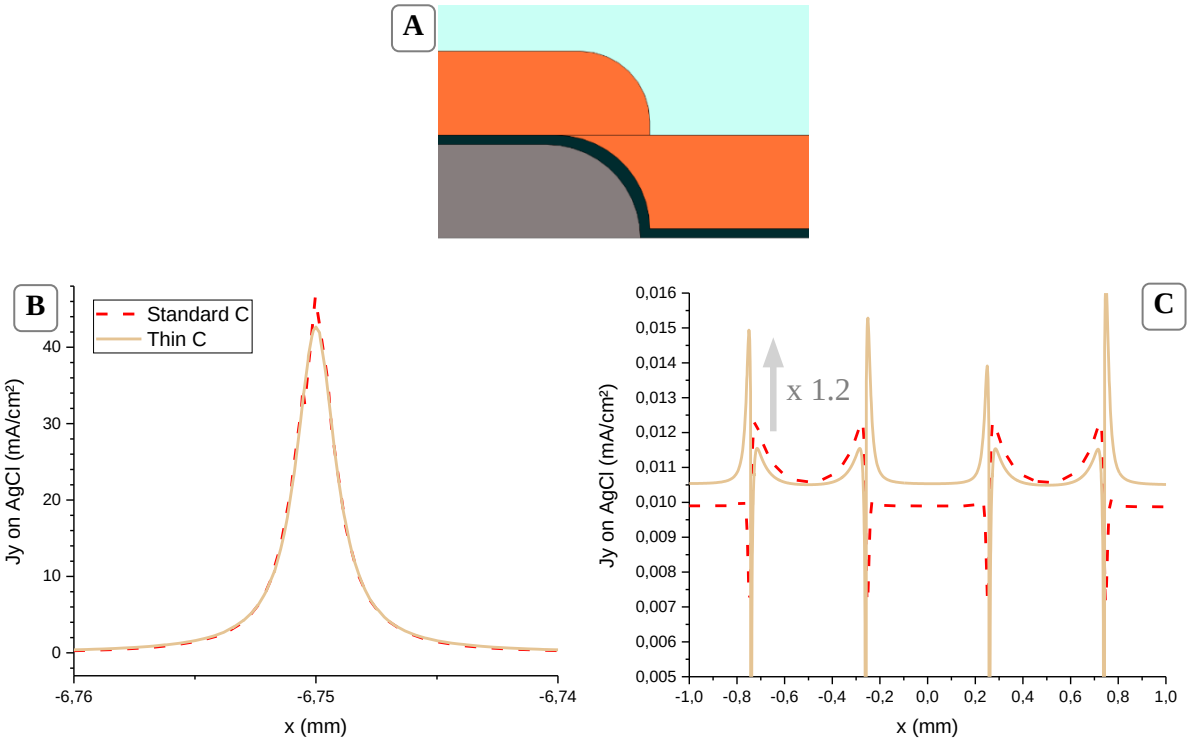

Figure 107. (A) Thin spacer configuration and associated normal current density distribution compared to a standard 20 µm carbon. Zoom on (B) the edge (C) the center of the electrodes

Results on **Figure 107A and B** show that the structuration of the active layer does not significantly change current peaks at the electrode center (+20%) nor the maxima at its edges.

To remember

Using a spacer is necessary to the well function of the Ag/AgCl system (McAdams et al., 2000). Reducing its thickness could allow the active layer to benefit from the grid shape of the conductive layer. The active surface therefore increases, but numerical results do not show a significant improvement on the current distribution neither at the edges nor at the center of the electrodes.

Nevertheless, using a thin spacer could also create a surface microstructuration and increase the active surface area, positively affecting electrodes lifetime. This hypothesis could be verified numerically by implementing the electrochemical reactions in the model.

4.3.3. Geometries adapted to planzar wearable devices

4.3.3.1. Standard system used on the same plane

The relative position of working and counter electrodes is also a parameter to take into account when looking at the spatial current density distribution. In practice, ITP electrodes are placed on the same plane on a patient skin, and not face-to-face as in the system previously depicted.

Numerical simulations are performed with electrodes placed next to each other in the beaker (**Figure 108A**).

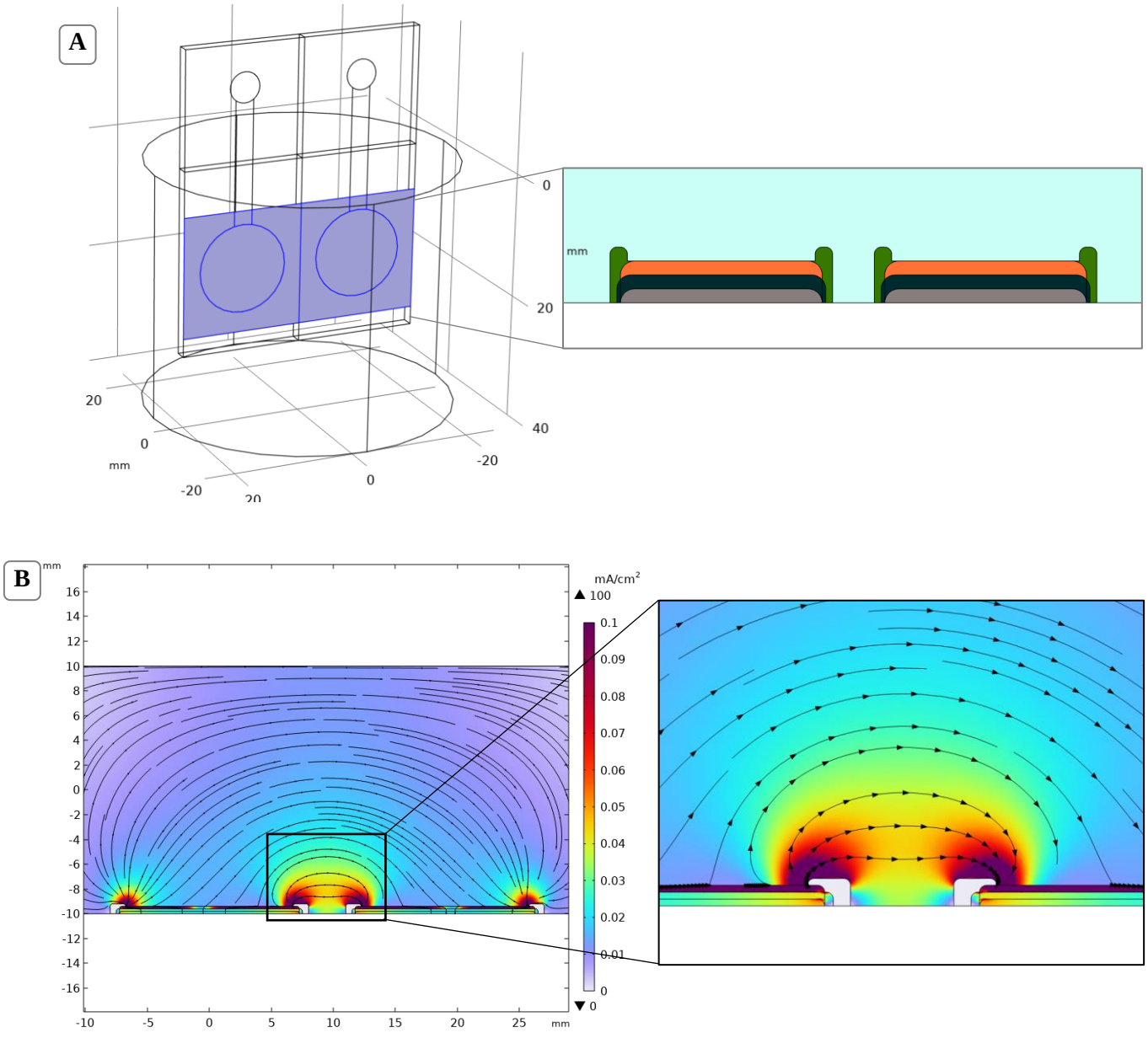

Figure 108. (A) 3D representation of ITP electrodes on the same plane and associated 2D cut plane (B) Surface current density norm distribution

Figure 108B shows that, even in favorable saline conditions, current density norm is higher in the gap between both electrodes. This observation is not surprising as the current takes the shortest pathway between working and counter electrodes to close the circuit. We can therefore assume that the chosen geometry is not suitable for use on the same plane as the consumption will not occur symmetrically.

To remember ❗

In addition to the current enhancement at the edges, the standard electrodes design is not adapted to wearable applications since the current distribution is asymmetrical when both disks are placed next to each other.

In the following parts, two alternative geometries are suggested to provide a more symmetrical if not homogeneous electrode consumption when used on the same plane. Associated 3D models are developed using the conductive silver layer (L1) only.

4.3.3.2. *InterDigitated Electrodes (IDE)*

Definition 🕮

***I**nter**D**igitated **E**lectrodes (**IDE**) take the form of interlocking comb-shaped arrays. They are mostly used to develop resistive and capacitive sensors thanks to their compactness yet providing a high contact area* **(RIVADENEYRA ET AL., 2014).**

Figure 109 shows that the IDE geometry indeed helps increasing the gap length between the working and counter electrode. No edge effect is visible at the perimeter of the metallic layer (**Figure 109C)**. If the addition of the full stack (including the EDL) was to cause one, it would be beneficial anyway as it would be distributed all over the surface.

Such interdigitated design can however be hardly adapted to iontophoretic drug delivery, as the reservoir must be carefully placed on top of one electrode. The same problem arises for MN coupling. An IDE-inspired electrode will be studied in Chapter 5, questioning the stretchability of such structure.

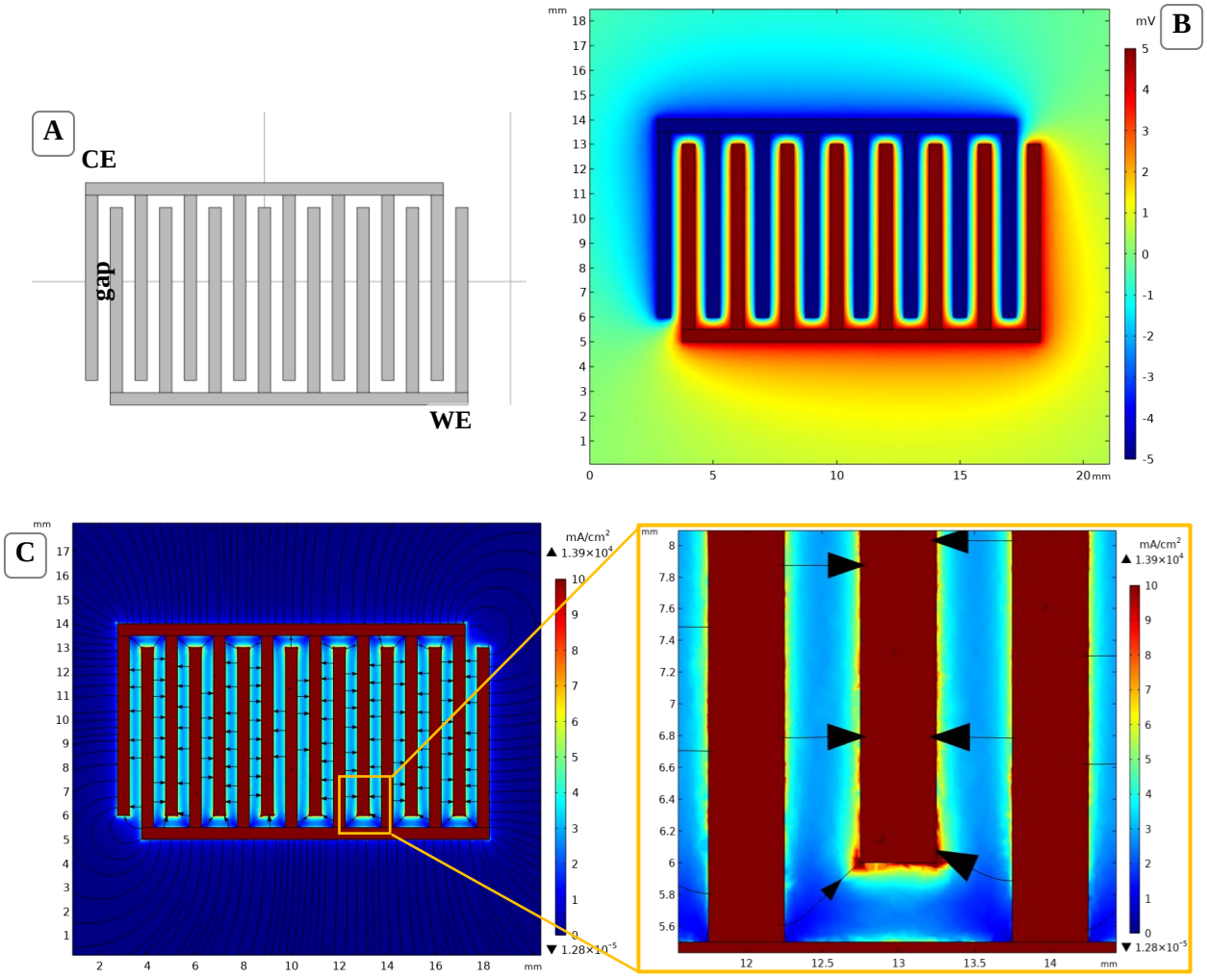

Figure 109. (A) IDE geometry (B) Potential and (C) Current density norm distribution on the Ag conductive layer. WE : Working Electrode, CE : Counter Electrode, Gap : WE/CE interspace

4.3.3.3. Ring-shaped electrodes

The simplest geometry to add a drug reservoir and a MN array on one side is a ring-shaped electrode. Despite the field enhancement at the perimeters that can be attenuated with the options provided before, this geometry would allow a symmetric consumption of both electrodes on the same plane (**Figure 110**).

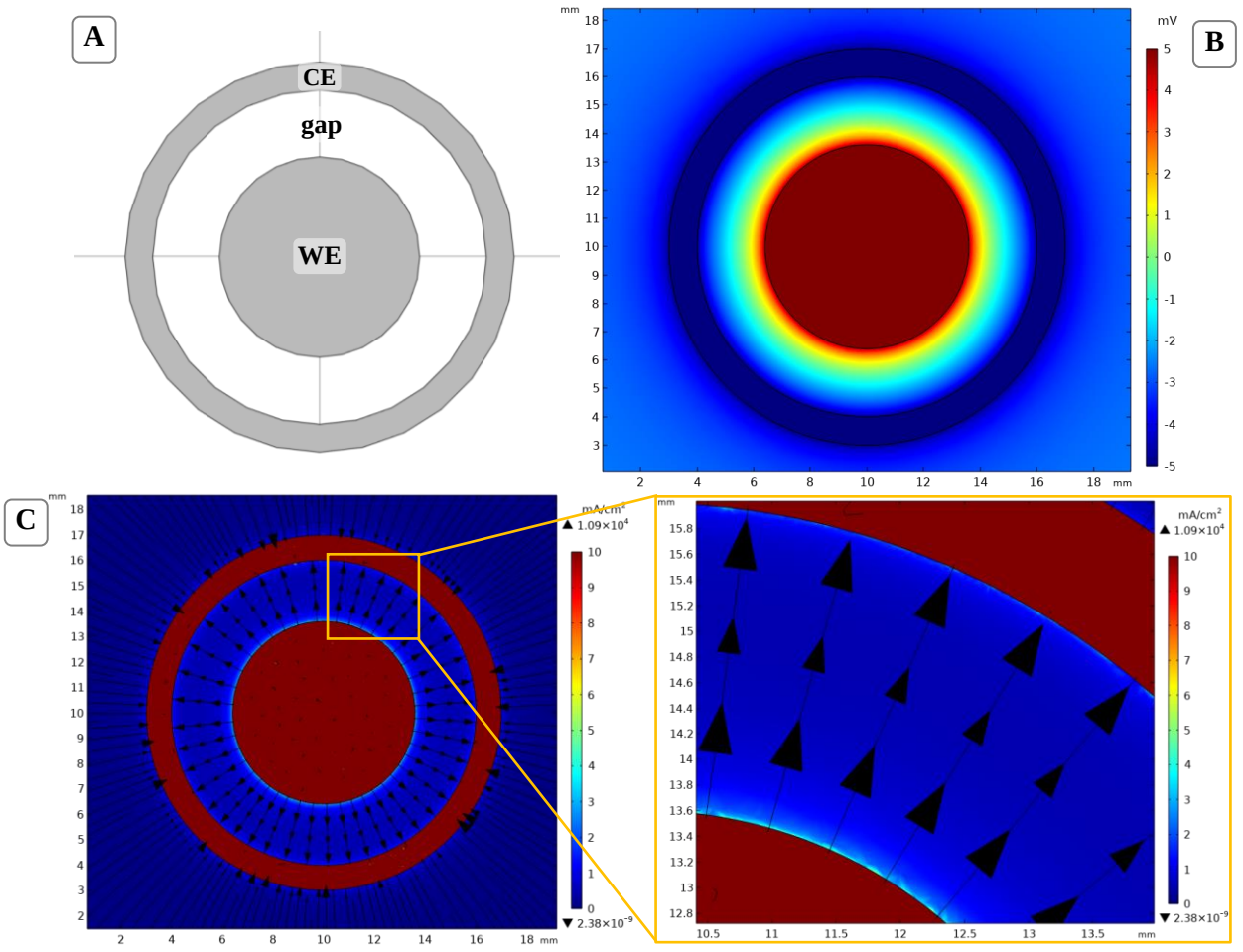

Figure 110. (A) Ring-shape geometry (B) Potential distribution and (C) Current density distribution on the Ag conductive layer

Depending on the inks used, the size of the WE and the CE can be adjusted. Chapter 3 (3.3.5.1) proved that these surfaces do not need to be equal and a smaller cathode is enough to use the electrodes at their full potential.

With a bit more time… ⌛

The optimal distance between the electrodes can also be determined numerically: a parametric study could be set to find a compromise between current intensity (small distance) and penetration depth (big distance). Results may differ with the addition of a microneedle array though, as field lines may be deviated from their initial trajectory.

4.3.4. Combination of microneedles and iontophoresis

The current density profiles studied so far focus on the iontophoretic device alone. In this subject, the combination of ITP and MNs is explored to enhance drug delivery. The addition of a MN array on top of one of the electrodes is expected to affect the field line distribution as the electrolyte flows through the hollow MN channels.

A 2D model cannot be used in this case because of the tubular shape of the MNs. A half-geometry 3D model is therefore built similarly to the one described in section 4.1.1.2, using the geometry of injection-molded PLLA MNs (**Figure 33**). This geometry implies that a MN array is placed on both WE and CE, which is not necessarily the case unless both electrodes contain a drug reservoir as suggested in Chapter 3 (**Figure 83**).

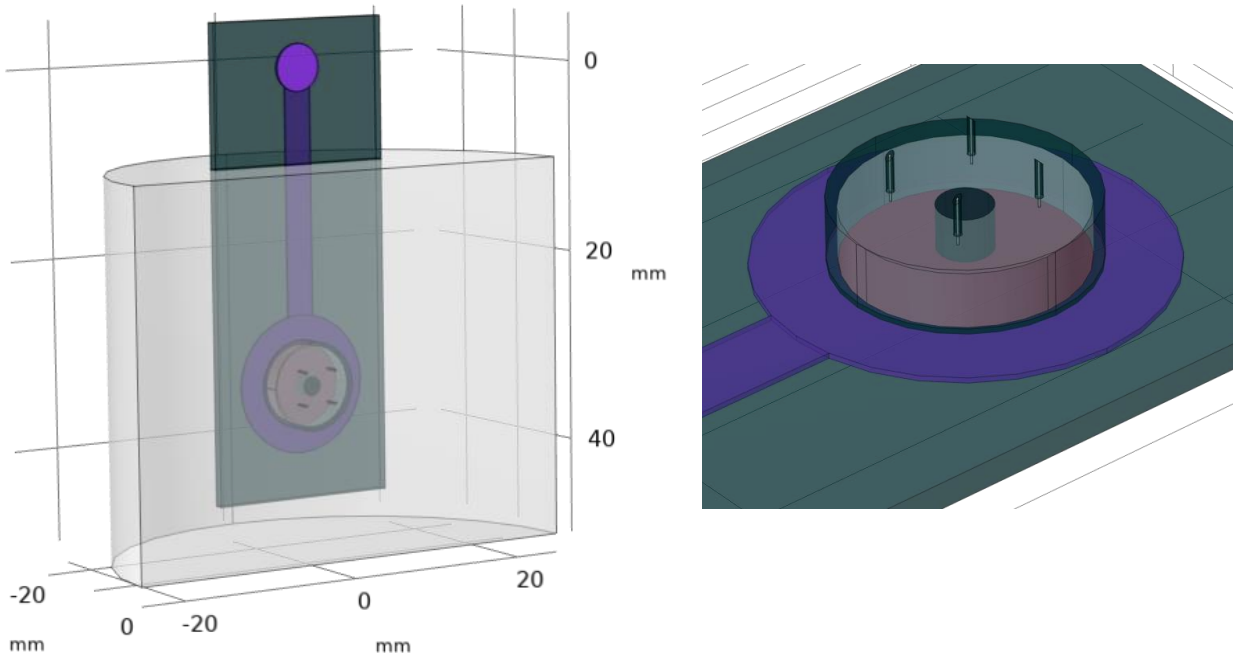

Figure 111. Geometry of the 3D numerical model combining ITP and MN array

Potential distribution on the cross section of the device shows a homogeneous distribution in the electrolyte contained in the array, but a significant potential gradient is observed within MN ducts (**Figure 112A**), causing a maximum current density in the this specific zone (**Figure 112B**). This phenomenon is certainly due to the small size of the duct (100 µm diameter) compared to the electrode which is constraining the current, and therefore ions, in this area.

These results look promising as the application of an electric field between WE and CE would help concentrating the ionized drug within MNs internal cavities. Once inserted, MNs can therefore release the drug directly to the deepest layers of the skin.

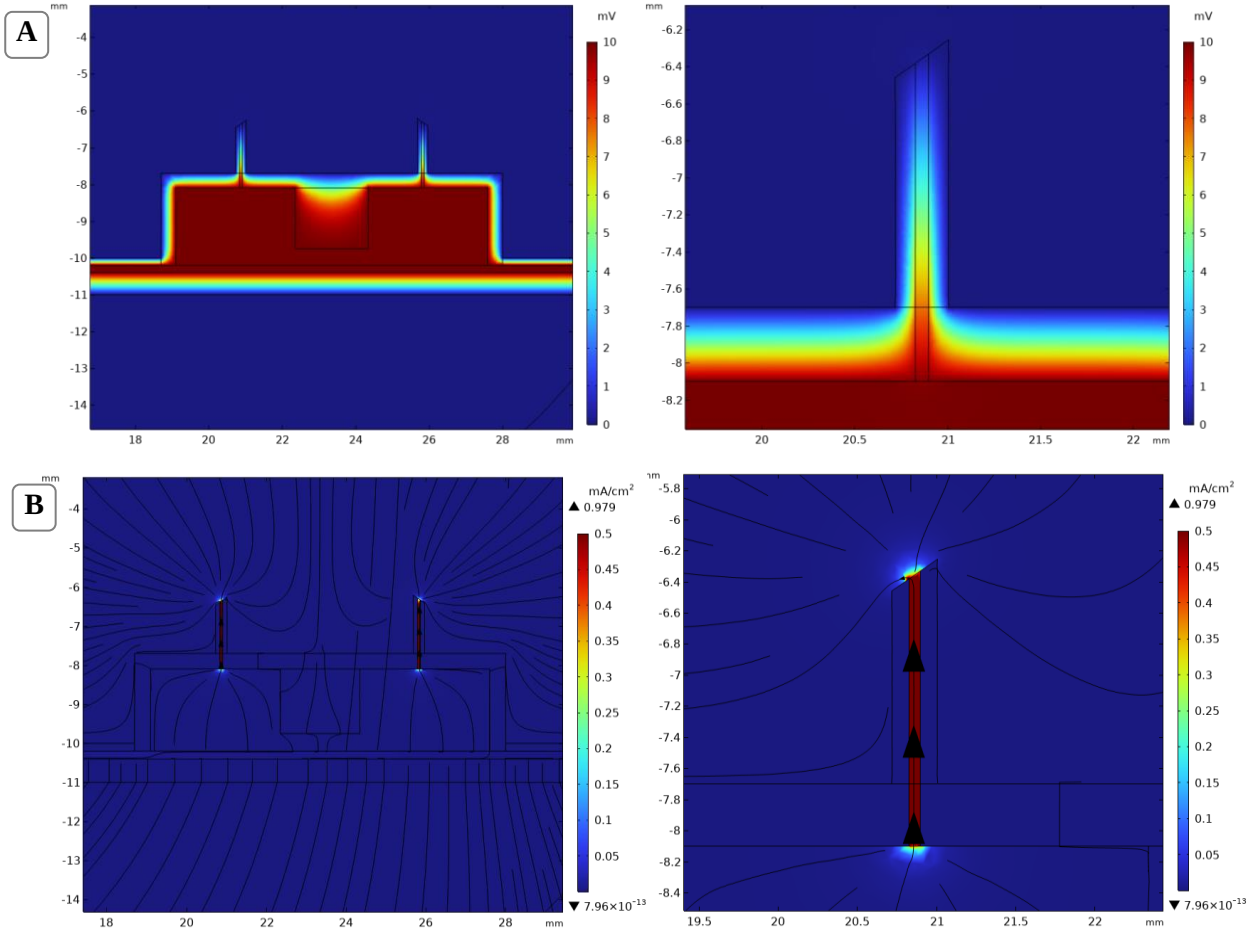

Figure 112. (A) Potential and (C) current density distribution on the cross section of the ITP+MN setup and associated zooms on one MN

To remember

The combination of ITP and MN can be an asset to avoid edge effect around the electrodes and maximize the current density within MN ducts. Ionic drugs can therefore concentrate in this area and be readily available to be delivered once the SC is perforated by the MNs.

The implementation of mass transport computations in the model would be valuable to identify which of electromigration or concentration gradient contributes the most to drug diffusion outside the MNs.

Conclusion

This chapter presents an electrical numerical model based on the experimental setup previously used for electrochemical characterizations. This model can therefore be validated using the experimental EIS data. Besides legitimating the use of the model, this step is necessary to work with realistic EDL parameters as this interfacial layer has a non-negligible influence on current distribution.

Numerical simulations on the available geometries allows to reach the following conclusions:

- The use of a **grid-shaped conductive layer** with 500 µm large cavities neither seems to create significant current peaks at the surface of the electrodes, nor reduces the hot spots at the perimeters with a DC signal. **Larger cavities** may provide more impactful results and increase electrodes lifetime as it may also increase the active surface area of the electrochemically active layer. Similar surface structuration could be induced by reducing the **thickness of the carbon layer**. Even though numerical results show no significant impact on current distribution, such geometry could increase reagents availability.
- Increasing the **frequency** of the signal reduces the field enhancement at the edges, while increasing the current at the surface. A **pulsed DC or an AC signal** could therefore be used in this regard. In the latter case though, the frequency should be adapted to the molecule to deliver.
- **New geometries** can be experimented to ensure a **symmetrical consumption** of the electrodes when used on the same plane. IDE and ring-shaped electrodes therefore gave rise to a new set of electrodes that are electrochemically and mechanically tested in the final chapter.
- Finally, the **combination of ITP and MNs** seems promising as it would help the current and therefore the ionized drug to be concentrated within the MN ducts, readily available to be delivered to the deepest layers of the skin.

It is important to keep in mind though that **the model developed in this chapter only considers the electrical behavior of the device in saline solution**. Further modifications are therefore necessary to improve the model and represent more reliably the desired application:

1. **Electrochemical reactions** could be implemented, therefore taking into account the formation of an insulating passivation layer. Such model could also help finding means to improve electrodes lifetime by comparing different physical and geometrical parameters.
2. Similar computations should be performed using a **human skin model in contact with ITP electrodes** instead of a saline solution. Both current distribution and drug diffusion are expected to differ in these two media.
3. **Total drug diffusion (due to both electromigration and concentration gradient)** could eventually be estimated in different configurations considering the physicochemical properties of the active principle to deliver (size, mass, charge, etc…).

CHAPTER 5

Chapter 5: Use cases

Introduction

This final Chapter presents two applicative studies that evolved in parallel.

The first use case deals with the use of iontophoresis (ITP) electrodes **on the same plane** and studies their **resistance to tensile stress** similarly to patient movements. New ITP electrode geometries and stacks are presented and are tested electrically and electrochemically under constraint. Unlike the standard stack presented earlier, these electrodes are designed to fulfill the applicative need.

On another hand, drug delivery itself is studied using a protein model to **evaluate the ability of biomolecules to migrate** across a diffusion skin phantom. Different configurations are compared: passive, ITP, microneedles (MN), and ITP+MN-assisted delivery.

5.1. From flexible to stretchable electrodes

As hinted by numerical simulations, the standard ITP electrodes geometry presented is not suitable to use in a wearable device, as their consumption will certainly be asymmetrical when placed next to each other on the same plane. Besides, we need to ensure that drug delivery is not impacted by patient movements, as the device may undergo traction cycles during use.

As discussed earlier, screen-printing is a suitable process to develop wearable devices as it allows the deposition of complex stacks and designs onto a large number of substrate materials. Thermoplastic polyurethane (TPU) has been selected as a stretchable substrate that does not require any surface modification prior to printing. However, despite the excellent tensile strength of TPU, electrodes may not perform under high mechanical constraints if the inks used in the standard stack are not stretchable. As Chapter 1 (**1.1.1.2**) mentions that human skin can be stretched up to 30% with natural limb motion, this part focuses on means to maintain electrodes performances under these conditions.

The new characterizations (electrical, mechanical and electrochemical on new geometries) presented in this part gave rise to a three-month internship topic that I supervised. Some of these results are therefore acquired by Emilie Neveux, technician student at IUT1 – Université Grenoble Alpes.

5.1.1. Stretchable inks and geometries

5.1.1.1. Ink alternatives for stretchable devices

Semi-stretchable stack

Medical grade stretchable inks are more and more available on the market to develop new generations of wearable devices. In the case of an ITP device though, specifications are more complex as Ag/AgCl particles need to be available at the surface of the active layer to perform the sacrificial electrochemical reactions previously described.

Despite different attempts of using commercial stretchable Ag/AgCl inks, the CP signal provides less satisfying lifetime performances despite similar Ag/AgCl ratio – these results will be shown in part **5.1.2.1**. This effect could be due to the encapsulation of metallic particles in the elastomeric matrix, reducing the surface area in contact with the electrolyte. **T**hermo**G**ravimetric **A**nalysis (**TGA**) coupled with **D**ifferential **S**canning **C**alorimetry (**DSC**) (STA449, Netzsch, Germany) is used between 20 and 1,000 °C (5 °C·min^{-1} gradient) to compare the proportions of solvent, polymer and metallic particles in each Ag/AgCl ink.

Definition 🕮

Thermogravimetric Analysis (TGA) *is used to identify fractions of components depending on their volatility. It consists in monitoring the weight change of a sample with increasing temperature* (RAJISHA ET AL., 2011). ***Differential Scanning Calorimetry (DSC)*** *can be used additionally to identify various thermal transitions such as melting, glass transition, crystallization, etc…* (BYRN ET AL., 2017).

Figure 113 indeed shows that the proportion of metallic particles is significantly lower (63%) than in the standard non-stretchable inks (74 and 77%). DSC (dotted) curves indicate that the polymer matrix used is different in standard and stretchable inks as the endo peak around 100 °C only appears on the green (stretchable) curve. This observation is not surprising as ink stretchability is most likely provided by the polymer base.

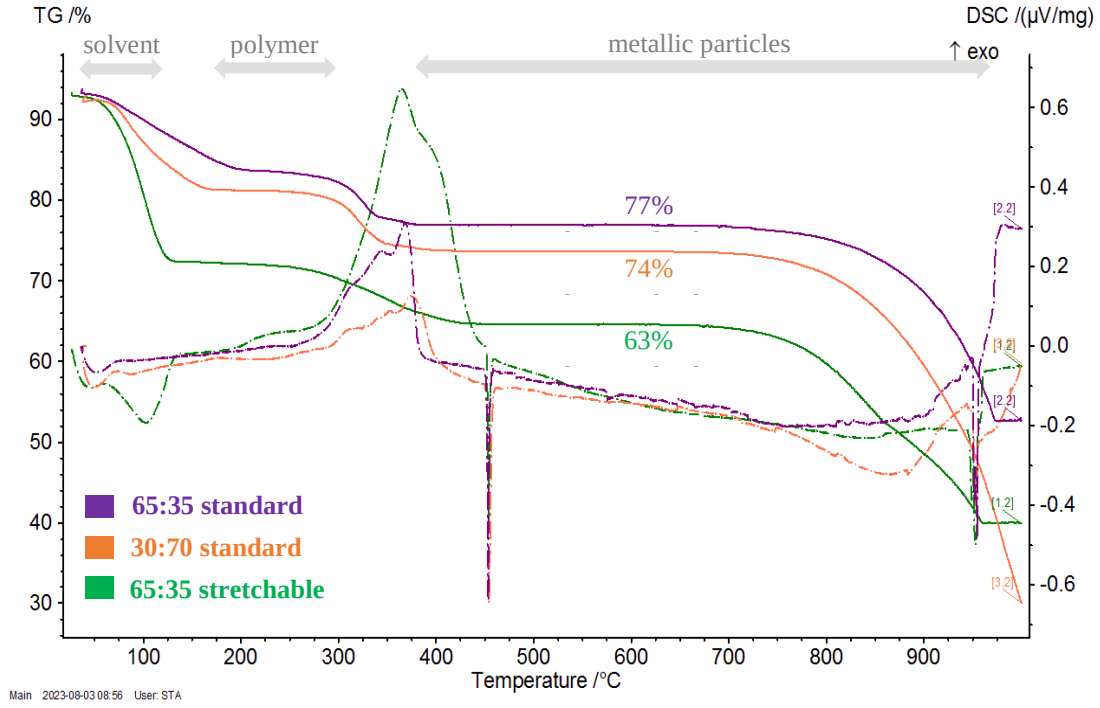

Figure 113. TGA (full lines) /DSC (dotted lines) analysis of Ag/AgCl inks

To maximize electrodes performance (lifetime), we suggest to fabricate ITP electrodes according to a "**S**emi-**S**tretchable" (**SS**) stack, using stretchable inks on Ag (L1), C (L2) and dielectric (L4) layers while keeping the ITP-grade active Ag/AgCl layer (L3) previously used. Despite its lack of stretchability, we do not expect this upper layer L3 to negatively impact the electrical behavior of the electrode as the power supply is granted by the conductive layer L1. On the contrary, possible cracks in the active layer could even increase the active surface area and help the electrolyte to diffuse deeper in the layer. These hypotheses will be verified later on.

In the following section on electrical testing, two stacks will therefore be compared:

- **Standard stack:** non-stretchable inks, ITP grade Ag/AgCl 65:35 L3
- **Semi-stretchable**: stretchable L1, L2, L4, ITP grade Ag/AgCl 65:35 L3

Both standard and stretchable inks are provided by Dupont, DE, USA. References and printing parameters are summarized in **Appendix 5**.

Electrical testing under tensile constraint

Mechanical testing probes (**Figure 114A and B**) are screen-printed on the same stretchable substrate as the electrodes (TPU). They are used in this part to evaluate the impact of a mechanical constraint on the electrical properties of each stretchable and non-stretchable ink and their combinations. A homemade bench (**Figure 114C**) is used to clamp the probe (black zone) and stretch it up to 30% of initial track length (red zone) while measuring the electrical resistance at the contact (green zone). Particular attention has been paid to the fact that the electrical contact is made on the outside of the jaws and therefore on an area that is not mechanically stressed. Since elastomer handling is sometimes difficult, the substrate is placed on a laser-cut polyethylene terephthalate (PET) frame, then fixed on the tray. The frame is then cut off before the start of the tests (cut palstic strips visible in **Figure 115**).

Each probe is composed of two independent tracks allowing simultaneous measurements of different inks.

Learning from mistakes 🔍

Because of the high elongation imposed to the samples during tensile tests, clamping issues may occur leading to outlying results, usually electrical contact loss. As both tracks are clamped together on the bench, we can easily identify if a test failed due to a loose clamping (both tracks lose contact) or if the electrical loss indeed occurs on the loading zone. Although each test is in any case repeated 4 to 5 times, this feature helps judging results reliability.

Two tests probes are designed: the first one is composed of a Ag (L1) and a Ag+C (L1+L2) track (**Figure 114A**), while the second is composed of a Ag+dielectric (L1+L4) and a Ag+C+Ag/AgCl (L1+L2+L3) track (**Figure 114B**). The width of the track is representative of the weakest region of ITP electrodes geometry, which generally corresponds to the electrical track between the active surface and the electrical contact.

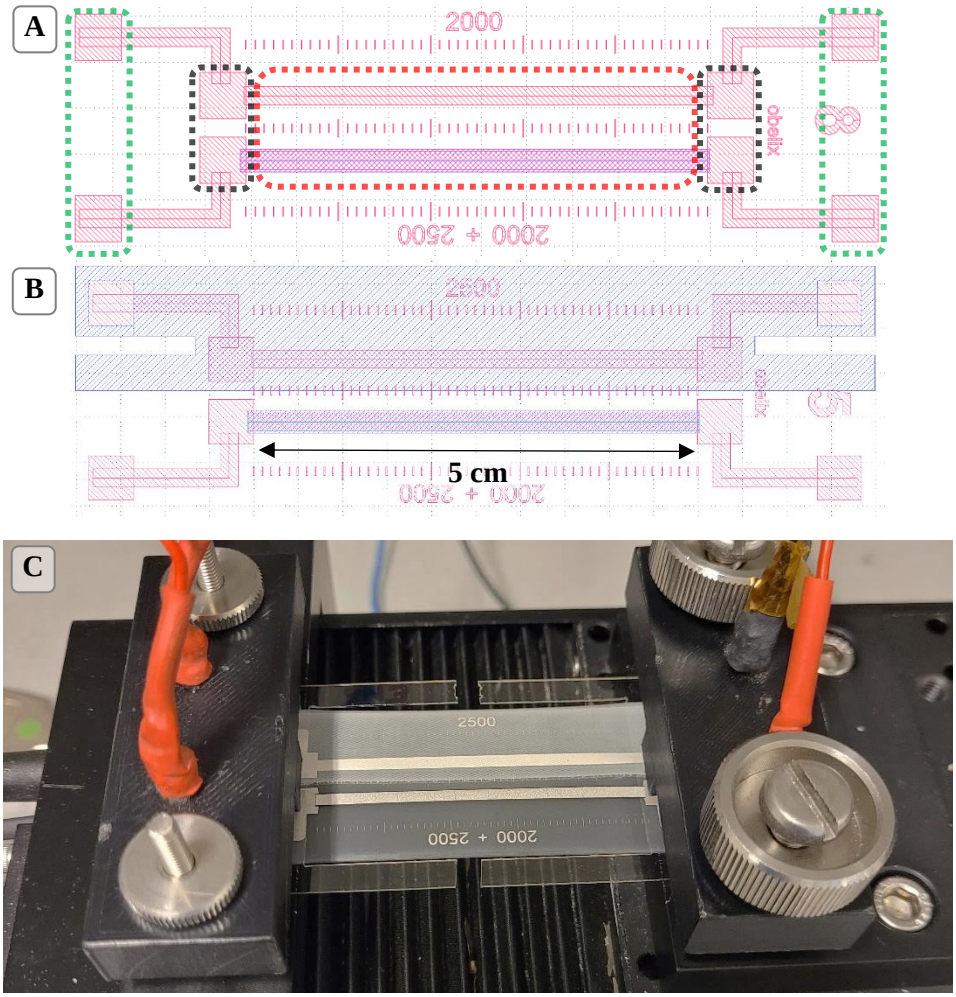

Figure 114. Mechanical testing probes of (A) L1 and L1+L2, (B) L1+L4 and L1+L2+L3, with the electrical contact for resistance measurement in green, the clamping zone in black and the loading zone in red. (C) Picture (by E. Neveux) of (B) installed on the homemade tensile/electrical bench

Two sets of experiments are performed on this bench: **cycling** and **relaxation** tests.

Cycling tests

In this part, the displacement of the jaw is actually controlled to mimic the tensile constraints that human skin can reach. Cycling tests are therefore designed to stretch the sample back and forth from 0 to 30% its initial length for 5 cycles. The table moves at approximately 0.1 $mm \cdot s^{-1}$ (quasi-static) and only the electrical resistance between both contacts is recorded every 10 seconds. Results are presented as the ratio of the electrical resistance measured (R) to the initial resistance (R0) between the electrical contacts, as a function of time and elongation. These plots help identifying and comparing the variation of electrical performance between 0 and 30% elongation for each stack.

The fact of cycling not only informs on the ability of the inks to resist such constraint, but also if they can resist the fatigue of a repeated “on and off” constraint.

Figure 115 shows the cycling results of a standard stack (A) compared to a semi-stretchable stack (B).

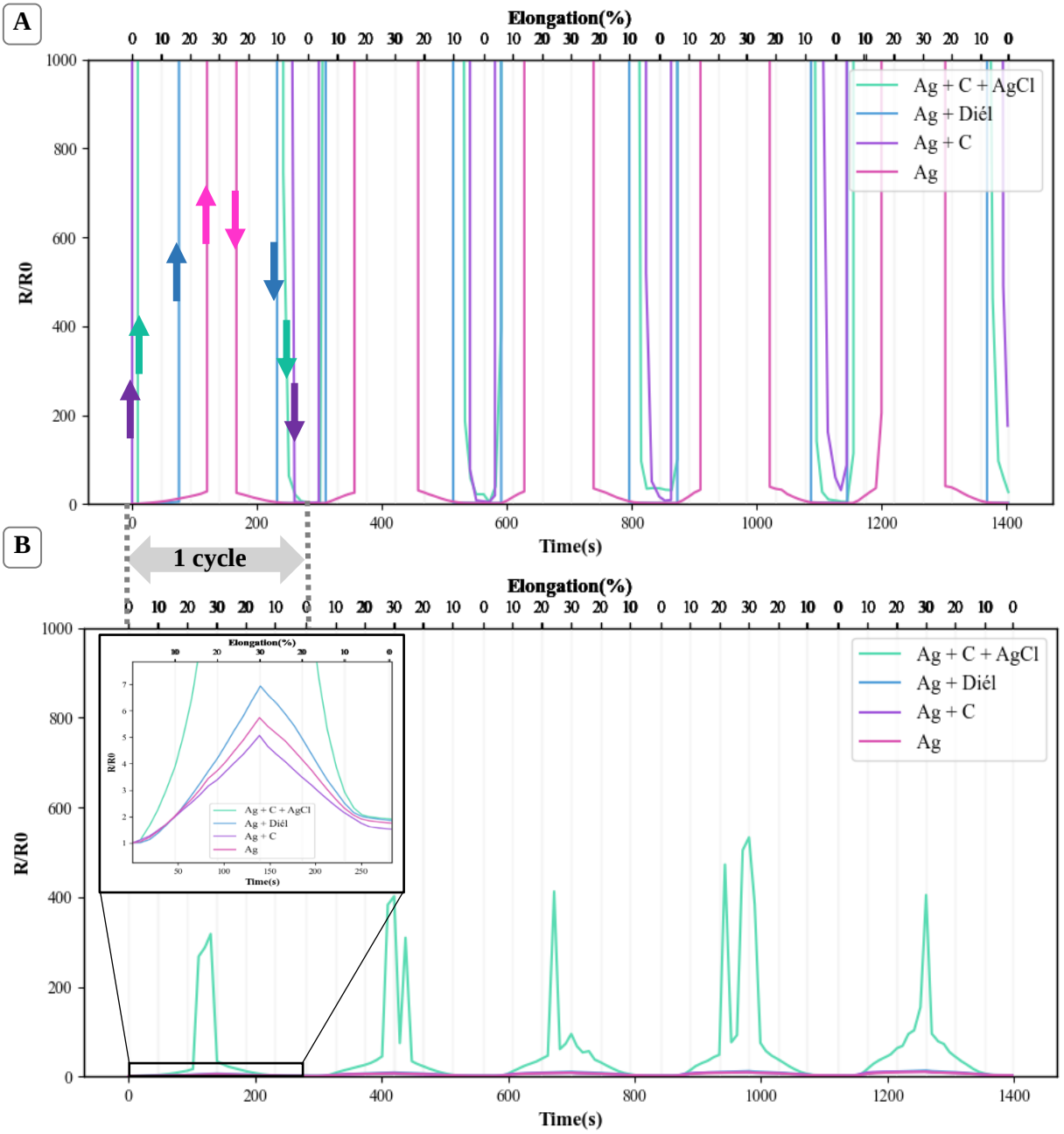

Figure 115. Evolution of R/R0 of (A) standard and (B) semi-stretchable stacks during 5 cycles of traction from 0 to 30%

Non-stretchable inks (**Figure 115A**) act like a power switch as the track is conductive at rest while the contact is lost once stretched. This phenomenon occurs on all testing probes, even though the conductive Ag layer alone (pink curve) only loses contact after 25% elongation in the first cycle, and 15% in the following cycles. Other probes combining multiple inks are even more sensitive to the tensile constraint and the track cracks below 5% elongation.

The semi-stretchable stack (**Figure 115B**) on the other hand displays a different behavior with bell-shaped curves. Stretchable inks (Ag, C and dielectric) remain conductive throughout the cycles, with an increase in electrical resistance of maximum 7 times the initial value in the first cycle (inset plot), and 15 times in the last cycle. When the non-stretchable Ag/AgCl ink is added on top though, this difference increases to a few hundred times the initial value. This observation proves that even though Ag and C inks are stretchable, the addition of a non-stretchable Ag/AgCl ink on top can change the mechanical (and therefore electrical) resistance of the stack. As the electrical contact is maintained throughout the test though, the SS stack is a more suitable alternative for a wearable ITP device than the standard one studied in Chapter 3.

To remember

In this part, mechanical testing probes were elongated up to 30% their initial length in a quasi-static manner, and back to their initial position for 5 cycles. The non-stretchable inks used in the standard stack show a very low mechanical resistance and the electrical contact is lost after a few percentage of elongation, but back once returned at the initial position. On the contrary, the semi-stretchable stack seems to resist to multiple elongation cycles, even though the electrical resistance increases, resulting in bell-shaped curves.

Relaxation tests

In these tests, R0 is measured at rest then samples are quickly stretched to 30% their initial length (dynamic). They remain at this position while the electrical resistance is measured every 35 seconds for 3.5 hours.

Results are only shown on the SS stack (**Figure 116**) since the standard stack loses electrical contact at 30% elongation and do not recover it during relaxation.

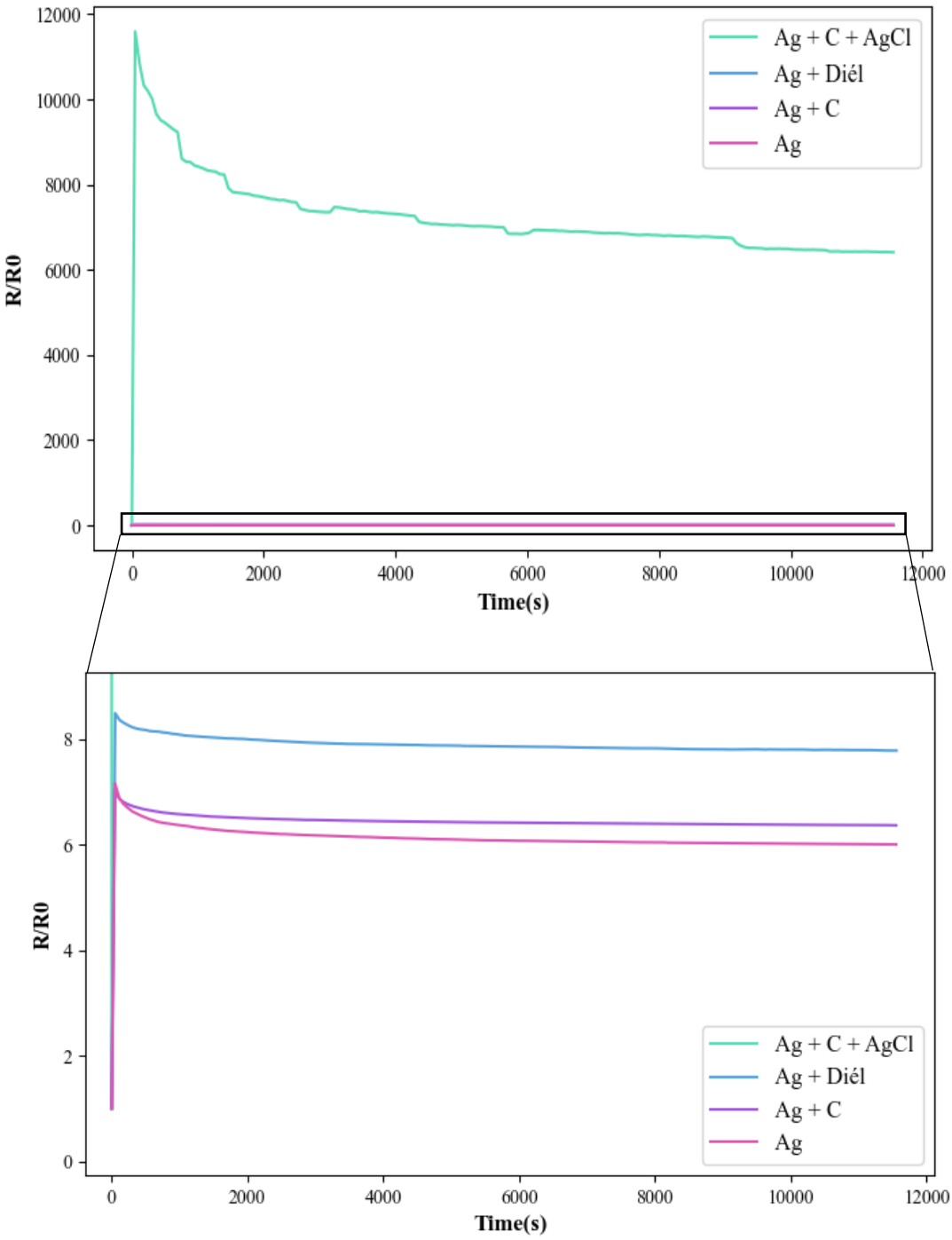

Figure 116. Evolution of R/R0 during relaxation of a semi-stretchable stack. Data by E. Neveux

We can first notice that in all cases, the maximum electrical resistance is higher than in cycling tests, especially for Ag+C+AgCl that almost reaches 12 kΩ. This phenomenon could be due to the difference in stretching speed as cycling and relaxation tests respectively use a quasi-static and dynamic configurations.

Then, the electrical resistance decreases over time. Interestingly, the curve profile is similar to a stress vs time curve of a viscoelastic material, where stress dissipates over time as relaxation occurs within polymer chains (GANGULY ET AL., 2020). Such behavior is described by the Maxwell model of viscoelastic material, composed of a spring and a dashpot in series (**Figure 117**) (PAPANICOLAOU AND ZAOUTSOS, 2019).

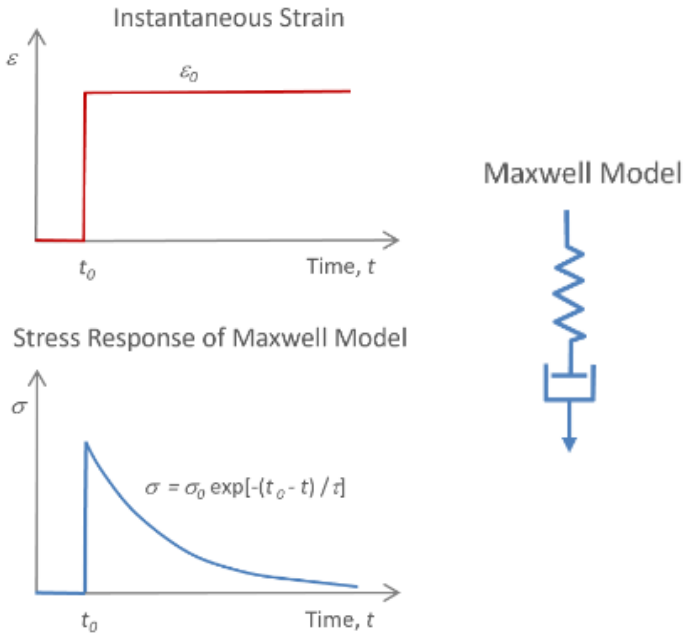

Figure 117. Maxwell model of viscoelastic material and associated stress-relaxation behavior to instantaneous strain. Drawings from https://polymerdatabase.com/

These rearrangements surely occur at the substrate level as TPU is known to display stress relaxation behavior (NASKAR AND DUTTA, 2014), but they can also occur in the elastomeric base of stretchable inks. Plastic deformation is also easily identified at the substrate level as the probe does not go back to its initial size by the end of the test.

In the presented tests though, **the electrical response is monitored instead of the stress response**. We can therefore assume that the molecular rearrangements within the polymer matrices progressively bring the metallic particles closer to each other, reducing the electrical resistance of the tracks.

In the case of stretchable inks (Ag, Ag+C and Ag+dielectric), the curve smoothly declines in 3.5 hours, with a reduction of around 16% of the maximum resistance. With the addition of a non-stretchable Ag/AgCl ink, the signal becomes more noisy and irregular. The stack loses around 40% of electrical resistance compared to the maximum value over time. This noisy response could either be due to internal cracks within the AgCl layer, or from the measurement itself as the resistance variation is higher than in the three other tests.

To remember 💡

Relaxation tests show the evidence of a viscoelastic behavior within the studied system, with a certain contribution from the substrate and possible chain rearrangements within stretchable inks as well. By the end of the 3.5-hour relaxation tests, stretchable inks keep a relatively consistent electrical performance with a smooth signal and electrical resistance variation. The resistance of the complete SS track (with Ag/AgCl) varies in a more significant and noisier fashion. This effect may be related to the dynamic deformation of the sample in the first place, causing more damage to the non-stretchable layer.

In both cycling and relaxation tests, it is important to understand how the electrical behavior observed translates on the electrochemical performance of the electrodes. L1 is therefore the most critical layer of the stack to ensure constant power supply either at rest or under constraint. When maintained under the maximum constraint human body can reach, L1 loses below 8 Ω in 3.5 hours. If a current density of 0.5 $mA \cdot cm^{-2}$ was to be applied on the track (1 cm^2 surface), the associated potential drop would correspond to 4 mV which is negligible to inhibit the desired electrochemical reactions.

Additionally, chronopotentiometry (CP) under constraint is also performed on new electrode geometries to study the influence of both electrode structure and ink composition.

5.1.1.2. New electrode designs

In this part, new electrode geometries are proposed to meet different needs for which the standard geometry was not suitable:

- Adaptation to uniplanar use (skin surface) with a symmetrical electrode consumption (anode and cathode in the same wearable device),
- Better current distribution with larger (1.5 mm) conductive grids,
- Resistance to skin tensile contraints (up to 30%),
- Inclusion of localised rigid components (MN array) to reduce the impact on device conformability,
- Enhanced delivery with larger electrode surfaces.

The associated layout named *Hatha* is presented in **Figure 118**.

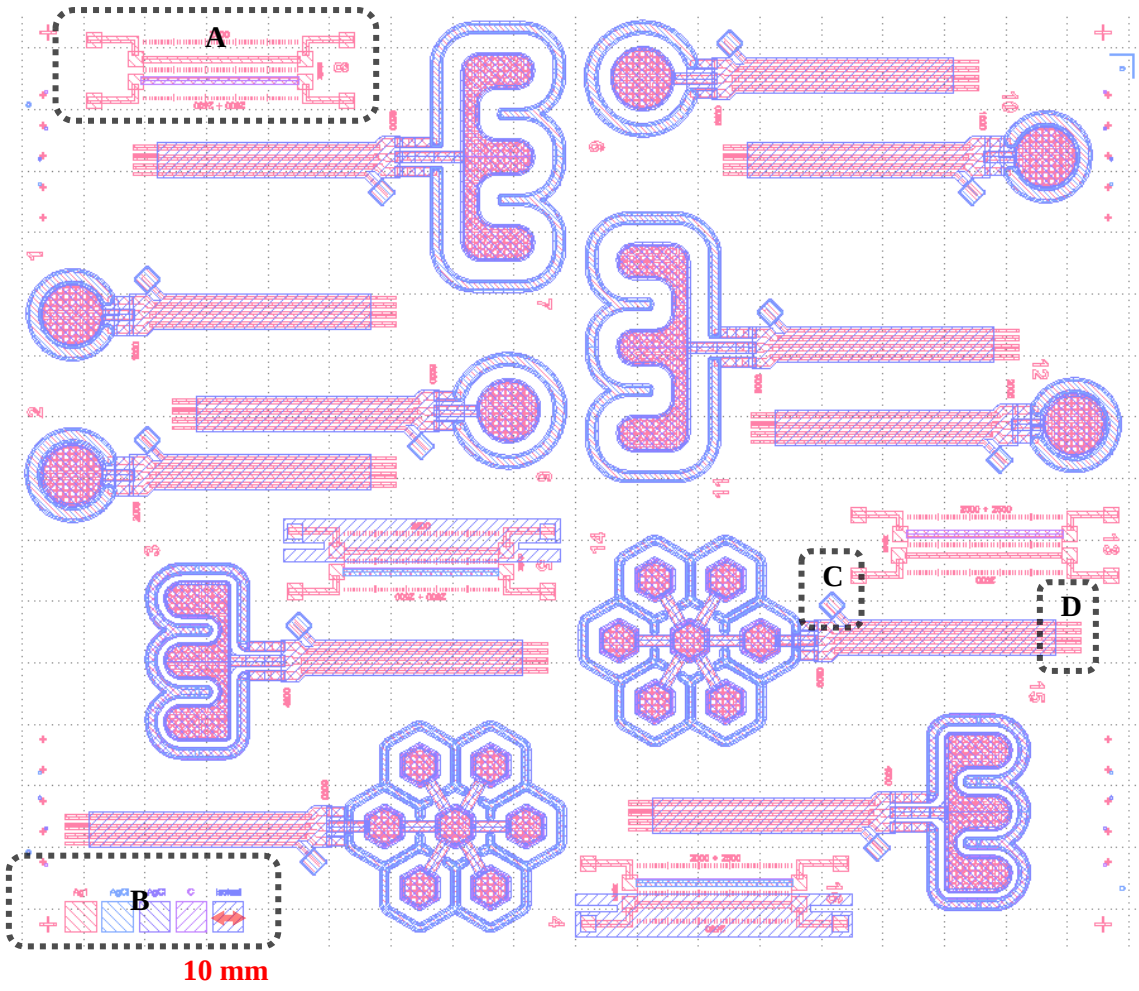

Figure 118. Complete four-layer *Hatha* layout for new ITP electrodes (A) mechanical testing probes (B) thickness probes (C) pseudo-reference electrodes (D) electrical contact

Similarly to the standard layout presented in Chapter 3 (**Figure 56**), mechanical testing (A) and thickness probes (B) are present. A 6 mm square Ag/AgCl pseudo-reference electrode (C) is added next to each ITP electrode to facilitate electrochemical monitoring. This electrode will not be subjected to mechanical

stress. Additionally, the electrical contact is designed and laser cut to be clipped into a **Z**ero **I**nsertion **F**orce (ZIF) connector (**Figure 119**) to replace alligator clips that can add a level of operator variability if not placed properly. The length of the electrical track is significantly extended compared to the standard geometry solely for characterization purposes, and may be reduced for the actual ITP application.

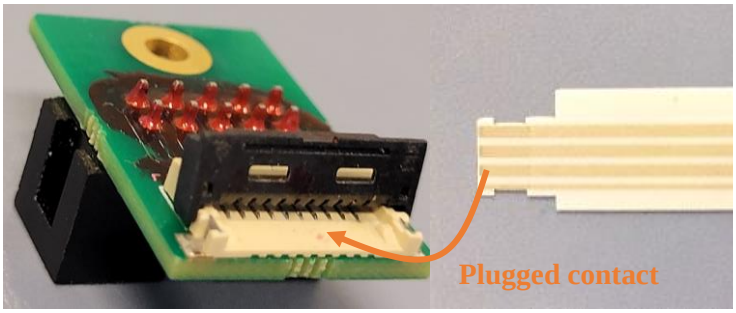

Figure 119. ZIF connector used for *Hatha* electrodes. Pictures by E. Neveux

Finally, the stack remains unchanged (Ag, C, Ag/AgCl, dielectric), with the exception of the grid size at the Ag conductive layer. According to numerical results obtained in Chapter 4 (**Figure 105**), a 1.5 mm wide grid (instead of 500 µm) could help creating more intense current peaks at the surface of large electrode and possibly increase the active surface area and reduce the electrode edge effect. It is placed below the central electrode only (**Figure 120**).

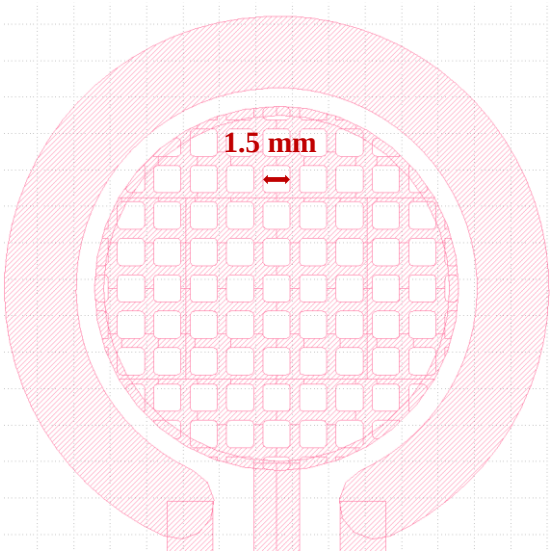

Figure 120. 1500 µm-wide conductive Ag (L1) grid on *Hatha* electrodes

Each electrode geometry is presented in the following paragraphs.

Ring-shaped electrodes

Chapter 4 (4.3.3) briefly introduced ring-shaped electrodes as a solution to provide a symmetrical redox consumption while keeping a large central electrode to place a drug reservoir or a MN array. The influence of the gap between the working (WE) and the counter (CE) electrodes on drug diffusion depth can be observed either by implementing mass transport to the numerical model, or experimentally using three different gap sizes (**Figure 121**).

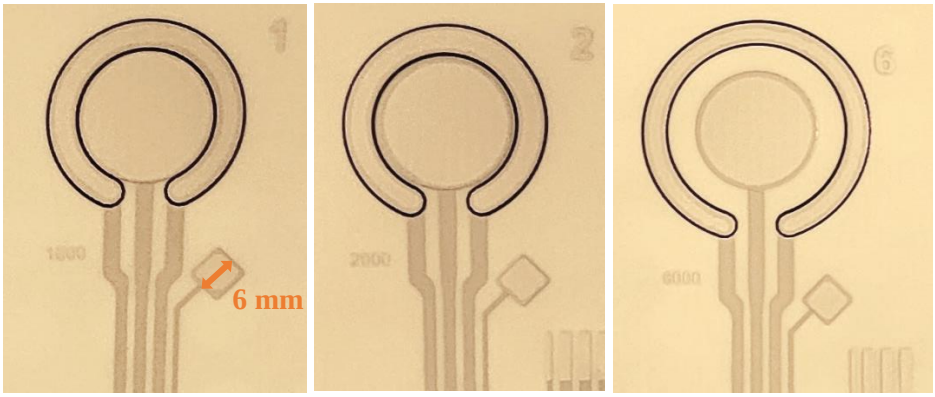

Figure 121. Pictures of ring-shaped electrodes with 1 mm (left), 2 mm (middle) and 6 mm (right) gaps. Pictures by E. Neveux.

Learning from mistakes 🔍

In practice, considering screen-printing process resolution as well as the carbon and dielectric overlap involved in the design, the 1 mm gap could not be produced reproducibly without short-cutting both electrodes. Ring-shaped electrodes with 2 and 6 mm gaps are therefore the only viable options ITP application. However, due to time constraints, only the 6 mm gap will be presented in this Chapter and the question regarding drug diffusion depth will remain open.

Comb-shaped electrodes

Also as previously mentioned, **I**nter**D**igitated **E**lectrode (IDE) are an interesting way to increase the contact area between two electrodes. An IDE-inspired comb-shaped electrode is therefore proposed for ITP application with a large central electrode to place MN arrays.

Figure 122 shows two gap sizes between WE and CE similarly to ring-shaped electrodes.

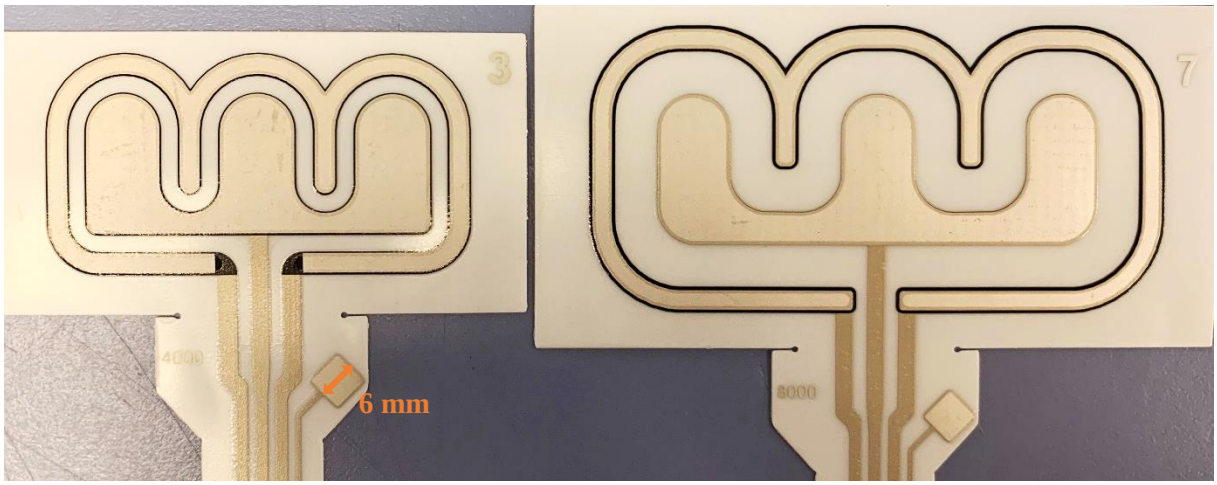

Figure 122. Comb-shaped electrodes with 4 mm (left) and 8 mm (right) gaps. N.B. The black (carbon) area on the left figure is due to a missing Ag/AgCl portion in the layout, but it does not affect the functionality of the device

Honeycomb-shaped electrodes

The last electrode geometry is inspired from honeycomb structure that is well known to hold tensile loads (DONG ET AL., 2021). The central electrode is composed of multiple cells where MN arrays could be placed, following "rigid islands" structure (MATSUHISA ET AL., 2019). Because of the volume and complexity of this structure, only a 6 mm gap size is considered (**Figure 123**).

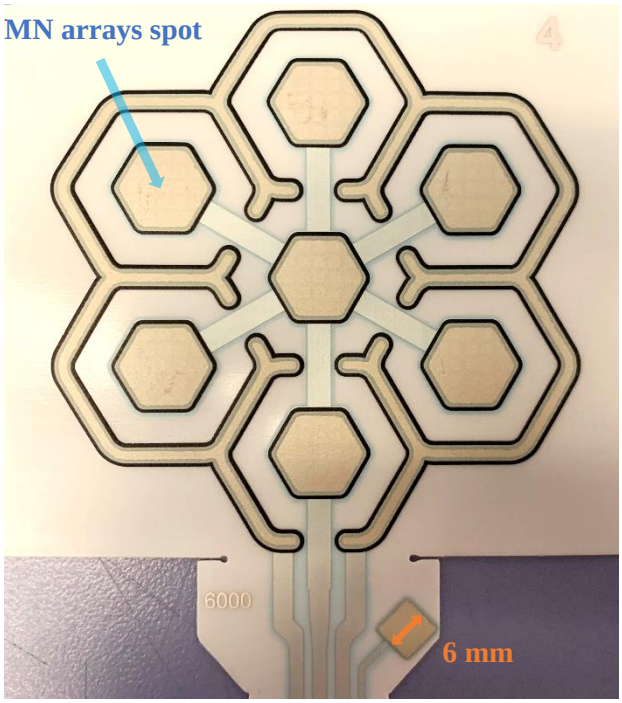

Figure 123. Honeycomb-shaped electrodes

5.1.2. Iontophoresis under constraint

Similarly to Chapter 3 (3.3.2), CP measurements are carried out to estimate electrodes performance or lifetime. For practical reasons, a handheld potentiostat (Palmsens4, Netherlands) is used for these tests to apply ~0.5 $mA \cdot cm^{-2}$ (rounded values) until reaching electrolysis. **Table 7** summarizes the surface area of each geometry and the associated current applied.

Table 7. Surface area and associated current applied in CP tests for each electrode geometry

Electrode geometry	Surface area of the WE (cm^2)	Applied current (mA)
Ring (all size)	2.8	1.5
Honeycomb	5.9	3.0
Small comb	6.3	3.0
Large comb	7.9	4.0

Measurements are performed both **at rest** (0% elongation) and **stretched** (30% elongation on the active area) manually on a 3D-printed tensile deck (**Figure 124**). Lifetimes are directly calculated on PSTrace software thanks to the time derivative function.

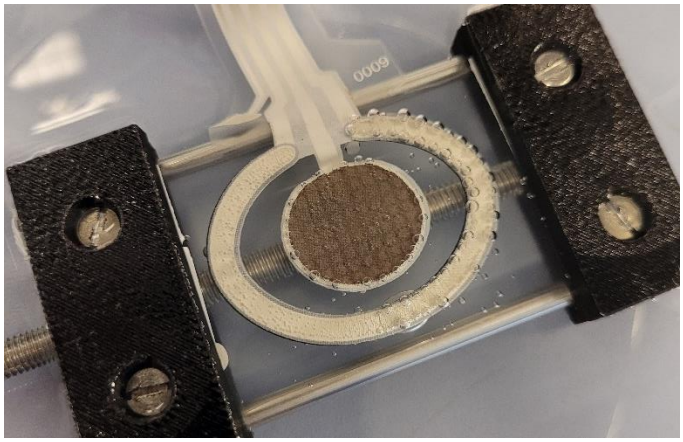

Figure 124. Example of ring-shaped electrode consumed in an electrolytic bath under tensile constraint. Picture by E. Neveux

5.1.2.1. Influence of stretchable inks

Ring-shaped electrodes with a 6 mm gap are first used to compare the following stacks:

- Standard (Dupont, DE, USA)
- Semi-stretchable (Dupont, DE, USA)
- Stretchable (Creative Materials, NY, USA)

As mentioned earlier, the only fully stretchable stack studied uses a stretchable Ag/AgCl ink (ref. 124-36) that is not explicitly developed for ITP applications. **Figure 125** shows that even though electrodes

performance seems constant with and without constraint on one measurement, lifetimes are significantly reduced (- 35 minutes) compared to the standard stack using an ITP-grade active layer.

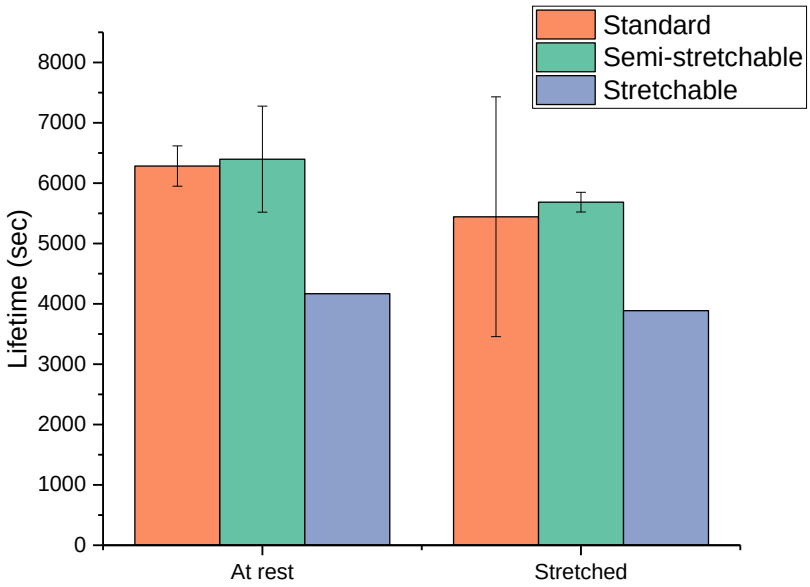

Figure 125. Lifetime comparison of standard (orange), semi-stretchable (green) and stretchable (blue) stacks on ring-shaped electrodes. Average on 3 tests for standard and semi-stretchable stacks

Concerning the standard stack, we can first notice on **Figure 125** that even without constraints, the variation between the three measurements is more significant (± 5.5 minutes) than in the previous geometry (± 1.1 minute) regardless of the potentiostat used. Further materials testing must be carried out on the new electrodes to understand the origin of these variations that can be due to the fabrication process (alignments, printing parameters,…) or the electrochemical characterization step (setup, electrolyte, temperature,…). In both steps though, operator variability may also occur.

Apart from this observation, we can clearly notice the important lifetime variability (± 30 minutes) on the stretched standard stack. This result proves that despite using a stretchable substrate, rigid inks cannot ensure a comparable performance when stretched or at rest.

Figure 126 shows visible cracks on the ring (red arrow), sectioning the outer electrode.

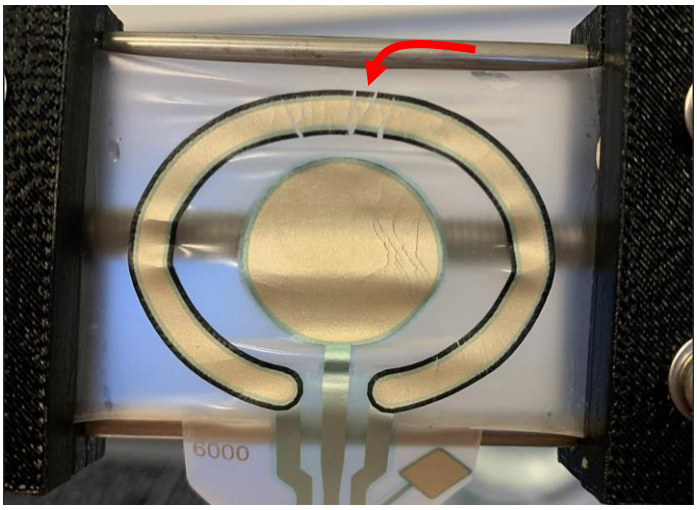

Figure 126. Cracks appearing on stretched ring-shaped electrodes with the standard stack

By changing the conductive, spacer and dielectric layer (respectively L1, L2 and L4) to stretchable inks (SS stack), electrodes performance when stretched become more consistent throughout the tests while keeping the average lifetime as satisfying as in the standard configuration. Surprisingly though, the variability at rest is higher than when stretched. This relatively high (± 13 minutes) standard deviation is caused by one measurement that gave a higher lifetime than the two others. Measurements should be repeated to obtain more reliable results.

Learning from mistakes 🔍

Because of all the elements included on the Hatha layout (3 different geometries, gap variations, testing probes), only 2 samples of each geometry were available for electrochemical testing for one printed batch. To provide more statistical data, a layout dedicated to one of these uniplanar geometries (e.g. ring-shaped) could be designed.

To remember ❗

CP measurements under tensile constraint show the limit of the standard stack that manifests unpredictable lifetime variability when stretched. A fully stretchable stack bypasses this drawback, but also reduces the overall electrode lifetime. The most suitable alternative is to keep the standard electrochemically active Ag/AgCl layer while using stretchable inks on the other levels (SS stack). In addition to the encouraging results previously obtained with the mechanical probes, electrochemical characterizations on SS ITP electrodes show comparable performances than the standard stack with reduced variability under constraint.

5.1.2.2. Influence of electrode geometry

The honeycomb-shaped electrode previously introduced (**Figure 123**) was designed to localize MN arrays acting as rigid islands. The stretchability of this structure is first studied with non-stretchable inks. Unfortunately, similar cracks as the ring-shaped electrode appear all over the outer electrode (**Figure 127A**) perpendicularly to the tensile force direction (yellow arrows). This effect drastically drops the electrode lifetime from almost 2 hours (± 6 seconds) to 11 minutes (± 4 minutes) (**Figure 127B**).

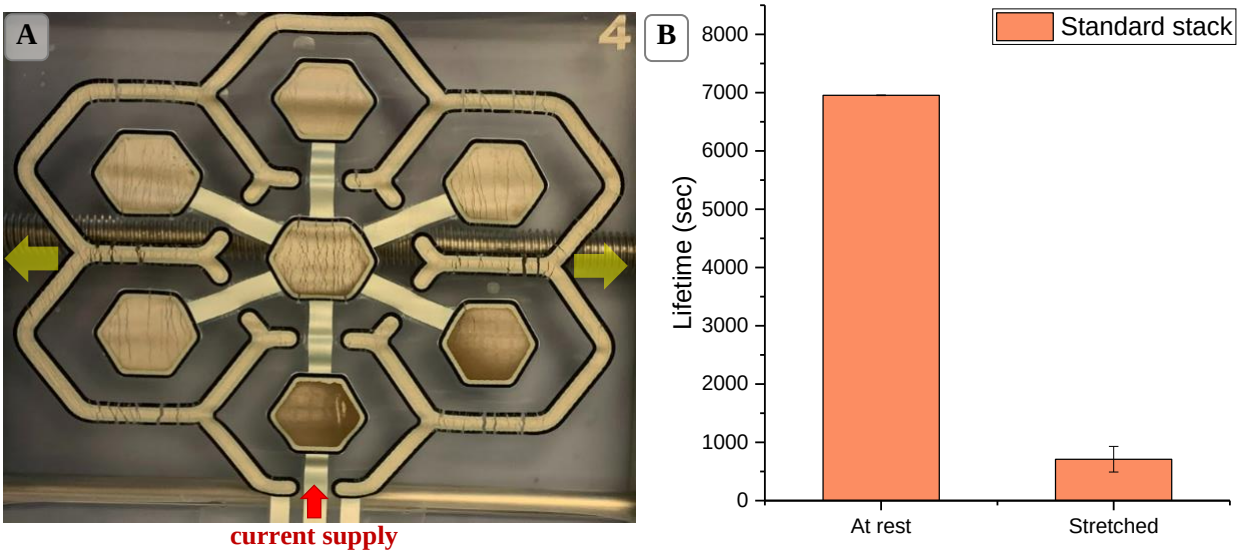

Figure 127. (A) Picture of an ongoing CP measurement on stretched honeycomb electrode and (B) Lifetime comparison of these electrodes at rest and stretched using a standard stack. Average on 2 tests

These discontinuities within the outer electrode does not allow a homogeneous consumption of the reagents, as the first power-supplied cells start to passivate (brown deposition) prior to the others.

We can argue that this phenomenon occurs due to the large surface of the electrode and the hard access of the current to the farthest cells. However, when using a SS stack, a more homogeneous electrode consumption is observed (**Figure 128A**).

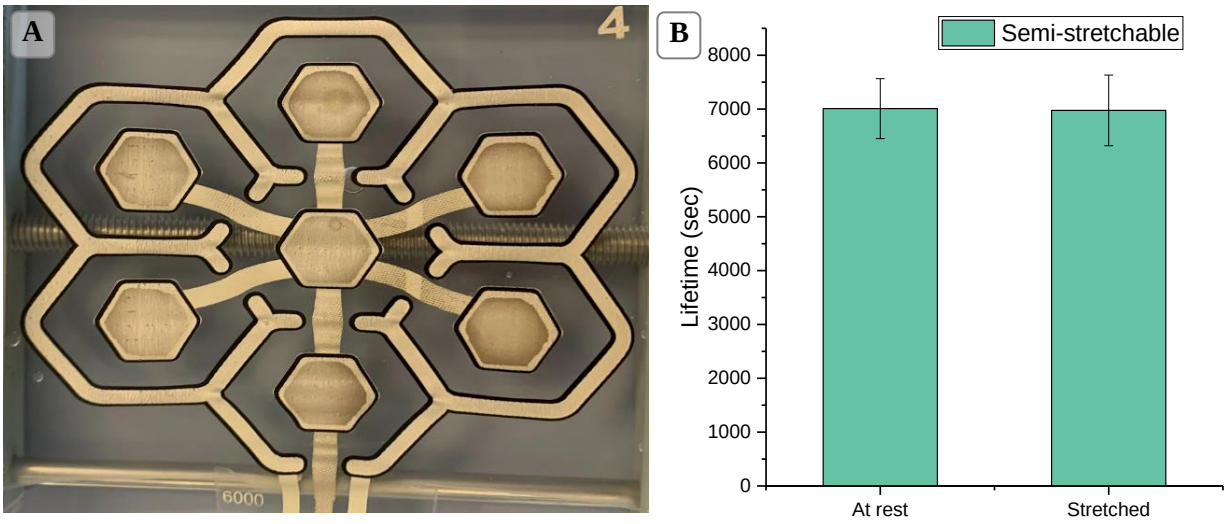

Figure 128. (A) Picture of an ongoing CP measurement on stretched honeycomb electrode and (B) Lifetime comparison of these electrodes at rest and stretched using a semi-stretchable stack. Average on 2 tests

Unlike the standard stack, only small cracks appear at the surface of the electrodes, probably generated at the Ag/AgCl layer (non-stretchable ink). The average lifetime and variability remain similar at rest and when stretched.

In other cases though, even the use of stretchable inks does not allow the structure to resist tensile constraints. For instance, SS comb-shaped electrodes display two weak zones at the inner electrode (red arrows), localizing the consumption at its center (**Figure 129A**). This zone is however not sectioned, as the reaction expands to the rest of the electrode once the central zone is passivated (**Figure 129**).

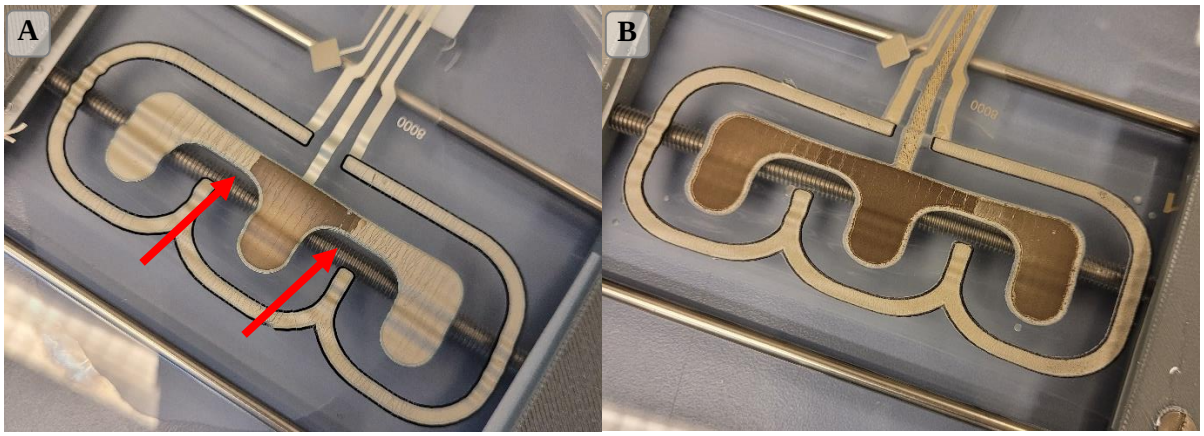

Figure 129. Pictures of a comb-shaped electrode using a semi-stretchable stack at different times of the reaction. (A) Consumption at the beginning of the test and (B) Consumption at the end of the test. Pictures by E. Neveux

To remember ❗

Honeycomb-shaped electrodes alone are not adapted to resist 30% elongation, as the outer electrode cracks perpendicularly to the constraint. By combining this structure with stretchable inks though, electrodes performance become reproducible either with or without constraint, with an average lifetime of up to 2 hours at the threshold current density for ITP. Stretchable inks alone may also fail to provide a consistent consumption with or without constraint, as shown in the case of comb-shaped electrodes.

This part therefore highlights that both **geometries and materials** must be carefully selected to develop a reliable wearable ITP device that maintains its performance regardless of skin tension and patient motion.

5.2. Towards transdermal delivery of proteins

The second part of this Chapter focuses on drug delivery application with the aim of administrating heavy compounds such as biomolecules or even micro-objects. Indeed, transdermal delivery is even more challenging for these types of compounds that are filtered by the SC, in opposition to small lipophilic compounds such as lidocaine or nicotine that are able to passively diffuse across the skin as mentioned in Chapter 1 (1.1.2.1).

First, the migration of a protein is quantified in different drug delivery configurations for relative comparisons in a diffusion gel which plays the role of a skin phantom. Then, a prospective device is proposed for a diabetic application, combining insulin delivery with a MN-based glucose sensor and an automatized interface respectively developed by two fellow PhD colleagues.

5.2.2. Delivery of a protein

The combination of ITP and MNs has been previously presented as a mean to deliver unusually heavy molecules for trandermal drug delivery (TDD) such as proteins. To verify this hypothesis, four major drug delivery setups are compared in this section (**Figure 130**).

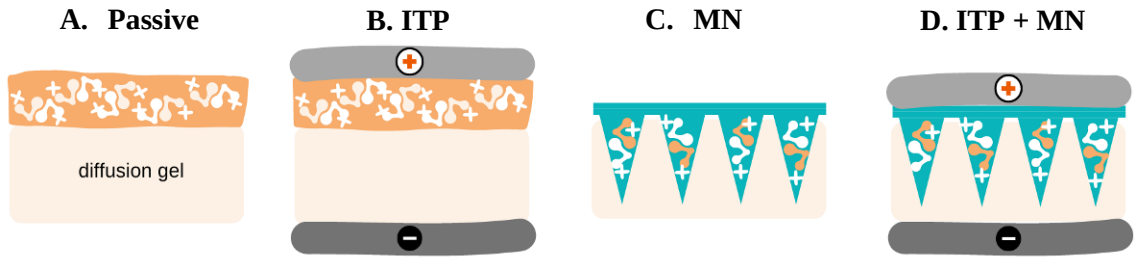

Figure 130. Drug delivery configurations compared. (A) Passive diffusion (B) Iontophoresis-assisted (C) Microneedle-assisted (D) Combination of iontophoresis and microneedles

A 10 g weight is added on top of each setup and each experiment is repeated three times. Electrodes used for ITP are semi-stretchable electrodes printed with the standard geometry (Chapter 3, 3.1) submitted to a constant current of 1 mA (Palmsens, Netherlands) with drug reservoirs placed under the working electrode (WE) to benefit from the effect of electroosmosis (KATIKANENI ET AL., 2009). For MN-assisted configurations, injection-molded arrays provided by Yamada Seiko Co. Ltd., Japan (Chapter 2, **Figure 33**).

5.2.2.1. Drug and skin models

Diffusion medium

As described in the literature review (Chapter 1, **1.1.1**), skin is a complex organ composed of multiple layers. Several artificial skin models are reported in the literature, but they all present benefits and drawbacks. A simplified agar-based solution is therefore used as a **diffusion model** to mimic skin density (CONDLIFFE ET AL., 2010). Such model allows the relative comparison of the diffusion rate of a molecule in the different configurations described on **Figure 130**. However, it is not representative of the mechanical behavior (viscoelasticity) of the skin, which means that these tests give no information on MNs ability to perforate the *stratum corneum*. For MNs used in this study, perforation success was previously validated on a multilayered commercial skin model (Chapter 2, **1.1.1.3**).

Protocol for formulating the diffusion patch

A 2 wt% agar gel is prepared by dissolving agar powder in PBS 1X. The mixture is boiled until transparent and poured in a petri dish. The gel is dried at room temperature for 1 hour, then covered and ready to use. 14 mm diameter disks are collected with a punch and used as a diffusion medium for each test.

Drug reservoir

In this part, bovine serum albumin (BSA) is used as a protein drug model due to its large molecular weight of 66,430 Da (TROMELIN ET AL., 2006). This biomolecule is often used in research for drug delivery as it is low cost, biocompatible, biodegradable and water soluble (ASSADPOUR AND JAFARI, 2019).

Protocol for preparing the BSA solution (MN delivery) and reservoir (passive and ITP delivery)

For MN-based delivery, ~150 µL of 1 $mg \cdot mL^{-1}$ BSA solution in PBS 1X is used so that the drug reservoir contains ~150 µg of BSA. **Figure 131** illustrates the following proceedings. Arrays are first placed on a holder to protect the MN tips (1). The drug solution is then poured at the back cavity of the array (2). The holder is finally placed in a vacuum bell for one minute, or until no more air bubbles are formed at the surface (3). A quick verification using a binocular microscope is made to ensure that MN ducts are properly filled.

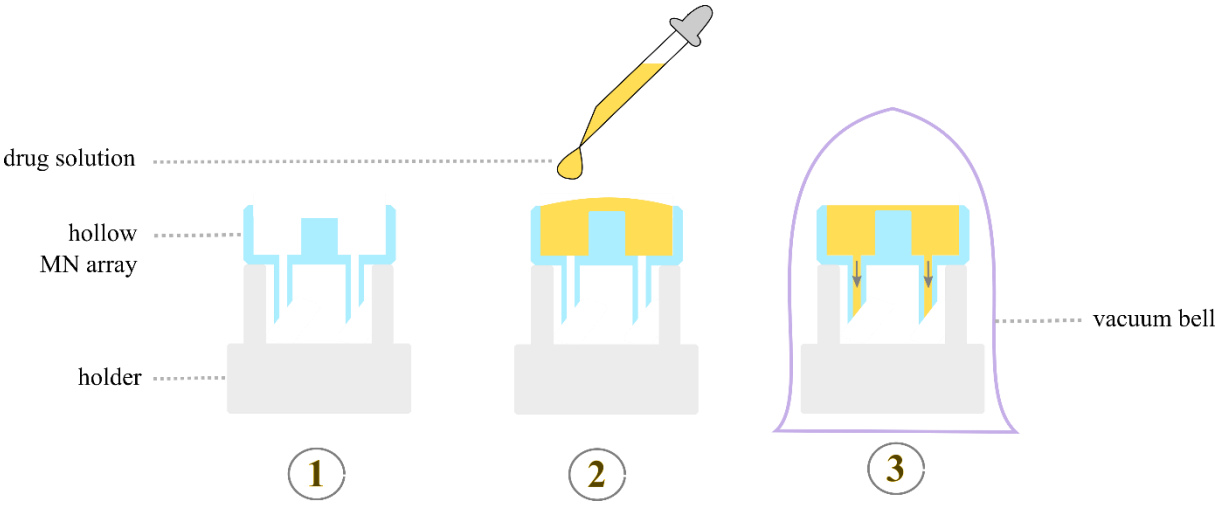

Figure 131. Drug loading proceeding on MN arrays. (1) The array is placed on a holder to protect MN tips (2) Drug solution is pipetted at the back of the array (3) The holder is placed in a vacuum bell to fill MN ducts and evacuate air bubbles

In other cases, a gel reservoir is prepared using a 2 wt% agar gel following the same protocol as for the diffusion medium. Once cooled at 60 °C (below the denaturation temperature of BSA, BORZOVA ET AL., 2016) a 2 $mg \cdot mL^{-1}$ solution of BSA in PBS 1X is added so that each 14 mm diameter disk cut contains ~150 µg of BSA. At the beginning of each test, all the reservoirs are weighted prior to the experiment to calculate the exact amount of BSA available for delivery.

Quantification methods

Different extraction and quantification methods (chromatography and spectroscopy) were explored in order to provide reliable and reproducible results regarding the quantity of drug delivered in the diffusion gel, and thus the efficiency of the drug delivery system.

High **P**erformance **L**iquid **C**hromatography (**HPLC**)

A quantification of BSA by HPLC (E2695, Waters, MA, USA) was first proposed according to protocols suggested in the literature (AL-RIMAWI, 2014; HAMIDI AND ZAREI, 2009) using a reversed-phase method (XTerra RP C18 4.6x150 mm, particle size 5 µm) and a gradient system. The elution program is set from 35 to 55% phase B in 15 minutes with phase A and B being respectively water (H_2O) and **AC**eto**N**itrile (**ACN**), both with 0.1 v% **T**ri**F**luoroacetic **A**cid (**TFA**).

Calibration

A first calibration curve is obtained by diluting a mother solution of 5 $mg \cdot mL^{-1}$ BSA in PBS 1X. The elution time of the compound is around 4.1 minutes. Each standard solution is measured 3 times and the associated chromatograms are shown in **Appendix 8**. The resulting calibration curve gives a satisfactory linear fit ($R^2 = 0.9989$) up to the 200 ppm (or $\mu g \cdot mL^{-1}$) (**Figure 132**).

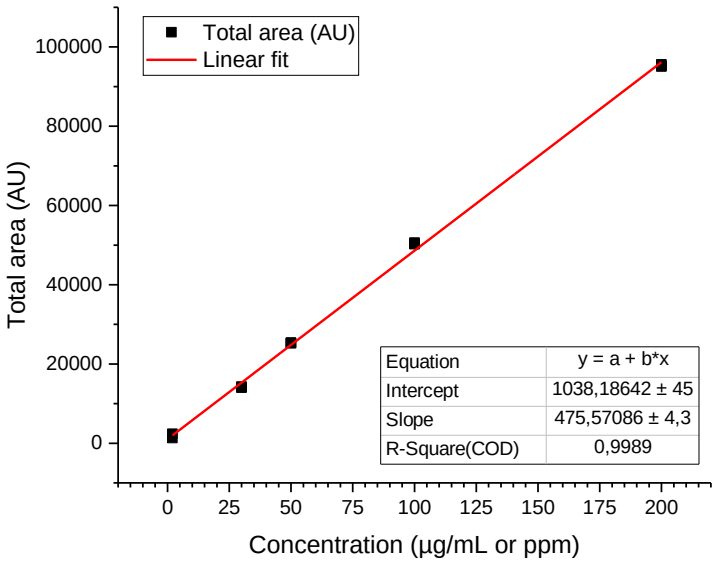

Figure 132. HPLC calibration curve using the area under the BSA peak until 200 ppm (linear region)

BSA extraction from the diffusion gel

In order to quantify the amount of drug that has actually migrated in the diffusion gel, BSA needs to be recovered from the agar into a solution for HPLC analysis. The most common strategy used to extract a molecule from a solid object is liquid/solid extraction. The extraction solvent is thus selected to solubilize the desired molecule.

Agar disks with a known amount of BSA (400 ppm) are placed in different solutions to define the most suitable extraction solvent among:

- H_2O
- ACN
- H_2O/ACN 50:50

Each of these solvents contains an additional 0.1 v% TFA to maximize protein recovery during HPLC (BOBÁLY ET AL., 2015). Considering the fragility of proteins, only mechanical stirring at room temperature is used overnight.

Similarly as standard solutions, samples are injected in the column and the area under the peak **at the same retention time (4.1 min)** is measured to calculate the extracted BSA using the calibration curve. We calculate the extraction efficiency as described in **Equation 26**:

$$Extraction\ efficiency\ (\%) = \frac{Extracted\ BSA\ (ppm)}{Initial\ concentration\ of\ BSA\ (ppm)} \times 100 \qquad (26)$$

Figure 133 shows that the extraction efficiencies obtained in each case are very poor (below 15%). Even though the solubility of BSA in water is high (40 $mg \cdot mL^{-1}$ according to SIGMA-ALDRICH, 1997), no BSA seems to be extracted from the agar gel.

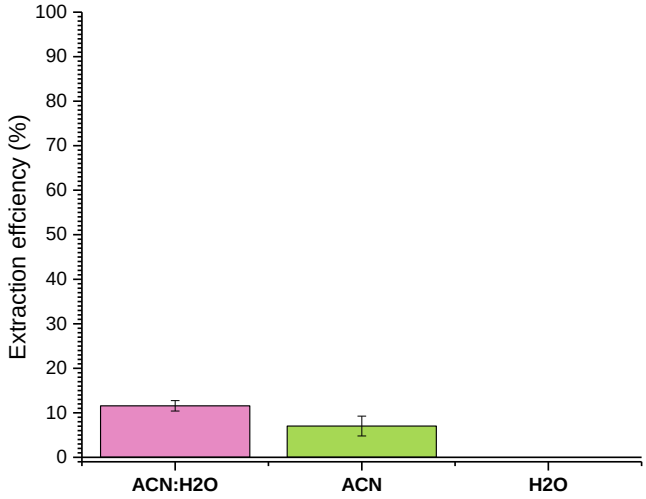

Figure 133. Liquid/solid extraction efficiency depending on the extraction solvent. Each solvent contains 0.1 v% TFA. Average on 3 samples

Actually, by looking at all the chromatograms combined (**Figure 134**), we can notice that the peaks obtained in the extracted samples (5.5 and 7.0 min) are not eluted at the same time as the peak associated with BSA with standard solutions (4.1 min). Even more surprisingly, the extracted samples that contain at most 400 ppm peaks are more intense than the most concentrated standard solution of 600 ppm.

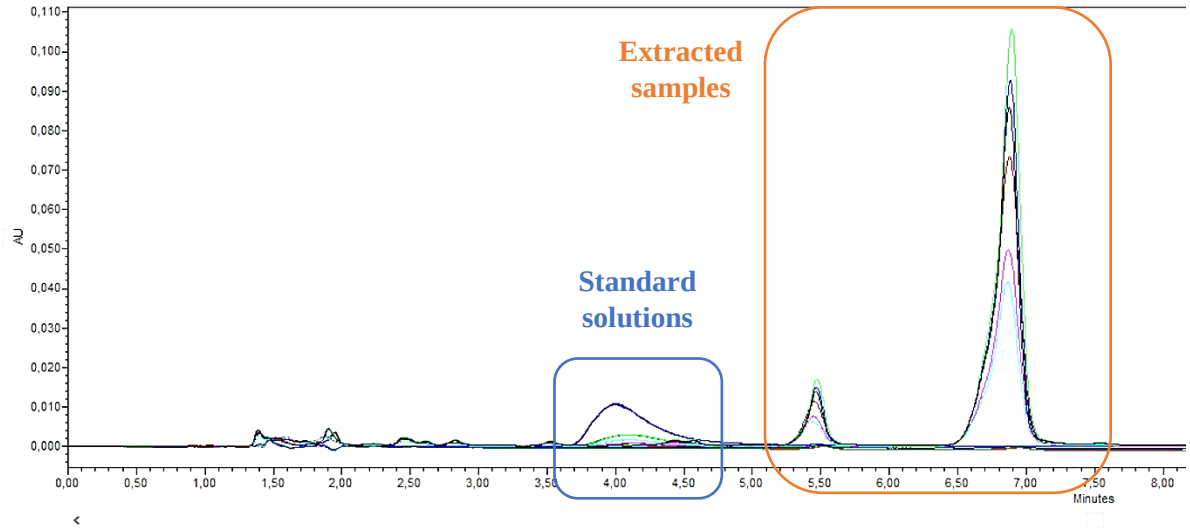

Figure 134. Superimposed chromatograms of standard solutions in PBS 1X (blue) and extracted samples in H_2O, ACN and ACN/H_2O (orange)

According to the literature, this phenomenon corresponds to the oligomerization of BSA, the triple peaks respectively representing the monomer, dimer and trimer forms of the protein (BHATTACHARYA ET AL., 2014; ZSOM, 1986). As many parameters (solvent, pH, temperature, stirring, steric repulsions,…) can cause this effect either prior, during or after drug delivery, an alternative quantification technique is preferable to quantify the overall amount of BSA without separating possible oligomers. The area under the three peaks could indeed be calculated and summed, but results dispersions may increase due to multi-step data processing.

To remember 💡

HPLC is first used to isolate and quantify BSA. A calibration curve is plotted with satisfactory linearity in the 2 to 200 ppm range. However, poor extraction efficiencies were recorded during liquid/solid extraction for all the solvents used (H_2O, ACN, H_2O/ACN). Actually, these results are due to the different elution times measured between the standard solutions and the extracted samples: monomer, dimer and trimer forms of BSA appear depending on the sample. HPLC is therefore not a suitable quantification method for this set of experiments.

Spectroscopy techniques: fluorescence and UV-visible

Definition 🕮

Spectroscopy *is defined as the science of absorption, emission and scattering of electromagnetic radiation by atoms and molecules (ZIELINKSI ET AL., 2023). In this part, two spectroscopy techniques are used:*

- ***Fluorescence spectroscopy*** *uses a fluorescent compound that emits a photon from its excited state. It is therefore important to know the excitation and emission wavelength of the used fluorophore to maximize signal intensity. Fluorimetry is a highly sensitive technique useful for trace analysis (ITAGAKI, 2000).*
- ***UV-Visible spectroscopy*** *is commonly used in analytical chemistry to obtain qualitative or quantitative information on a compound that absorbs light in the UV (200-400 nm) or the visible (400-800 nm) regions.*

In order to save time both on extraction and quantification steps, a commercial **F**luorescein **I**so**T**hio**C**yanate (**FITC)** labelled BSA (Sigma-Aldrich, MA, USA) is used in drug delivery tests along with spectroscopy analyses. In this configuration, the diffusion gel can be directly dissolved in spectroscopy grade TFA (Uvasol®, Sigma-Aldrich, MA, USA), which is also the best organic solvent to solublize BSA (> 50 $mg \cdot mL^{-1}$, HOUEN ET AL., 1996). Quantifying the label instead of the protein helps avoiding any dispersion in the results due to structural changes of the protein itself.

Measurements are carried out on a 96-well plate reader (Infinite M1000, Tecan, Switzerland). Each sample is measured at 12 different locations of the well (**Figure 135**) and the average value is calculated. If the standard deviation is unusually high (due to the higher concentrations at the well perimeter commonly observed with BSA), the measurement is repeated in another well.

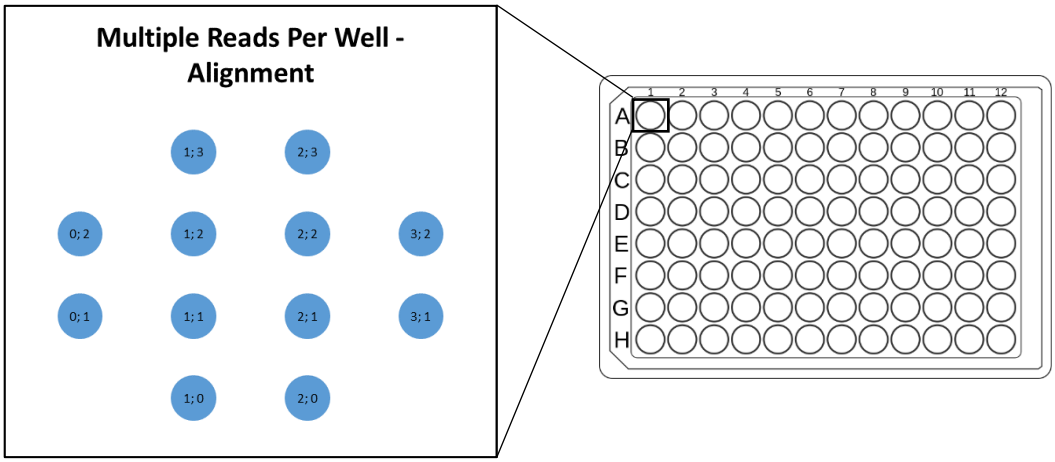

Figure 135. Alignment of measured points in each well

Fluorescence spectrosopy is initially used to quantify the amount of fluorescent label (FITC) present in the diffusion gel. Standard solutions are prepared in TFA to keep the same solvent environment in both standard and unknown samples. According to the excitation/emission spectra of FITC (**Figure 136A**), the respective excitation and emission wavelength used are 495 and 520 nm. **Figure 136B** shows that the calibration curve does not intercept the y axis anywhere close to zero, which means that the standard solution containing no FITC-BSA already emits a fluorescence response at the working wavelength. TFA is indeed reported to emit a fluorescence response at 520 nm (JUMAAH ET AL., 2022). A linear region can still be identified in the 100-300 ppm range.

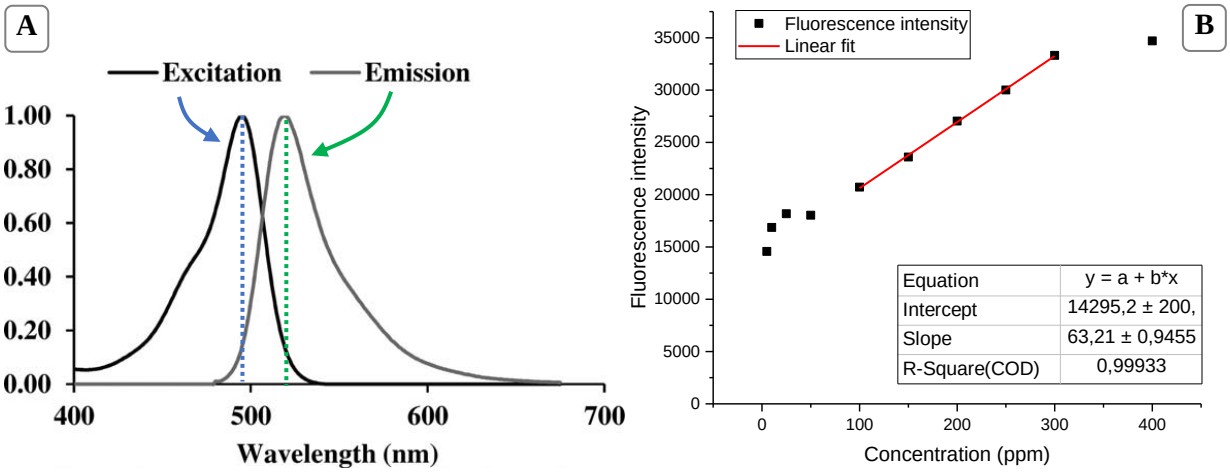

Figure 136. (A) Excitation/Emission spectra of FITC (Shams-Nateri and Piri, 2015) and (B) Fluorescence intensity of 10 standard solutions at excitation and emission wavelengths of 495 and 520 nm respectively

Besides, as the standard solutions prepared have a **visible** yellow color, we can also expect the samples to absorb light in the blue/indigo region. An alternative technique is therefore to choose a colorimetric calibration using UV-visible spectroscopy. A first wavelength scan is performed on the most concentrated solution to identify the maximum absorbance peak at 440 nm (**Figure 137A**). The colorimetric calibration curve on **Figure 137B** uses the exact same standard solutions as **Figure 136B**, and shows a very satisfactory linear fit ($R^2 = 0.9997$) in the 5 to 300 ppm range.

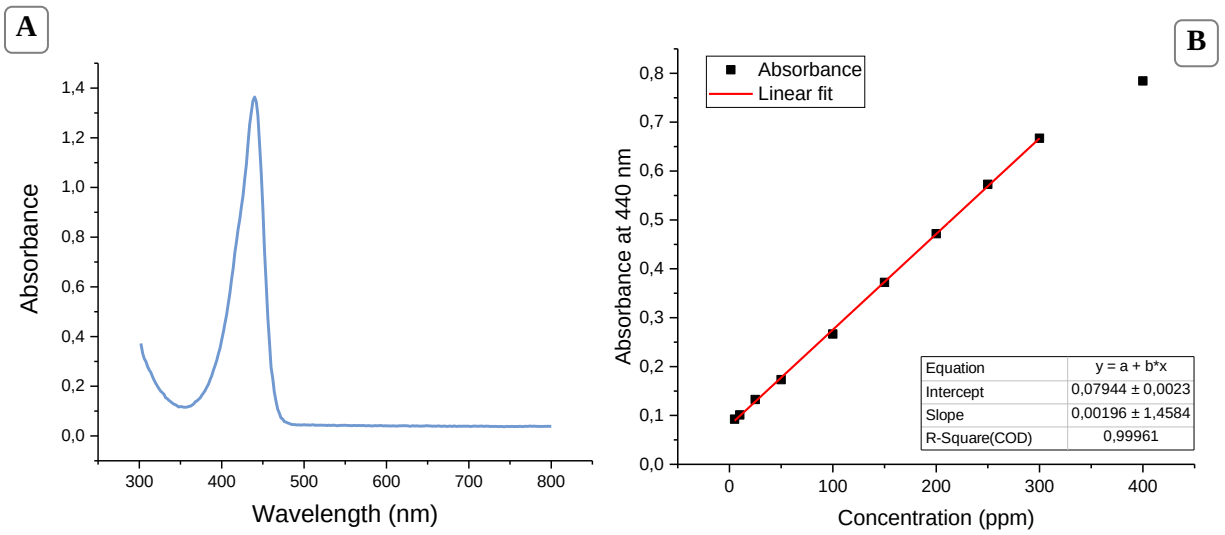

Figure 137. (A) Absorbance scan of FITC-BSA and (B) Associated calibration curve at 440 nm

In delivery experiments, the diffusion gel is dissolved in 500 µL TFA and each reservoir contains a maximum mass of drug of 150 µg, so all the samples analyzed contain less than 300 ppm FITC-BSA. In addition, the samples to analyze are not considered as complex, as the only other chemical compounds in solution are the salts contained in PBS and agar, that do not absorb light at 440 nm (SANSONETTI ET AL., 2021; YIN ET AL., 2012). This method is therefore suitable for these experiments and quantitative results are calculated according to the linear equation obtained (**Figure 137B**).

Learning from mistakes 🔍

*Each set of experiments actually requires a new calibration curve. Standard solutions need indeed to be prepared and measured along with unknown samples to reduce possible errors due to solvent evaporation as **TFA is highly volatile**. Uncertainties due to the spectrometer itself are also avoided, as the lamp power may change in several months.*

5.2.2.2. Quantitative results

To compare the amount of FITC-BSA that has successfully migrated in the diffusion gel, delivery efficiency is calculated as follows **(Equation 27)**:

$$Delivery\ efficiency\ (\%) = \frac{Concentration\ of\ BSA\ quantified\ (ppm)}{Concentration\ of\ BSA\ initially\ in\ the\ reservoir\ (ppm)} \times 100 \quad (27)$$

First protein delivery attempt

In the first set of experiments, passive diffusion is compared to ITP, MN and their combination. Each experiment is conducted for **one hour** and repeated three times. The average delivery efficiencies and associated standard deviations are summarized on **Figure 138**.

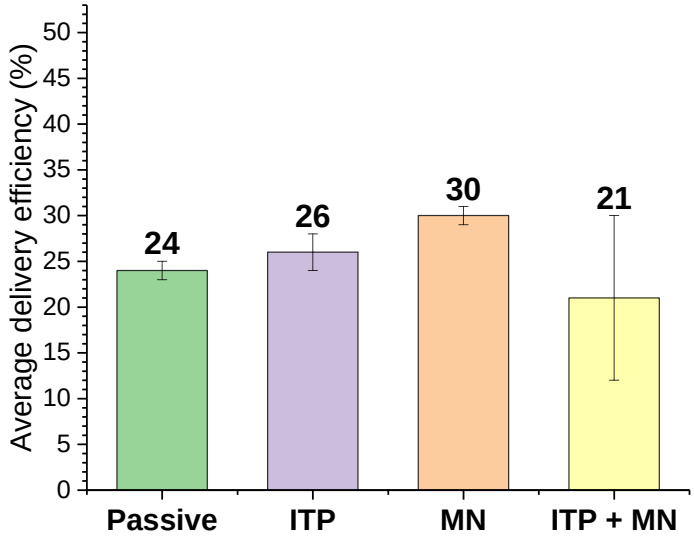

Figure 138. Average FITC-BSA delivery efficiency after 1 hour in each configuration: passive, iontophoresis-assisted (ITP), microneedle-assisted (MN) and their combination (ITP+MN)

This set of experiments gives the following information:

- It first shows that for all configurations, around a fourth of the reservoir is transferred to the diffusion gel.
- While results are quite reproducible for passive, ITP and MN-assisted delivery, variations are higher when ITP and MNs are combined. This variability may be due to the ITP/MN interface that is only granted by suction of the electrolyte contained in the MN array on the electrode surface. No additional adhesive is used in this case to maintain both objects.
- We can also observe during the experiments that the liquid contained inside the tip of the MNs diffuse in the gel while the liquid present above the needles does not seem to easily flow.

Intermediate experiments

To solve the problems mentioned above, preliminary experiments are carried out prior to the second drug delivery attempt.

A surfactant, Tween 20 (Sigma-Aldrich, MA, USA) is added to PBS at 1 v% to reduce the surface tension between the wall of the PLLA MNs and the aqueous drug solution. The reduction of the contact angle on a PLLA sheet is indeed observed by drop shape analysis (DSA25E, Krüss, Germany) as depicted on **Figure 139**.

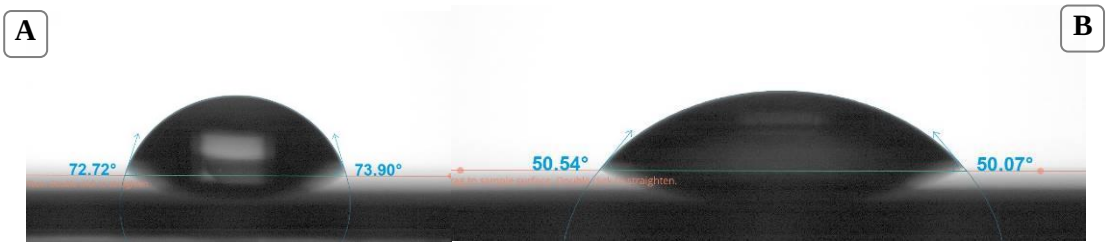

Figure 139. Comparison of the contact angle on PLLA of a 5 µl droplet of (A) PBS 1X and (B) PBS 1X + 1v% Tween 20 (not to scale)

Delivery on a single 45-minute experiment gives promising results compared to the initial MN configuration (**Figure 140**). A triplicate will therefore be carried out in the second attempt.

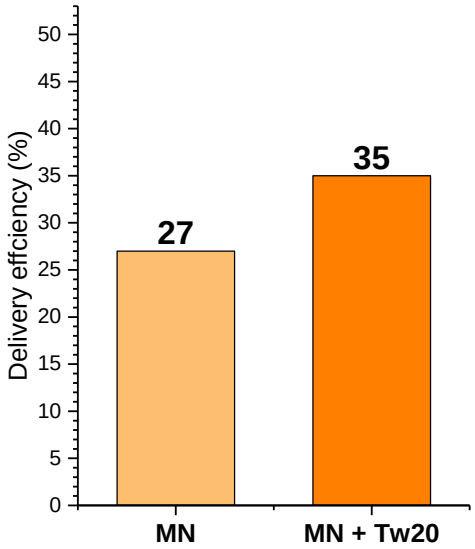

Figure 140. Comparison of delivery efficiencies in MN configuration with and without surfactant (Tween 20)

Two conductive gels are also studied to improve the electrical interface between the WE and the diffusion gel or MN array: a hydrogel (Axelgaard, CA, USA) and a dry gel (35 µm thickness, Henkel, Germany), both in the form of thin sheets. These gels are first compared in the ITP configuration and only used on the WE. We can first notice during the experiment that the hydrogel swells once in contact

with liquid, while the dry gel keeps its initial thickness. **Figure 141A** also shows that the delivery performance seems reduced when using the hydrogel at the electrode/gel interface. The **D**ry **G**el (**DG**) though gives similar results as ITP alone. It will therefore be used only at the interface between ITP electrode and MN array for the second set of experiments, as depicted on **Figure 141B**.

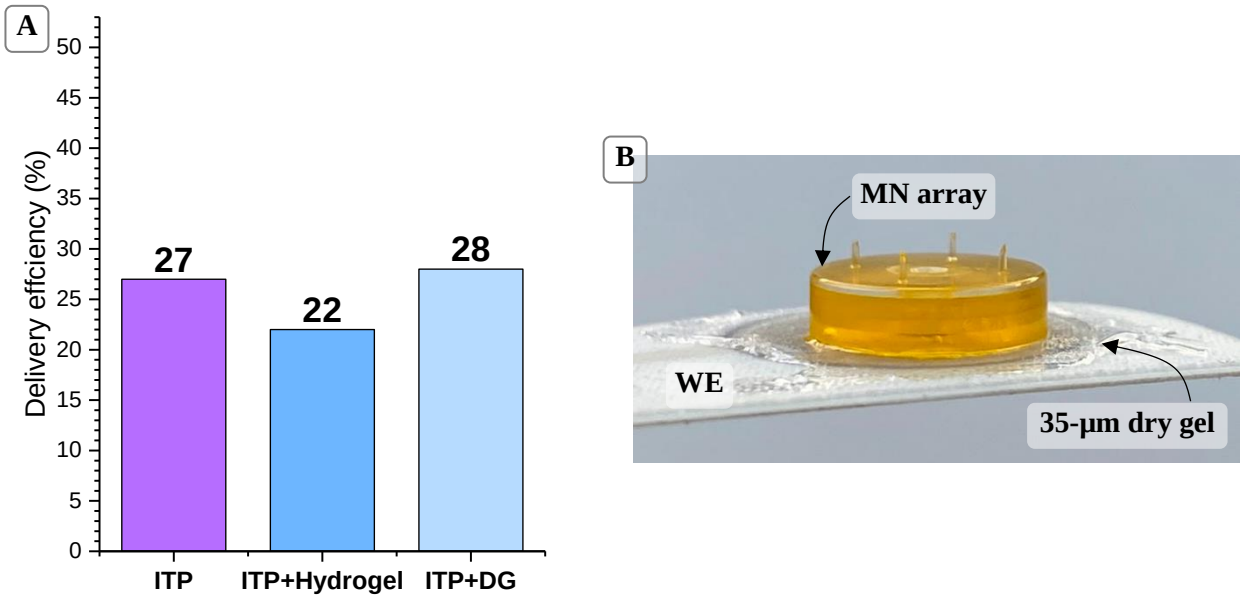

Figure 141. (A) Comparison of delivery efficiencies in ITP configuration with and without a conductive gel (hydrogel or dry gel (DG)). (B) Picture of the ITP+MN configuration using a dry gel at the interface

Second protein delivery attempt

A second set of experiments is carried out similarly to the first attempt, but by adding 1 v% surfactant (Tween 20) in MN-based configurations and a conductive dry gel (DG) at the MN/ITP interface. **Figure 142** summarizes the average delivery efficiency on three experiments performed for **45 minutes**. Compared to the previous attempt, the experiment time is reduced due to the lack of stability of the weight placed on top of MN arrays when used alone. This unstability is probably responsible for the larger result variability (standard deviation) for MN alone compared to the first attempt.

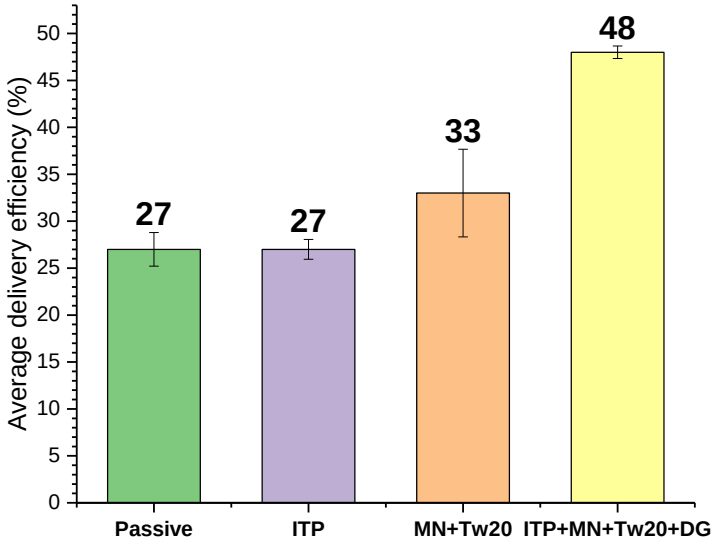

Figure 142. Average FITC-BSA delivery efficiency after 45 minutes in each configuration. MNs contain 1% surfactant in solution, while ITP+MN use both 1% surfactant and a conductive gel at their interface

Finally, the combination of ITP and MN shows promising results with the addition of both surfactant in the drug reservoir and conductive gel at the electrode/array interface. Almost half of the reservoir is delivered in 45 minutes. This significant improvement is also visible with the naked eye, with the migration of the yellow compound up to the bottom of the diffusion gel (**Figure 143**).

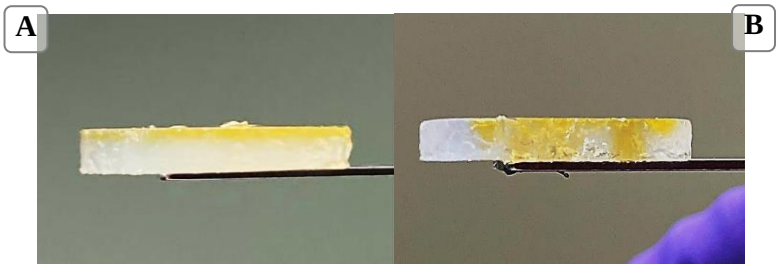

Figure 143. Pictures of the diffusion gel at the end of the experiment for (A) passive and (B) active (ITP+MN+Tw20+DG) diffusion

With a bit more time… ⧖

Two other sets of experiments could be designed to gather more information on the techniques compared:

- The **diffusion depth** of each technique can be estimated by quantifying gel layers instead of the whole diffusion gel. Thick layers (> 200 µm) or thin layers (< 60 µm) could be respectively cut with a vibratome or a microtome. These experiments could give a quantitative approach to the observations made on **Figure 143**. A thicker diffusion gel should therefore be used to prevent the drug from reaching the bottom of the sample.
- A sweep in **delivery time** could be implemented to plot delivery efficiency as a function of delivery time. We expect the results to discriminate each technique depending on the associated drug diffusion rate and identify the most suitable candidate for different time ranges. Such characterizations were previously made by DONNELLY ET AL., 2012 on 24 hours (Chapter 1, **Figure 29**), showing a significant difference in drug permeation (among which FITC-BSA and insulin) only after multiple hours of diffusion.

5.2.3. Perspectives: Integration of glucose sensor and insulin delivery

To develop a useful and practical device for patients with diabetes, a more complete system should be investigated to combine glucose sensor with insulin delivery. Such devices already exist on the market subcutaneously (Libre Sense, Abbott, IL, USA), but not yet transdermally.

In my Laboratory, an additional side project has therefore been initiated along with two fellow PhD students: Bastien Darmau and Pierre Bouvet.

Bastien's PhD project consists in developing a transdermal biosensor for electrochemical glucose monitoring by amperometry. Swellable MNs are used to extract interstitial fluids (ISF) by capillarity towards the glucose-selective biosensor. At the lab scale, he could prove using glucose spikes that his device has a sensitivity of 1.62 ± 0.01 µA·mM^{-1}·cm^{-2} (**Figure 144**).

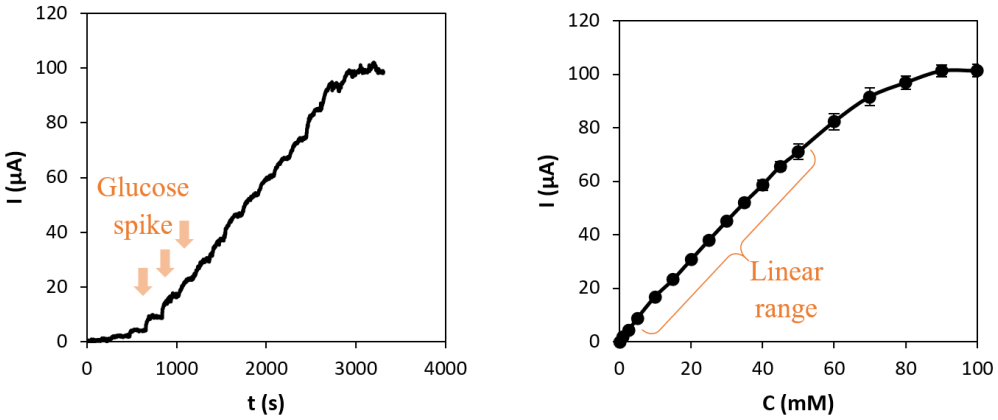

Figure 144. (A) Sensor amperometric response to glucose spikes and (B) Associated calibration curve. B. Darmau PhD project

By combining this technology with the ITP+MN-assisted delivery setup proposed earlier, both sensing and drug delivery could be controlled simultaneously with a single generator.

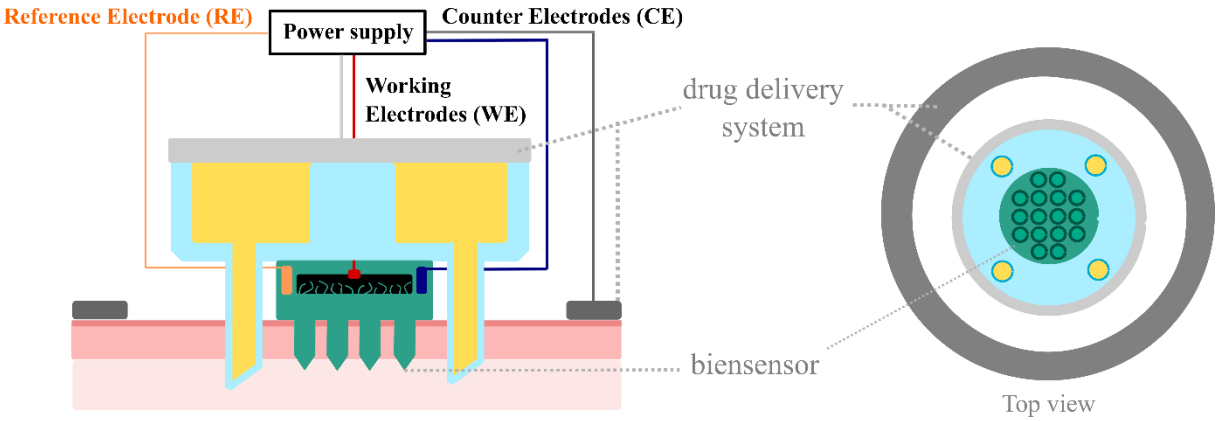

Figure 145. Schematic representation of the electrochemical device combining MN-based glucose biosensor and insulin drug delivery

Additionally, Pierre started to develop a Python program to define as a threshold value (for example 140 $mg \cdot dl^{-1}$ (LAKHANI ET AL., 2018)) above which ITP is initiated. Once the glucose level is back below the threshold, drug delivery can be stopped while glucose monitoring is maintained. On the long run, personalized medicine could even be developed as monitoring could be followed on a smartphone. In this case, both nutritional information directly implemented by the user and machine learning could be used to predict the glucose level of the patient throughout the day, along with a suitable drug delivery response. This kind of artificial intelligence is already used with hypodermal glucose sensors and insulin pumps, especially with the creation of the company Diabeloop in 2015 from CEA-Leti labs.

The realistic efficiency of our device could not be experimentally proven, as *in vivo* experiments are not included in this thesis work. Other studies mentioned in Chapter 1 (**Figure 30**) successfully used similar integrated device to witness the effect of insulin delivery on blood glucose level on diabetic rats (LI ET AL., 2021), consistent with the results previously obtained with FITC-BSA.

Hopefully, the development of tissue engineering will enable similar experiments to be carried out at the lab scale without implying animal testing in the early stages of research. Testing devices can therefore be designed to couple the monitoring of MN perforation, drug delivery and therapeutic effect on biological tissues.

Conclusion

This final chapter studies two use cases in parallel.

In the first part, ITP electrode geometries adapted to a uniplanar use are designed, printed and characterized under tensile stress to mimic the maximal mechanical constraint that a human arm could reach. Stretchable inks are implemented to the stack to provide additional tensile strength. The semi-stretchable stack (non-stretchable active layer only) seems to be the best compromise between stretchability and performance as it allows a better mechanical resistance in the weakest regions (thin outer electrode). This stack also helps maintaining a similar electrode lifetime with and without constraint.

In the second part of the chapter, BSA migration is monitored using passive, MN-assisted, ITP-assisted and ITP+MN-assisted delivery. Promising results are obtained in the latter case, with almost half of the drug reservoir delivered in 45 minutes. The integration of both technologies required further adjustments though, such as the addition of a conductive adhesive gel at the electrode/array interface and a surfactant in the drug reservoir. Finally, a prototype of a combined MN-based glucose sensor and insulin delivery is discussed.

Overall, this chapter helps getting closer to the desired application and opens the doors to future engineering development to integrate both technologies on a single wearable device.

Conclusions, critical analysis and perspectives

Conclusions

In this thesis, microneedles (MNs) and iontophoresis (ITP) are studied in parallel before finally being coupled for preliminary protein permeation studies.

Regarding MNs, we first studied the *in vitro* perforation efficiency of different polymer formulations compared to silicon MNs on human abdomen skin explant. Even though their mechanical strength needs to be checked beforehand, polymer MNs can indeed offer similar performances while providing additional functions such as dissolution or swelling to free the active principle to deliver. In a second phase, we were interested in the ability to upscale this technology for future industrial expansion. More specifically, the fabrication of hollow polymer MNs was investigated as they are usually mentioned as more challenging to manufacture. They also have the advantage to be adaptable to different applications post-processing unlike dissolving and swellable MNs that contain the drug of interest within their matrix. Injection molding and thermoforming therefore appear as suitable options, which is a good news to reduce the production cost of such device in the long run. High-resolution 3D-printing (more specifically vat polymerization) can also become a more customizable alternative with the development of photocurable biobased, biocompatible and bioresorbable polymers.

In comparison to MNs, ITP is an older technology yet not well known by the public. Research papers associated to this subject identified water electrolysis as parasitic reactions responsible for extreme pH variations and skin burns. Ag/AgCl electrodes are therefore presented as a safer alternative as their electrochemical consumption is more favorable than water's. It inevitably implies that these electrodes have a limited lifetime though. In this study, flexible and stretchable Ag/AgCl electrodes are screen-printed and electrochemically characterized to identify their lifetime and means to increase it. Numerical simulations are complementarily used to spatially visualize the current density distribution depending on input signals (AC or DC) and electrodes geometry to avoid additional risks of burns. The latest model developed combines ITP and MN, showing promising results in this regard as the current density is concentrated within MN ducts. Finally, we studied the ability of stretchable electrodes to perform under tensile stress, as patients' motion should not affect drug delivery efficiency.

Finally, a simple drug diffusion setup is used to compare protein permeation using passive, ITP, MN, and ITP+MN configurations. This part highlights that the combination of both technologies can indeed be efficient for such application as long as some improvements are implemented on the device. For instance, a surfactant can be added to the reservoir to improve liquid flow in MN cavities. A conductive adhesive gel is also used in a second stage at the ITP/MN interface to ensure electrical continuity.

In general, this project leads to optimistic results as it identified both technologies as industrially viable, easy to monitor and efficient when combined for delivery of macromolecules.

Critical analysis and perspectives

As hinted by the various subjects covered in the thesis, this PhD project treats a multitude of disciplines. However, despite its medical final application, transdermal drug delivery is studied on **a materials science** perspective only.

- **Polymer sciences** has been useful to fabricate and characterize microneedles (Chapter 2), but also to develop screen-printed ITP electrodes (Chapter 3) and move towards a stretchable device (Chapter 5).
- **Electrochemistry** plays a crucial role to understand mechanisms involved in Ag/AgCl iontophoretic devices (Chapter 3).
- **Numerical modeling** appears as a powerful tool to spatially visualize vectors such as current density (Chapter 4), which gives a hint on drug delivery trajectories. Additionally, it informs on potential weaknesses of the electrodes geometries used and can predict more suitable options for the future.
- **Electrical engineering** is also part of the topics covered in this thesis with the use of a coupled mechanical and electrical bench to follow metallic tracks wear throughout tensile cycles close to human skin motion (Chapter 5). Impedance spectroscopy also highlights the electrical behavior of ITP electrodes depending on their wear (Chapter 3).
- Finally, **analytical chemistry** helps following quantitatively the diffusion of a protein drug model, BSA, in different drug delivery configurations.

Some important questions have been answered on the materials scale and short-term perspectives are discussed in each chapter. However, the practical usefulness of the studied device can only be confirmed through collaborations between research teams of different expertise and at different level of product development. The next steps towards a practical device is therefore to work with pharmaceutical and medical researchers both to target a specific application and consider realistic clinical specifications once the regulatory requirements are met (**Figure 146**).

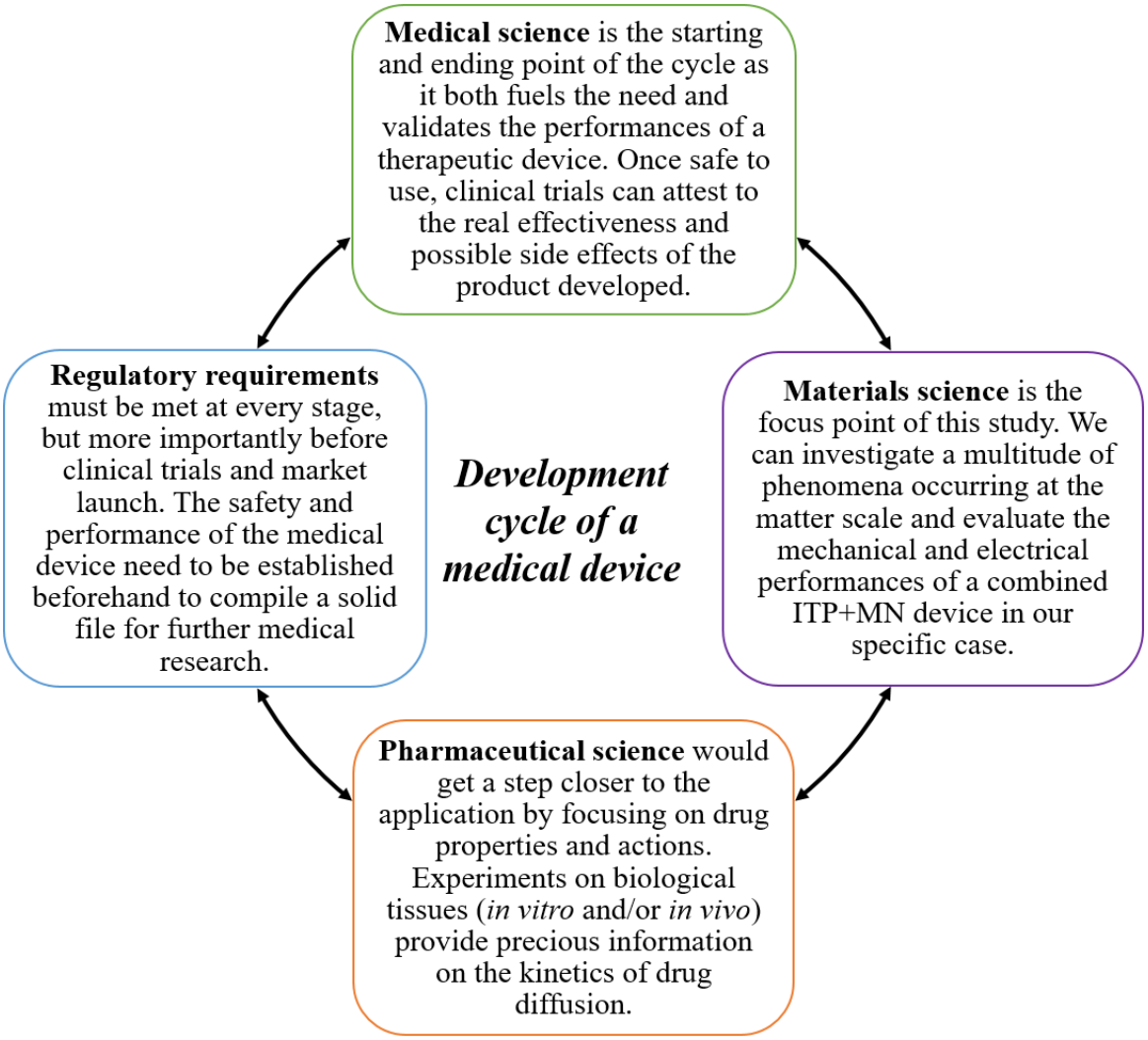

Figure 146. Schematic representation of the development cycle of a medical device and all the actors involved

Appendices

Appendix 1. Evaluation of the environmental impact of the project and improvement perspectives

Research and **D**evelopment (**R&D**) inevitably has a non-negligible environmental impact as it is often based on the principle of failure and success. In this PhD project more specifically, the development and optimization of fabrication processes has the most important environmental cost, both for microneedles (MNs) and iontophoresis (ITP). In each case, the amount of consumable items are estimated to raise awareness. Thankfully, some of them can be reused for future projects on similar topics. When possible, means to improve research sustainability are suggested in **purple**.

Microneedle fabrication

In this thesis, industrial processes are explored to evaluate the viability of microneedle technology for future upscaling. Even though biobased and biodegradable materials are selected for this purpose, these processes imply a significant amount of material loss.

The thermoforming process has been adapted for this project and the development of micro-objects in general by purchasing a 10x10 cm mothertool instead of the 32x38 cm already in place. Master mold and polymer sheet sizes are therefore reduced accordingly. **Thermoformed MNs** developed in the lab required the use of:

- **Massive aluminium molds (2* 2x10x10 cm).** Two of them were manufactured for this thesis, but the second one is designed to be a more viable option for MN fabrication. As presented in Chapter 2 (**2.2.3.1**), some elements of the mold (bottom block and top plate) can remain fixed. Small MN inserts (9 mm diameter) can then be independently manufactured with the desired array design. Other top plates can be manufactured if new array sizes are required, but they can be used repeatedly in various MN projects.
- **Extruded polymer sheets (~270* 10x10 cm, 625 mg, 50 µm thickness)**. Almost 300 PLLA sheets were used for the development of thermoformed MNs and compare parameters influence of their geometry and mechanical resistance. Besides, extrusion itself is a material costly process as meters of polymers can be wasted before reaching the desired sheet thickness. This aspect could not be estimated for this project though as commercial sheets were used.

Similarly, **injection molded MNs** were not developed in CEA for this project, but the following points can be highlighted:

- 3D-printing is considered to print injection molds instead of using metallic resources like we did for thermoforming. Stereolithography apparatus (SLA) and (DLP) (**2.2.2**) are both very economic techniques as very little material is wasted: apart from the photocured parts, the excess resin remains in the tank and can be used for future printings. However, post-processing can use

a significant amount of solvent (**~250 mL of isopropanol (IPA) per array**). An agitated IPA bath can be used as an alternative to clean multiple parts before renewal.

- Injection-molded MN arrays were developed and sent by airplane from Japan following a discussion with Yamada Seiko Co Ltd research team (**2 packages, 50 x 66 mg PLLA and 50 x 77 mg PGA arrays**). With further development of polymer micro-injection, local companies could be approached to reduce transport constraints.

Screen-printing electrodes

Screen-printing is commonly used to provide flexible and stretchable electrodes and electronic devices. It is a very interesting tool to save metallic materials by depositing thin layers within a 10 µm order of magnitude. However, this process can also be environmentally costly at each level of the process.

Energy

- The screen-printing machine used for this thesis is located in a **clean room**. Clean rooms are known to consume a significant amount of energy to maintain air pressure, extraction, temperature and humidity conditions. For this specific application, such precautionary measures are not necessary and could be avoided if the machine is dedicated to similar applications for instance.

Screens

- **63x63 cm stainless steel (x9) and polyester (x2) screens** were used for the project. Since these screens are specific to the electrode design studied (standard and *Hatha* geometries), recyling screens could be a solution to value these materials and avoid unused screen storage over years.

Materials

- ITP electrodes are printed in batches of **32x38 cm with 27 electrodes** on each batch. Printing parameters are manually optimized for each new material involved in the process (screen, ink, substrate). We can therefore estimate that around **200 batches** were printed throughout the PhD, among which ~20% are operable for electrochemical characterizations. This step represent a significant waste of TPU sheets and metallic inks, but is inevitable in R&D to familiarize with new ink formulations and substrate adhesion constraints. These parameters could however be classified and accessible for all users of the machine to gain time on parameters adjustments and therefore the number of batches necessary for process optimization.

Cleaning

- Finally, organic solvents are again used to clean the screens after printing. We can estimate that we need **1L of cyclopentanone per batch**, each of them requiring 4 screens (Ag, C, Ag/AgCl and dielectric layers). Novel formulations could lead to "greener" alternatives that could use water-based products for the this final step.

Numerical pollution

Without mentioning the inevitable amount of electricity used to perform various characterizations and numerical computations, the data generated were (thankfully enough) stored on CEA network during the past three years. As any other network, servers are copied and maintained powered continuously. Characterization data represent a volume of 11 Go, while numerical simulations use up to 50 Go. By the end of each PhD, sorting out unnecessary data seems necessary to transfer only the most useful information to the lab. Additionally, compressing files could help archiving past students work while using less storage.

Disposable device

Finally, we can also argue on the viability of the transdermal device itself, since it has a limited lifetime caused by:

- **A limited amount of drug in the reservoir**. In this case, the drug reservoir could be designed to be refilled once emptied, either manually or by a pumping system.
- **Consumption of Ag/AgCl electrodes**. Chapter 3 suggests means to increase electrodes lifetimes, such as switching polarities after consumption to benefit from the reversible properties of Ag and AgCl. This strategy cannot be used forever though, as the electrodes start to degrade anyway after three switches.

Transdermal patches are overall inevitably disposable as their adhesion degrades with time. To evaluate if the environmental impact of such device is positive, we must compare it subcutaneous injections that also generate a considerable amount of material waste due to sterilization constraints.

In conclusion, the consumption of resources is obviously inevitable in R&D. It is important to acknowledge it though and propose ways to limit our consumption as much as possible, because these resources are not infinite.

Appendix 2. Available transdermal drugs for systemic delivery approved in the USA and EU (Bird and Ravindra, 2020; Pastore et al., 2015)

Drug (Tradename, Year of FDA approval)	Indication	Site of application	Dose and delivery rate	Duration of application
Asenapine (Secuado®, 2009)	Antipsychotic	Hip, abdomen, upper arm or upper back area	3.8-7.6 mg/day	24 hours
Buprenorphine (Butrans®, 2010)	Chronic pain	Upper outer arm, upper chest, upper back or the side of the chest	5-20 mg, 5-20 µg/h	7 days
Clonidine (Catapres-TTS®, 1984)	Hypertension	Upper outer arm or upper chest	2.5-7.5 mg, 0.1-0.3 mg/day	7 days
Oestradiol (Estraderm®, 1986)	Female Hormone Replacement Therapy (HRT)	Trunk of the body including the buttocks and abdomen	4-8 mg, 0.05-0.10 mg/day	3-4 days
Oestradiol (Climara®, 1994)	Female HRT	Lower abdomen or upper quadrant of the buttock	2-7.6 mg, 0.025-0.1 mg/day	7 days
Oestradiol (Vivelle®, 1994)	Female HRT	Trunk of the body including abdomen and buttocks	4.33-8.66 mg, 0.05-0.1 mg/day	3-4 days
Oestradiol (Alora®, 1996)	Female HRT	Lower abdomen, upper quadrant of the buttock or outer aspect of the hip	0.77-3.1 mg, 0.025-0.1 mg/day	3-4 days
Oestradiol (Vivelle-Dot®, 1999)	Female HRT	Lower abdomen	0.39-1.56 mg, 0.025-0.1 mg/day	3-4 days
Oestradiol (Menostar®, 2004)	Female HRT	Lower abdomen	1 mg, 0.014 mg/day	7 days
Oestradiol (Minivelle®, 2012)	Female HRT	Lower abdomen or buttocks	0.62-1.65 mg, 0.0375-0.1 mg/day	3-4 days
Oestradiol (E)/Norethindrone (NT) (Combipatch®, 1998)	Female HRT	Lower abdomen	0.62/2.7 or 0.51/4.8 mg E/NT, 0,05 mg E/day, 0,14-0,25 mg NT/day	3-4 days
Oestradiol (Evamist®, 2007)	Menopausal symptoms	Inside of the forearm	1.53 mg per spray (90µL)	One spray daily (starting dose)
Ethiny oestradiol (EE)/Norelgestromin (NL) (Ortho Evra®, 2001)	Female contraception	Buttock, abdomen, upper outer arm or upper torso	0.75/6.00 mg EE/NL, 0.035/0.15	7 days

			EE/NL mg/day	
Oestradiol (E)/Levonorgestrel (L) (Climara Pro®, 2003)	Female HRT	Lower abdomen	4.40/1.39 mg E/L, 0.045/0.015 E/L mg/day	7 days
Fentanyl (Duragesic®, 1990)	Chronic pain	Chest, back, flank or upper arm	2.1-16.8 mg, 12.5-100 µg/h	72 hours
Granisetron (Sancuso®, 2008)	Chemotherapy-induced nausea and vomiting	Upper outer arm	34.3 mg, 3.1 mg/day	Up to 7 days
Methylphenidate (Daytrana®, 2006)	ADHD	Hip area, avoiding the waistline	27.5-82.5 mg, 1.1-3.3 mg/h	Up to 9 hours/day
Nitroglycerin (Nitro-Dur, 1995)	Angina pectoris	Chest, shoulder, upper arm or back (hairless area)	20-160 mg, 0.1-0.8 mg/h	12-14 hours
Nitroglycerin (Minitran®, 1996)	Angina pectoris	Chest, shoulder, upper arm or back (hairless area)	9-54 mg, 0.1-0.6 mg/h	12-14 hours
Oxybutynin (Oxytrol®, 2003)	Overactive bladder	Abdomen, buttocks or hip	36 mg, 3.9 mg/day	3-4 days
Rivastigmine (Exelon®, 2007)	Alzheimer's and Parkinson's disease	Upper/lower back, upper arm or chest	9-27 mg, 4.6-13.3 mg/day	24 hours
Rotigotine (Neupro®, 2007)	Parkinson's disease, restless legs syndrome	Abdomen, thigh, hip, flank, shoulder or upper arme	2.25-18 mg, 1-8 mg/day	24 hours
Scopolamine (Transderm Scop®, 1981)	Motion sickness	Behind one ear	1.5 mg, 1.0 mg/3 days	72 hours
Selegiline (Emsam®, 2006)	Major depressive disorder	Upper chest or back, upper thigh or the outer surface of the upper arm	20-40 mg, 6-12 mg/day	24 hours
Testosterone (Androderm®, 1995)	Hypogonadism	Back, abdomen, thighs or upper arm	9.7-24.3 mg, 2-5 mg/day	24 hours
Testosterone (Axiron®, 2010)	Hypogondism	Axilla (armpit)	30 mg per pump actuation	2 pump actions daily (starting dose)
Nicotine (Nicoderm CQ®, 1991)	Smoking cessation	Anywhere on the body, avoiding joints	36-114 mg, 7-21 mg/day	24 hours
Nicotine (Nicorette®)	Smokine cessation	Intact, non-hairy, non-irritated, clean and dry area on the upper body or upper outer arm	8.3-24.9 mg, 5-15 mg/16 hours	16 hours
Nicotine (Nicorette® Invisipatch®)	Smoking cessation	Intact, non-hairy, clean and dry area on the thigh, arm or chest	15.75-38.7 mg, 10-25 mg/16 hours	16 hours

Nicotine (Habitrol®, 1990)	Smoking cessation	Upper body or the outer part of the arm	17.5-52.5 mg, 7-21 mg/day	24 hours
Sumatriptan (Zecuity®, 2013)	Migraine	Upper arm or thigh	36 mg, 6.5 mg/4 hours	4 hours
Capsaicin (Qutenza®, 2009)	Neuropathic pain	Most painful areas excluding face and scalp	179 mg	1 hour, up to 4 patches
Diclofenac epolamine (Flector®, 2007)	Topical treatment acute pain	Most painful areas	180 mg	12 hours
Lidocaine (Lidoderm®, 1999)	Post-herpetic neuralgia pain	Most painful areas, avoiding contact with the eyes	700 mg, 21 mg/12 hours	12 hours, up to 3 patches a day
Lidocaine (L)/Tetracaine (T) (Synera®, 2005)	Local dermal analgesia	Site of venipuncture, I.V. cannulation or superficial dermatological procedure	70/70 L/T mg, 1.7/1.6 L/T mg/ 30 min	20-30 minutes
Menthol (M)/Methyl salicylate (MS) (Salonpas®, 2008)	Muscles and joints pain	Affected area	3% M/10% MS	Up to 8-12 hours

Appendix 3. Microneedle designs of thermoforming molds

Appendix 4. Study of the influence of the carbon spacer on ITP electrodes consumption

Screen-printed Ag/AgCl layer can be used for other applications such as **E**lectro**C**ardio**G**raphy (**ECG**) monitoring. This topic has been explored in the lab by Lucie Borget during her internship in 2021. Electrodes of identical geometries are used, but the carbon spacer (L2) is removed.

CP characterizations of these electrodes compared to the ITP electrodes (with C spacer) show significant differences in curve profiles (**Figure 147**). Even though the electrolysis plateau appears later, the voltage between the working (positive) electrode and the reference electrode increases up to 10 V for the same current density applied (0.65 $mA \cdot cm^{-2}$).

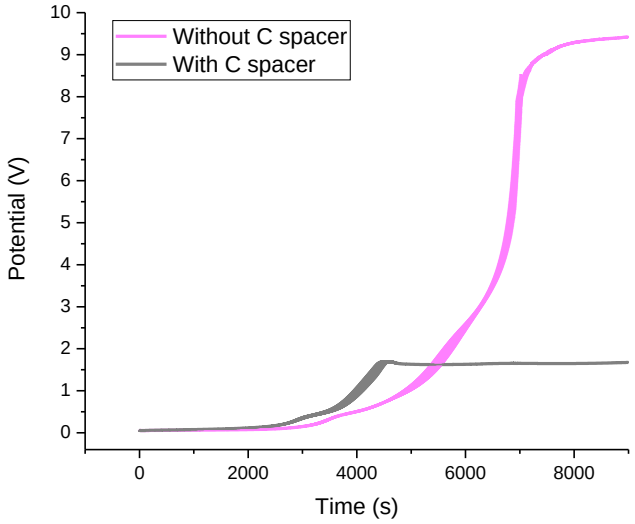

Figure 147. Chronopotentiometry (CP) profiles of standard electrodes (gray) and electrodes without C spacer (pink) when applying a direct current density of 0.65 $mA \cdot cm^{-2}$. Average on 3 results

At the end of the reaction, both anodes looks identical at the surface but thanks to the substrate transparency, noticeable differences are visible at the back of the electrodes (**Figure 148**).

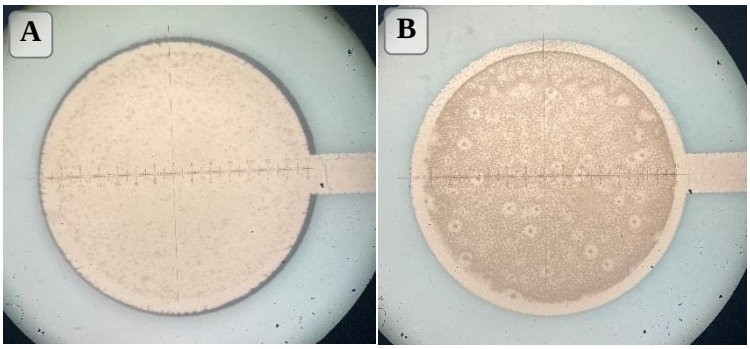

Figure 148. Back view of used anodes (A) with and (B) without the carbon spacer (magnification x10)

Without the carbon spacer, the conductive layer seems damaged and changes color by the end of the reaction. We can assume that this layer participated to the electrochemical reactions induced, altering the electrical conductivity of the device which eventually translates into a substantial increase in

potential. McAdams et al., 2000 indeed explain that separating the active (L3) and the conductive layer (L1) by an inert intermediate layer helps maintaining a constant electrical input regardless of the electrochemical consumption at the surface. This layer is therefore necessary for a safe use of ITP electrodes.

Appendix 5. Screen printing parameters and ink references

Layer	Supplier	Reference	Stretchable ?	Printing speed ($mm \cdot s^{-1}$)	Pressure (N)	Snap off (mm)	Annealing parameters
L1 (Silver)	Dupont	5000	No	120	100	2	IR oven, 135°C, 2 min
	Dupont	5025	No	120	100	2	oven, 120°C, 5 min
	Dupont	PE874	Yes	120	100	2	oven, 120°C, 10 min
	Creative Materials	127-7	Yes	50	140	2	oven, 120°C, 15 min
L2 (Carbon)	Dupont	7102	No	100	100	2	oven, 120°C, 5 min
	Dupont	PE671	Yes	80	120	2.3	oven, 150°C, 10 min
	Creative Materials	128-09	Yes	50	140	2	oven, 150°C, 15 min
L3 (Ag/AgCl)	Dupont	5876	No	120	100	2	oven, 120°C, 5 min
	Dupont	5874	No	120	100	2	oven, 120°C, 5 min
	Dupont-based formulation	5874+ 6.5%NW	No	120	100	2	oven, 150°C, 5 min
	Creative Materials	124-36	Yes	120	100	2	oven, 150°C, 15 min
L4 (Insulator)	Dupont	5018	No	120	100	2	UV conveyor, 2 $m \cdot min^{-1}$, twice
	Dupont	PE773	Yes	50	100	2	oven, 150°C, 30 min
	Creative Materials	126-26	Yes	20	100	2	oven, 150°C, 1h30

Appendix 6. Calculation tools of resistance correction factors in four-point probe measurements

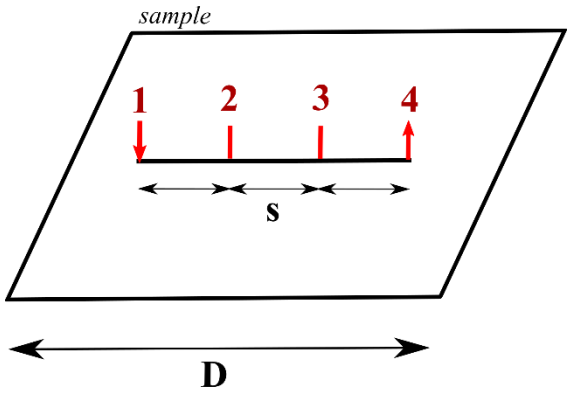

D / s	Circle	Square	Rectangle L/W=2	Rectangle L/W=3	Rectangle L/W=4
1				0.9988	0.9994
1.25				1.2467	1.2248
1.5			1.4788	1.4893	1.4893
1.75			1.7196	1.7238	1.7238
2			1.9475	1.9475	1.9475
2.5			2.3532	2.3541	2.3541
3	2.2662	2.4575	2.7000	2.7005	2.7005
4	2.9289	3.1127	3.2246	3.2248	3.2248
5	3.3625	3.5098	3.5749	3.5750	3.5750
7.5	3.9273	4.0095	4.0361	4.0362	4.0362
10	4.1716	4.2209	4.2357	4.2357	4.2357
15	4.3646	4.3882	4.3947	4.3947	4.3947
20	4.4364	4.4516	4.4553	4.4553	4.4553
32	4.4791	4.4878	4.4899	4.4899	4.4899
40	4.5076	4.5120	4.5129	4.5129	4.5129
Infinity	**4.5324**	**4.5324**	**4.5325**	**4.5325**	**4.5324**

Modified from MDC EUROPE, 2022

Appendix 7. Study of the influence of EDL parameters on EIS spectra

Influence of EDL thickness

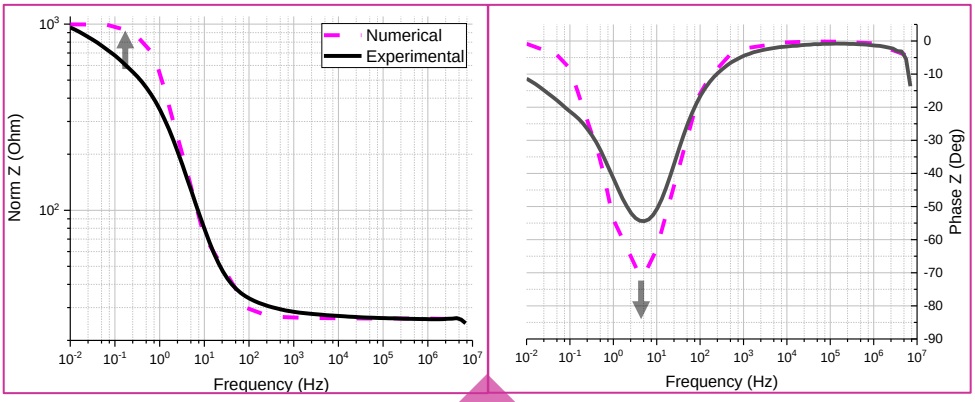

e x2 = 10 nm

Optimized parameters

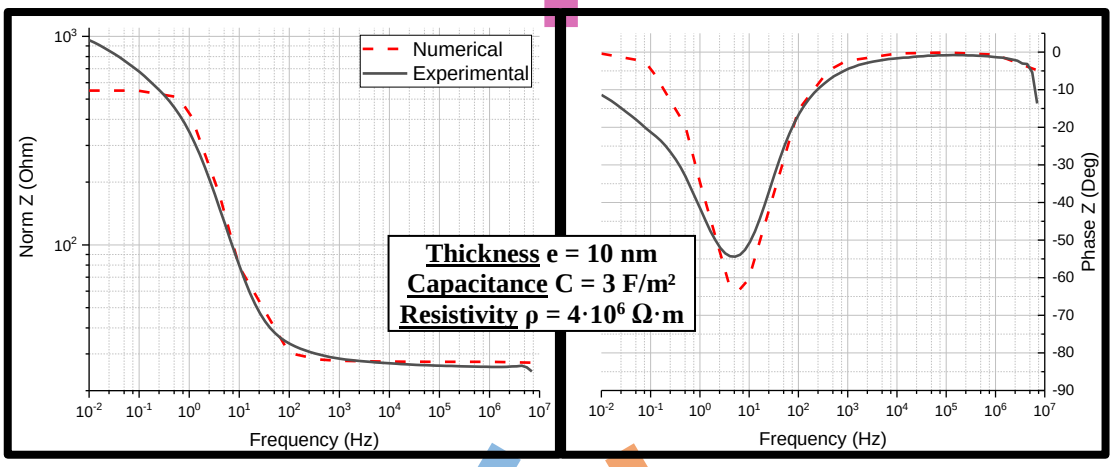

C x2 = 6 F·m^{-2}

ρ x2 = 8·10^{6} Ω·m

Influence of EDL capacitance

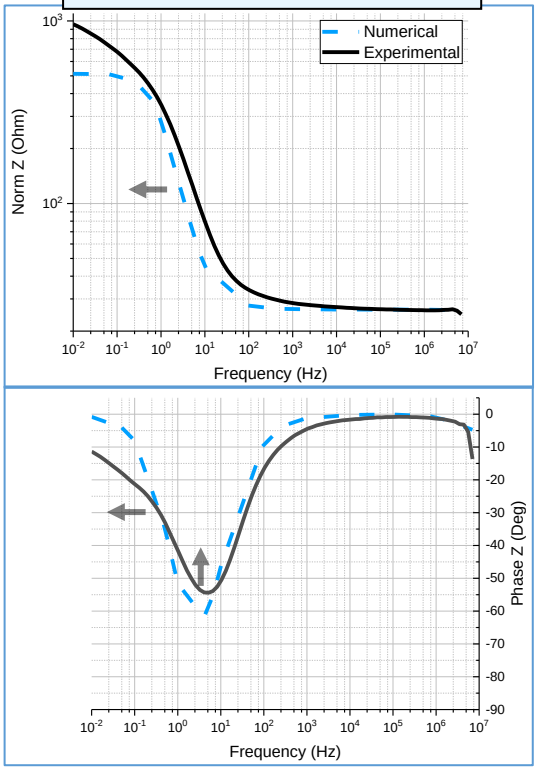

Influence of EDL resistivity

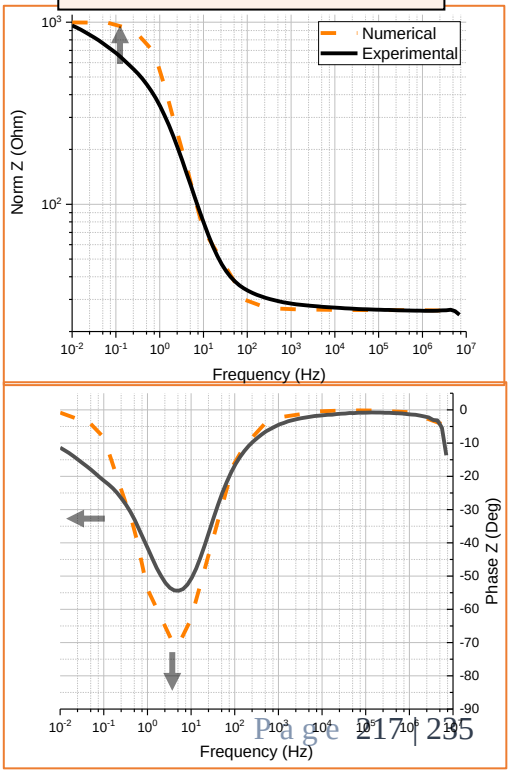

Appendix 8. Chromatograms of standard BSA solutions in PBS 1X

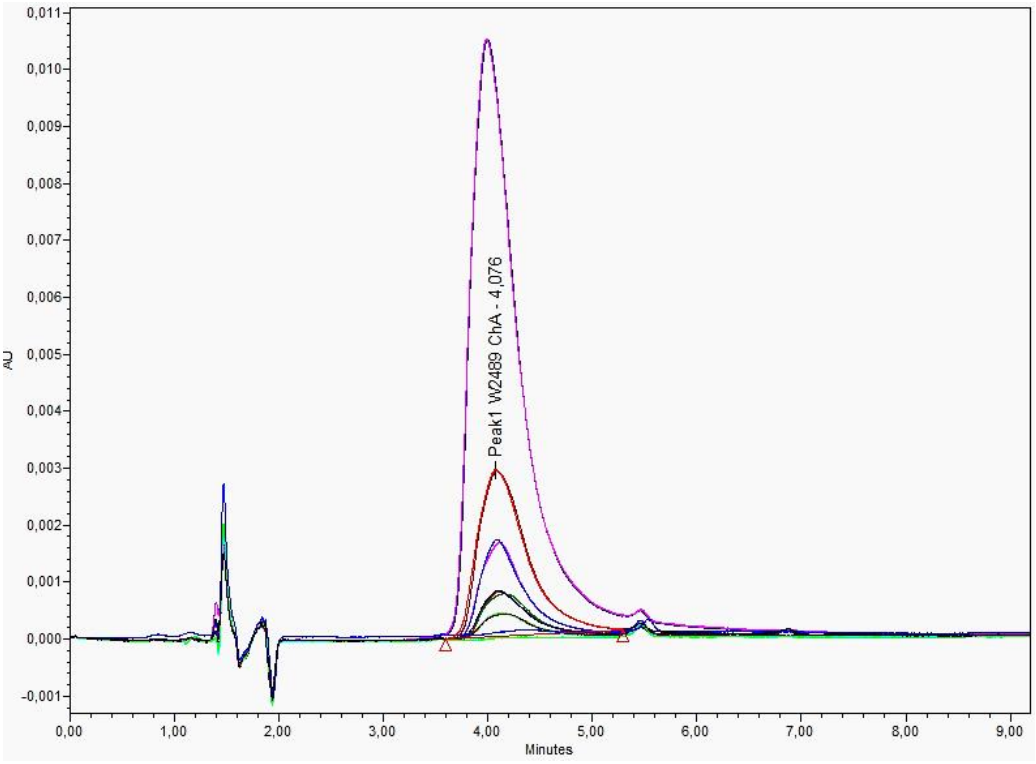

Standard solutions from 2 to 600 ppm, 3 injections for each sample

Bibliography

1. AAT Bioquest, Inc., 2023. Quest Calculate™ PBS (Phosphate Buffered Saline) (1X, pH 7.4) Preparation and Recipe. [WWW Document]. URL https://www.aatbio.com/resources/buffer-preparations-and-recipes/pbs-phosphate-buffered-saline (accessed 6.2.23).
2. Abd, E., Yousuf, S., Pastore, M., Telaprolu, K., Mohammed, Y., Namjoshi, S., Grice, J., Roberts, M., 2016. Skin models for the testing of transdermal drugs. CPAA Volume 8, 163–176. https://doi.org/10.2147/CPAA.S64788
3. AJ Torriero, A., 2019. Understanding the Differences between a Quasi-Reference Electrode and a Reference Electrode. MACIJ 3. https://doi.org/10.23880/MACIJ-16000144
4. Alarcón-Segovia, L.C., Daza-Agudelo, J.I., Rintoul, I., 2021. Multifactorial Effects of Gelling Conditions on Mechanical Properties of Skin-Like Gelatin Membranes Intended for In Vitro Experimentation and Artificial Skin Models. Polymers 13, 1991. https://doi.org/10.3390/polym13121991
5. Aldawood, F.K., Andar, A., Desai, S., 2021. A Comprehensive Review of Microneedles: Types, Materials, Processes, Characterizations and Applications. Polymers (Basel) 13, 2815. https://doi.org/10.3390/polym13162815
6. Alkilani, A.Z., McCrudden, M.T.C., Donnelly, R.F., 2015. Transdermal Drug Delivery: Innovative Pharmaceutical Developments Based on Disruption of the Barrier Properties of the stratum corneum. Pharmaceutics 7, 438. https://doi.org/10.3390/pharmaceutics7040438
7. Al-Rimawi, F., 2014. Development and Validation of HPLC-UV Method for Determination of Bovine Serum Albumin and Myoglobin Proteins. IRJPAC 4, 585–593. https://doi.org/10.9734/IRJPAC/2014/9391
8. Amin, R., Knowlton, S., Hart, A., Yenilmez, B., Ghaderinezhad, F., Katebifar, S., Messina, M., Khademhosseini, A., Tasoglu, S., 2016. 3D-printed microfluidic devices. Biofabrication 8, 022001. https://doi.org/10.1088/1758-5090/8/2/022001
9. Anglin, E.J., Cheng, L., Freeman, W.R., Sailor, M.J., 2008. Porous silicon in drug delivery devices and materials. Adv Drug Deliv Rev 60, 1266–1277. https://doi.org/10.1016/j.addr.2008.03.017
10. Aoyagi, S., Sato, J., Takahashi, T., Suzuki, M., Matsumoto, S., Kansai University 3-3-35 Yamate-cho, Suita, Osaka 564-8680, Japan, Murata Machinery Ltd. 2 Nakajima, Hashizume, Inuyama-shi, Aichi 484-8502, Japan, Sanei Seiki Co., Ltd. 2-30-16 Yaguchi, Ota-ku, Tokyo 146-0093, Japan, 2020. Fabrication of Microneedle from Stretched Biodegradable Polymer Sheet by 3D Laser Machining. JRM 32, 390–400. https://doi.org/10.20965/jrm.2020.p0390
11. Assadpour, E., Jafari, S.M., 2019. 1 - An overview of biopolymer nanostructures for encapsulation of food ingredients, in: Jafari, S.M. (Ed.), Biopolymer Nanostructures for Food Encapsulation Purposes, Nanoencapsulation in the Food Industry. Academic Press, pp. 1–35. https://doi.org/10.1016/B978-0-12-815663-6.00001-X
12. Avicenna, Gruner, O.C., 1973. A treatise on the Canon of medicine of Avicenna: incorporating a translation of the first book. AMS Press, [New York.
13. Bagniefski, T., Burnette, R.R., 1990. A comparison of pulsed and continuous current iontophoresis. Journal of Controlled Release 11, 113–122. https://doi.org/10.1016/0168-3659(90)90125-D
14. Bakshi, P., Vora, D., Hemmady, K., Banga, A.K., 2020. Iontophoretic skin delivery systems: Success and failures. International Journal of Pharmaceutics 586, 119584. https://doi.org/10.1016/j.ijpharm.2020.119584
15. Banga, A.K., 1998. Electrically Assisted Transdermal And Topical Drug Delivery, 0 ed. CRC Press. https://doi.org/10.4324/9780203483985

16. Bardal, S.K., Waechter, J.E., Martin, D.S., 2011. Chapter 2 - Pharmacokinetics, in: Bardal, S.K., Waechter, J.E., Martin, D.S. (Eds.), Applied Pharmacology. W.B. Saunders, Philadelphia, pp. 17–34. https://doi.org/10.1016/B978-1-4377-0310-8.00002-6
17. Barry, B.W., 1987. Mode of action of penetration enhancers in human skin. Journal of Controlled Release 6, 85–97. https://doi.org/10.1016/0168-3659(87)90066-6
18. Betts, J.G., Desaix, P., Johnson, E., Johnson, J.E., Korol, O., Kruse, D., Poe, B., Wise, J.A., Womble, M., Young, K.A., 2013. Anatomy & Physiology.
19. Bhattacharya, A., Prajapati, R., Chatterjee, S., Mukherjee, T.K., 2014. Concentration-Dependent Reversible Self-Oligomerization of Serum Albumins through Intermolecular β-Sheet Formation. Langmuir 30, 14894–14904. https://doi.org/10.1021/la5034959
20. Bird, D., Ravindra, N.M., 2020. Transdermal drug delivery and patches—An overview. MEDICAL DEVICES & SENSORS 3, e10069. https://doi.org/10.1002/mds3.10069
21. Bobály, B., Mikola, V., Sipkó, E., Márta, Z., Fekete, J., 2015. Recovery of Proteins Affected by Mobile Phase Trifluoroacetic Acid Concentration in Reversed-Phase Chromatography. Journal of Chromatographic Science 53, 1078–1083. https://doi.org/10.1093/chromsci/bmu169
22. Bocchino, A., Teixeira, S.R., Iadanza, S., Melnik, E., Kurzhals, S., Mutinati, G., O'Mahony, C., 2022. Development and Characterization of Passivation Methods for Microneedle-Based Biosensors 4.
23. Boer, M., Duchnik, E., Maleszka, R., Marchlewicz, M., 2016. Structural and biophysical characteristics of human skin in maintaining proper epidermal barrier function. Postepy Dermatol Alergol 33, 1–5. https://doi.org/10.5114/pdia.2015.48037
24. Borzova, V., Markossian, K., Chebotareva, N., Kleimenov, S., Poliansky, N., Muranov, K., Stein-Margolina, V., Shubin, V., Markov, D., 2016. Kinetics of Thermal Denaturation and Aggregation of Bovine Serum Albumin. PloS one 11, e0153495. https://doi.org/10.1371/journal.pone.0153495
25. Brannon, H.L., 2022. Skin Layers and How They Protect You [WWW Document]. Verywell Health. URL https://www.verywellhealth.com/skin-anatomy-1068880 (accessed 12.21.22).
26. Buckley, G., 2016. Homeostasis - Definition and Examples. Biology Dictionary. URL https://biologydictionary.net/homeostasis/ (accessed 12.21.22).
27. Byrn, S.R., Zografi, G., Chen, X. (Sean), 2017. Differential Scanning Calorimetry and Thermogravimetric Analysis, in: Solid State Properties of Pharmaceutical Materials. John Wiley & Sons, Ltd, pp. 124–141. https://doi.org/10.1002/9781119264408.ch10
28. Bystrova, S., Luttge, R., 2011. Micromolding for ceramic microneedle arrays. Microelectronic Engineering, Proceedings of the 36th International Conference on Micro- and Nano-Engineering (MNE) 88, 1681–1684. https://doi.org/10.1016/j.mee.2010.12.067
29. Cevc, G., Vierl, U., 2010. Nanotechnology and the transdermal route: A state of the art review and critical appraisal. J Control Release 141, 277–299. https://doi.org/10.1016/j.jconrel.2009.10.016
30. Champeau, M., 2020. Dissolving microneedles for an optimal transdermal delivery of an active principle used in photodynamic therapy : development and proof of concept (These de doctorat). Université de Lille (2018-2021).
31. Champeau, M., Jary, D., Mortier, L., Mordon, S., Vignoud, S., 2020. A facile fabrication of dissolving microneedles containing 5-aminolevulinic acid. International Journal of Pharmaceutics 586, 119554. https://doi.org/10.1016/j.ijpharm.2020.119554
32. Chander, H., Burch, R.F., Talegaonkar, P., Saucier, D., Luczak, T., Ball, J.E., Turner, A., Kodithuwakku Arachchige, S.N.K., Carroll, W., Smith, B.K., Knight, A., Prabhu, R.K., 2020. Wearable Stretch Sensors for Human Movement Monitoring and Fall Detection in

Ergonomics. Int J Environ Res Public Health 17, 3554. https://doi.org/10.3390/ijerph17103554
33. Chemtob, S., 2004. Chapter 19 - Basic Pharmacologic Principles, in: Polin, R.A., Fox, W.W., Abman, S.H. (Eds.), Fetal and Neonatal Physiology (Third Edition). W.B. Saunders, pp. 179–190. https://doi.org/10.1016/B978-0-7216-9654-6.50022-9
34. Chen, A.I., Balter, M.L., Chen, M.I., Gross, D., Alam, S.K., Maguire, T.J., Yarmush, M.L., 2016. Multilayered tissue mimicking skin and vessel phantoms with tunable mechanical, optical, and acoustic properties. Med. Phys. 43, 3117–3131. https://doi.org/10.1118/1.4951729
35. Chen, X., Prow, T.W., Crichton, M.L., Jenkins, D.W.K., Roberts, M.S., Frazer, I.H., Fernando, G.J.P., Kendall, M.A.F., 2009. Dry-coated microprojection array patches for targeted delivery of immunotherapeutics to the skin. Journal of Controlled Release 139, 212–220. https://doi.org/10.1016/j.jconrel.2009.06.029
36. Chitrakar, C., Hedrick, E., Adegoke, L., Ecker, M., 2022. Flexible and Stretchable Bioelectronics. Materials 15, 1664. https://doi.org/10.3390/ma15051664
37. Cho, K.R., Kim, M., Kim, B., Shin, G., Lee, S., Kim, W., 2022. Investigation of the AgCl Formation Mechanism on the Ag Wire Surface for the Fabrication of a Marine Low-Frequency-Electric-Field-Detection Ag/AgCl Sensor Electrode. ACS Omega 7, 25110–25121. https://doi.org/10.1021/acsomega.2c01481
38. Choi, Y.S., Hong, S.R., Lee, Y.M., Song, K.W., Park, M.H., Nam, Y.S., 1999. Study on gelatin-containing artificial skin: I. Preparation and characteristics of novel gelatin-alginate sponge. Biomaterials 20, 409–417. https://doi.org/10.1016/S0142-9612(98)00180-X
39. Cilurzo, F., Gennari, C.G.M., Minghetti, P., 2012. Adhesive properties: a critical issue in transdermal patch development. Expert Opinion on Drug Delivery 9, 33–45. https://doi.org/10.1517/17425247.2012.637107
40. Clowes, H.M., Scott, R.C., Heylings, J.R., 1994. Skin absorption: Flow-through or static diffusion cells. Toxicology in Vitro 8, 827–830. https://doi.org/10.1016/0887-2333(94)90078-7
41. COMSOL Documentation, n.d. Theory Background for the Layered Shell Interface [WWW Document]. URL https://doc.comsol.com/5.5/doc/com.comsol.help.sme/sme_ug_layered_shell.09.04.html (accessed 6.6.23).
42. COMSOL Learning Center, n.d. Using Symmetry to Reduce Model Size [WWW Document]. COMSOL. URL https://www.comsol.fr/support/learning-center/article/Using-Symmetry-to-Reduce-Model-Size-35921 (accessed 6.16.23).
43. Condliffe, J., Schiffter, H.A., Cleveland, R.O., Coussios, C.-C., 2010. An acoustic microscopy technique to assess particle size and distribution following needle-free injection. The Journal of the Acoustical Society of America 127, 2252–2261. https://doi.org/10.1121/1.3314252
44. Cordeiro, A.S., Tekko, I.A., Jomaa, M.H., Vora, L., McAlister, E., Volpe-Zanutto, F., Nethery, M., Baine, P.T., Mitchell, N., McNeill, D.W., Donnelly, R.F., 2020. Two-Photon Polymerisation 3D Printing of Microneedle Array Templates with Versatile Designs: Application in the Development of Polymeric Drug Delivery Systems. Pharm Res 37, 174. https://doi.org/10.1007/s11095-020-02887-9
45. Courtenay, A.J., McAlister, E., McCrudden, M.T.C., Vora, L., Steiner, L., Levin, G., Levy-Nissenbaum, E., Shterman, N., Kearney, M.-C., McCarthy, H.O., Donnelly, R.F., 2020. Hydrogel-forming microneedle arrays as a therapeutic option for transdermal esketamine delivery. Journal of Controlled Release 322, 177–186. https://doi.org/10.1016/j.jconrel.2020.03.026

46. Cracowski, J.-L., Roustit, M., 2020. Human Skin Microcirculation. Comprehensive Physiology 10, 50.
47. Cruz, S.M.F., Rocha, L.A., Viana, J.C., 2018. Printing Technologies on Flexible Substrates for Printed Electronics, in: Rackauskas, S. (Ed.), Flexible Electronics. InTech. https://doi.org/10.5772/intechopen.76161
48. Cullander, C., Rao, G., Guy, R., 1993. Why Silver/Silver Chloride? Criteria For Iontophoresis Electrodes, Prediction Percutaneous Penetration 381–390.
49. Daly, C.H., 1982. Biomechanical Properties of Dermis. Journal of Investigative Dermatology 79, 17–20. https://doi.org/10.1038/jid.1982.4
50. Davidson, A., Al-Qallaf, B., Das, D.B., 2008. Transdermal drug delivery by coated microneedles: Geometry effects on effective skin thickness and drug permeability. Chemical Engineering Research and Design 86, 1196–1206. https://doi.org/10.1016/j.cherd.2008.06.002
51. Delalleau, A., 2018. Rhéologie des tissus mous 165.
52. Delalleau, A., Josse, G., Lagarde, J.-M., Zahouani, H., Bergheau, J.-M., 2006. Characterization of the mechanical properties of skin by inverse analysis combined with the indentation test. Journal of Biomechanics 39, 1603–1610. https://doi.org/10.1016/j.jbiomech.2005.05.001
53. Demir, B., Rosselle, L., Voronova, A., Pagneux, Q., Quenon, A., Gmyr, V., Jary, D., Hennuyer, N., Staels, B., Hubert, T., Abderrahmani, A., Plaisance, V., Pawlowski, V., Boukherroub, R., Vignoud, S., Szunerits, S., 2022. Innovative transdermal delivery of insulin using gelatin methacrylate-based microneedle patches in mice and mini-pigs. Nanoscale Horiz. 7, 174–184. https://doi.org/10.1039/D1NH00596K
54. Deng, Y., Winter, G., Myschik, J., 2012. Preparation and validation of a skin model for the evaluation of intradermal powder injection devices. European Journal of Pharmaceutics and Biopharmaceutics 81, 360–368. https://doi.org/10.1016/j.ejpb.2012.03.008
55. di Cagno, M.P., Clarelli, F., Våbenø, J., Lesley, C., Rahman, S.D., Cauzzo, J., Franceschinis, E., Realdon, N., Stein, P.C., 2018. Experimental Determination of Drug Diffusion Coefficients in Unstirred Aqueous Environments by Temporally Resolved Concentration Measurements. Mol. Pharmaceutics 15, 1488–1494. https://doi.org/10.1021/acs.molpharmaceut.7b01053
56. DiRienzo, M., Newman, P., 2023. Total Global Silver Demand Posts Record High of 1.24 Billion Ounces in 2022 |. URL https://www.silverinstitute.org/total-global-silver-demand-posts-record-high-1-24-billion-ounces-2022/ (accessed 6.13.23).
57. Dixit, N., Bali, V., Baboota, S., Ahuja, A., Ali, J., 2007. Iontophoresis - An Approach for Controlled Drug Delivery: A Review. curr drug deliv 4, 1–10. https://doi.org/10.2174/156720107779314802
58. Dong, L., Jiang, C., Wang, J., Wang, D., 2021. Design of Shape Reconfigurable, Highly Stretchable Honeycomb Lattice With Tunable Poisson's Ratio. Frontiers in Materials 8, 191. https://doi.org/10.3389/fmats.2021.660325
59. Donnelly, R.F., Singh, T.R.R., Garland, M.J., Migalska, K., Majithiya, R., McCrudden, C.M., Kole, P.L., Mahmood, T.M.T., McCarthy, H.O., Woolfson, A.D., 2012. Hydrogel-Forming Microneedle Arrays for Enhanced Transdermal Drug Delivery. Adv Funct Mater 22, 4879–4890. https://doi.org/10.1002/adfm.201200864
60. Draelos, Z.D., 2009. Chapter 18 - Proper Skin Hydration and Barrier Function, in: Tabor, A., Blair, R.M. (Eds.), Nutritional Cosmetics, Personal Care & Cosmetic Technology. William Andrew Publishing, Boston, pp. 355–363. https://doi.org/10.1016/B978-0-8155-2029-0.50025-9
61. Dunare, C., Marland, J.R.K., Blair, E.O., Tsiamis, A., Moorel, F., Terry, J.G., Walton, A.J., Smith, S., 2019. Test Structures for Characterising the Silver Chlorination Process During

Integrated Ag/AgCl Reference Electrode Fabrication, in: 2019 IEEE 32nd International Conference on Microelectronic Test Structures (ICMTS). Presented at the 2019 IEEE 32nd International Conference on Microelectronic Test Structures (ICMTS), IEEE, Kita-Kyushu City, Fukuoka, Japan, pp. 58–63. https://doi.org/10.1109/ICMTS.2019.8730966
62. Dupont, F., 2014. Intégration de la mesure d'impédance dans un système de stimulation électrique implantable multi-applications : proposition d'une nouvelle stratégie de stimulation.
63. Ebnesajjad, S., 2003. 7 - Injection Molding, in: Ebnesajjad, S. (Ed.), Melt Processible Fluoroplastics. William Andrew Publishing, Norwich, NY, pp. 151–193. https://doi.org/10.1016/B978-188420796-9.50010-2
64. Erdő, F., Hashimoto, N., Karvaly, G., Nakamichi, N., Kato, Y., 2016. Critical evaluation and methodological positioning of the transdermal microdialysis technique. A review. Journal of Controlled Release 233, 147–161. https://doi.org/10.1016/j.jconrel.2016.05.035
65. Everett, J.S., Sommers, M.S., 2013. Skin Viscoelasticity: Physiologic Mechanisms, Measurement Issues, and Application to Nursing Science. Biol Res Nurs 15, 338–346. https://doi.org/10.1177/1099800411434151
66. Évora, A.S., Adams, M.J., Johnson, S.A., Zhang, Z., 2021. Corneocytes: Relationship between Structural and Biomechanical Properties. SPP 34, 146–161. https://doi.org/10.1159/000513054
67. Faraji Rad, Z., Prewett, P.D., Davies, G.J., 2021. An overview of microneedle applications, materials, and fabrication methods. Beilstein J. Nanotechnol. 12, 1034–1046. https://doi.org/10.3762/bjnano.12.77
68. Farrington, M., 2012. Chapter 12 - Chemotherapy of infections, in: Bennett, P.N., Brown, M.J., Sharma, P. (Eds.), Clinical Pharmacology (Eleventh Edition). Churchill Livingstone, Oxford, pp. 162–172. https://doi.org/10.1016/B978-0-7020-4084-9.00051-3
69. Fayomi, O., Maconochie, I., Body, R., 2007. Is skin turgor reliable as a means of assessing hydration status in children? Emerg Med J 24, 124–125. https://doi.org/10.1136/emj.2006.045229
70. Frank H., K., Michael A., C., 2005. CHAPTER 26 - Practical Approaches to Pharmacological Studies in Nonhuman Primates, in: Sonia, W.-C. (Ed.), The Laboratory Primate, Handbook of Experimental Animals. Academic Press, London, pp. 437–447. https://doi.org/10.1016/B978-012080261-6/50026-X
71. Gamry Instruments, n.d. Basics of EIS: Electrochemical Research-Impedance Gamry Instruments [WWW Document]. URL https://www.gamry.com/application-notes/EIS/basics-of-electrochemical-impedance-spectroscopy/ (accessed 6.5.23).
72. Ganguly, S., Das, P., Das, N.Ch., 2020. Chapter 16 - Characterization tools and techniques of hydrogels, in: Chen, Y. (Ed.), Hydrogels Based on Natural Polymers. Elsevier, pp. 481–517. https://doi.org/10.1016/B978-0-12-816421-1.00016-1
73. Garland, M.J., Caffarel–Salvador, E., Migalska, K., Woolfson, A.D., Donnelly, R.F., 2012. Dissolving polymeric microneedle arrays for electrically assisted transdermal drug delivery. Journal of Controlled Release 159, 52–59. https://doi.org/10.1016/j.jconrel.2012.01.003
74. Gentile, P., Chiono, V., Carmagnola, I., Hatton, P., 2014. An Overview of Poly(lactic-co-glycolic) Acid (PLGA)-Based Biomaterials for Bone Tissue Engineering. IJMS 15, 3640–3659. https://doi.org/10.3390/ijms15033640
75. Gera, A.K., Burra, R.K., 2022. The Rise of Polymeric Microneedles: Recent Developments, Advances, Challenges, and Applications with Regard to Transdermal Drug Delivery. JFB 13, 81. https://doi.org/10.3390/jfb13020081
76. Gerstel, M.S., Place, V.A., 1976. Drug delivery device. US3964482A.
77. Giboz, J., Copponnex, T., Mele, P., 2007. Microinjection molding of thermoplastic polymers: a review 15.

78. Gill, H.S., Prausnitz, M.R., 2007. Coated microneedles for transdermal delivery. Journal of Controlled Release 117, 227–237. https://doi.org/10.1016/j.jconrel.2006.10.017
79. Gittard, S., Chen, B., Xu, H., Ovsianikov, A., Chichkov, B., Monteiro-Riviere, N., Narayan, J., 2013. The Effects of Geometry on Skin Penetration and Failure of Polymer Microneedles. Journal of adhesion science and technology 27, 227–243. https://doi.org/10.1080/01694243.2012.705101
80. Gupta, J., Gill, H.S., Andrews, S.N., Prausnitz, M.R., 2011. Kinetics of skin resealing after insertion of microneedles in human subjects. Journal of Controlled Release 154, 148–155. https://doi.org/10.1016/j.jconrel.2011.05.021
81. Ha, H., Payer, J., 2011. The Effect of Silver Chloride Formation on the Kinetics of Silver Dissolution in Chloride Solution. Electrochim Acta 56, 2781–2791. https://doi.org/10.1016/j.electacta.2010.12.050
82. Hamidi, M., Zarei, N., 2009. A reversed-phase high-performance liquid chromatography method for bovine serum albumin assay in pharmaceutical dosage forms and protein/antigen delivery systems. Drug Testing and Analysis 1, 214–218. https://doi.org/10.1002/dta.33
83. Harden, J.L., Viovy, J.-L., 1996. Numerical studies of pulsed iontophoresis through model membranes. Journal of Controlled Release 38, 129–139. https://doi.org/10.1016/0168-3659(95)00110-7
84. Hart, S.R., Simoes, M.A., Park, P., 2016. (54) SYNTHETIC SKIN AND TISSUE MODEL.
85. Heckele, M., Schomburg, W.K., 2003. Review on micro molding of thermoplastic polymers. J. Micromech. Microeng. 14, R1. https://doi.org/10.1088/0960-1317/14/3/R01
86. Hernandez-Montelongo, J., Muñoz-Noval, A., García-Ruíz, J., Torres-Costa, V., Martin-Palma, R., Manso-Silvan, M., 2015. Nanostructured porous silicon: The winding road from photonics to cell scaffolds. A review. Frontiers in Bioengineering and Biotechnology 3.
87. Holmgaard, R., Nielsen, J.B., 2009. Dermal absorption of pesticides – evaluation of variability and prevention.
88. Houen, G., Bechgaard, K., Bechgaard, K., Songstad, J., Leskelä, M., Polamo, M., Homsi, M.N., Kuske, F.K.H., Haugg, M., Trabesinger-Rüf, N., Weinhold, E.G., 1996. The Solubility of Proteins in Organic Solvents. Acta Chem. Scand. 50, 68–70. https://doi.org/10.3891/acta.chem.scand.50-0068
89. Howard, J.P., Drake, T.R., Kellogg, D.L., 1995. Effects of alternating current iontophoresis on drug delivery. Archives of Physical Medicine and Rehabilitation 76, 463–466. https://doi.org/10.1016/S0003-9993(95)80579-6
90. Huang, Y., Yu, H., Wang, L., Shen, D., Ni, Z., Ren, S., Lu, Y., Chen, X., Yang, J., Hong, Y., 2022. Research progress on cosmetic microneedle systems: Preparation, property and application. European Polymer Journal 163, 110942. https://doi.org/10.1016/j.eurpolymj.2021.110942
91. Ita, K., 2018. Ceramic microneedles and hollow microneedles for transdermal drug delivery: Two decades of research. Journal of Drug Delivery Science and Technology 44, 314–322. https://doi.org/10.1016/j.jddst.2018.01.004
92. Ita, K.B., 2014. Transdermal drug delivery: progress and challenges. Journal of Drug Delivery Science and Technology 24, 245–250. https://doi.org/10.1016/S1773-2247(14)50041-X
93. Itagaki, H., 2000. Chapter 3 - Fluorescence Spectroscopy, in: Tanaka, T. (Ed.), Experimental Methods in Polymer Science, Polymers, Interfaces and Biomaterials. Academic Press, Boston, pp. 155–260. https://doi.org/10.1016/B978-0-08-050612-8.50009-X
94. Jamali, Y., Jamali, M., Golshani, M., 2019. A new method of brain stimulation at ultra-high frequency.

95. Javadzadeh, Y., Azharshekoufeh Bahari, L., 2017. Chapter 8 - Therapeutic Nanostructures for Dermal and Transdermal Drug Delivery, in: Grumezescu, A.M. (Ed.), Nano- and Microscale Drug Delivery Systems. Elsevier, pp. 131–146. https://doi.org/10.1016/B978-0-323-52727-9.00008-X
96. Jefferson Labs resources, 2016. Silver - Energy Education [WWW Document]. URL https://energyeducation.ca/encyclopedia/Silver (accessed 6.12.23).
97. Johnson, A.R., Caudill, C.L., Tumbleston, J.R., Bloomquist, C.J., Moga, K.A., Ermoshkin, A., Shirvanyants, D., Mecham, S.J., Luft, J.C., DeSimone, J.M., 2016. Single-Step Fabrication of Computationally Designed Microneedles by Continuous Liquid Interface Production. PLOS ONE 11, e0162518. https://doi.org/10.1371/journal.pone.0162518
98. Joodaki, H., Panzer, M.B., 2018. Skin mechanical properties and modeling: A review. Proc Inst Mech Eng H 232, 323–343. https://doi.org/10.1177/0954411918759801
99. Juan, J., Marlen, I., Luisa, C., Diaz-, R., Luisa, A., Casas, N., 2012. Nanocarrier Systems for Transdermal Drug Delivery, in: Sezer, A.D. (Ed.), Recent Advances in Novel Drug Carrier Systems. InTech. https://doi.org/10.5772/50314
100. Jumaah, M., Khairuddean, M., Owaid, S., 2022. Benzothiazole Pyrazoline: Acid-Switchable Absorption and Fluorescence of Photoinduced Electron Transfer (PET). Journal of Fluorescence 32. https://doi.org/10.1007/s10895-021-02782-5
101. Kalia, Y.N., Naik, A., Garrison, J., Guy, R.H., 2004. Iontophoretic drug delivery. Advanced Drug Delivery Reviews, Breaking the Skin Barrier 56, 619–658. https://doi.org/10.1016/j.addr.2003.10.026
102. Kalra, A., Lowe, A., 2016. Mechanical Behaviour of Skin: A Review. J Material Sci Eng 5. https://doi.org/10.4172/2169-0022.1000254
103. Kao, A., 2016. Spatial Mechanical Behaviour of Skin 251.
104. Kapalka, G.M., 2010. Chapter 2 - Pharmacokinetics, in: Kapalka, G.M. (Ed.), Nutritional and Herbal Therapies for Children and Adolescents, Practical Resources for the Mental Health Professional. Academic Press, San Diego, pp. 13–46. https://doi.org/10.1016/B978-0-12-374927-7.00002-9
105. Karande, P., Jain, A., Ergun, K., Kispersky, V., Mitragotri, S., 2005. Design principles of chemical penetration enhancers for transdermal drug delivery. Proceedings of the National Academy of Sciences 102, 4688–4693. https://doi.org/10.1073/pnas.0501176102
106. Karande, P., Jain, A., Mitragotri, S., 2006. Relationships between skin's electrical impedance and permeability in the presence of chemical enhancers. J Control Release 110, 307–313. https://doi.org/10.1016/j.jconrel.2005.10.012
107. Kasha, P.C., Banga, A.K., 2008. A Review of Patent Literature for Iontophoretic Delivery and Devices 10.
108. Katan, T., Szpak, S., Bennion, D.N., 1974. Silver/Silver Chloride Electrodes: Surface Morphology on Charging and Discharging. J. Electrochem. Soc. 121, 757. https://doi.org/10.1149/1.2401904
109. Katikaneni, S., Badkar, A., Nema, S., Banga, A.K., 2009. Molecular charge mediated transport of a 13kD protein across microporated skin. International Journal of Pharmaceutics 378, 93–100. https://doi.org/10.1016/j.ijpharm.2009.05.050
110. Keaton, J.R., 2018. Young's Modulus, in: Bobrowsky, P.T., Marker, B. (Eds.), Encyclopedia of Engineering Geology, Encyclopedia of Earth Sciences Series. Springer International Publishing, Cham, pp. 955–956. https://doi.org/10.1007/978-3-319-73568-9_298
111. Kim, A., Green, P.G., Rao, G., Guy, R.H., 1993. Convective solvent flow across the skin during iontophoresis. Pharm Res 10, 1315–1320. https://doi.org/10.1023/a:1018969713547

112. Kim, M., Jung, B., Park, J.-H., 2012. Hydrogel swelling as a trigger to release biodegradable polymer microneedles in skin. Biomaterials 33, 668–678. https://doi.org/10.1016/j.biomaterials.2011.09.074
113. Kim, Y.-C., Park, J.-H., Prausnitz, M.R., 2012. Microneedles for drug and vaccine delivery. Advanced Drug Delivery Reviews 64, 1547–1568. https://doi.org/10.1016/j.addr.2012.04.005
114. Kochhar, J., Quek, T.C., Soon, W., Choi, J., Zou, S., Kang, L., 2013. Effect of Microneedle Geometry and Supporting Substrate on Microneedle Array Penetration into Skin. Journal of pharmaceutical sciences 102. https://doi.org/10.1002/jps.23724
115. Kolarsick, P.A.J., Kolarsick, M.A., Goodwin, C., 2011. Anatomy and Physiology of the Skin. SKIN CANCER.
116. Kollros, M., 2018. Dermocosmétologie à l'officine: conseils et prévention.
117. Korth Kristalle, 2021. AgCl – Silver Chloride: [WWW Document]. URL https://www.korth.de/en/materials/detail/Silver%20Chloride (accessed 6.12.23).
118. Krieger, K.J., Bertollo, N., Dangol, M., Sheridan, J.T., Lowery, M.M., O'Cearbhaill, E.D., 2019. Simple and customizable method for fabrication of high-aspect ratio microneedle molds using low-cost 3D printing. Microsystems and Nanoengineering 5. https://doi.org/10.1038/s41378-019-0088-8
119. Kubota, M., Hanai, Y., Yamaguchi, T., 1982. Silver-silver chloride electrode and manufacturing method thereof. US4324680A.
120. Lakhani, O.J., Kumar, S., Tripathi, S., Desai, M.A., Seth, C., 2018. Correlation between Basal Insulin Glargine Dose Required in Achieving Target Fasting Blood Glucose and Various Clinical and Laboratory Parameters in Hospitalized Noncritical Patients. Indian J Endocrinol Metab 22, 469–472. https://doi.org/10.4103/ijem.IJEM_297_17
121. Lamouche, G., Kennedy, B.F., Kennedy, K.M., Bisaillon, C.-E., Curatolo, A., Campbell, G., Pazos, V., Sampson, D.D., 2012. Review of tissue simulating phantoms with controllable optical, mechanical and structural properties for use in optical coherence tomography. Biomed. Opt. Express 3, 1381. https://doi.org/10.1364/BOE.3.001381
122. Lanke, S.S.S., Kolli, C.S., Strom, J.G., Banga, A.K., 2009. Enhanced transdermal delivery of low molecular weight heparin by barrier perturbation. Int J Pharm 365, 26–33. https://doi.org/10.1016/j.ijpharm.2008.08.028
123. Larrañeta, E., Lutton, R.E.M., Woolfson, A.D., Donnelly, R.F., 2016. Microneedle arrays as transdermal and intradermal drug delivery systems: Materials science, manufacture and commercial development. Materials Science and Engineering: R: Reports 104, 1–32. https://doi.org/10.1016/j.mser.2016.03.001
124. Leone, M., Nejadnik, R., Kersten, G., O'Mahony, C., Bouwstra, J., van der Maaden, K., 2018. Universal Applicator for Digitally-Controlled Pressing Force and Impact Velocity Insertion of Microneedles into Skin. Pharmaceutics 10. https://doi.org/10.3390/pharmaceutics10040211
125. Leung, P., Ko, E.C., Siu, W., Pang, E.S., Lau, C.B., 2016. Selected Topical Agents Used in Traditional Chinese Medicine in the Treatment of Minor Injuries- A Review. Front Pharmacol 7, 16. https://doi.org/10.3389/fphar.2016.00016
126. Lévêque, J.L., Poelman, M.C., Rigal, J. de, Kligman, A.M., 1988. Are Corneocytes Elastic? DRM 176, 65–69. https://doi.org/10.1159/000248674
127. Lhernould, M.S., 2012. Hollow Polymer Microneedles for pharmaceutical applications. Microneedles 2012, Cork 1.
128. Lhernould, M.S., Tailler, S., Deleers, M., Delchambre, A., 2015. HIGHLY CUSTOMISABLE HOLLOW POLYMER MICRONEEDLE SOLUTIONS [WWW Document]. URL https://www.ondrugdelivery.com/wp-content/uploads/2018/02/Novinject-HR.pdf (accessed 12.27.22).

129. Li, X., Huang, X., Mo, J., Wang, H., Huang, Q., Yang, C., Zhang, T., Chen, H.-J., Hang, T., Liu, F., Jiang, L., Wu, Q., Li, H., Hu, N., Xie, X., 2021. A Fully Integrated Closed-Loop System Based on Mesoporous Microneedles-Iontophoresis for Diabetes Treatment. Advanced Science 8, 2100827. https://doi.org/10.1002/advs.202100827
130. Loder, E.W., Rayhill, M., Burch, R.C., 2018. Safety Problems With a Transdermal Patch for Migraine: Lessons From the Development, Approval, and Marketing Process. Headache: The Journal of Head and Face Pain 58, 1639–1657. https://doi.org/10.1111/head.13424
131. Loizidou, E.Z., Inoue, N.T., Ashton-Barnett, J., Barrow, D.A., Allender, C.J., 2016. Evaluation of geometrical effects of microneedles on skin penetration by CT scan and finite element analysis. European Journal of Pharmaceutics and Biopharmaceutics 107, 1–6. https://doi.org/10.1016/j.ejpb.2016.06.023
132. Low, Z.W.K., Li, Z., Owh, C., Chee, P.L., Ye, E., Dan, K., Chan, S.Y., Young, D.J., Loh, X.J., 2020. Recent innovations in artificial skin. Biomater. Sci. 8, 776–797. https://doi.org/10.1039/C9BM01445D
133. Lvovich, V.F., Matthews, E., Riga, A.T., Kaza, L., 2010. AC electrokinetic platform for iontophoretic transdermal drug delivery. Journal of Controlled Release 145, 134–140. https://doi.org/10.1016/j.jconrel.2010.04.015
134. Mahdizadeh, S., Khaleghi Ghadiri, M., Gorji, A., 2015. Avicenna's Canon of Medicine: a review of analgesics and anti-inflammatory substances. Avicenna J Phytomed 5, 182–202.
135. Makvandi, P., Kirkby, M., Hutton, A.R.J., Shabani, M., Yiu, C.K.Y., Baghbantaraghdari, Z., Jamaledin, R., Carlotti, M., Mazzolai, B., Mattoli, V., Donnelly, R.F., 2021. Engineering Microneedle Patches for Improved Penetration: Analysis, Skin Models and Factors Affecting Needle Insertion. Nano-Micro Lett. 13, 93. https://doi.org/10.1007/s40820-021-00611-9
136. Manikkath, J., Hegde, A.R., Parekh, H.S., Mutalik, S., 2016. Chapter 7 - Peptide Dendrimers in Delivery of Bioactive Molecules to Skin, in: Hamblin, M.R., Avci, P., Prow, T.W. (Eds.), Nanoscience in Dermatology. Academic Press, Boston, pp. 89–97. https://doi.org/10.1016/B978-0-12-802926-8.00007-0
137. Manschot, J., 1985. THE MECHANICAL PROPERTIES OF HUMAN SKIN IN VIVO.
138. Marieb, E.N., 2014. Essentials of Human Anatomy & Physiology, 11th edition. ed. Pearson, Boston.
139. Martin, R.C.G., O'Connor, R., 2017. Chapter 98C - Microwave ablation and irreversible electroporation, in: Jarnagin, W.R. (Ed.), Blumgart's Surgery of the Liver, Biliary Tract and Pancreas, 2-Volume Set (Sixth Edition). Elsevier, Philadelphia, pp. 1448-1458.e2. https://doi.org/10.1016/B978-0-323-34062-5.00127-8
140. Matsuhisa, N., Chen, X., Bao, Z., Someya, T., 2019. Materials and structural designs of stretchable conductors. Chem. Soc. Rev. 48, 2946–2966. https://doi.org/10.1039/C8CS00814K
141. McAdams, E.T., Zhou, D.M., MAILLEY, P.A.N., Mikler, C., 2000. Electrode de transfert d'un courant electrique traversant la peau d'un patient. WO2000027467A1.
142. McAllister, D.V., Wang, P.M., Davis, S.P., Park, J.-H., Canatella, P.J., Allen, M.G., Prausnitz, M.R., 2003. Microfabricated needles for transdermal delivery of macromolecules and nanoparticles: Fabrication methods and transport studies. Proceedings of the National Academy of Sciences 100, 13755–13760. https://doi.org/10.1073/pnas.2331316100
143. MDC EUROPE, 2022. Resistivity Theory and Data Correction Coefficients depending on sample size. URL https://www.mdc-europe.com/resistivity-theory-and-data-correction-coefficients-depending-on-sample-size/ (accessed 8.30.23).

144. Migalska, K., Morrow, D.I.J., Garland, M.J., Thakur, R., Woolfson, A.D., Donnelly, R.F., 2011. Laser-Engineered Dissolving Microneedle Arrays for Transdermal Macromolecular Drug Delivery. Pharm Res 28, 1919–1930. https://doi.org/10.1007/s11095-011-0419-4
145. Migdadi, E.M., Courtenay, A.J., Tekko, I.A., McCrudden, M.T.C., Kearney, M.-C., McAlister, E., McCarthy, H.O., Donnelly, R.F., 2018. Hydrogel-forming microneedles enhance transdermal delivery of metformin hydrochloride. J Control Release 285, 142–151. https://doi.org/10.1016/j.jconrel.2018.07.009
146. Miyamoto, S., Shimono, K., 2020. Molecular Modeling to Estimate the Diffusion Coefficients of Drugs and Other Small Molecules. Molecules 25, 5340. https://doi.org/10.3390/molecules25225340
147. Nagarkar, R., Singh, M., Nguyen, H.X., Jonnalagadda, S., 2020. A review of recent advances in microneedle technology for transdermal drug delivery. Journal of Drug Delivery Science and Technology 59, 101923. https://doi.org/10.1016/j.jddst.2020.101923
148. Naskar, K., Dutta, J., 2014. Investigation on Morphology, Mechanical, Dynamic mechanical and Thermal Behaviour of Blends Based on Ethylene Vinyl Acetate (EVA) and Thermoplastic Polyurethane (TPU). RSC Adv. 4. https://doi.org/10.1039/C4RA07823C
149. Neupane, R., Boddu, S.H.S., Renukuntla, J., Babu, R.J., Tiwari, A.K., 2020. Alternatives to Biological Skin in Permeation Studies: Current Trends and Possibilities. Pharmaceutics 12, 152. https://doi.org/10.3390/pharmaceutics12020152
150. Okabe, K., Yamaguchi, H., Kawai, Y., 1986. New iontophoretic transdermal administration of the beta-blocker metoprolol. Journal of Controlled Release 4, 79–85. https://doi.org/10.1016/0168-3659(86)90043-X
151. Olatunji, O., Das, D., Al-Qallaf, B., 2009. Simulation based optimization of microneedle geometry to improve drug permeability in skin. 7th International Industrial Simulation Conference 2009, ISC 2009.
152. Oltulu, P., Ince, B., Kokbudak, N., Findik, S., Kilinc, F., 2018. Measurement of epidermis, dermis, and total skin thicknesses from six different body regions with a new ethical histometric technique. Turkish Journal of Plastic Surgery 26, 56. https://doi.org/10.4103/tjps.TJPS_2_17
153. O'Mahony, C., 2014. Structural characterization and in-vivo reliability evaluation of silicon microneedles. Biomed Microdevices 16, 333–343. https://doi.org/10.1007/s10544-014-9836-6
154. O'Mahony, C., Grygoryev, K., Ciarlone, A., Giannoni, G., Kenthao, A., Galvin, P., 2016. Design, fabrication and skin-electrode contact analysis of polymer microneedle-based ECG electrodes. J. Micromech. Microeng. 26, 084005. https://doi.org/10.1088/0960-1317/26/8/084005
155. O'Mahony, C., Sebastian, R., Tjulkins, F., Whelan, D., Bocchino, A., Hu, Y., O'Brien, J., Scully, J., Hegarty, M., Blake, A., Slimi, I., Clover, A.J.P., Lyness, A., Kelleher, A.-M., 2023. Hollow silicon microneedles, fabricated using combined wet and dry etching techniques, for transdermal delivery and diagnostics. International Journal of Pharmaceutics 637, 122888. https://doi.org/10.1016/j.ijpharm.2023.122888
156. O'Neil, M., Heckelman, P., Dobbelaar, P., Roman, K., Kenney, C., Karaffa, L., 2013. The Merck index: An encyclopedia of chemicals, drugs, and biologicals [WWW Document]. URL https://hero.epa.gov/hero/index.cfm/reference/details/reference_id/3378176 (accessed 5.2.23).
157. Pan, Y., Birngruber, R., Rosperich, J., Engelhardt, R., 1995. Low-coherence optical tomography in turbid tissue: theoretical analysis. Appl. Opt. 34, 6564. https://doi.org/10.1364/AO.34.006564

158. Papanicolaou, G.C., Zaoutsos, S.P., 2019. 1 - Viscoelastic constitutive modeling of creep and stress relaxation in polymers and polymer matrix composites, in: Guedes, R.M. (Ed.), Creep and Fatigue in Polymer Matrix Composites (Second Edition), Woodhead Publishing Series in Composites Science and Engineering. Woodhead Publishing, pp. 3–59. https://doi.org/10.1016/B978-0-08-102601-4.00001-1
159. Pargar, F., Kolev, H., Koleva, D.A., van Breugel, K., 2018. Microstructure, surface chemistry and electrochemical response of Ag|AgCl sensors in alkaline media. J Mater Sci 53, 7527–7550. https://doi.org/10.1007/s10853-018-2083-0
160. Park, J.-H., Allen, M.G., Prausnitz, M.R., 2004. Biodegradable polymer microneedles: fabrication, mechanics and transdermal drug delivery, in: The 26th Annual International Conference of the IEEE Engineering in Medicine and Biology Society. Presented at the 26th Annual International Conference of the IEEE Engineering in Medicine and Biology Society, IEEE, San Francisco, CA, USA, pp. 2654–2657. https://doi.org/10.1109/IEMBS.2004.1403761
161. Pastore, M.N., Kalia, Y.N., Horstmann, M., Roberts, M.S., 2015. Transdermal patches: history, development and pharmacology. Br J Pharmacol 172, 2179–2209. https://doi.org/10.1111/bph.13059
162. Pauleau, Y., Barna, P.B., 1996. Protective Coatings and Thin Films: Synthesis, Characterization and Applications. Springer Science & Business Media.
163. Peroff, A., 2019. Open Circuit Potential (OCP). Pine Research Instrumentation Store. URL https://pineresearch.com/shop/kb/software/methods-and-techniques/basic-methods/open-circuit-potential-ocp/ (accessed 6.5.23).
164. Pham, P., 2013. Champs électriques alternatifs et milieux biologiques.
165. Pham, P., Howorth, M., Planat-Chrétien, A., Tardu, S., 2007. Numerical Simulation of the Electrical Double Layer Based on the Poisson-Boltzmann Models for AC Electroosmosis Flows 10.
166. Pham, P., Roux, S., Matonti, F., Dupont, F., Agache, V., Chavane, F., 2013. Post-implantation impedance spectroscopy of subretinal micro-electrode arrays, OCT imaging and numerical simulation: towards a more precise neuroprosthesis monitoring tool. J. Neural Eng. 10, 046002. https://doi.org/10.1088/1741-2560/10/4/046002
167. Picard, G., Chouaib, F., Sanchez, S., 2003. Chronopotentiométrie.
168. Pikal, M.J., 2001. The role of electroosmotic flow in transdermal iontophoresis. Advanced Drug Delivery Reviews, Special issue dedicated to Dr. Eric Tomlinson, Advanced Drug Delivery Reviews, A Selection of the Most Highly Cited Articles, 1991-1998 46, 281–305. https://doi.org/10.1016/S0169-409X(00)00138-1
169. Pogue, B.W., Patterson, M.S., 2006. Review of tissue simulating phantoms for optical spectroscopy, imaging and dosimetry. J Biomed Opt 11, 041102. https://doi.org/10.1117/1.2335429
170. Prausnitz, M.R., Langer, R., 2008. Transdermal drug delivery. Nat Biotechnol 26, 1261–1268. https://doi.org/10.1038/nbt.1504
171. Prausnitz, M.R., Mitragotri, S., Langer, R., 2004. Current status and future potential of transdermal drug delivery. Nat Rev Drug Discov 3, 115–124. https://doi.org/10.1038/nrd1304
172. Prodduturi, S., Sadrieh, N., Wokovich, A., Doub, W., Westenberger, B., Buhse, L., 2009. Transdermal Delivery of Fentanyl from Matrix and Reservoir Systems: Effect of Heat and Compromised Skin. Journal of pharmaceutical sciences 99, 2357–66. https://doi.org/10.1002/jps.22004
173. Purdue University, Department of Physics and Astronomy, n.d. Significant Figures [WWW Document]. URL https://web.ics.purdue.edu/~lewicki/physics218/significant (accessed 7.3.23).

174. Rahman, Md.S., Hasan, Md.S., Nitai, A.S., Nam, S., Karmakar, A.K., Ahsan, Md.S., Shiddiky, M.J.A., Ahmed, M.B., 2021. Recent Developments of Carboxymethyl Cellulose. Polymers 13, 1345. https://doi.org/10.3390/polym13081345
175. Rahman, T., Ichiki, T., 2017. Fabrication and Characterization of a Stabilized Thin Film Ag/AgCl Reference Electrode Modified with Self-Assembled Monolayer of Alkane Thiol Chains for Rapid Biosensing Applications. Sensors 17, 2326. https://doi.org/10.3390/s17102326
176. Rajisha, K.R., Deepa, B., Pothan, L.A., Thomas, S., 2011. 9 - Thermomechanical and spectroscopic characterization of natural fibre composites, in: Zafeiropoulos, N.E. (Ed.), Interface Engineering of Natural Fibre Composites for Maximum Performance, Woodhead Publishing Series in Composites Science and Engineering. Woodhead Publishing, pp. 241–274. https://doi.org/10.1533/9780857092281.2.241
177. Randles, J.E.B., 1947. Kinetics of rapid electrode reactions. Discuss. Faraday Soc. 1, 11–19. https://doi.org/10.1039/DF9470100011
178. Rawat, S., Vengurlekar, S., Rakesh, B., Jain, S., Srikarti, G., 2008. Transdermal Delivery by Iontophoresis. Indian J Pharm Sci 70, 5–10. https://doi.org/10.4103/0250-474X.40324
179. Reddy, Y.K., Reddy, D.M., Kumar, M.A., 2012. Transdermal Drug Delivery System: A Review.
180. Reilly, J.P., 1998. Applied bioelectricity: from electrical stimulation to electropathology. Springer, New York.
181. Rivadeneyra, A., Fernández-Salmerón, J., Banqueri, J., López-Villanueva, J.A., Capitan-Vallvey, L.F., Palma, A.J., 2014. A novel electrode structure compared with interdigitated electrodes as capacitive sensor. Sensors and Actuators B: Chemical 204, 552–560. https://doi.org/10.1016/j.snb.2014.08.010
182. Riviere, J.E., Heit, M.C., 1997. Electrically-assisted transdermal drug delivery. Pharm Res 14, 687–697. https://doi.org/10.1023/a:1012129801406
183. Roustit, M., Blaise, S., Cracowski, J.-L., 2013. Trials and tribulations of skin iontophoresis in therapeutics 9.
184. Saepang, K., Li, S.K., Chantasart, D., 2021. Effect of Pulsed Direct Current on Iontophoretic Delivery of Pramipexole across Human Epidermal Membrane In Vitro. Pharm Res 38, 1187–1198. https://doi.org/10.1007/s11095-021-03055-3
185. Saghafi, M., Chinnathambi, S., Lemay, S.G., 2023. High-frequency phenomena and electrochemical impedance spectroscopy at nanoelectrodes. Current Opinion in Colloid & Interface Science 63, 101654. https://doi.org/10.1016/j.cocis.2022.101654
186. Sandby-Møller, J., Poulsen, T., Wulf, H.C., 2003. Epidermal Thickness at Different Body Sites: Relationship to Age, Gender, Pigmentation, Blood Content, Skin Type and Smoking Habits. Acta Dermato-Venereologica 83, 410–413. https://doi.org/10.1080/00015550310015419
187. Sansonetti, A., Bertasa, M., Corti, C., Rampazzi, L., Monticelli, D., Scalarone, D., Sassella, A., Canevali, C., 2021. Optimization of Copper Stain Removal from Marble through the Formation of Cu(II) Complexes in Agar Gels. Gels 7, 111. https://doi.org/10.3390/gels7030111
188. Sargioti, N., Levingstone, T.J., O'Cearbhaill, E.D., McCarthy, H.O., Dunne, N.J., 2023. Metallic Microneedles for Transdermal Drug Delivery: Applications, Fabrication Techniques and the Effect of Geometrical Characteristics. Bioengineering 10, 24. https://doi.org/10.3390/bioengineering10010024
189. Sartawi, Z., Blackshields, C., Faisal, W., 2022. Dissolving microneedles: Applications and growing therapeutic potential. Journal of Controlled Release 348, 186–205. https://doi.org/10.1016/j.jconrel.2022.05.045

190. Shahzad, Y., Louw, R., Gerber, M., du Plessis, J., 2015. Breaching the skin barrier through temperature modulations. Journal of Controlled Release 202, 1–13. https://doi.org/10.1016/j.jconrel.2015.01.019
191. Shams-Nateri, A., Piri, N., 2015. Prediction of emission spectra of fluorescence materials using principal component analysis. Color Research & Application 41. https://doi.org/10.1002/col.21959
192. Shinde, J., Panchal, D.C.V., Poul, D.B.N., Patil, D.S.S., 2022. TRANSDERMAL DRUG DELIVERY SYSTEM: A PAINLESS METHOD FOR HEALTHY SKIN-A REVIEW. World Journal of Pharmaceutical Research.
193. Shinwari, M.W., Zhitomirsky, D., Deen, I.A., Selvaganapathy, P.R., Deen, M.J., Landheer, D., 2010. Microfabricated reference electrodes and their biosensing applications. Sensors (Basel) 10, 1679–1715. https://doi.org/10.3390/s100301679
194. Sigma-Aldrich, 1997. ALBUMIN, BOVINE [WWW Document]. URL https://www.sigmaaldrich.com/deepweb/assets/sigmaaldrich/product/documents/147/858/a4919pis.pdf (accessed 7.24.23).
195. Singh, I., Morris, A.P., 2011. Performance of transdermal therapeutic systems: Effects of biological factors. Int J Pharm Investig 1, 4–9. https://doi.org/10.4103/2230-973X.76721
196. Sloan, J.B., 1986. Iontophoresis in dermatology.
197. Sloan, K.B., Wasdo, S.C., Rautio, J., 2006. Design for optimized topical delivery: Prodrugs and a paradigm change. Pharm Res 23, 2729–2747. https://doi.org/10.1007/s11095-006-9108-0
198. Sonia, T.A., Sharma, C.P., 2014. 2 - Routes of administration of insulin, in: Sonia, T.A., Sharma, C.P. (Eds.), Oral Delivery of Insulin, Woodhead Publishing Series in Biomedicine. Woodhead Publishing, pp. 59–112. https://doi.org/10.1533/9781908818683.59
199. Sophocleous, M., Atkinson, J.K., 2017. A review of screen-printed silver/silver chloride (Ag/AgCl) reference electrodes potentially suitable for environmental potentiometric sensors. Sensors and Actuators A: Physical 267, 106–120. https://doi.org/10.1016/j.sna.2017.10.013
200. Soullard, L., Bayle, P.-A., Lancelon-Pin, C., Rolere, S., Texier, I., Jean, B., Nonglaton, G., 2023. Optimization of the methacrylation of carboxymethylcellulose and use for the design of hydrogels and cryogels with controlled structure and properties. Cellulose 30, 6203–6217. https://doi.org/10.1007/s10570-023-05266-w
201. Sozio, P., Cerasa, L.S., Marinelli, L., Di Stefano, A., 2012. Transdermal donepezil on the treatment of Alzheimer's disease. Neuropsychiatr Dis Treat 8, 361–368. https://doi.org/10.2147/NDT.S16089
202. Sparavigna, A.C., 2014. Paper-based Metamaterials: Honeycomb and Auxetic Structures. International Journal of Sciences 22–25. https://doi.org/10.18483/ijSci.597
203. Suikkola, J., Björninen, T., Mosallaei, M., Kankkunen, T., Iso-Ketola, P., Ukkonen, L., Vanhala, J., Mäntysalo, M., 2016. Screen-Printing Fabrication and Characterization of Stretchable Electronics. Sci Rep 6, 25784. https://doi.org/10.1038/srep25784
204. Tanner, T., Marks, R., 2008. Delivering drugs by the transdermal route: review and comment. Skin Research and Technology 14, 249–260. https://doi.org/10.1111/j.1600-0846.2008.00316.x
205. Thorpe, C.T., Birch, H.L., Clegg, P.D., Screen, H.R.C., 2015. Chapter 1 - Tendon Physiology and Mechanical Behavior: Structure–Function Relationships, in: Gomes, M.E., Reis, R.L., Rodrigues, M.T. (Eds.), Tendon Regeneration. Academic Press, Boston, pp. 3–39. https://doi.org/10.1016/B978-0-12-801590-2.00001-6
206. Tjon, K.C.E., Yuan, J., 2020. Fabrication of Thin Film Silver/Silver Chloride Electrodes with Finely Controlled Single Layer Silver Chloride. JoVE 60820. https://doi.org/10.3791/60820

207. Tromelin, A., Andriot, I., Guichard, E., 2006. 9 - Protein–flavour interactions, in: Voilley, A., Etiévant, P. (Eds.), Flavour in Food, Woodhead Publishing Series in Food Science, Technology and Nutrition. Woodhead Publishing, pp. 172–207. https://doi.org/10.1533/9781845691400.2.172
208. Tuan-Mahmood, T.-M., McCrudden, M.T.C., Torrisi, B.M., McAlister, E., Garland, M.J., Singh, T.R.R., Donnelly, R.F., 2013. Microneedles for intradermal and transdermal drug delivery. Eur J Pharm Sci 50, 623–637. https://doi.org/10.1016/j.ejps.2013.05.005
209. Turner, J.G., White, L.R., Estrela, P., Leese, H.S., 2021. Hydrogel-Forming Microneedles: Current Advancements and Future Trends. Macromolecular Bioscience 21, 2000307. https://doi.org/10.1002/mabi.202000307
210. Uchida, T., Kadhum, W.R., Kanai, S., Todo, H., Oshizaka, T., Sugibayashi, K., 2015. Prediction of skin permeation by chemical compounds using the artificial membrane, Strat-M^{TM}. European Journal of Pharmaceutical Sciences 67, 113–118. https://doi.org/10.1016/j.ejps.2014.11.002
211. van der Geest, R., Elshove, D.A.R., Danhof, M., Lavrijsen, A.P.M., Boddé, H.E., 1996. Non-invasive assessment of skin barrier integrity and skin irritation following iontophoretic current application in humans. Journal of Controlled Release 41, 205–213. https://doi.org/10.1016/0168-3659(96)01329-6
212. Van der Maaden, K., Jiskoot, W., Bouwstra, J., 2012. Microneedle technologies for (trans)dermal drug and vaccine delivery. Journal of Controlled Release, Drug Delivery Research in Europe 161, 645–655. https://doi.org/10.1016/j.jconrel.2012.01.042
213. Vijayan, V., Connolly, J.P., Condell, J., McKelvey, N., Gardiner, P., 2021. Review of Wearable Devices and Data Collection Considerations for Connected Health. Sensors (Basel) 21, 5589. https://doi.org/10.3390/s21165589
214. Vranić, E., 2003. Iontophoresis: fundamentals, developments and application. Bosn J of Basic Med Sci 3, 54–58. https://doi.org/10.17305/bjbms.2003.3530
215. Wang, B., Petrossians, A., Weiland, J.D., 2014. Reduction of Edge Effect on Disk Electrodes by Optimized Current Waveform. IEEE Trans Biomed Eng 61, 2254–2263. https://doi.org/10.1109/TBME.2014.2300860
216. Wang, Q.L., Ren, J.W., Chen, B.Z., Jin, X., Zhang, C.Y., Guo, X.D., 2018. Effect of humidity on mechanical properties of dissolving microneedles for transdermal drug delivery. Journal of Industrial and Engineering Chemistry 59, 251–258. https://doi.org/10.1016/j.jiec.2017.10.030
217. Wang, R., Jiang, G., Aharodnikau, U.E., Yunusov, K., Sun, Y., Liu, T., Solomevich, S.O., 2022. Recent Advances in Polymer Microneedles for Drug Transdermal Delivery: Design Strategies and Applications. Macromolecular Rapid Communications 43, 2200037. https://doi.org/10.1002/marc.202200037
218. Ward, R.M., Kern, S.E., 2017. 19 - Principles of Pharmacokinetics, in: Polin, R.A., Abman, S.H., Rowitch, D.H., Benitz, W.E., Fox, W.W. (Eds.), Fetal and Neonatal Physiology (Fifth Edition). Elsevier, pp. 201–207. https://doi.org/10.1016/B978-0-323-35214-7.00019-6
219. Williams, A.C., Barry, B.W., 2012. Penetration enhancers. Advanced Drug Delivery Reviews, MOST CITED PAPERS IN THE HISTORY OF ADVANCED DRUG DELIVERY REVIEWS: A TRIBUTE TO THE 25TH ANNIVERSARY OF THE JOURNAL 64, 128–137. https://doi.org/10.1016/j.addr.2012.09.032
220. Wing, D., Prausnitz, M.R., Buono, M.J., 2013. Skin pretreatment with microneedles prior to pilocarpine iontophoresis increases sweat production. Clinical Physiology and Functional Imaging 33, 436–440. https://doi.org/10.1111/cpf.12053
221. Wivell, S.C., 1996. (73) Assignee: Chesebrough-Pond's USA Co.,.

222. Worgull, M., Kolew, A., Heilig, M., Schneider, M., Dinglreiter, H., Rapp, B., 2011. Hot embossing of high performance polymers. Microsyst Technol 17, 585–592. https://doi.org/10.1007/s00542-010-1155-0
223. Wu, W., 2019. Stretchable electronics: functional materials, fabrication strategies and applications. Science and Technology of Advanced Materials 20, 187–224. https://doi.org/10.1080/14686996.2018.1549460
224. Wu, X.-M., Todo, H., Sugibayashi, K., 2007. Enhancement of skin permeation of high molecular compounds by a combination of microneedle pretreatment and iontophoresis. Journal of Controlled Release 118, 189–195. https://doi.org/10.1016/j.jconrel.2006.12.017
225. Xiang, C., Papadantonakis, K.M., Lewis, N.S., 2016. Principles and implementations of electrolysis systems for water splitting. Mater. Horiz. 3, 169–173. https://doi.org/10.1039/C6MH00016A
226. Xu, C., Willenbacher, N., 2018. How rheological properties affect fine-line screen printing of pastes: a combined rheological and high-speed video imaging study. J Coat Technol Res 15, 1401–1412. https://doi.org/10.1007/s11998-018-0091-2
227. Yan, G., Li, S.K., Higuchi, W.I., 2005. Evaluation of constant current alternating current iontophoresis for transdermal drug delivery. Journal of Controlled Release 110, 141–150. https://doi.org/10.1016/j.jconrel.2005.09.006
228. Yang, J., Li, Y., Ye, R., Zheng, Y., Li, X., Chen, Y., Xie, X., Jiang, L., 2020. Smartphone-powered iontophoresis-microneedle array patch for controlled transdermal delivery. Microsyst Nanoeng 6, 112. https://doi.org/10.1038/s41378-020-00224-z
229. Yao, K., Zhou, J., Huang, Q., Wu, M., 2022. Encoding of tactile information in hand via skin-integrated wireless haptic interface. Nature Machine Intelligence 4, 893–903. https://doi.org/10.1038/s42256-022-00543-y
230. Ye, R., 2021. Applications of 3D printing in dentistry - 3ERP [WWW Document]. Rapid Prototyping & Low Volume Production. URL https://www.3erp.com/blog/applications-of-3d-printing-in-dentistry/ (accessed 8.7.23).
231. Yin, P., Wang, Y., Yanyan, Q., Hou, L., Liu, X., Qin, J., Duan, Y., Liu, P., Qiu, M., Li, Q., 2012. Bufalin-loaded mPEG-PLGA-PLL-cRGD nanoparticles: Preparation, cellular uptake, tissue distribution, and anticancer activity. International journal of nanomedicine 7, 3961–9. https://doi.org/10.2147/IJN.S32063
232. Young, M.E., Carroad, P.A., Bell, R.L., 1980. Estimation of diffusion coefficients of proteins. Biotechnology and Bioengineering 22, 947–955. https://doi.org/10.1002/bit.260220504
233. Zakzewski, C.A., Li, J.K.-J., 1991. Pulsed mode constant current iontophoretic transdermal metaprolol tartrate delivery in established acute hypertensive rabbits. Journal of Controlled Release 17, 157–162. https://doi.org/10.1016/0168-3659(91)90055-I
234. Zavanelli, N., Yeo, W.-H., 2021. Advances in Screen Printing of Conductive Nanomaterials for Stretchable Electronics. ACS Omega 6, 9344–9351. https://doi.org/10.1021/acsomega.1c00638
235. Zhang, J., Hu, Q., Wang, S., Tao, J., Gou, M., 2019. Digital Light Processing Based Three-dimensional Printing for Medical Applications. Int J Bioprint 6, 242. https://doi.org/10.18063/ijb.v6i1.242
236. Zhang, J., Xie, Z., Zhang, N., Zhong, J., 2017. Chapter 13 - Nanosuspension drug delivery system: preparation, characterization, postproduction processing, dosage form, and application, in: Andronescu, E., Grumezescu, A.M. (Eds.), Nanostructures for Drug Delivery, Micro and Nano Technologies. Elsevier, pp. 413–443. https://doi.org/10.1016/B978-0-323-46143-6.00013-0

237. Zhang, P., Dalton, C., Jullien, G.A., 2009. Design and fabrication of MEMS-based microneedle arrays for medical applications. Microsyst Technol 15, 1073–1082. https://doi.org/10.1007/s00542-009-0883-5
238. Zheng, Y., Ye, R., Gong, X., Yang, J., Liu, B., Xu, Y., Nie, G., Xie, X., Jiang, L., 2023. Iontophoresis-driven microneedle patch for the active transdermal delivery of vaccine macromolecules. Microsystems and Nanoengineering 9. https://doi.org/10.1038/s41378-023-00515-1
239. Zhu, Z., Hassanin, H., Jiang, K., 2010. A soft moulding process for manufacture of net-shape ceramic microcomponents. Int J Adv Manuf Technol 47, 147–152. https://doi.org/10.1007/s00170-008-1864-z
240. Zielinksi, T.J., Sweeney, R., Harvey, E., Hanson, D.M., 2023. Quantum States of Atoms and Molecules.
241. Zsom, R.L.J., 1986. Dependence of preferential bovine serum albumin oligomer adsorption on the surface properties of monodisperse polystyrene latices. Journal of Colloid and Interface Science 111, 434–445. https://doi.org/10.1016/0021-9797(86)90046-9

Graphical Abstract, Labex Arcane 2022 contest (2nd prize)